ISBN 978-82-326-2222-1 (printed version)
ISBN 978-82-326-2223-8 (electronic version)
ISSN 1503-8181

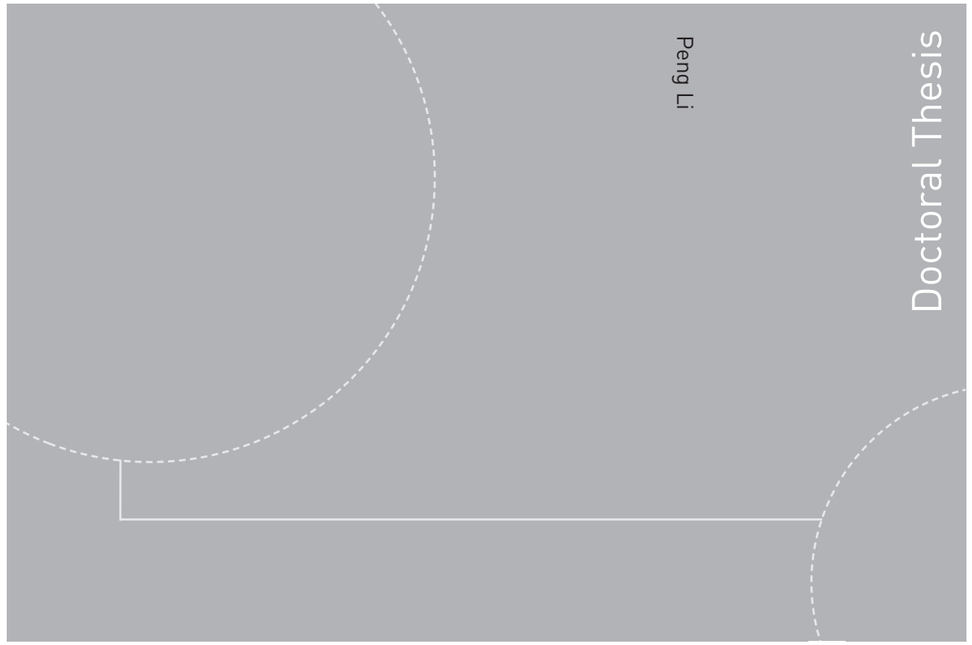

Doctoral theses at NTNU, 2017:75

Peng Li

A Theoretical and Experimental Study of Wave-induced Hydroelastic Response of a Circular Floating Collar

NTNU
Norwegian University of
Science and Technology
Faculty of Engineering Science and Technology
Department of Marine Technology

NTNU
Norwegian University of
Science and Technology

Doctoral theses at NTNU, 2017:75

NTNU

NTNU
Norwegian University of
Science and Technology

Peng Li

A Theoretical and Experimental Study of Wave-induced Hydroelastic Response of a Circular Floating Collar

Thesis for the degree of Philosophiae Doctor

Trondheim, April 2017

Norwegian University of Science and Technology
Faculty of Engineering Science and Technology
Department of Marine Technology

NTNU
Norwegian University of
Science and Technology

NTNU
Norwegian University of Science and Technology

Thesis for the degree of Philosophiae Doctor

Faculty of Engineering Science and Technology
Department of Marine Technology

ISBN 978-82-326-2222-1 (printed version)
ISBN 978-82-326-2223-8 (electronic version)
ISSN 1503-8181

Doctoral theses at NTNU, 2017:75

Printed by Skipnes Kommunikasjon as

to my parents
to my elder sister

Abstract

Wave-induced hydroelastic response of a circular plastic collar used as a floater of a net cage in aquaculture is studied by means of theory, model tests and numerical simulations.

A low-frequency linear slender-body theory for vertical radiation loads on an elastic semi-submerged torus based on matched asymptotic expansions is developed. Low frequency means that the corresponding wavelength is long relative to the cross-sectional radius. Linear vertical excitation load is calculated by either solving the diffraction problem with a cross-sectional averaged vertical incident wave velocity along the torus or by using a generalized Haskind relation. A curved beam equation with tension effects is used to predict the vertical wave-induced response of a semi-submerged torus in the frequency domain. The theory is verified by comparing with WAMIT. The analysis shows that three-dimensional flow, strong hydrodynamic frequency dependency and hydroelasticity are essential for the considered vertical wave loads and responses of the torus.

Model tests of both an elastic and a nearly rigid torus were performed in regular waves of different wave periods and steepness in order to validate the low-frequency slender-body theory. The bending stiffness of the elastic model was Froude scaled. Vertical accelerations along the torus, mooring line forces and the free-surface elevation at four positions in the wave tank were measured. Overtopping and out of water of parts of the torus models occurred in steep waves. Experimental precision errors and bias errors, for instance, due to tank-wall interference are discussed.

There is reasonable agreement between experiments and theoretically/numerically predicted linear response. The agreement between numerical methods and experiments is generally unsatisfactory for the nonlinear response. The two sets of experimental results show that the second, third and fourth harmonic vertical accelerations of the torus matter and cannot be explained by a perturbation method with the wave steepness as a small parameter.

Acknowledgements

First and foremost I would like to thank my supervisor Prof. Odd M. Faltinsen for his great contributions to this work. It is his patient guidance and continuous encouragement that enabled me to finish the work and write this thesis. His perpetual energy and enthusiasm in research extremely motivated me in my studies. He showed me how to dissect the challenges into as many different ways as possible and to look at them from different angles, which make me benefit throughout these years.

I want to thank all the lectures who taught courses in my first year and helped me understand so much knowledge on marine hydrodynamics.

I am grateful to Prof. Marilena Greco and she has been partly involved in my work by providing numerical results. I wish to thank Prof. Claudio Lugni (INSEAN)for the help of improving the accuracy of processing the experimental data. Prof. Nicholas Newman for his help with the use of WAMIT. Bureau Veritas for the free use and Dr. Xiaobo Chen and Dr. Guillaume de-Hautecloque for discussions of HydroStar and Torgeir Wahl for his help during the experiments are greatly appreciated. I also want to express my appreciation for the valuable suggestions from and discussions with Prof. Trygve Kristiansen, Dr. David Kristiansen, Dr. Yanlin Shao, Dr. Babak Ommani, Mohsen Bardestani, Isar Ghamari and Yugao Shen. I am thankful to Dr. Zhiyu Jiang, Dr. Xiaopeng Wu, Dr. Kai Wang, Zhao He, Dr. Qin Zhang, Dr. Zhenju Chuang, Dr. Jikun You and Dr. Renato Skejic who have always been helpful. Dr. Xu Xiang is acknowledged for proof-reading parts of the thesis. Special thanks to Ping Fu for her encouragement and help.

The major part of this work was financially supported by the Research Council of Norway through the Center for Research-based Innovation in Aquaculture Technology (CREATE), SINTEF Fisheries and Aquaculture. This support was appreciated.

My deepest gratitude goes to my parents and my elder sister for their support, encouragement and unflagging love throughout my life. My family, I love you.

Nomenclature

General Rules

- Only the most used symbols are listed in the following sections
- Meaning of symbols are given when introduced in the thesis
- Sometimes the same symbol is used to indicate different quantities
- Vectors are represented by bold symbols

Abbreviations

2D	Two-dimensional
3D	Three-dimensional
BEM	Boundary Element Method
CFD	Computational Fluid Dynamics
COG	Center of gravity
DFT	Discrete Fourier Transform
Exp	Experimental values
FPS	Frames per second
HDPE	High-density polyethylene
RAO	Response Amplitude Operator

Bold Symbols

$\mathbf{n}$	Normal vector
$\mathbf{u}$	Water velocity vector
$\mathbf{U}_B$	Vector of instantaneous body velocity
$\mathbf{x}$	Position vector

Greek Letters

(ρ, β, z)	Cylindrical coordinate system
α_n	Phase angle of mode n
δ	Dirac delta function
η_1	Surge motion
η_2	Sway motion

η_5	Pitch angle
λ	Wave length
μ	Mean value or dynamic viscosity of water
ν	Wave number or kinematic viscosity of water
Ω	Water domain
ω	Circular frequency
ω_i	Natural frequency associated with 2D transverse sloshing modes
ρ	Mass density of water
σ	Standard deviation
ε	Nondimensional slenderness parameter
φ	Velocity potential
φ^F	Far-field velocity potential
φ^N	Near-field velocity potential
φ_0	Incident wave potential
ζ	Free-surface elevation
ζ_a	Wave amplitude of incident waves

Mathematical Operators

$\nabla\times$	Curl
∇	Gradient
$\nabla\cdot$	Divergence
∇^2	Laplacian
$\sum$	Summation

Roman Letters

$\mathbf{H}_0$	Struve function of zero order
S_B	Wetted body surface
$\bar{S}_B$	Mean wetted body surface
a	Radius of the cross-section of the torus
$a_{33}^{(n)}$	Sectional vertical added mass coefficient of mode n
a_n	Generalized coordinate of vertical motion of mode n
$b_{33}^{(n)}$	Sectional vertical damping coefficient of mode n
b_n	Generalized coordinate of radial motion of mode n
b_{tank}	Width of wave tank
c	Radius of the torus
E	Sum of the kinetic and potential energy in the water domain
EI	Bending stiffness

$f_3^{(n)}$	Sectional vertical wave excitation force of mode n
f_3^D	Vertical diffraction force per unit length
f_3^{FK}	Vertical Froude-Kriloff force per unit length
F_v	Viscous force
G	Green function
g	Acceleration of gravity
H	Wave height of incident waves
h	Depth of wave tank
J_n	Bessel function of the first kind of the n-th order
K_n	Modified Bessel function of the n-th order
k_s	Spring stiffness
KC	Keulegan-Carpenter number
L_{tank}	Length of wave tank
m	Torus mass per unit length
$Or'\theta$	Polar coordinate system
$Ox_By_Bz_B$	A body-fixed Cartesian coordinate system with origin at COG
$Oxyz$	Earth-fixed Cartesian coordinate system
$Oy'z'$	Local Cartesian coordinate system
p	Pressure
Q	Source density
r_a	Amplitude of relative vertical motion
s	Arc length along a structure
S_∞	Vertical circular cylindrical control surface at infinity from the structure
S_C	Mean wetted cross-sectional surface of the torus
T	Wave period of incident waves
t	Time
T_{as}	Axial stiffness
T_p	Pre-tension of the mooring lines
U_a	Flow velocity amplitude
v_r	Radial motion
w	Vertical motion
w_a	Amplitude of absolute vertical motion
Y_n	Bessel function of the second kind of the n-th order

Super-scripts

$(n\omega)$	n-th harmonic
(n)	Mode n

Sub-scripts

$\bar{S}_B$	On mean wetted body surface
S_C	On mean wetted cross-sectional surface of the torus

Contents

Chapter 1

Introduction

1.1 Background and motivation

Fishing in oceans, lakes and rivers has historically been a major source of food. However, with the increased knowledge and development of fisheries and aquaculture, it was realized that living aquatic resources, although renewable, are not infinite and need to be properly managed. The Food and Agriculture Organization of the United Nations (FAO) reported that the increasing demand for marine food production has put a strain on natural populations (FAO, 2010). According to FAO, the ocean's ability to produce enough seafood has diminished over the years and only 20% of wild seafood stocks have a sustainable capacity, the rest are at or beyond the limit of what they can produce.

Aquaculture is important in bridging the gap between the decreasing capture of wild fish and the increasing world demand for food. During the past three decades, global aquaculture production expanded at an average annual rate of more than 8%, from 5.2 million tons in 1981 to 62.7 million tons in 2011. Aquaculture's contribution to total food fish supply grew from 9% in 1980 to 48% in 2011 (FAO, 2014). Worldwide, the rapid and massive growth of aquaculture production makes seafood become the most heavily traded food commodities, with 38% of all fish produced being exported in 2010. World trade of fish and fish products increased from $8 billion in 1976 to $128 billion in 2012, which translates into an average annual growth rate of 4.0% (WBG, 2014). Fish farming is the principal form of aquaculture and farm-raised fish are mainly used for human consumption. However, fish farms also produce ornamental fish, roe, fish oil, bait fish and fish for pet food. Worldwide, the most important fish species used in fish farming are carp, salmon, tilapia and catfish. People will continue to depend on fish farming for food sources as populations increase and the rapid expansion of global aquaculture production has continued with no sign of peaking. Aquaculture can be broken down into two basic categories: marine-based aquaculture and land-based aquaculture. The following description is based on marine-based aquaculture.

1.1.1 Aquaculture in Norway

Aquaculture in Norway dates back to 1850 when the first brown trout were hatched. By around 1900 rainbow trouts were imported from Denmark and the first attempts at pond culture were initiated. An increasing interest was shown after World War II, followed by a breakthrough in the early 1960s when for the first time rainbow trout was successfully transferred to sea water. The first successful feeding of Atlantic salmon also took place during this same period. A technological breakthrough came around 1970 when the first cage was constructed. Norway's long and sheltered coastline surrounded by cold, fresh seawater, with its thousands of islands and inlets, as well as the Gulf stream providing a reliable and stable temperature, provide excellent opportunities for fish farming. Since the advent of commercial salmon farming around 1970 (see Figure 1.1), the aquaculture industry has grown to become an industry of major importance. Not just to the Norwegian economy at large, but especially to the many communities found along the coast where other economic opportunities are sometimes limited. Today, farming of salmon and rainbow trout is taking place in close to 160 municipalities all along the Norwegian coast, from Lillesand in the south to South-Varanger in the north. Along with the growth in salmon and rainbow trout farming, interest has also become oriented towards other marine species such as the Atlantic cod and the Atlantic halibut (FAO, 2005).

Figure 1.1: Manufacturing of the floater of the first Polarcirkel cage in 1974. (AKVA group)

There are also challenges related to the Norwegian fish farming industries. Spread of waste materials from the fish farm, introduction of non-indigenous species caused by escaped fish, and the disease burden influence the marine environment. Salmon lice and fish escape are considered by the industry to be the two most important problems. Close collaboration between researchers and industry has made the Norwegian fish farming industry become the chief developer of modern marine

aquaculture, both in Norway and internationally. Today, advances in technology coupled with improvements in design that yield more productive operations have significantly increased the practice of fish farms and there is no other form of animal food production where such a high biomass is gathered in such a small area.

(a) Fixed cage (www.thefishsite.com)

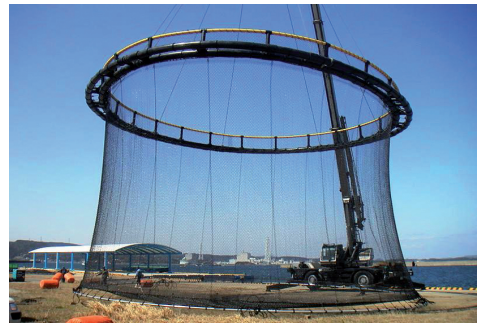

(b) Floating cage (PMM Marine)

(c) Submersible cage (InnovaSea)

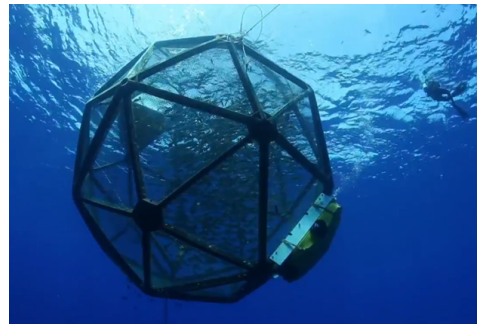

(d) Submerged cage (InnovaSea)

Figure 1.2: Four basic types of fish cages.

1.1.2 Fish cage classifications and common components

Cages have developed a great deal since their inception and today there is a diversity of types and designs. There are also different ways to classify types of cages. Figure 1.2 shows four basic types proposed by Beveridge (2008): *a*) Fixed cages, which consist of a net supported by posts driven into the bottom of a lake or river. They are comparatively inexpensive and simple to build, but their use is restricted to sheltered shallow sites with suitable substrates. *b*) Floating cages, which have a buoyant frame or collar that support the net cage. They are less limited than most other types of cages in terms of site requirements and can be made in a great variety of designs, and are the most widely used ones. *c*) Submersible cages, which rely on a frame or rigging to maintain shape. The advantage

over other designs is that its position in the water column can be changed to take advantage of prevailing environmental conditions. Generally these cages are kept at the surface during calm weather and submerged during adverse weather. *d*) Submerged cages, which can be boxes with gaps between the slats to facilitate water flow. They are anchored to the substrate by stones or posts and used in flowing waters. On the other hand, Loverich and Gace (1997) classified the cages into four classes according to the effects of the currents and waves. *a*) Gravity cages, which rely on buoyancy and weight to hold the shape of the cage and volume against externally applied forces. *b*) Anchor tensioned cages, which rely on anchor tension to hold their shape. *c*) Self-tensioned and supporting cages, where the self-tension structure resists net deformations. *d*) Rigid cages with self-supporting structures made of jointed beams and trusses.

The different classes of cages can be built in several types and sizes. However most of them present the following common components as illustrated in Figure 1.3: floating system, net, services system, mooring system and anchor system (Olivares and Brynjolfsson, 2003).

The *floating system* provides buoyancy and holds the system at a suitable level in the water. In some cages this component is an important part to hold the shape of the cage. Common flotation materials include high-density polyethylene (HDPE) pipes, metal or plastic drums, rubber tires and metal drums coated with tar or fiberglass. The buoyant force varies depending of size and materials used. The assembly of the system can be by connectors, stitching or tying.

The function of the *net* is to contain and protect the fish and to provide a marine habitat. The net is normally flexible and made of synthetic netting of nylon or polythene fibers reinforced with polythene ropes, although recently new stronger materials like Spectra or Dyneema have appeared. The nets are kept stretched vertically with weights at the bottom of the cage or fastened by rope to the framework depending of the type of cages. Rigid cages made of metal netting mounted on rigid metal frameworks are also used. The flexible net cage is most used due to cost. The netting may have 10 million meshes, which prohibits complete Computational Fluid Dynamics (CFD) and structural modeling.

The *services system* provides operating and maintenance services, for example: feeding, cleaning, monitoring or grading. One way to provide this is by a catwalk around the cage or along part of the cage. Some cages use their flotation collars like catwalks and access for these services. Alternative methods to provide these services are by access from a boat or a more stable platform such as a barge or a raft.

The *mooring system* holds the cage in the suitable position according to the direction and depth decided in the design, and sometimes helps to maintain the shape of the cage. The mooring joins the cage at the anchor system. The materials used in the mooring systems are sea steel lines, chains, reinforced plastic ropes and mechanical connectors. The mooring force capacity depends on both the material and size, and can be adjusted to the requirements. Attachment to the system is by metallic connectors and ties.

There are basically three types of *anchor systems*: pile anchors, dead weight anchors and mooring anchors. Pile anchors are buried piles in the seabed. They

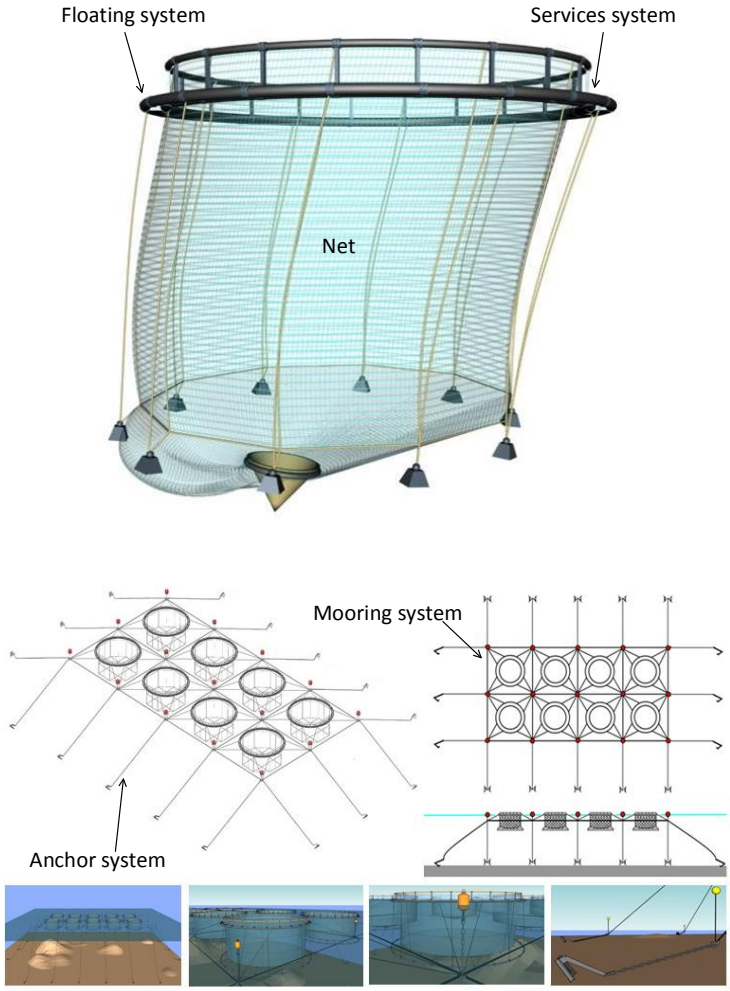

Figure 1.3: Principal components of the cage for fish farming. (Upper figure: SINTEF Fisheries and Aquaculture; lower figure: Toford Plastic Manufacturing Corporation)

are effective, especially for systems where a small space is necessary. Dead weight anchors are usually concrete blocks. Their one big advantage is that they are fairly consistent in holding power. The third type is mooring anchors which have to hold into a particular seabed when pulled from one direction only. The anchors are joined to the mooring system usually by chains and metallic connectors.

Fish cages can be installed in close proximity to one another, to form clusters that can be fed from a single feeder platform and withstand strong currents and waves as shown in Figure 1.4. Square cages are typically clustered together in a

steel platform with between 4 and 28 cages per site with little distance (2 to $4m$) between adjacent cages. Circular cages (typically 6 to 12 per site) are arranged in mooring grids in single, double or triple rows but with typically greater space between them ($> 10m$) than square cages. Initially, cage arrangements within sites are chosen based on logistical considerations such as moorings, shelter and accessibility. Nowadays, cage arrangements have moved towards positioning cage grid mooring systems perpendicular to the dominant current direction to maximize water flow, oxygen supply and the removal of wastes from individual cages (Jensen et al., 2010). Recently, membrane-type and closed cages have been proposed.

Figure 1.4: Left figure: square cages (www.undark.org); right figure: circular cages (www.worldfishing.net).

1.1.3 HDPE floaters

The detailed studies in the thesis relate to cages with high-density polyethylene (HDPE) floaters. They are highly flexible structures and currently widely used in industrial marine aquaculture in many parts of the world due to the versatility of the materials used, the simplicity in the various farming operations and the relatively contained investment capital required. Main structural elements of these cages are the HDPE pipes, which can be assembled in various ways in order to produce collars of different sizes and shapes. There may be one to three such pipes making up a frame. Figure 1.5 shows that the HDPE pipes are held together by a series of brackets with stanchions disposed throughout the entire circumference in order to form the floating collar ring, which is the main structure on which the fish net pen is secured. The presence of the floating filler in the pipes ensures that the cage floats, even if the pipes become damaged and flooded. When used to build circular cages, HDPE pipes are limited by their torsion. Generally, the minimum radius to close and weld a round cage is approximately 25 times the pipe's external diameter. A narrow working platform can be built on top of the circular frame. In Atlantic salmon farming, the floaters currently being installed have a circumference of at least $100m$, in general. In the Mediterranean, the most common floaters have a circumference of 40 to $50m$, but cages with a circumference of around $200m$ are used for tuna farming. These gravity cages maintain the net pen shape and volume

through a system of weights, also known as a sinker system, fixed at the bottom end of the net.

Figure 1.5: Details of HDPE floaters. The straight pipes in the upper photo (FAO) are forced into circles and squares and welded together to become the floaters in the lower photos (www.worldfishing.net).

There are several different HDPE materials used for pipes (FAO, 2015). Those used for cage construction are mainly PE80 or PE100. These codes, according to ISO 4427, relate to the minimum required strength (MRS) of the pipe, measured after 50 years at a temperature of 20°C, and expressed in Bar: PE80 (=MRS 8.0); PE100 (=MRS 10.0). PE80 indicates an HDPE grade where the pipe will rupture at a pressure of at least $8.0MPa$ over a 50 year service life at 20°C. In the case of the PE100 pipe, the pressure would be at $10.0MPa$. This means that, assuming we have pipes of the same dimensions, pipes made of PE100 material may function at a higher operating pressure than pipes made of PE80. The density of PE80 is slightly lower than that of the PE100, with specific-gravity values of $0.945g/cm^3$ and $0.950g/cm^3$, respectively. Therefore, a cage built with PE100 HDPE will be more rigid and stronger than a cage made with PE80 HDPE assuming both pipes are of the same dimensions. However, it will be slightly less flexible in handling dynamic loads. The external diameter of HDPE pipes used for cage building is usually expressed in millimeters. The diameter of the pipes will determine the buoyancy of the cage collar. The more exposed the site, the more buoyancy will be needed and the pipe diameter will need to be larger. Another factor of HDPE

is wall thickness. Different pressure-resistance grades imply a different pipe wall thickness and as a consequence, cage weight, strength, resistance and flexibility will be different. Therefore, the higher the pipe pressure-resistance is, the thicker the pipe wall thickness will be. HDPE pipes use the standard dimension ratio (SDR) as a method of rating the piping. The SDR is the ratio of pipe outside diameter D in mm to wall thickness s in mm. The pipe wall will be thinner with a high SDR ratio. Therefore, a high SDR pipe has a lower pressure rating, and a low SDR pipe has a higher pressure rating.

1.1.4 Environmental factors and challenges for fish farms

Wave, wind and current loads have to be considered in design and installation of fish farms. Table 1.1 shows classification of significant wave height and current speed by the Norwegian government (Klebert et al., 2015).

Table 1.1: Norwegian aquaculture site classification scheme for waves and currents. H_s: wave height; T_p: wave period; V_c: current speed.

Wave	$H_s(m)$	$T_p(s)$	Degree of exposure	Current	$V_c(m/s)$	Degree of exposure
A	0.0-0.5	0.0-2.0	Small	a	0.0-0.3	Small
B	0.5-1.0	1.6-3.2	Moderate	b	0.3-0.5	Moderate
C	1.0-2.0	2.5-5.1	Medium	c	0.5-1.0	Medium
D	2.0-3.0	4.0-6.7	High	d	1.0-1.5	High
E	>3.0	5.3-18.0	Extreme	e	>1.5	Extreme

The *current* affects water exchange, feed dispersion, cage net weights and sinkers, net shape and rearing volumes and design of mooring system. Current accounts for $70-75$ percent of total forces on a typical mid-size fish cage (*i.e.* with a production between $3000-4000$ tonnes/year) in medium current conditions defined in Table 1.1.

Wind accounts for approximately $5-10$ percent of the total forces on a cage mooring system. Wind can generate pull on the jump net and also have an indirect influence on cages through wind-driven current and wind-generated waves.

Waves account for approximately $20-25$ percent of the total forces affecting the mooring and the equipment on a typical mid-size fish cage ($3000-4000$ tonnes/year). Five factors influence the formation of wind-generated waves: wind speed; the uninterrupted distance of open water over which the wind blows without significant change in direction (called the fetch); width of area affected by fetch; time duration-the wind has blown over a given area; water depth. All of these factors work together to determine the waves. Currents also indirectly influence the waves, as winds against currents generate shorter and steeper waves.

The loads on the fish farm are divided into two types: *a*) vertical static loads due to weight and buoyancy. They depend on area and density of the netting, weights of frame components, weight of rigging, weight of ballast and, in opposition, the flotation force. *b*) dynamic loads, which are caused by the currents, winds and waves with reaction in the moorings and anchors of the cage. These depend of material used, shape of panel, size of the mesh, current velocity and density of water.

Figure 1.6: Collapsed fish farms due to harsh weather. (www.thetower.org)

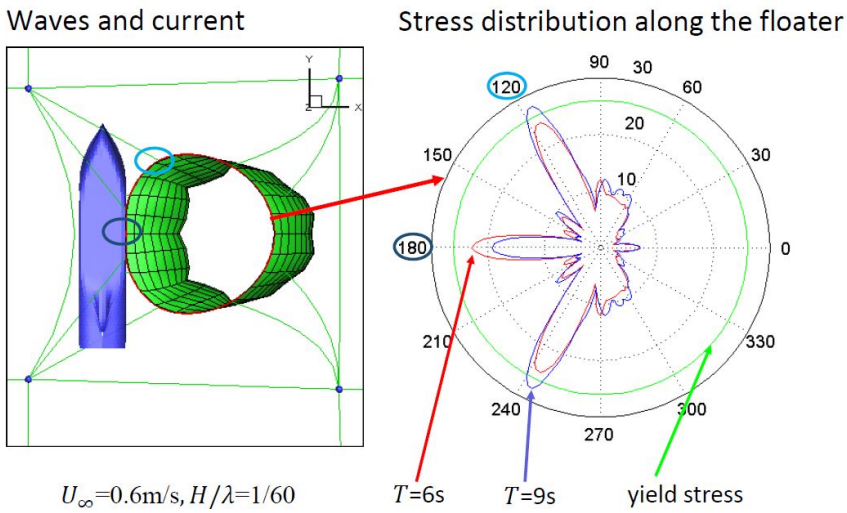

Figure 1.7: Bending stress distribution in the floater in harsh weather with current velocity $U_\infty = 0.6m/s$, wave height-to-wave length ratio $H/\lambda = 1/60$ and two wave periods $T = 6s$ and $9s$. (Yugao Shen)

One of the greatest environmental and/or economic challenges that the fish farming industry experiences is the escape of farmed fish. There are many causes

of escape: ranging from poor operating routines, boat collisions, attacks by predators to technical installation failures and structural failure of one or more of the components of a fish farm. Structural failure as shown in Figure 1.6 is the dominant cause for escapes. Snap loads in the netting due to relative vertical motions between the floater and the sinker tube can cause net rupture (Bardestani and Faltinsen, 2013). Shen et al. (2016) analyzed the effect of a well boat at a fish farm and showed that the bending stress in the floater in harsh weather could exceed the yield stress at the contact area between the well boat and the floater and at the connections between mooring lines and floater. Figure 1.7 shows the stress distributions along the floater from 0° to 360° for two cases with current velocity $U_\infty = 0.6m/s$, wave height-to-wave length ratio 1/60 and two wave periods $T = 6s$ and $9s$. Blue line represents the yield stress $26MPa$. The peak stress appears at the positions where the mooring lines at 117° and 143° are attached. The stresses are $25MPa$ and $27.5MPa$ for $T = 6s$ and $9s$ at 117° and 143°, respectively. There are also local peak values in the contact region between the well boat and the fish farm (180°) which are $22.3MPa$ and $19.5MPa$ for $T = 6s$ and $9s$, respectively.

1.2 Previous floater studies

In this study, the focus is on the wave-induced response of the floating collar without the net cage and a complete mooring system. The floating net cage aquaculture system is normally circular or square with floating HDPE pipe as shown in Figure 1.5. The floater experiences direct environmental loads as well as forces from the mooring system and the net cage (Kristiansen and Faltinsen (2012) and Kristiansen and Faltinsen (2015)). Wave forces acting on the floater are complex, not only because of the special shape but also because its large motion, making the calculation of correct hydrodynamic loads difficult. Figure 1.8 illustrates that the circular floater of HDPE can be considerably deformed in bad weather and has a tendency to follow the waves.

Figure 1.8: Open cage fish farm of circular floating collar of HDPE in bad weather. Large elastic deformations of the floater are clearly seen. (Left: Fusion Marine; right: Hvalpsund Net AS)

Many studies of wave and current induced loads on the floater are based on strip theory by using Morison's equation with mass (C_M) and drag (C_D) coefficients or by using 2D linear potential flow theory with drag-force corrections from Morison's equation and by assuming a rigid floater. The Morison's equation (Faltinsen, 1990) is used widely in offshore engineering for cylinders with small cross-sectional size relative to the incident wave length. Strip theory means that the floater is divided into many mini-segments and that the flow at each segment is assumed hydrodynamically independently of each other. The cross-section of the mini-segment corresponds to the cross-section of the floater. The forces on the whole floater can be obtained by summing the forces on each mini-segment. Huang et al. (2006), Li et al. (2007) and Zhao et al. (2009) have used Morison's equation. Ormberg (1991) used frequency-dependent 2D added mass, damping and wave excitation loads similarly as is done in seakeeping analysis of ships by strip theory. Viscous effects on the horizontal forces were accounted for as drag-force corrections from Morison's equation.

Newman (1977*b*) investigated the forces on a floating rigid torus by using slender-body theory and explained peaks in the hydrodynamic forces to near-standing waves within the torus. 3D flow interactions were thereby included. In addition the heave, surge and pitch motions of the torus due to incident waves were calculated.

In reality, hydroelasticity matters in the analysis of wave-induced loads on floaters made by HDPE. Hydroelasticity means that there is mutual interaction between inertial, hydrodynamic and elastic forces (Heller and Abramson (1959) and Bishop and Price (1979)). Dong et al. (2010) proposed an analytical method to investigate the elastic deformations of a circular ring subjected to second-order waves based on the curved beam theory. Wave-induced forces on a mini-segment was calculated using Morison's equation. Li et al. (2013) combined the effect of hydroelasticity with Morison's equation. A low-frequency slender-body theory for the wave-induced response on an elastic semi-submerged torus was derived by Li and Faltinsen (2012).

The acceptable accuracy of linear potential flow theory assumes that both the wave height and the response are small compared to the cross-dimension. This is typically not the case for the floater in harsh weather. As a step towards using a rational method to combine nonlinear wave effects and flow separation, 2D studies were made by Kristiansen and Faltinsen (2008*a*) and Kristiansen and Faltinsen (2008*b*). They developed a Computational Fluid Dynamics (CFD) numerical wave tank (NWT) for fully nonlinear wave body interaction problems for a 2D moored semi-submerged circular cylinder. Laminar flow were assumed and the Navier-Stokes equation with incompressible fluid were applied. The motivation for their studies was analysis of the floater of a fish farm. Also, two sets of model tests have been conducted. Results were compared with linear potential flow theory, semi-empirical theories and simulations with the Constrained Interpolation Profile (CIP)-based numerical wave tank. An instability phenomenon was observed both in the experiments and in the numerical simulations when the wave frequency was two times the natural frequency in sway. Higher order harmonics of the wave loads can be significant when resonance oscillations are excited and should be taken into

account when fatigue life of fish farms are designed. Tang et al. (2011) developed a two-dimensional fully nonlinear numerical wave tank based on the boundary element method (BEM) to calculate the wave forces on a semi-submerged circular cylinder. The latter method does not account for flow separation. Numerical and physical models were adopted to investigate the dynamic properties of the circular cylinder with and without a fish net. The first- to third-order of sway, heave and roll response amplitude operator of the semi-submerged circular cylinder with or without a fish net were also investigated.

1.3 Outline of the present study

This chapter first introduces the background and motivation of the thesis and then give a review of previous floater studies. The structure and the main contributions of the present work are outlined afterwards. In Chapter 2, the mathematical formulation of the physical problem is presented first, next a low-frequency slender-body theory for the vertical added mass, damping and wave excitation loads on an elastic semi-submerged torus is derived based on linear potential flow. The verification studies of the low-frequency slender-body theory are presented in Chapter 3. An elastic and an rigid torus model tests are described in Chapter 4 with focus on the wave-induced vertical accelerations of a moored torus in regular deep-water waves. In Chapter 5, experimental and numerical results are compared for linear horizontal motion, linear vertical accelerations and sum-frequency vertical accelerations of the rigid torus. In Chapter 6, experimental linear vertical accelerations of the rigid torus are compared with a linear frequency-domain method and a weak-scatter method. The weak-scatter method also predicts the second harmonic acceleration component. Experimental higher-harmonic torus accelerations are presented in Chapter 5 and Chapter 6. Finally, a summary of the present work and suggestions for further work are given in Chapter 7.

1.4 Main contributions

We summarize the main contributions of the present work as follows.

- A low-frequency linear slender-body theory is derived by matched asymptotic expansions with a near-field and far-field solution to study wave-induced vertical elastic response of an elastic semi-submerged torus in the frequency domain. The effect of current is neglected. Low frequency corresponds to a wave length that is long relative to the cross-dimension of the torus. Generalized added mass, damping and wave excitation loads are derived. The diffraction loads are either based on a mean vertical incident wave velocity along the torus or by using a generalized Haskind relation. The theory is verified by comparing with WAMIT.

- The low-frequency linear slender-body theory combined with a curved beam equation with tension for the floater shows that hydroelasticity is important

and that 3D effects cause pronounced frequency-dependent hydrodynamic interaction on the scale of the torus diameter. The latter fact means that a strip theory and Morison's equation are not applicable.

- Two model test series have been performed in regular waves of different wave periods and steepness and used to validate the low-frequency slender-body theory. One model is an elastic circular torus and another model is a nearly rigid circular torus. The bending stiffness of the elastic model has been Froude scaled. Error analysis has been performed.

- The experiments show that the second, third and fourth harmonic measured accelerations of the torus matter and cannot be explained by a perturbation method with the wave steepness as a small parameter.

Chapter 2

Linear analytical wave-induced vertical elastic response of a semi-submerged torus

2.1 General assumptions

We consider incident regular waves on a semi-submerged elastic torus in water of infinite depth and infinite horizontal extent. Potential flow of incompressible water is assumed. A linear frequency-domain solution for vertical responses will be analytically derived based on a long-wave length assumption and matched asymptotic expansions. A long-wave length assumption means that the considered wave lengths are long relative to the cross-sectional diameter of the torus. Matched asymptotic expansions involves defining a far-field and near-field solution that are matched. In the far-field solution we do not see the details of the cross-section of the torus while we in the near-field see the cross-sectional details. We define a Cartesian coordinate system (x, y, z) and a cylindrical coordinate system (ρ, β, z) with the mean free-surface at $z = 0$. The z-axis coincides with the torus axis and is positive upwards. The incident waves propagate along the x-axis. A far-field view where we cannot see the cross-sectional details is presented in Figure 2.1 where c means the radius of the circular center-line curve of the torus. The definitions of the local Cartesian coordinate system $Oy'z'$ and polar coordinate system $Or'\theta$ used in analyzing the near-field solution are presented in Figure 2.2.

2.2 Governing equations

The water velocities are denoted $\mathbf{u}(\mathbf{x}, t) = (u, v, w)$, which are a function of location $\mathbf{x} = (x, y, z)$ and time t in a Cartesian coordinate system fixed in space (Faltinsen,

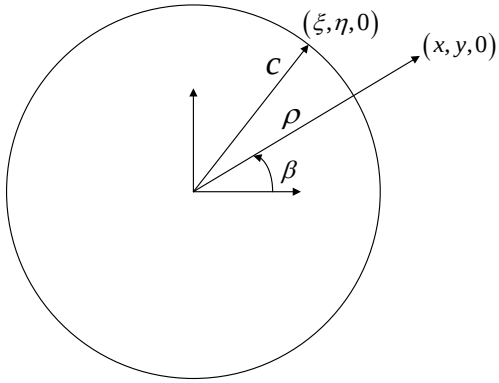

Figure 2.1: Far-field view of one torus with parameter and coordinate definitions. $(x, y, 0)$ is the field point and $(\xi, \eta, 0)$ is a point on the torus. c is the torus radius, β is the angle and ρ is the distance to the field point from the origin.

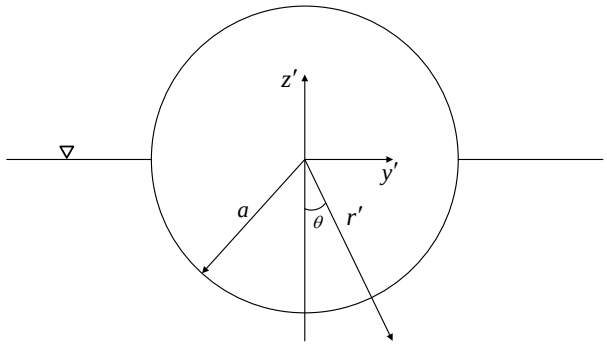

Figure 2.2: Cross-section of a torus with local coordinate systems.

1990). Since the flow is irrotational, *i.e.* $\nabla \times \mathbf{u} = 0$, the water velocities can be defined as a gradient of a velocity potential $\varphi(\mathbf{x}, t)$, *i.e.*

$$\mathbf{u} = \nabla\varphi \equiv \mathbf{i}\frac{\partial\varphi}{\partial x} + \mathbf{j}\frac{\partial\varphi}{\partial y} + \mathbf{k}\frac{\partial\varphi}{\partial z} \tag{2.1}$$

Since the water is incompressible *i.e.* $\nabla\cdot\mathbf{u} = 0$, it follows that the velocity potential φ has to satisfy the Laplace equation (Eq. 2.2) in the water domain, *i.e.*

$$\nabla^2\varphi = \frac{\partial^2\varphi}{\partial x^2} + \frac{\partial^2\varphi}{\partial y^2} + \frac{\partial^2\varphi}{\partial z^2} = 0 \tag{2.2}$$

We assume that the structure has no forward speed and that the current velocity is zero.

2.3 Boundary conditions

The complete mathematical problem of finding a velocity potential consists of the solution of the Laplace equation with relevant conditions along the boundaries of the potential flow domain. Since we consider a frequency-domain solution, initial conditions are not needed. However, we need to specify a radiation condition specifying outgoing waves caused by the torus.

Free-surface boundary condition

The free-surface boundary condition consists of two parts, *i.e.* the *kinematic* and *dynamic* conditions. The kinematic free-surface condition follows by assuming that a liquid particle on the free surface remains on the free surface $z = \zeta(x, y, t)$. Then, the kinematic free-surface condition can be written using that the substantial derivative $\dfrac{\mathrm{D}}{\mathrm{D}t}(z - \zeta) = 0$, *i.e.*

$$\frac{\partial \zeta}{\partial t} + \frac{\partial \varphi}{\partial x}\frac{\partial \zeta}{\partial x} + \frac{\partial \varphi}{\partial y}\frac{\partial \zeta}{\partial y} - \frac{\partial \varphi}{\partial z} = 0 \quad on \quad z = \zeta\,(x, y, t) \tag{2.3}$$

Here ζ is the wave elevation. The dynamic free-surface condition is simply that the water pressure is equal to the constant atmospheric pressure on the free-surface. Then, the dynamic free-surface condition can be written using Bernoulli's equation as

$$g\zeta + \frac{\partial \varphi}{\partial t} + \frac{1}{2}\left(\nabla\varphi \cdot \nabla\varphi\right) = 0 \quad on \quad z = \zeta\,(x, y, t) \tag{2.4}$$

The free-surface conditions Eq. (2.3) and Eq. (2.4) are difficult to satisfy on the free surface due to nonlinearities. Assuming small wave steepness and small vertical body motions relative to the wave amplitude, Eq. (2.3) and Eq. (2.4) can be linearized to the mean free surface at $z = 0$. The result is

$$\frac{\partial \zeta}{\partial t} = \frac{\partial \varphi}{\partial z} \quad on \quad z = 0 \tag{2.5}$$

$$g\zeta + \frac{\partial \varphi}{\partial t} = 0 \quad on \quad z = 0 \tag{2.6}$$

Eq. (2.5) and Eq. (2.6) can be combined to give

$$\frac{\partial^2 \varphi}{\partial t^2} + g\frac{\partial \varphi}{\partial z} = 0 \quad on \quad z = 0 \tag{2.7}$$

When the velocity potential φ is oscillating harmonically in time with circular frequency ω, we can write Eq. (2.7) as

$$-\omega^2\varphi + g\frac{\partial \varphi}{\partial z} = 0 \quad on \quad z = 0 \tag{2.8}$$

Body boundary condition

The body boundary condition within potential flow theory expresses that the body velocity in the normal direction of the body surface is equal to water velocity in the normal direction of the body surface. In the linearized problem, the body boundary condition is satisfied on the mean wetted position of the body surface, *i.e.* on $\bar{S}_B$. This can be expressed as

$$\frac{\partial \varphi}{\partial n} = \mathbf{U}_B \cdot \mathbf{n} \quad on \quad \bar{S}_B \tag{2.9}$$

Here $\partial/\partial n$ denotes differentiation along the normal to the body surface. The positive normal direction is defined to be into the fluid domain. Furthermore, $\mathbf{U}_B$ is the body velocity and $\mathbf{n} = (n_1, n_2, n_3)$ is the unit normal vector.

2.4 Curved beam equation with axial stiffness

The prediction of the vertical motion w of the torus is based on a generalized Euler-Bernoulli beam equation that accounts for curvature and axial stiffness. The equation is

$$\begin{aligned} &m\frac{\partial^2 w}{\partial t^2} + \rho g b_w w + EI\frac{\partial^4 w}{\partial s^4} + \frac{EI}{c^2}\frac{\partial^2 w}{\partial s^2} - \frac{\partial}{\partial s}\left(T_{as}\frac{\partial w}{\partial s}\right) \\ &= f_3(s)^{\text{added mass}+\text{damping}} + f_3(s)^{\text{wave excit}} + f_3^{\text{moorings}} \end{aligned} \tag{2.10}$$

Here the differentiation $\partial/\partial s = c^{-1}\partial/\partial\beta$ is along the center line of the torus where β is defined in Figure 2.1, and m is the torus mass per unit length. EI is the bending stiffness and the bending stiffness term $\frac{EI}{c^2}\frac{\partial^2 w}{\partial s^2}$ is a consequence of curvature effect of the torus (see Appendix A). The term is needed together with $EI\frac{\partial^4 w}{\partial s^4}$ in order to describe a rigid torus when $EI \to \infty$. f_3^{moorings} denotes the vertical component of the mooring line forces that formally must be expressed in term of Dirac delta functions since it is not uniformly distributed along the torus. T_{as} is the axial stiffness following from a static analysis of the moored torus. The details of the mooring line arrangement is illustrated in Appendix B. Furthermore, $f_3^{\text{added mass}+\text{damping}}$ is the vertical added mass and damping force per unit length of the torus and $f_3^{\text{wave excit}}$ is the vertical wave excitation force on the torus per unit length of the torus. The term $\rho g b_w w$ is caused by the change of the buoyancy force due to the motion w. Here ρ is the mass density of water, g is the gravitational acceleration. Since we consider a semi-submerged torus, b_w is $2a$ with a as the radius of the cross-section of the torus. Since structural damping is unknown, it was not included. However, it is believed to be small for the lowest structural modes.

Since the response is symmetric about the x-axis for waves propagating in the positive x-direction, the vertical motion w of the torus can be expressed as the

following Fourier series:

$$w = a_0(t) + \sum_{n=1}^{\infty} a_n(t)\cos(n\beta) \tag{2.11}$$

The x- and y-coordinates of the center line of the torus is given by $x = c\cos\beta$, $y = c\sin\beta$. a_0 and $a_1\cos\beta$ describe heave at the torus axis and vertical motion due to pitch motion, respectively. The other terms in Eq. (2.11) are purely elastic modes. Mode n has the mode shape $\cos n\beta$ in the following studies.

In order to obtain the wave-induced elastic responses of the circular plastic collar of a fish farm, Eq. (2.11) is inserted into Eq. (2.10), and then Eq. (2.10) are multiplied successively by $\cos(m\beta), m = 0, 1, ...$ and integrated from $\beta = 0$ to 2π. This leads to, for instance, generalized added mass, damping and wace excitation forces on the torus. The equations of motion for each mode amplitude $a_n(t)$ are then obtained.

We will start with studying the radiation problems, that means forced vertical motions of the torus associated with the different Fourier components (modes). There are no incident waves. Then the wave excitation problem with the torus restrained from moving is examined.

2.5 Low-frequency slender-body theory

Many vessels of interest in marine hydrodynamics are slender, with one length dimension exceeding the others by an order of magnitude. For ships, submarines, sailboats, and fish, this shape is generally a consequence of the advantage of a streamlined body form that minimizes the resistance, with the longitudinal length scale substantially greater than the cross-dimensional lengths. For these vessels it is logical to simplify the hydrodynamics analysis by suitable approximations based on the slenderness of the body. Slender-body theory is a methodology that can be used to take advantage of the slenderness of a body to obtain an approximation to the flow field surrounding it. Slender-body theory originated in the field of aerodynamics, first as a technique for predicting the stability characteristics of dirigibles. Newman and Tuck (1964) developed the slender-body theory in analyzing wave-induced heave and pitch of a rigid ship with zero or forward speed at small frequencies.

The geometry of the torus meets the requirement of the fundamental assumption of slender-body theory that the diameter $2a$ of the cross-section of the torus is much smaller than the length $2\pi c$ of the torus. To formalize this assumption, we define the nondimensional slenderness parameter $a/c = \varepsilon \ll 1$. Before describing the slender-body theory applied on the torus, it is convenient to rewrite Eq. (2.2) from Cartesian coordinate form to cylindrical coordinate form as follows

$$\nabla^2\varphi = \frac{1}{\rho}\frac{\partial}{\partial\rho}\left(\rho\frac{\partial\varphi}{\partial\rho}\right) + \frac{1}{\rho^2}\frac{\partial^2\varphi}{\partial\beta^2} + \frac{\partial^2\varphi}{\partial z^2} = 0 \tag{2.12}$$

The boundary value problem Eq. (2.8), Eq. (2.9) and Eq. (2.12) can be simplified. Geometrically, the components of the unit normal vector $\mathbf{n} = (n_\rho, n_\beta, n_z)$ in the

cylindrical coordinate system have the following order

$$n_\rho = O(1), \quad n_\beta = O(\varepsilon), \quad n_z = O(1) \tag{2.13}$$

The consequence is that the normal derivative in the body boundary condition given by Eq. (2.9) can be approximated by the two-dimensional normal derivative in the $\rho - z$ plane. A consequence of the slenderness assumption is that the Laplace equation can be approximated in the near field of a cross-section of the torus. We adopt an inner region reference frame, fixed with respect to the scale of the cross-section. From this viewpoint, $a = O(1)$ whereas $c = O(1/\varepsilon)$. As $\varepsilon \to 0$, the cross-section scale remains fixed while the diameter or perimeter of the torus tends to infinity. The water velocity field then appears nearly constant in the tangential direction, with $\partial/\partial\beta = O(\varepsilon)$. In this inner region it follows that

$$\left|\frac{1}{c}\frac{\partial\varphi}{\partial\beta}\right| \ll \left(\left|\frac{\partial\varphi}{\partial\rho}\right|, \left|\frac{\partial\varphi}{\partial z}\right|\right) \tag{2.14}$$

with a similar result for the second derivatives. Thus 3D Laplace equation reduces to a 2D Laplace equation in the polar coordinate system defined in Figure 2.2, *i.e.*

$$\frac{\partial^2\varphi}{\partial r'^2} + \frac{1}{r'}\frac{\partial\varphi}{\partial r'} + \frac{1}{r'^2}\frac{\partial^2\varphi}{\partial\theta^2} = 0 \tag{2.15}$$

Similarly, the body boundary condition of Eq. (2.9) can be replaced by

$$\frac{\partial\varphi}{\partial r'} = U_{Br'} n_{r'} \quad on \ r' = a \tag{2.16}$$

Here $U_{Br'}$ is the normal component of local cross-section of the torus velocity $\mathbf{U}_B$ and $n_{r'}$ is the normal component of local cross-section of the unit normal vector $\mathbf{n}$.

The near-field solution will in addition satisfy the linear free-surface condition Eq. (2.8). The radiation condition will be taken care of by matching with the far-field solution. It is not appropriate to apply the radiation condition in the inner region, nor to the inner solution, since the radiation condition holds only at a large distance compared to all the cross-sectional body dimensions. Since the radiation condition cannot be applied to the inner solution, the inner solution, at this stage, is not unique, nor is it well-behaved at infinity.

This deficiency results from the assumption of two-dimensional flow, and thus a three-dimensional solution of the Laplace equation is required to bridge the gap between the inner solution and the condition at infinity which corresponds to the outer solution. Since we consider vertical motions of a free-surface piercing body, the appropriate outer solution is a distribution of three-dimensional sources, along the center line of the torus, which satisfy radiation condition at infinity and can be matched with the inner solution near the torus. The near-field (inner) and far-field (outer) solutions will be consistent provided they can be matched in an overlap region $\varepsilon c \ll \rho \ll c$ far from the torus in the inner region but very close to the torus in the outer region. The approach outlined here is essentially the method of matched asymptotic expansions. This method is useful because the two

separate problems are simpler to solve analytically, compared to the exact solution valid everywhere throughout the fluid. The inner solution is simplified because it is two-dimensional, whereas the outer solution is simplified by neglecting the body boundary condition.

We start with deriving frequency-dependent generalized added mass and damping coefficients for different vertical modes which can be used in a long-wavelength approximation of the generalized vertical wave excitation loads. Matched asymptotic expansions explained above are applied with a far-field solution and a near-field solution valid at the cross-section of the torus.

2.6 Far-field flow description due to forced vertical motions

The velocity potential φ^F in the far-field satisfies the 3D Laplace equation with radiation conditions and the classical linear free-surface condition Eq. (2.8). All oscillatory quantities are assumed to be time-harmonic with circular frequency ω. The governing equation and the free-surface condition are:

$$\nabla^2 \varphi^F = 0 \tag{2.17}$$

$$-\nu\varphi^F + \frac{\partial \varphi^F}{\partial z} = 0 \quad on \quad z = 0, \quad \nu = \omega^2/g \tag{2.18}$$

The velocity potential due to a body can be represented in terms of flow singularities satisfying the free-surface condition Eq. (2.18) and the radiation condition (Newman, 1977*a*). The flow singularities will be sources in our problem. Since we do not see the details of the cross-dimensions of the torus in the far-field, the flow appears as a line distribution of sources along the center line of the torus. The torus as seen in the far-field is shown in Figure 2.1. The coordinates of the center line can be expressed as:

$$\xi = c\cos\alpha, \quad \eta = c\sin\alpha, \quad \zeta = 0 \tag{2.19}$$

The field point has coordinates (x, y, z) and a source point has coordinates (ξ, η, ζ). In the far field view, $\zeta = 0$. We consider forced vertical torus separately for each Fourier mode. The associated source density varies as $Q\cos(n\alpha)\exp(-i\omega t)$ along the center line of the torus. Here i is the complex unit. That means the far-field velocity potential is

$$\varphi^F = \frac{Q\exp(-i\omega t)}{4\pi} c \int_0^{2\pi} \cos(n\alpha)\, G(x, y, z; \xi, \eta, 0)\, \mathrm{d}\alpha \tag{2.20}$$

Derivations by Havelock (1942, 1955) (see Faltinsen (1990)) give the following

source expression (Green function) $G(x,y,z;\xi,\eta,\zeta)\exp(-i\omega t)$ with

$$\begin{aligned} G(x,y,z;\xi,\eta,\zeta) &= \frac{1}{R}+\frac{1}{R'} \\ &- \frac{4\nu}{\pi}\int_0^\infty \left[\nu\cos k(z+\zeta) - k\sin k(z+\zeta)\right]\frac{K_0(kr)}{k^2+\nu^2}\,\mathrm{d}k \\ &- 2\pi\nu\exp(\nu(z+\zeta))\,Y_0(\nu r) \\ &+ i2\pi\nu\exp(\nu(z+\zeta))\,J_0(\nu r) \end{aligned} \tag{2.21}$$

Here $R=\sqrt{(x-\xi)^2+(y-\eta)^2+(z-\zeta)^2}$ is the distance from the field point to the source point, and $R'=\sqrt{(x-\xi)^2+(y-\eta)^2+(z+\zeta)^2}$, $r=\sqrt{(x-\xi)^2+(y-\eta)^2}$. We should note that the expression is the same if we simultaneously interchange x with ξ, y with η and z with ζ. Further, J_0 is the Bessel function of the first kind of zero order; Y_0 is the Bessel function of the second kind of zero order; K_0 is the modified Bessel function of zero order (see Abramowitz and Stegun (1964)).

We will now derive an inner expansion of the far-field expansion by assuming that νa is small. Here a is the radius of the cross-section of the torus. When we analyze vertical motions, we are as a first approximation interested in symmetric terms relative to a vertical center surface going along the center line of the torus. We have divided the Green function (Eq. 2.21) into three parts and studied each part separately, *i.e.*

$$\begin{aligned} G(x,y,z;\xi,\eta,\zeta) &= G_1+G_2+G_3 \\ G_1 &= \frac{1}{R}+\frac{1}{R'} \\ G_2 &= -2\pi\nu\exp(\nu(z+\zeta))\,Y_0(\nu r)+i2\pi\nu\exp(\nu(z+\zeta))\,J_0(\nu r) \\ G_3 &= -\frac{4\nu}{\pi}\int_0^\infty\left[\nu\cos k(z+\zeta)-k\sin k(z+\zeta)\right]\frac{K_0(kr)}{k^2+\nu^2}\,\mathrm{d}k \end{aligned} \tag{2.22}$$

We first study the two first term of Eq. (2.21) which is $G_1(x,y,z;\xi,\eta,0)$ and define $x=\rho\cos\beta, y=\rho\sin\beta$. Then the far-field velocity potential associated with $G_1(x,y,z;\xi,\eta,0)$ is

$$\begin{aligned} \varphi_1^F &= \frac{Q\exp(-i\omega t)}{4\pi}c\int_0^{2\pi}\cos(n\alpha)\left(\frac{1}{R}+\frac{1}{R'}\right)\mathrm{d}\alpha \\ &= \frac{Q\exp(-i\omega t)}{2\pi}c\int_0^{2\pi}\frac{\cos(n\alpha)}{\sqrt{\rho^2+c^2+z^2-2\rho c\cos(\alpha-\beta)}}\,\mathrm{d}\alpha \end{aligned} \tag{2.23}$$

If we introduce $\mu=\alpha-\beta$, Eq. (2.23) can be rewritten as

$$\varphi_1^F = \frac{Q\exp(-i\omega t)\cos(n\beta)}{2\pi}c\int_0^{2\pi}\frac{\cos(n\mu)}{\sqrt{r'^2+2\rho c(1-\cos\mu)}}\,\mathrm{d}\mu \tag{2.24}$$

Here $r'=\sqrt{(\rho-c)^2+z^2}$ is the radius in a local polar coordinate system $Or'\theta$ with origin at the center line of the torus (see Figure 2.2). In order to find the inner

expansion of Eq. (2.24), the integral in Eq. (2.24) can be rewritten as follows

$$\begin{aligned} c\int_0^{2\pi} \frac{\cos(n\mu)}{\sqrt{r'^2 + 2\rho c(1-\cos\mu)}}\,\mathrm{d}\mu \;=\; \\ c\int_0^{2\pi} \frac{1}{\sqrt{r'^2 + 2\rho c(1-\cos\mu)}}\,\mathrm{d}\mu \;-\; c\int_0^{2\pi} \frac{1-\cos(n\mu)}{\sqrt{r'^2 + 2\rho c(1-\cos\mu)}}\,\mathrm{d}\mu \end{aligned} \tag{2.25}$$

The first integral on the right hand side of Eq. (2.25) can be transferred to the complete elliptic integral of the first kind K and the lowest order term of the inner expansion around $r' = 0$ is a symmetric term relative to the cross-section of the torus which we are interested in. It can be expressed as

$$\frac{4c}{\sqrt{r'^2 + 4\rho c}} K\left(2\sqrt{\frac{\rho c}{r'^2 + 4\rho c}}\right) \approx 2\ln\left(\frac{8c}{r'}\right) \tag{2.26}$$

Similarly, the lowest order term of the inner expansion of the second integral on the right hand side of Eq. (2.25) is found by performing Taylor expansion around $r' = 0$ which leads to

$$\frac{1}{\sqrt{2}}\int_0^{2\pi} \frac{1-\cos(n\mu)}{\sqrt{1-\cos\mu}}\,\mathrm{d}\mu \tag{2.27}$$

The lowest order term of the inner expansion of the two first term of Eq. (2.21) which is $G_1(x,y,z;\xi,\eta,0)$ associated with $G(x,y,z;\xi,\eta,0)$ is obtained by using Eq. (2.26) and Eq. (2.27). We get

$$\begin{aligned} \varphi_{I1}^F &= \frac{Q\exp(-i\omega t)\cos(n\beta)}{\pi}\left[\ln\left(\frac{8c}{r'}\right) - K_n\right] \\ K_n &= \frac{1}{2\sqrt{2}}\int_0^{2\pi} \frac{1-\cos(n\mu)}{\sqrt{1-\cos(\mu)}}\,\mathrm{d}\mu \\ &= 2\left(1 + \frac{1}{3} + \frac{1}{5} + \ldots + \frac{1}{2n-1}\right), \quad n \geq 1 \end{aligned} \tag{2.28}$$

This expression is the same as the result shown in Faltinsen (2011), which considers the limiting case that the forcing frequency $\omega \to 0$.

We discuss now the two last terms $G_2(x,y,z;\xi,\eta,0)$ in the Green function, which contains the effect of far-field waves. The distance r from the field point $(x,y,0)$ to the source point $(\xi,\eta,0)$ can be expressed as

$$r = \sqrt{\rho^2 + c^2 - 2\rho c\cos(\alpha-\beta)} \tag{2.29}$$

Then, we can write the first kind Bessel function $J_0(\nu r)$ and the second kind Bessel function $Y_0(\nu r)$ using summation theorems of expansion in products of Bessel functions according to Gradshteyn and Ryzhik (1994) on page 993. The formula assumes that $c < \rho$ and $\alpha - \beta > 0$. If ρ and c are replaced by each other, the result will be the same in Eq. (2.29). Considering this characteristic and the

first kind Bessel function $J_0(\nu r)$, only the second kind Bessel function $Y_0(\nu r)$ has to be written in the piecewise form as below

$$J_0(\nu r) = J_0(\nu c)\, J_0(\nu \rho) + 2\sum_{m=1}^{\infty} J_m(\nu c)\, J_m(\nu \rho)\cos[m(\alpha-\beta)]$$
$$Y_0(\nu r) = \begin{cases} J_0(\nu c)\, Y_0(\nu \rho) + 2\sum\limits_{m=1}^{\infty} J_m(\nu c)\, Y_m(\nu \rho)\cos[m(\alpha-\beta)], & \rho \geq c \\ J_0(\nu \rho)\, Y_0(\nu c) + 2\sum\limits_{m=1}^{\infty} J_m(\nu \rho)\, Y_m(\nu c)\cos[m(\alpha-\beta)], & \rho \leq c \end{cases} \tag{2.30}$$

This means that we have to evaluate the integrals associated with the two last terms $G_2(x, y, z; \xi, \eta, 0)$ in the Green function of Eq. (2.20) as follows

$$\begin{aligned} \int_0^{2\pi} J_0(\nu r)\cos(n\alpha)\, \mathrm{d}\alpha &= 2\pi J_n(\nu c)\, J_n(\nu \rho)\cos(n\beta) \\ \int_0^{2\pi} Y_0(\nu r)\cos(n\alpha)\, \mathrm{d}\alpha &= \begin{cases} 2\pi J_n(\nu c)\, Y_n(\nu \rho)\cos(n\beta), & \rho \geq c \\ 2\pi J_n(\nu \rho)\, Y_n(\nu c)\cos(n\beta), & \rho \leq c \end{cases} \end{aligned} \tag{2.31}$$

Since we in the near field consider a problem that is symmetric with respect to the vertical center line of the cross-section, we focus on the symmetric term relative to the cross-section of the torus. So a first term inner expansion of each of these terms involves then

$$\begin{gathered} 2\pi\left[J_n(\nu c)\right]^2\cos(n\beta) \\ 2\pi J_n(\nu c)\, Y_n(\nu c)\cos(n\beta) \end{gathered} \tag{2.32}$$

However, we need to also examine the next order term which is the second term of Taylor expansion of Eq. (2.31) about $\rho = c$ involving the second kind Bessel function $Y_0(\nu r)$. This term involves the first derivative of the first kind Bessel function $J_n(\nu \rho)$ and the second kind Bessel function $Y_n(\nu \rho)$. Since the expression has a discontinuity in the first derivative at $\rho = c$, we then define $\rho = c + y'$ and have to make a Taylor expansion of Eq. (2.31) separately for $y' > 0$ and $y' < 0$. The jump in the derivative at $\rho = c$ is proportional to

$$\begin{aligned} &\frac{\mathrm{d}}{\mathrm{d}\rho}\left[J_n(\nu c)\, Y_n(\nu \rho) - J_n(\nu \rho)\, Y_n(\nu c)\right]\Big|_{\rho=c} \\ &= -J_n(\nu c)\, Y_{n+1}(\nu c)\,\nu + J_{n+1}(\nu c)\, Y_n(\nu c)\,\nu = \frac{2}{\pi c} \end{aligned} \tag{2.33}$$

We have here used that $\varrho_n'(\gamma) = -\varrho_{n+1}(\gamma) + \dfrac{n}{\gamma}\varrho_n(\gamma)$ where $\varrho_n(\gamma)$ is $J_n(\gamma)$ or $Y_n(\gamma)$ and that the Wronskian $W\{J_n(\gamma), Y_n(\gamma)\} = \dfrac{2}{\pi\gamma}$ (Abramowitz and Stegun, 1964). The two lowest order expressions involving Eq. (2.31) can then be expressed as Eq. (2.32) plus a linear term in y' and a linear term in $|y'|$. According to the

statement above we define:

$$\begin{aligned} f(y') &= ay', \quad y' \geq 0 \\ f(y') &= by', \quad y' \leq 0 \\ f(y') &= c_1 |y'| + c_2 y' \end{aligned} \tag{2.34}$$

We can get c_1 and c_2 from the equation system for all y':

$$\begin{aligned} c_1 &= \frac{a-b}{2} = \frac{1}{\pi c} \\ c_2 &= \frac{a+b}{2} = \frac{1}{2} J_n(\nu c)\, \nu \left[-Y_{n+1}(\nu c) + \frac{n}{\nu c} Y_n(\nu c) \right] \\ &\quad + \frac{1}{2} Y_n(\nu c)\, \nu \left[-J_{n+1}(\nu c) + \frac{n}{\nu c} J_n(\nu c) \right] \end{aligned} \tag{2.35}$$

As mentioned above, only the symmetric terms relative to the cross-section of the torus are kept. It follows that the inner expansion of the far-field expression due to the two last terms $G_2(x, y, z; \xi, \eta, 0)$ in Eq. (2.21) can be expressed as

$$\begin{aligned} \varphi_{I2}^F &= \frac{Q \exp(-i\omega t) \cos(n\beta)}{\pi} (1 + \nu z)\, \nu c \pi^2 \\ &\quad \times \left\{ -J_n(\nu c)\, Y_n(\nu c) - \frac{1}{\pi c} |y'| + i \left[J_n(\nu c) \right]^2 \right\} \end{aligned} \tag{2.36}$$

The term associated with $|y'|$ causes a discontinuity in the derivative at $y' = 0$. We will by examining all parts of the velocity potential show that there is not an unphysical discontinuity in the derivative of the total velocity potential.

We study the remaining term $G_3(x, y, z; \xi, \eta, 0)$ in the Green function, *i.e.*

$$I_G = -\frac{4\nu}{\pi} \int_0^\infty \left[\nu \cos(kz) - k \sin(kz) \right] \frac{K_0(kr)}{k^2 + \nu^2}\, \mathrm{d}k \tag{2.37}$$

Eq. (2.37) is divided into two parts as follows, and we will study these two parts separately.

$$\begin{aligned} I_G &= -\frac{4\nu}{\pi} (I_1 - I_2) \\ I_1 &= \nu \int_0^\infty \cos(kz) \frac{K_0(kr)}{k^2 + \nu^2}\, \mathrm{d}k \\ I_2 &= \int_0^\infty k \sin(kz) \frac{K_0(kr)}{k^2 + \nu^2}\, \mathrm{d}k \end{aligned} \tag{2.38}$$

We start with the following reformulation of I_1 by using expression 9.6.21 in Abramowitz and Stegun (1964) which uses integral to represent $K_0(kr)$

$$\begin{aligned} I_1 &= \nu \int_0^\infty \cos(kz) \frac{K_0(kr)}{k^2 + \nu^2}\, \mathrm{d}k \\ &= \nu \int_0^\infty \int_0^\infty \frac{\cos(k|z|)}{k^2 + \nu^2} \frac{\cos(krt)}{\sqrt{t^2 + 1}}\, \mathrm{d}k \mathrm{d}t \end{aligned} \tag{2.39}$$

Then, further reformulation on integral of combination of trigonometric functions $\cos(k\,|z|)\cos(krt)$ and rational function $\dfrac{1}{k^2+\nu^2}$ could be done according to expression 3.742(3) in Gradshteyn and Ryzhik (1994) as follows

$$I_1 = \frac{\pi}{4}\int_0^\infty \frac{\mathrm{d}t}{\sqrt{t^2+1}}\left[\exp\left(-\nu\left||z|-rt\right|\right) + \exp\left(-\nu\left(|z|+rt\right)\right)\right] \tag{2.40}$$

We rewrite Eq. (2.40) as

$$\begin{aligned} I_1 = {} & \frac{\pi}{4}\exp\left(-\nu\,|z|\right)\int_0^{|z|/r}\frac{\exp\left(\nu rt\right)}{\sqrt{t^2+1}}\,\mathrm{d}t + \frac{\pi}{4}\exp\left(\nu\,|z|\right)\int_{|z|/r}^\infty\frac{\exp\left(-\nu rt\right)}{\sqrt{t^2+1}}\,\mathrm{d}t \\ & + \frac{\pi}{4}\exp\left(-\nu\,|z|\right)\int_0^\infty\frac{\exp\left(-\nu rt\right)}{\sqrt{t^2+1}}\,\mathrm{d}t \end{aligned} \tag{2.41}$$

This means

$$\begin{aligned} I_1 = {} & \frac{\pi}{4}\exp\left(\nu\,|z|\right)\int_0^\infty\frac{\exp\left(-\nu rt\right)}{\sqrt{t^2+1}}\,\mathrm{d}t + \frac{\pi}{4}\exp\left(-\nu\,|z|\right)\int_0^\infty\frac{\exp\left(-\nu rt\right)}{\sqrt{t^2+1}}\,\mathrm{d}t \\ & + \frac{\pi}{4}\exp\left(-\nu\,|z|\right)\int_0^{|z|/r}\frac{\exp\left(\nu rt\right)}{\sqrt{t^2+1}}\,\mathrm{d}t - \frac{\pi}{4}\exp\left(\nu\,|z|\right)\int_0^{|z|/r}\frac{\exp\left(-\nu rt\right)}{\sqrt{t^2+1}}\,\mathrm{d}t \end{aligned} \tag{2.42}$$

We study now the term I_2. Firstly, $K_0\left(kr\right)$ is represented by an integral as follows

$$\begin{aligned} I_2 &= \int_0^\infty k\sin\left(kz\right)\frac{K_0\left(kr\right)}{k^2+\nu^2}\,\mathrm{d}k \\ &= -\int_0^\infty\int_0^\infty \frac{k\sin\left(k\,|z|\right)}{k^2+\nu^2}\frac{\cos\left(krt\right)}{\sqrt{t^2+1}}\,\mathrm{d}k\mathrm{d}t \end{aligned} \tag{2.43}$$

The integral of combination of trigonometric and rational functions could be rewritten similarly as Eq. (2.41) and Eq. (2.42) according to expression 3.742(5) in Gradshteyn and Ryzhik (1994), *i.e.*

$$\begin{aligned} I_2 &= \frac{\pi}{2}\left[\sinh\left(\nu\,|z|\right)\int_{|z|/r}^\infty\frac{\exp\left(-\nu rt\right)}{\sqrt{t^2+1}}\,\mathrm{d}t - \exp\left(-\nu\,|z|\right)\int_0^{|z|/r}\frac{\cosh\left(\nu rt\right)}{\sqrt{t^2+1}}\,\mathrm{d}t\right] \\ &= \frac{\pi}{2}\left[\sinh\left(\nu\,|z|\right)\int_0^\infty\frac{\exp\left(-\nu rt\right)}{\sqrt{t^2+1}}\,\mathrm{d}t - \exp\left(-\nu\,|z|\right)\int_0^{|z|/r}\frac{\cosh\left(\nu rt\right)}{\sqrt{t^2+1}}\,\mathrm{d}t\right. \\ &\quad \left. - \sinh\left(\nu\,|z|\right)\int_0^{|z|/r}\frac{\exp\left(-\nu rt\right)}{\sqrt{t^2+1}}\,\mathrm{d}t\right] \end{aligned} \tag{2.44}$$

Based on Eq. (2.42) and Eq. (2.44), the following expression can be obtained

$$\begin{aligned} I_1 - I_2 = {} & \frac{\pi}{2}\exp\left(-\nu\,|z|\right)\int_0^\infty\frac{\exp\left(-\nu rt\right)}{\sqrt{t^2+1}}\,\mathrm{d}t \\ & + \frac{\pi}{2}\exp\left(-\nu\,|z|\right)\int_0^{|z|/r}\frac{\exp\left(\nu rt\right)}{\sqrt{t^2+1}}\,\mathrm{d}t \end{aligned} \tag{2.45}$$

The first integral in Eq. (2.45) can be expressed as follows using expression 12.1.8 in Abramowitz and Stegun (1964), *i.e.*

$$\int_0^\infty \frac{\exp(-\nu r t)}{\sqrt{t^2+1}}\,\mathrm{d}t \;=\; \frac{\pi}{2}\left[\mathbf{H}_0(\nu r) \;-\; Y_0(\nu r)\right] \tag{2.46}$$

Here $\mathbf{H}_0$ is the Struve function of zero order. This leads to

$$\begin{aligned} I_G \;&=\; -\frac{4\nu}{\pi}\left(I_1 \;-\; I_2\right) \\ &= -\nu\pi\exp(\nu z)\left[\mathbf{H}_0(\nu r) - Y_0(\nu r)\right] - 2\nu\exp(\nu z)\int_0^{|z|/r}\frac{\exp(\nu r t)}{\sqrt{t^2+1}}\,\mathrm{d}t \end{aligned} \tag{2.47}$$

We define $t = \dfrac{|z|}{r}u$, substitute it into Eq. (2.47) and change the integration variable to u, then make Taylor expansion of exponential function of integral and keep the first two terms. This means

$$\begin{aligned} I_G \;&=\; -\nu\pi\exp(\nu z)\left[\mathbf{H}_0(\nu r) - Y_0(\nu r)\right] - 2\nu\exp(\nu z)\,|z|\int_0^1 \frac{\exp(\nu\,|z|\,u)}{\sqrt{(|z|\,u)^2+r^2}}\,\mathrm{d}u \\ &= -\nu\pi\exp(\nu z)\left[\mathbf{H}_0(\nu r) - Y_0(\nu r)\right] \\ &-2\nu\exp(\nu z)\,|z|\left[\int_0^1 \frac{1}{\sqrt{(|z|\,u)^2+r^2}}\,\mathrm{d}u + \int_0^1 \frac{\nu\,|z|\,u}{\sqrt{(|z|\,u)^2+r^2}}\,\mathrm{d}u\right] \end{aligned} \tag{2.48}$$

The last two integral expressions follow from a Taylor expansion at $u = 0$ of the exponential function $\exp(\nu\,|z|\,u)$ in the integrand in Eq. (2.48). The two lowest order terms 1 and $\nu\,|z|\,u$ are kept which are symmetric term and antisymmetric term respectively in term of u in order to get continuous result. We now study the contribution of the part I_G to the inner expansion of the velocity potential, *i.e.*

$$\varphi_{I3}^F \;=\; \frac{Q\exp(-i\omega t)}{4\pi}c\int_0^{2\pi}\cos(n\alpha)\,I_G\,\mathrm{d}\alpha \tag{2.49}$$

We study the first part involving the Struve and Bessel functions close to the torus. The first two order terms are obtained by making Taylor expansion at $\rho = c$ in Eq. (2.29) and defining $\mu = \alpha - \beta$. The term involving the Bessel function Y_0 can be handled in the same way as led to Eq. (2.36) and will be combined with this term. The term involving the Struve function can formally be rewritten as:

$$\begin{aligned} &\int_0^{2\pi}\mathbf{H}_0\left(\nu\sqrt{\rho^2+c^2-2\rho c\cos(\alpha-\beta)}\right)\cos(n\alpha)\;\mathrm{d}\alpha \\ &=\;\cos(n\beta)\int_0^{2\pi}\mathbf{H}_0\left(\nu\sqrt{\rho^2+c^2-2\rho c\cos\mu}\right)\cos(n\mu)\;\mathrm{d}\mu \end{aligned} \tag{2.50}$$

We have here introduced the local coordinate system $Oy'z'$ defined in Figure 2.2. Furthermore, we should note that $z = z'$. Special attention must be paid when

calculating the inner expansion due to the two integrals in Eq. (2.48). The integral

$$-2\nu\exp(\nu z)\,|z|\int_0^1 \frac{\nu\,|z|\,u}{\sqrt{(|z|\,u)^2+r^2}}\,\mathrm{d}u \;=\; -2\nu^2\exp(\nu z)\left[\sqrt{z^2+r^2}\;-\;r\right] \tag{2.51}$$

is the order of $O(\nu^2 z)$ which is a higher-order term due to low-frequency assumption and can be neglected. The integral

$$\frac{-2\nu\exp(\nu z)\,|z|\,c}{4}\int_0^{2\pi}\int_0^1 \frac{\cos(n\mu)}{\sqrt{(|z|\,u)^2+r^2}}\,\mathrm{d}u\,\mathrm{d}\mu \tag{2.52}$$

has been first derived for one asymptotic expression for small z when $y'=0$. We now study the outer integral

$$c\int_0^{2\pi}\frac{\cos(n\mu)}{\sqrt{(|z|\,u)^2+r^2}}\,\mathrm{d}\mu \tag{2.53}$$

The procedure is similar as done for Eq. (2.25) which gives

$$\begin{aligned}\frac{4c}{\sqrt{r'^2+(u^2-1)\,z^2+4\rho c}}K\left(2\sqrt{\frac{\rho c}{r'^2+(u^2-1)\,z^2+4\rho c}}\right)\\ \approx\; 2\ln\left(\frac{8c}{\sqrt{r'^2+(u^2-1)\,z^2}}\right)\end{aligned} \tag{2.54}$$

and $-2K_n$. Then, we make a Taylor expansion of the exponential function and keep the lowest order term. This means

$$\begin{aligned}-\nu\,|z|\int_0^1\left[\ln\left(\frac{8c}{\sqrt{r'^2+(u^2-1)\,z^2}}\right)-K_n\right]\mathrm{d}u\\ =\;-\nu\,|z|\left[\ln\left(\frac{8c}{r'}\right)-K_n+1\right]-\nu\theta y'\end{aligned} \tag{2.55}$$

When $z=0$, Eq. (2.52) gives the asymptotic expression $\nu\dfrac{\pi}{2}\,|y'|$ for small y'. Then the two asymptotic expressions are combined to get an asymptotic expression for both small y' and small z by requiring that 2D Laplace equation is satisfied. We get correctly to $O(Q\nu a)$

$$\begin{aligned}\varphi_{I3}^F \;=\; &\frac{Q\exp(-i\omega t)\cos(n\beta)}{\pi}\\ &\times\left\{-\frac{\nu\pi c}{4}(1+\nu z)\int_0^{2\pi}\mathbf{H}_0(\nu r)\Big|_{\rho=c}\cos(n\mu)\;\mathrm{d}\mu\right.\\ &+\frac{\pi^2}{2}(1+\nu z)\,\nu c\left[J_n(\nu c)\,Y_n(\nu c)+\frac{1}{\pi c}\,|y'|\right]\\ &\left.-\nu\,|z|\left[\ln\left(\frac{8c}{r'}\right)-K_n+1\right]+\nu\left(\frac{\pi}{2}\,|y'|-\theta y'\right)\right\}\end{aligned} \tag{2.56}$$

The total inner expansion of the far-field expansion is combining Eq. (2.28), Eq. (2.36) and Eq. (2.56), *i.e.*

$$\begin{aligned}\varphi_I^F \;=\; & \frac{Q\exp\left(-i\omega t\right)}{\pi}\cos\left(n\beta\right) \\ & \times\left\{\left(1\;-\;\nu\left|z\right|\right)\left[\ln\left(\frac{8c}{r'}\right)\;-\;K_n\right]\;-\;\nu\left|z\right|\;-\;\nu\theta y'\right. \\ & \;+\;\left(1+\nu z\right)\nu c\pi^2\left\{-\frac{1}{2}J_n\left(\nu c\right)Y_n\left(\nu c\right)\;+\;i\left[J_n\left(\nu c\right)\right]^2\right\} \\ & \left.-\;\frac{\nu\pi c}{4}\left(1+\nu z\right)\int_0^{2\pi}\mathbf{H}_0\left(\nu r\right)\Big|_{\rho=c}\cos\left(n\mu\right)\;\mathrm{d}\mu\right\}\end{aligned} \tag{2.57}$$

We see that the term involves $|y'|$, which causes a discontinuity in the derivative at $y'=0$ in Eq. (2.36) is canceled to the order of $Q\nu$ by the terms involving $|y'|$ in Eq. (2.56). This means no discontinuity in the derivative of the total velocity potential.

2.7 Near-field solution and matching with far-field solution

As described in Section 2.5, the details of the torus cross section are seen in the near-field description. The draft of the section is assumed to be equal to the radius a of the cross section. Since the first and second derivatives with respect to the tangential direction are much smaller than the first and second derivatives respect to the other two directions which are radial and vertical directions of the torus (Eq. 2.14), the near-field velocity potential appears nearly constant in the tangential direction of the torus. An implicit assumption is that we do not consider a high Fourier mode. Thus the governing equation for the near-field velocity potential φ^N is the 2D Laplace equation in the cross-sectional plane as shown in Eq. (2.15). The boundary conditions are linearized and the free-surface and body-boundary conditions are:

$$-\nu\varphi^N\;+\;\frac{\partial\varphi^N}{\partial z'}\;=\;0\quad on\;\;z'\;=\;0 \tag{2.58}$$

$$\frac{\partial\varphi^N}{\partial r'}\;=\;-\dot{a}_n\cos\left(n\beta\right)\cos\theta\quad on\;\;r'\;=\;a,\;\;z'\leq 0 \tag{2.59}$$

The two terms of free-surface condition in Eq. (2.58) are of different orders. The first term $-\nu\varphi^N$ is the order of φ^N and the second term $\dfrac{\partial\varphi^N}{\partial z'}$ is the order of φ^N/ε which is much larger than the first term. However, we still keep the order of φ^N arisen from $\dfrac{\partial\varphi^N}{\partial z'}$ in order to satisfy the linearized free-surface condition and will later make approximations. The boundary conditions in Eq. (2.59) demand that there is no water flow through the boundaries of the circle.

In order to obtain the velocity potential in the near-field, we start with Ursell (1949)'s study. Ursell (1949) considered the heave motion of a semi-submerged circular cylinder in infinitely deep water. He assumed that the amplitude of forced heave motion was small and then the amplitude of radiated wave was proportional to it. Since both the cylinder and torus are circular section, we will use the local coordinate systems shown in Figure 2.2 to introduce his expressions. In order to find the velocity potential, firstly, a series of infinite-fluid multipoles are combined to satisfy the linearized free-surface condition and the symmetry condition which is $\partial\varphi_U/\partial\theta = 0$, at $\theta = 0$. The expression is

$$\frac{gb}{\pi\omega}\sum_{m=1}^{\infty} A'_{2m}a^{2m}\left[\frac{\cos(2m\theta)}{r'^{2m}} + \frac{\nu\cos(2m-1)\,\theta}{(2m-1)\,r'^{2m-1}}\right]\exp(-i\omega t) \tag{2.60}$$

Since Eq. (2.60) goes to zero as $r' \to \infty$, a 2D wave source (Green function $G_{2D,U}$) which satisfies the linearized free-surface condition, symmetry condition and 2D radiation condition is added. The source singularity is at the center of the circular cylinder. The velocity potential φ_U can be then presented as follows.

$$\varphi_U = \frac{gb}{\pi\omega}\left\{G_{2D,U} + \sum_{m=1}^{\infty} A'_{2m}a^{2m}\left[\frac{\cos(2m\theta)}{r'^{2m}} + \frac{\nu\cos(2m-1)\,\theta}{(2m-1)\,r'^{2m-1}}\right]\right\}\exp(-i\omega t) \tag{2.61}$$

The source $G_{2D,U}$ can be approximated as Newman (1978) did for small νa. In addition,we introduce constants K_n and C_n in order to get a near-field solution that matches with the far-field. This means the velocity potential in the near-field is expressed as:

$$\begin{aligned}\varphi^N = {} & \dot{a}_n\cos(n\beta) \\ & \times\left\{A_0\left\{(1+\nu z')\left[\ln\left(\frac{8c}{r'}\right) - K_n + C_n\right] + \nu z' - \nu y'\theta\right\}\right. \\ & \left. + \sum_{m=1}^{\infty} A_{2m}\left[\frac{\cos(2m\theta)}{r'^{2m}} + \frac{\nu\cos(2m-1)\,\theta}{(2m-1)\,r'^{2m-1}}\right]\right\}\end{aligned} \tag{2.62}$$

A_0 and A_{2m} are complex unknowns which must be determined from the body boundary conditions Eq. (2.59). In practice the terms of A_{2m} will lead to an infinite system of simultaneous equations, which can be truncated and solved by numercial methods. Ursell (1949) proved that this process is convergent for a circular body profile. r' is the radial distance from the center of the section. Eq. (2.62) satisfies correctly the free-surface condition and the 2D Laplace equation with an error $(\nu^2 a^2)$.

The coefficient C_n in Eq. (2.62) for the near field potential can be found by matching asymptotic expansion of the far field with Eq. (2.57) and the near field velocity potentials. The matching is performed by setting the expression for the far field potential equal to the near field potential. r' goes to infinity in the near field expression. This procedure demands the two potentials to be equal. The far field

expression is used as close to the torus as possible, while the near field description is used as far out from the section as possible. The result is

$$C_n = \pi\nu c\Bigg\{ -\frac{\pi}{2} J_n(\nu c)\, Y_n(\nu c) + i\pi \left[J_n(\nu c)\right]^2 - \frac{1}{4}\int_0^{2\pi} \mathbf{H}_0\left(\nu c\sqrt{2(1-\cos\mu)}\right)\cos(n\mu)\,\mathrm{d}\mu \Bigg\} \tag{2.63}$$

We can evaluate the Struve function by Eq. (2.50). The body boundary conditions Eq. (2.59) lead to the following equation

$$A_0\left\{-\nu\cos\theta\left[\ln\left(\frac{8c}{a}\right) - K_n + C_n\right] - \frac{1}{a} - \nu\theta\sin\theta\right\} - \sum_{m=1}^{\infty} A_{2m}\left[\frac{2m\cos(2m\theta)}{a^{2m+1}} + \frac{\nu\cos(2m-1)\theta}{a^{2m}}\right] = -\cos\theta \tag{2.64}$$

The complex values of A_0 and A_{2m} follow by satisfying Eq. (2.64) at given values of θ when $0 \le \theta \le \pi/2$. The solution is consistent with previous asymptotic solution for $\nu a \to 0$ by Faltinsen (2011) but contains additional terms which make the solution applicable to a broader frequency range. However, it is not valid for high frequencies.

The main difference between Eq. (2.62) and the near field velocity potential by Newman (1978) is the constants K_n and C_n, which influence strongly the low-frequency asymptotic. The reason of this difference is due to that a straight line distribution of sources has been applied to represented the geometry of the ship by Newman (1978) in the far field, while a line distribution of sources along the center line of the torus has been applied to represented the geometry of the torus in the far field in our study.

The 2D vertical added mass and damping coefficients $a_{33}^{(n)}$ and $b_{33}^{(n)}$ for mode n can be determined by integrating the linearized hydrodynamic pressure force due to the pressure term $-\rho\partial\varphi^N/\partial t$ over the mean wetted surface of the cross-section. The torus section is given a forced harmonic oscillation with velocity $\dot{a}_n\cos(n\beta)$ of mode n. The dynamic pressure $-\rho\partial\varphi^N/\partial t$ is found by differentiating the near field velocity potential φ^N for vertical motion mode n with respect to t. The dynamic pressure is multiplied with the negative $z'-$component of the body normal vector $\cos\theta$ and the radius a of the cross section and then integrated over the mean wetted surface from $\theta = -\pi/2$ to $\theta = \pi/2$. The result is the added mass and damping loads in $z'-$direction per unit length on the torus due to the forced motion of mode

n. This leads to the following 2D vertical force due to the forced motion:

$$\begin{aligned} f_3 &= -\rho \int_{-\pi/2}^{\pi/2} \frac{\partial \varphi^N}{\partial t} \cos\theta a \mathrm{d}\theta = f_3^N \ddot{a}_n \cos(n\beta) \\ f_3^N &= -\rho \int_{-\pi/2}^{\pi/2} a\mathrm{d}\theta \cos\theta \Bigg\{ A_0 \Bigg\{ (1 - \nu a \cos\theta) \left[\ln\left(\frac{8c}{a}\right) - K_n + C_n \right] \\ &\qquad - \nu a \cos\theta - \nu a\theta \cos\theta \Bigg\} \\ &\qquad + \sum_{m=1}^{\infty} A_{2m} \left[\frac{\cos(2m\theta)}{a^{2m}} + \frac{\nu \cos(2m-1)\theta}{(2m-1)\, a^{2m-1}} \right] \Bigg\} \end{aligned} \tag{2.65}$$

The expression of f_3^N can be analytically integrated.

$$\begin{aligned} f_3^N &= -\rho a \Bigg\{ A_0 \left\{ \left(2 - \frac{1}{2}\pi\nu a\right) \left[\ln\left(\frac{8c}{a}\right) - K_n + C_n \right] - \frac{3}{4}\pi\nu a \right\} \\ &\qquad + A_2 \frac{\pi\nu}{2a} - \sum_{m=1}^{\infty} A_{2m} \frac{2\cos(m\pi)}{a^{2m}(4m^2-1)} \Bigg\} \end{aligned} \tag{2.66}$$

The 2D vertical added mass and damping coefficients are formally defined by

$$f_3^{\text{added mass + damping}} = -a_{33}^{(n)} \ddot{a}_n \cos(n\beta) - b_{33}^{(n)} \dot{a}_n \cos(n\beta) \tag{2.67}$$

By equalizing Eq. (2.65) and Eq. (2.67) we get

$$\begin{aligned} f_3^{\text{added mass + damping}} &= f_3^N \ddot{a}_n \cos(n\beta) \\ \left(i\omega a_{33}^{(n)} - b_{33}^{(n)}\right) \dot{a}_n \cos(n\beta) &= \left[-i\omega \mathbf{Re}\left(f_3^N\right) + \omega \mathbf{Im}\left(f_3^N\right)\right] \dot{a}_n \cos(n\beta) \end{aligned} \tag{2.68}$$

This means that

$$a_{33}^{(n)} = -\mathbf{Re}\left(f_3^N\right), \quad b_{33}^{(n)} = -\omega \mathbf{Im}\left(f_3^N\right) \tag{2.69}$$

When $\omega \to 0$, we get that

$$\frac{a_{33}^{(n)}}{0.5\rho\pi a^2} = \frac{4}{\pi} \left\{ \frac{2}{\pi} \left[\ln\left(\frac{8c}{a}\right) - K_n \right] + \frac{3 - 4\ln 2}{\pi} \right\}, \quad b_{33}^{(n)} = 0 \tag{2.70}$$

The generalized added mass and damping coefficients of the torus associated with the modes $\cos(n\beta), n = 0, 1, \ldots$ are:

$$\begin{aligned} A_{33}^{(n)} &= a_{33}^{(n)} c \int_0^{2\pi} \cos^2(n\beta)\, \mathrm{d}\beta \\ B_{33}^{(n)} &= b_{33}^{(n)} c \int_0^{2\pi} \cos^2(n\beta)\, \mathrm{d}\beta \end{aligned} \tag{2.71}$$

2.8 Generalized vertical excitation force

The torus is semi-submerged and assumed to be at rest. We consider incident deep-water regular waves with wave amplitude ζ_a propagating along the positive x-axis. According to linear wave theory for deep water, deep water implies $h > \lambda/2$ (Dean and Dalrymple, 1991). h is the water depth and $\lambda = 2\pi/\nu$ is the wave length. We assume long wave theory, that is, the waves are much longer than the cross-sectional diameter of the torus, *i.e.* $\lambda/a \gg 1$. The incident wave potential is expressed as

$$\varphi_0 \;=\; \frac{g\zeta_a}{\omega}\exp\left(\nu z \;+\; i\nu x \;-\; i\omega t\right) \tag{2.72}$$

The wave elevation is found by differentiating φ_0 with respect to time and inserting the expression in the dynamic linear condition $g\zeta + \partial\varphi_0/\partial t = 0$ on $z = 0$. The wave elevation ζ is then expressed as

$$\zeta \;=\; i\zeta_a \exp\left(i\nu x \;-\; i\omega t\right) \tag{2.73}$$

It is understood that it is the real part of the expression that has physical meaning. We divide the vertical wave excitation loads into a Froude-Kriloff part and a diffraction part.

Linear Froude-Kriloff force

The linear Froude-Kriloff force is obtained by properly integrating the undisturbed incident dynamic pressure

$$p^{FK} \;=\; \rho g\zeta_a i \exp\left(\nu z \;+\; i\nu x \;-\; i\omega t\right) \tag{2.74}$$

from the incident waves over the mean wetted surface of the torus. We make a Taylor expansion at $z = 0$ of the exponential function $\exp(\nu z)$ and keep the two lowest order terms 1 and νz. Therefore, an approximation of the Froude-Kriloff pressure on the torus is

$$p^{FK} \;=\; \rho g\zeta_a i\left(1 \;+\; \nu z\right)\exp\left(i\nu x_{CL} \;-\; i\omega t\right) \tag{2.75}$$

where $x_{CL} = c\cos\beta$ is the x-coordinate of the center line of the torus. Since mode superposition will be used to calculate the response of the torus, and each modal equation will have a generalized added mass and damping coefficient, generalized restoring coefficient and generalized excitation forces. It will then be most practical to express the wave forces as a Fourier sum involving Bessel functions. We can write

$$\exp\left(i\nu c\cos\beta\right) \;=\; J_0\left(\nu c\right) \;+\; \sum_{m=1}^{\infty} 2i^m J_m\left(\nu c\right)\cos\left(m\beta\right) \tag{2.76}$$

We denote S_C as the mean wetted cross-sectional surface of the torus and note that for one torus that

$$-\int_{S_C}\left(1+\nu z\right)n_3\,\mathrm{d}s \;=\; a\int_{-\pi/2}^{\pi/2}\left(1-\nu a\cos\theta\right)\cos\theta\,\mathrm{d}\theta \;=\; 2a\left(1-\pi\nu a/4\right) \tag{2.77}$$

This means that the vertical Froude-Kriloff force per unit length on the cross-section of the torus can be approximated as

$$f_3^{FK} = \rho g \zeta_a i \left[J_0(\nu c) + \sum_{m=1}^{\infty} 2 i^m J_m(\nu c) \cos(m\beta) \right] \times b_w (1 - \pi \nu a/4) \exp(-i\omega t) \tag{2.78}$$

We can interpret Eq. (2.78) as follows. There is one term shown by Eq. (2.79) representing the change in buoyancy force per unit length due to the incident wave elevation.

$$\rho g b_w \zeta_a i \left[J_0(\nu c) + \sum_{m=1}^{\infty} 2 i^m J_m(\nu c) \cos(m\beta) \right] \exp(-i\omega t) \tag{2.79}$$

The other term shown by Eq. (2.80) is the mean displaced mass per unit length times the vertical acceleration of the incident waves at the mean free-surface.

$$-\rho g b_w \zeta_a \frac{\pi \nu a}{4} i \left[J_0(\nu c) + \sum_{m=1}^{\infty} 2 i^m J_m(\nu c) \cos(m\beta) \right] \exp(-i\omega t) \tag{2.80}$$

Linear diffraction force

Fundamentally, the linear diffraction force can be obtained by integrating the diffraction pressure which changes the pressure filed due to the presence of the torus over the mean wetted surface of the torus. The diffraction potential φ_D can be found in a similar way as the radiation problem by solving a boundary value problem. The diffraction potential φ_D must also satisfy the Laplace equation and the free-surface condition. In order to compensate for the disturbance of the incident wave around the torus by an additional condition at the body boundary, the normal gradient of the diffraction potential is equal but opposite in sign to the normal gradient of the incident potential. In this way we ensure that the normal component of the total velocity on the torus is equal to zero as follows

$$\frac{\partial(\varphi_0 + \varphi_D)}{\partial n} = 0 \quad on \quad S_C \tag{2.81}$$

Since the radiation problem has already been solved in our study, an approximation of the diffraction force involving forced oscillations with minus the incident vertical wave velocity and acceleration at $z = z_m$ along the torus can be applied. Here z_m is a weighted z-coordinate of the torus and obtained as follows

$$z_m = \frac{2 \int_{-a}^{0} z' f_{y'}(z') \, \mathrm{d}z'}{\pi a^2} \tag{2.82}$$

where $f_{y'}(z')$ is the function that describes the width of the cross section of the torus for different z'. The latter choice of z_m has not been rationally justified. The

vertical diffraction force per unit length is then $a_{33}^{(m)} a_{3\zeta} + b_{33}^{(m)} w_\zeta$. $a_{3\zeta}$ and w_ζ are the vertical acceleration and velocity of the incident waves at $z = z_m$, respectively. Here

$$w_\zeta = \frac{\partial \varphi_0}{\partial z}, \qquad a_{3\zeta} = \frac{\partial^2 \varphi_0}{\partial z \partial t} \tag{2.83}$$

where

$$\begin{aligned} w_\zeta &= -\omega \zeta_a \exp\left(\nu z_m + i\nu x_{CL} - i\omega t\right) = \\ -\omega \zeta_a \exp\left(\nu z_m - i\omega t\right) &\left[J_0\left(\nu c\right) + \sum_{m=1}^{\infty} 2 i^m J_m\left(\nu c\right) \cos\left(m\beta\right) \right] \end{aligned} \tag{2.84}$$

and similarly for $a_{3\zeta}$. Since Eq. (2.84) is a Fourier-series in β, we can use the results from the forced vertical motion problem. The vertical diffraction force per unit length is therefore

$$\begin{aligned} f_3^D = &\zeta_a \exp\left(\nu z_m - i\omega t\right) \left[J_0\left(\nu c\right) \left(-i\omega^2 a_{33}^{(0)} + \omega b_{33}^{(0)} \right) \right. \\ &\left. + \sum_{m=1}^{\infty} 2 i^m J_m\left(\nu c\right) \left(-i\omega^2 a_{33}^{(m)} + \omega b_{33}^{(m)} \right) \cos\left(m\beta\right) \right] \end{aligned} \tag{2.85}$$

Another way to express the diffraction force is by using Green's second identity in a similar way as is done in deriving the Haskind relationship (Haskind, 1948). We then avoid the ambiguity in specifying z_m in Eq. (2.85). We denote the diffraction potential φ_D and introduce a velocity potential φ_3 that satisfies the body boundary condition $\partial \varphi_3 / \partial n = n_3$ and the same free-surface and radiation conditions as φ_D. The vertical diffraction force is first expressed as

$$f_3^D = -\rho i \omega \int_{S_C} \varphi_D n_3 \, \mathrm{d}s = -\rho i \omega \int_{S_C} \varphi_D \frac{\partial \varphi_3}{\partial n} \, \mathrm{d}s \tag{2.86}$$

Applying Green's second identity, we can get:

$$f_3^D = -\rho i \omega \int_{S_C} \varphi_D \frac{\partial \varphi_3}{\partial n} \, \mathrm{d}s = -\rho i \omega \int_{S_C} \frac{\partial \varphi_D}{\partial n} \varphi_3 \, \mathrm{d}s \tag{2.87}$$

We now use that the incident wave potential φ_0 and the diffraction potential φ_D satisfies the body boundary condition Eq. (2.81). The vertical diffraction force can then be finally expressed as:

$$\begin{aligned} f_3^D &= -\rho i \omega \int_{S_C} \frac{\partial \varphi_D}{\partial n} \varphi_3 \, \mathrm{d}s = \rho i \omega \int_{S_C} \frac{\partial \varphi_0}{\partial n} \varphi_3 \, \mathrm{d}s \\ \approx \rho i \omega &\int_{S_C} n_3 \frac{\partial \varphi_0}{\partial z} \varphi_3 \, \mathrm{d}s \approx \rho i \omega^2 \zeta_a \exp\left(-i\omega t\right) \int_{S_C} n_3 \left(1 + \nu z\right) \varphi_3^S \, \mathrm{d}s \end{aligned} \tag{2.88}$$

We have here introduced the velocity potential

$$\varphi_3^S = \left[J_0\left(\nu c\right) + \sum_{m=1}^{\infty} 2 i^m J_m\left(\nu c\right) \cos\left(m\beta\right) \right] \varphi_3 \tag{2.89}$$

The solution can be expressed by Eq. (2.62), *i.e.*

$$\begin{aligned}\varphi_3^S &= J_0(\nu c)\,\varphi_0^N + \sum_{m=1}^{\infty} 2i^m J_m(\nu c)\cos(m\beta)\,\varphi_m^N \\ \varphi_m^N &= A_0\left\{(1+\nu z')\left[\ln\left(\frac{8c}{r'}\right) - K_m + C_m\right] + \nu z' - \nu y'\theta\right\} \\ &\quad + \sum_{n=1}^{\infty} A_{2n}\left[\frac{\cos(2n\theta)}{r'^{2n}} + \frac{\nu\cos(2n-1)\,\theta}{(2n-1)\,r'^{2n-1}}\right]\end{aligned} \tag{2.90}$$

Here A_0 and A_{2n} are a function of the mode m. Eqs. (2.86) to (2.88) involve integrations over the mean cross-sectional wetted area.

The theoretical solution of Eq. (2.88) is:

$$\begin{aligned}f_3^D &\approx \rho i\omega^2\zeta_a \exp(-i\omega t)\int_{S_C} n_3(1+\nu z)\,\varphi_3^S\,\mathrm{d}s \\ &= -\rho a i\omega^2\zeta_a \exp(-i\omega t)\left[J_0(\nu c)(Z_1 - Z_3)\right. \\ &\quad \left. + \sum_{m=1}^{\infty} 2i^m J_m(\nu c)\cos(m\beta)(Z_2 - Z_3)\right]\end{aligned} \tag{2.91}$$

The expressions of Z_1, Z_2 and Z_3 are as follows.

$$\begin{aligned}Z_1 &= A_0\left\{\left(\frac{4}{3}\nu^2a^2 - \nu a\pi + 2\right)\left[\ln\left(\frac{8c}{a}\right) + C_0\right]\right. \\ &\quad \left. + \nu a\left(\frac{16}{9}\nu a - \frac{3}{4}\pi\right)\right\} + A_2\frac{\pi\nu}{4a} \\ Z_2 &= A_0\left\{\left(\frac{4}{3}\nu^2a^2 - \nu a\pi + 2\right)\left[\ln\left(\frac{8c}{a}\right) - K_m + C_m\right]\right. \\ &\quad \left. + \nu a\left(\frac{16}{9}\nu a - \frac{3}{4}\pi\right)\right\} + A_2\frac{\pi\nu}{4a} \\ Z_3 &= \sum_{n=1}^{\infty} A_{2n}\left[\frac{2\cos(n\pi)}{a^{2n}(4n^2-1)} + \frac{4\nu^2\cos(n\pi)}{a^{2n-2}(16n^4 - 32n^3 + 8n^2 + 8n - 3)}\right]\end{aligned} \tag{2.92}$$

2.9 Equations of vertical motions

We substitute w given by Eq. (2.11) into Eq. (2.10) and use the fact that $\partial/\partial s = c^{-1}\partial/\partial\beta$. The resulting equation are then multiplied successively by $\cos(m\beta), m = 0, 1, \ldots$ and integrated along the center line of the torus which means multiplying the equation with the torus radius c and integrating from $\beta = 0$ to 2π. Eq. (2.10)

becomes as follows

$$\begin{aligned}
&\int_0^{2\pi} \left\{ m \left[\ddot{a}_0 + \sum_{n=1}^{\infty} \ddot{a}_n \cos(n\beta) \right] + \rho g b_w \left[a_0 + \sum_{n=1}^{\infty} a_n \cos(n\beta) \right] \right. \\
&\left. + \frac{EI}{c^4} \sum_{n=1}^{\infty} \left(n^4 - n^2\right) a_n \cos(n\beta) + \frac{T_{as}}{c^2} \sum_{n=1}^{\infty} n^2 a_n \cos(n\beta) \right\} \cos(m\beta)\, c\, \mathrm{d}\beta \\
&= \int_0^{2\pi} \left(f_3(\beta)^{\text{added mass + damping}} + f_3(\beta)^{\text{wave excit}} \right. \\
&\left. + \sum_{i=1}^{8} T_{p,3} \delta(\beta - \beta_i) \right) \cos(m\beta)\, c\, \mathrm{d}\beta
\end{aligned} \tag{2.93}$$

Here $T_{p,3}$ is the vertical component of pre-tension of the mooring lines. β_i describes the attachment positions between mooring lines and torus. δ is the Dirac delta function. Due to the property of orthogonal functions shown in Eq. (2.94)

$$\int_0^{2\pi} \cos(m\beta) \cos(n\beta)\, \mathrm{d}\beta \begin{cases} = 0, & m \neq n \\ = 2\pi, & m = n = 0 \\ = \pi, & m = n = 1, 2, \ldots \end{cases} \tag{2.94}$$

The coupled second order differential equation system arises by using Eq. (2.78) and Eq. (2.85) to express the wave excitation loads. We get

$$\begin{aligned}
&\left(m + a_{33}^{(0)}\right) \ddot{a}_0 + b_{33}^{(0)} \dot{a}_0 + \rho g b_w a_0 = \frac{1}{2\pi} \int_0^{2\pi} \sum_{i=1}^{8} T_{p,3} \delta(\beta - \beta_i)\, \mathrm{d}\beta + \\
&\left[\left(1 - \frac{\pi \nu a}{4}\right) \rho g b_w - \left(\omega^2 a_{33}^{(0)} + i\omega b_{33}^{(0)}\right) \exp(\nu z_m) \right] \zeta_a J_0(\nu c)\, i \exp(-i\omega t)
\end{aligned}$$

$$\begin{aligned}
&\left(m + a_{33}^{(m)}\right) \ddot{a}_m + b_{33}^{(m)} \dot{a}_m + \left[\rho g b_w + \frac{EI}{c^4} \left(m^4 - m^2\right) \right] a_m \\
&+ \frac{1}{\pi c^2} \sum_{n=1}^{\infty} \sum_{i=1}^{8} n^2 T_{as}^{(i)} \int_{\beta_i}^{\beta_{i+1}} \cos(n\beta) \cos(m\beta)\, \mathrm{d}\beta a_n = \\
&\frac{1}{\pi} \int_0^{2\pi} \sum_{i=1}^{8} T_{p,3} \delta(\beta - \beta_i) \cos(m\beta)\, \mathrm{d}\beta \\
&+ \left[\left(1 - \frac{\pi \nu a}{4}\right) \rho g b_w - \left(\omega^2 a_{33}^{(m)} + i\omega b_{33}^{(m)}\right) \exp(\nu z_m) \right] \\
&\times \zeta_a 2 J_m(\nu c)\, i^{m+1} \exp(-i\omega t), \quad m = 1, 2, \ldots
\end{aligned} \tag{2.95}$$

The axial tension T_{as} is treated in a simplified manner. This allows for simplification of calculations, rather than solving the structural problem by a finite element model. The simplified calculation procedure is explained in detail in Appendix B. In summary, T_{as} is assumed to be piecewise constant along the torus, divided in

eight sections defined by the crow foot mooring arrangement. In calm conditions, the set-up is symmetric with respect to the $x-z$ plane, and the values are found in static conditions from the pre-tensions in the moorings. The term representing the axial stiffness in Eq. (2.95) is given analytically by

$$\int_{\beta_i}^{\beta_{i+1}} \cos(n\beta)\cos(m\beta)\,\mathrm{d}\beta = \begin{cases} \dfrac{(\beta_{i+1}-\beta_i)\,[m\sin m\cos n - n\cos m\sin n]}{m^2-n^2}, & m \neq n \\ \dfrac{\sin(2m\beta_{i+1}) - \sin(2m\beta_i) + 2m\,(\beta_{i+1}-\beta_i)}{4m}, & m = n \end{cases} \tag{2.96}$$

Alternatively and more accurately we can use Eq. (2.91) to express the diffraction force part of Eq. (2.95). The modal equations are found by dividing the resulting expressions in Eq. (2.93) with $2\pi c$ and πc for $n = 0$ and $n = 1, 2, ...$ respectively. Eq. (2.95) shows that the curved Euler-Bernoulli beam equation (Eq. 2.10) which involves the vertical motion represented by Fourier series could be decomposed to individual modal equations. Since the axial tension T_{as} on the left hand side of Eq. (2.95) is assumed to be piecewise constant along the torus and integrated piecewise, the term associated with the axial tension T_{as} will provide coupling effect between different modes. The vertical motion of each mode n can be obtained from Eq. (2.95) by using the generalized added mass, damping and excitation force that we have already derived. Then, the total vertical motion at any point on the torus just simply superposes the vertical motion of each mode multiplied with $\cos(n\beta)$ which defines the point position in Figure 2.1.

2.10 Summary

A low-frequency slender-body theory for the vertical added mass, damping loads on an elastic semi-submerged torus has been derived by matched asymptotic expansions with a near-field and far-field solution. Linear Froude-Kriloff force is obtained by property integrating the undisturbed incident dynamic pressure from the incident waves over the mean wetted surface of the torus, and linear diffraction force is approximately obtained by forcing oscillations with minus the incident vertical wave velocity and acceleration at a mean position, then multiplied with damping and added mass respectively. A Haskind-type expression for linear diffraction force is also presented.

Chapter 3

Verification studies of the low-frequency slender-body theory

In this chapter, the most important verification tests performed in the development of the low-frequency slender-body theory are presented. Before getting into the various forms and strategies of testing and checking studies, we must understand what is meant by verification and validation and what is the difference between the two. Verification of a computer program means to check that the program is actually a correct representation of the mathematical model that forms the basis for it. Validation is the demonstration that the verified computer program is an adequate representation of the physical reality (ITTC, 1990). Another definitions of verification and validation is that verification is intended to check whether the program conforms to specifications or solves its equations correctly. While validation is intended to ensure the program meets the expectations and requirements or solves the correct equations. The latter is with respect to the physical problem being studied. Thus, verification is a purely mathematical exercise that does not address the physics.

We will in the following present some of the verification test studies that have been performed for testing the low-frequency slender-body theory.

The low-frequency slender-body theory has been verified by using WAMIT. WAMIT is a computer program based on the linear and second-order potential theory for analyzing floating or submerged bodies, in the presence of ocean waves. The boundary integral equation method (BIEM), also known as the panel method, is used to solve for the velocity potential and fluid pressure on the submerged surfaces of the bodies. Separate solutions are carried out simultaneously for the diffraction problem, giving the effects of incident waves on the body, and the radiation problems for each of the prescribed modes of motion of the bodies. These solutions are then used to obtain the relevant hydrodynamic parameters including added-mass and damping coefficients, exciting forces, response amplitude operators

(*RAO*'s), the pressure and fluid velocity, and the mean drift forces and moments. Specifically, the radiation and diffraction velocity potentials on the body wetted surface are determined from the solution of an integral equation obtained by using Green's theorem with the frequency-domain source-potential satisfying the free-surface and radiation conditions as the Green function. In addition to the conventional six degrees of rigid-body motion WAMIT is also able to handle generalized modes to represent a wide variety of physical phenomena including hydroelastic deformations.

WAMIT includes two options to consider the wave-body interaction which are low-order method and higher-order method. The conventional low-order method, where the body geometry is represented by small quadrilateral panels and the velocity potential is assumed constant on each panel, often require a fine discretization of the body. As the panel size decreased and the number of panels increased, the representation of the body geometry and the hydrodynamic results will become more accurate. One way to check the accuracy of the results is to perform convergence study. However, the computational time will increase with increasing number of panels. In order to reduce the computational time and increase the accuracy of the results a higher-order method is introduced, where both the body geometry and the velocity potential are represented by B-splines.

The higher-order method first divides the body into sub-surfaces that are discontinuous between the common edge (corner) as 'patch', then, each patch will be further divided into panels by using B-splines. The other important subject to consider is the manner in which the velocity potential is represented on each patch. Desirable properties of this representation are that it should be smooth and continuous, corresponding to the physical solution for the fluid flow over the surface, with control over the accuracy. B-splines here are used to provide a continuous representation of the solution, so the order of B-splines should be selected to ensure continuity of derivatives as well as higher-order derivatives on each patch. More specifically, on each patch the velocity potential is represented by a tensor product of B-spline basis functions

$$\phi\left(u,v\right) \;=\; \sum_{j=1}^{M_v}\sum_{i=1}^{M_u}\phi_{ij}U_i\left(u\right)V_j\left(v\right) \tag{3.1}$$

Here a pair of parametric coordinates (u, v) are used to define the position on each patch. U_i and V_j are the B-spline basis functions of u and v, and M_u and M_v are the number of basis functions in u and v, respectively. The unknown coefficients ϕ_{ij} are determined ultimately by substituting this representation in the integral equation for the potential. The total number of unknowns on a patch is $M_u \times M_v$. In the low order panel method, the accuracy of the numerical solution depends on the number of panels. In the higher-order method the accuracy depends on two parameters: the order of the basis functions and their number M_u and M_v. Order is defined as the degree of the polynomial plus one.

An elastic semi-submerged torus used in model tests which is detailed described in Chapter 4 with torus radius $c = 0.75m$ and cross-sectional radius $a = 0.019m$ is studied. One quarter of the torus model is established in WAMIT because a torus

has two planes of symmetry. This can be exploited to minimize computing time and to increase the accuracy of calculation since large number of panel subdivisions on each patch can be used. The non-dimensional results are functions of the non-dimensional wave number νa and a/c which is 0.0253 in our case.

The 3D generalized added mass and damping coefficients obtained by WAMIT are transformed to the equivalent sectional values $a_{33}^{(n)}$ and $b_{33}^{(n)}$ by means of Eq. (2.71). The 3D generalized forces obtained by WAMIT is done similarly and the sectional vertical wave-excitation force amplitudes are denoted $f_3^{(n)}$. We have considered twenty modes. The comparisons of generalized added mass, damping coefficients, vertical excitation forces and response amplitude operators (RAO's) of the torus for the modes number $n = 0, 1, ..., 11$ are shown in this chapter. The comparisons of generalized added mass, damping coefficients, vertical excitation forces and response amplitude operators of the torus for the modes number $n = 12, 13, ..., 19$ are shown in Appendix C.

3.1 Verification of generalized added mass and damping coefficients

The sectional added mass and damping are made non-dimensional as $a_{33}^{(n)}/m$ and $b_{33}^{(n)}/m\omega$, respectively. Here $m = 0.5\rho\pi a^2$. The added mass and damping coefficients for the twelve lowest modes are presented in Figures 3.1 to 3.3 and in Figures 3.4 to 3.6, respectively, in the practical interest frequency range correspond to νa from 0 to 0.279 showing good agreement between low-frequency slender-body theory and WAMIT. There is also as expected an increasing difference with increasing νa.

The strip theory results are presented in Figure 3.7 in order to illustrate together with Figures 3.1 to 3.6 the fact that there are important 3D wave effects on the scale of the torus radius. The strip theory calculations have been done with a Boundary Element Method (BEM) using 100 panels on the mean wetted body surface. Strip theory predicts that added mass goes to infinity when the frequency goes to zero while the 3D calculations approach a finite value, which is mode number dependent and equal to $4.758m$ in heave for the studied case. The strip-theory calculated damping coefficient approaches zero when the frequency goes to zero but with a different asymptotic behavior than low-frequency slender-body theory and WAMIT.

The strip theory does not predict the strong oscillatory behavior as a function of νa as the 3D theories do. The oscillatory behavior are due to hydrodynamic interaction on the scale of the torus radius c. The added mass may become negative for certain frequencies according to the 3D theories. Furthermore, the damping coefficients become zero for certain values of νa by the 3D methods. The zeroes depend on the mode number. Zero damping means that there are no radiated far-field waves. When $\nu a > 0$, the zeroes of the damping coefficients correspond to zeroes of the Bessel function $J_n(\nu a)$ according to low-frequency slender-body theory. Strip theory calculations are common in engineering calculations of wave-

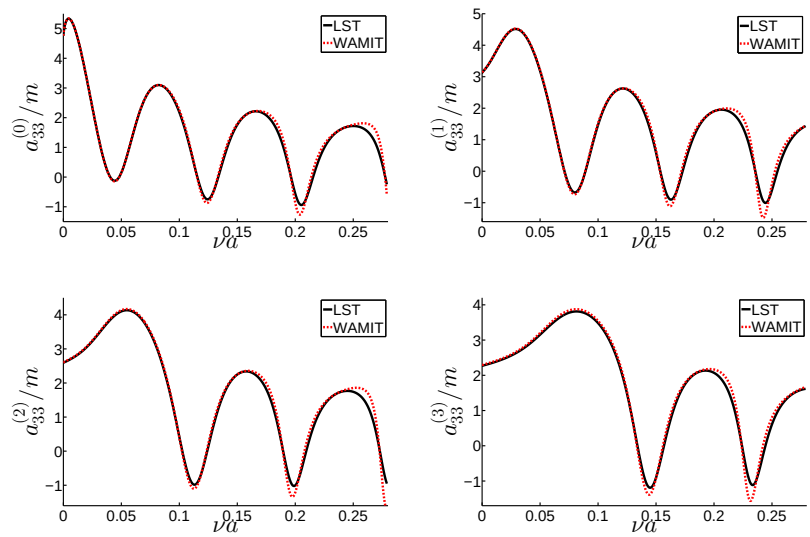

Figure 3.1: Comparison of sectional vertical added mass coefficients $a_{33}^{(n)}$ of a torus for the modes number $n = 0, 1, 2, 3$ with $a/c = 0.0253$ by means of the low-frequency slender-body theory (LST) and WAMIT versus nondimensional wave number νa. m is displaced cross-sectional mass.

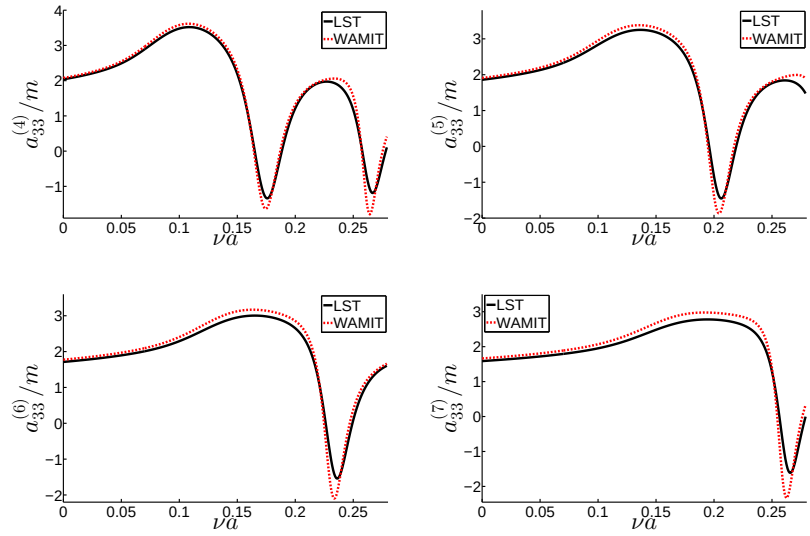

Figure 3.2: Comparison of sectional vertical added mass coefficients $a_{33}^{(n)}$ of a torus for the modes number $n = 4, 5, 6, 7$ with $a/c = 0.0253$ by means of the low-frequency slender-body theory (LST) and WAMIT versus nondimensional wave number νa. m is displaced cross-sectional mass.

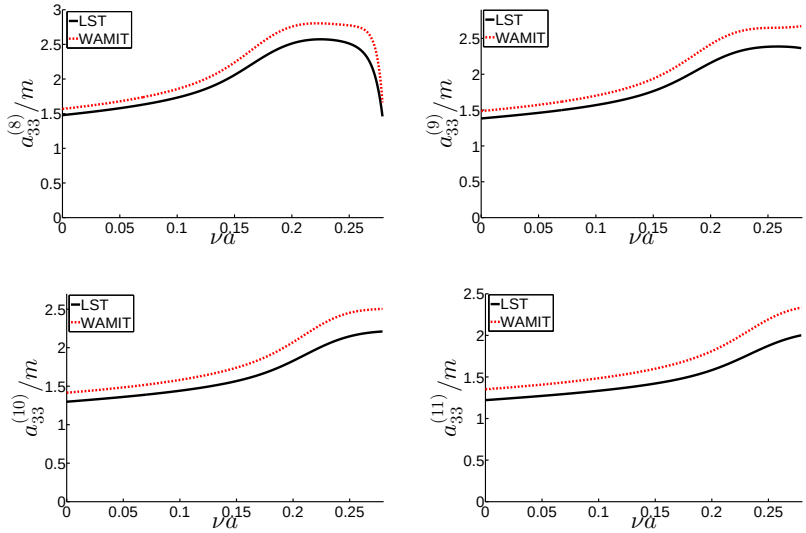

Figure 3.3: Comparison of sectional vertical added mass coefficients $a_{33}^{(n)}$ of a torus for the modes number $n = 8, 9, 10, 11$ with $a/c = 0.0253$ by means of the low-frequency slender-body theory (LST) and WAMIT versus nondimensional wave number νa. m is displaced cross-sectional mass.

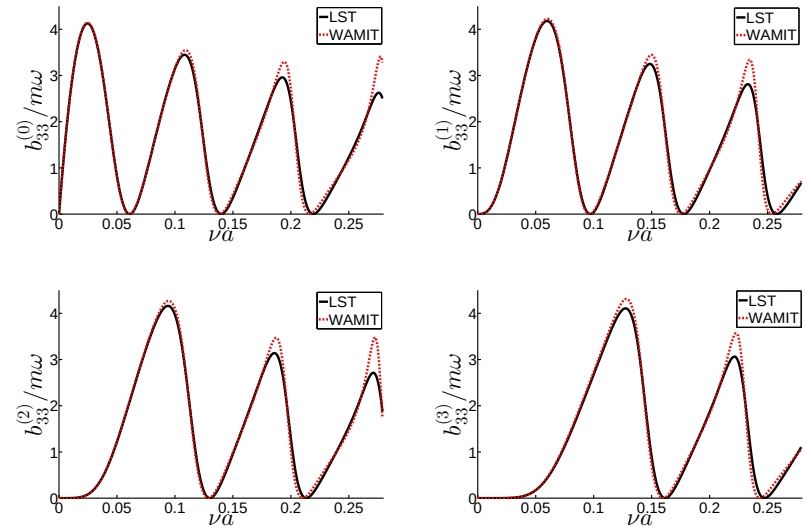

Figure 3.4: Comparison of sectional vertical damping coefficients $b_{33}^{(n)}$ of a torus for the modes number $n = 0, 1, 2, 3$ with $a/c = 0.0253$ by means of the low-frequency slender-body theory (LST) and WAMIT versus nondimensional wave number νa. m is displaced cross-sectional mass.

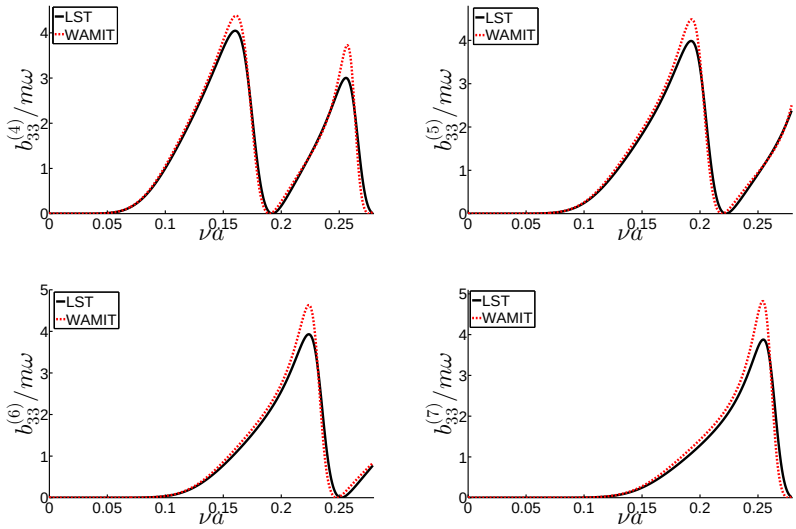

Figure 3.5: Comparison of sectional vertical damping coefficients $b_{33}^{(n)}$ of a torus for the modes number $n = 4, 5, 6, 7$ with $a/c = 0.0253$ by means of the low-frequency slender-body theory (LST) and WAMIT versus nondimensional wave number νa. m is displaced cross-sectional mass.

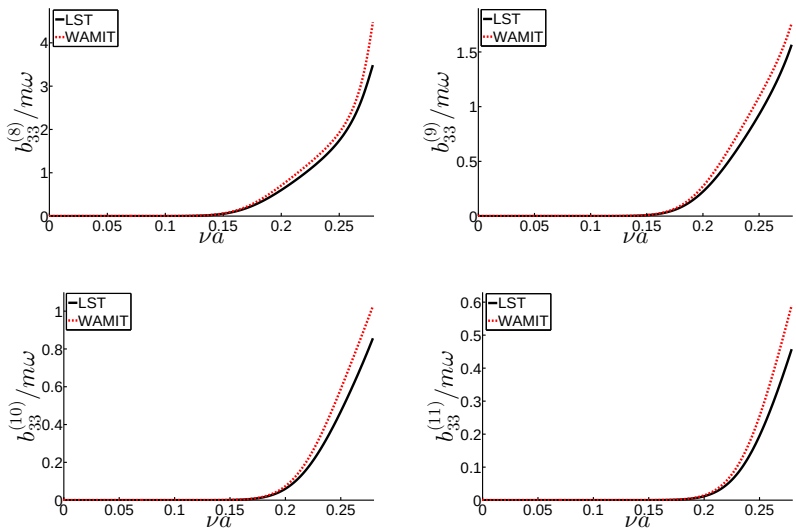

Figure 3.6: Comparison of sectional vertical damping coefficients $b_{33}^{(n)}$ of a torus for the modes number $n = 8, 9, 10, 11$ with $a/c = 0.0253$ by means of the low-frequency slender-body theory (LST) and WAMIT versus nondimensional wave number νa. m is displaced cross-sectional mass.

induced loads on the floater of a fish farm. The presented results illustrate the limitations of such an approach.

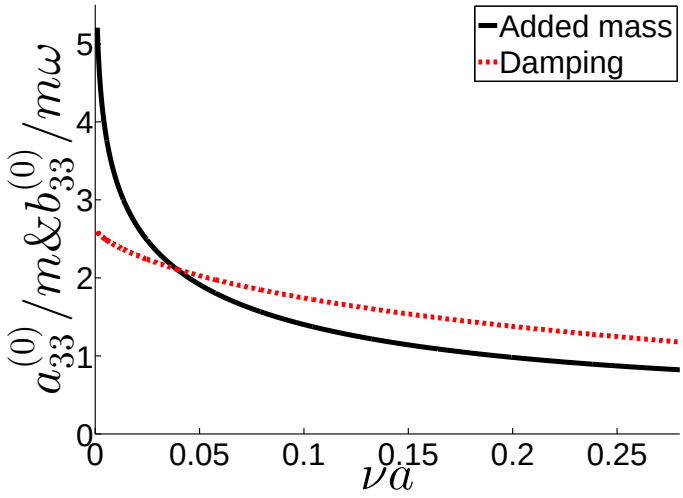

Figure 3.7: Strip theory calculations of 2D heave added mass and damping coefficients versus nondimensional wave number νa. m is displaced cross-sectional mass.

We have in Figures 3.8 and 3.9 illustrated the wave field due to forced heave motion by plotting the wave amplitude as a function of radial distance ρ from the torus center for selected frequencies by means of WAMIT. The wave amplitude ζ_{ra} caused by heave oscillation is made non-dimensional by forced heave motion amplitude as ζ_{ra}/η_{3a} and the radial distance ρ defined in Figure 2.1 is made non-dimensional by the radius of torus as ρ/c. The evaluation of the free-surface requires special caution close to the body surface since this analysis requires a higher degree of numerical precision. Within a distance on the order of the dimensions of the adjacent panel, field-point quantities cannot be computed reliably (Newman and Lee, 1992). One should notice that the discontinuity of radiated wave amplitude around $\rho/c = 1.0$ is due to the present of torus. In general, the wave amplitude inside the torus increases with the increasing of frequencies and the maximum amplitude appears at the center of the torus for the studied cases. Figure 3.8 shows the wave field due to forced heave motion for frequencies with zero damping which are $\nu a = 0, 0.061, 0.139, 0.216$. The far-field wave amplitudes outside the torus are zero as expected. Figure 3.9 shows the wave field due to forced heave motion for frequencies with maximum damping which are $\nu a = 0.025, 0.109, 0.195, 0.277$. The far-field radiated wave amplitude outside the torus decays as $1/\sqrt{\rho}$ as expected from the source expression G_1 in Eq. (2.21).

The comparisons between WAMIT and the low-frequency slender-theory theory of the generalized added mass coefficient as illustrated in Figures 3.1 to 3.3 show increasing differences with increasing mode number. These differences appear from

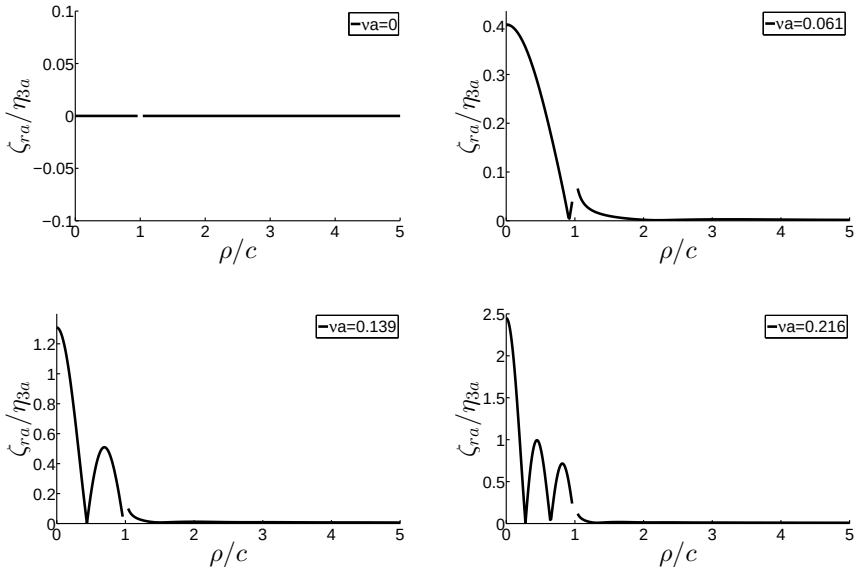

Figure 3.8: Radiated wave amplitude due to forced heave motion as a function of radial distance ρ from the torus center for selected frequencies with zero damping which are $\nu a = 0, 0.061, 0.139, 0.216$ by means of WAMIT.

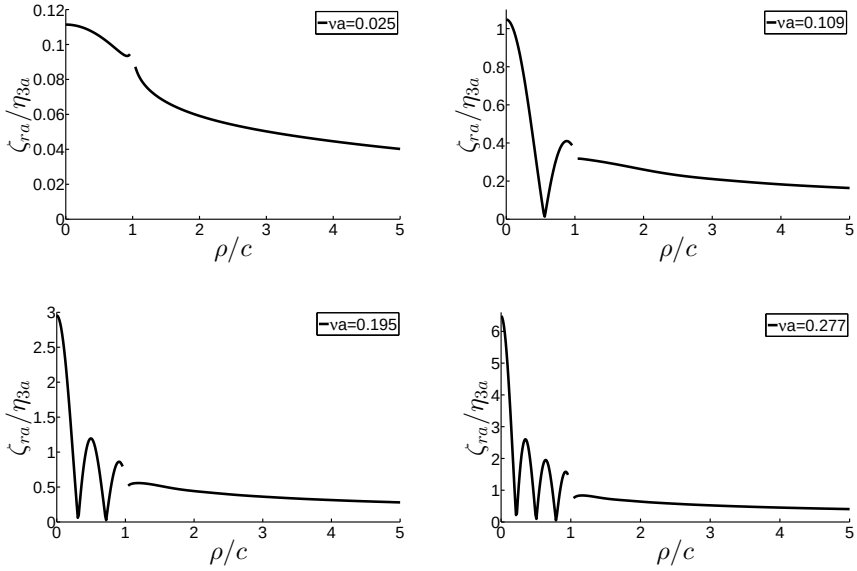

Figure 3.9: Radiated wave amplitude due to forced heave motion as a function of radial distance ρ from the torus center for selected frequencies with maximum damping which are $\nu a = 0.025, 0.109, 0.195, 0.277$ by means of WAMIT.

$\omega = 0$ in the added mass coefficients and remain of similar magnitude for all frequencies. We have illustrated the differences in vertical added mass coefficients for $\omega = 0$ as a function of mode number n in Figure 3.10. A reason to the differences for higher modes may be that the near-field solution should have satisfied 2D Helmholtz equation instead of 2D Laplace equation. The 2D Helmholtz equation follows by substituting solution form $\varphi^N = \overline{\varphi}^N \cos(n\beta)$ in the 3D Laplace equation which gives

$$\frac{\partial^2 \overline{\varphi}^N}{\partial y'^2} + \frac{\partial^2 \overline{\varphi}^N}{\partial z'^2} - \frac{n^2}{c^2}\overline{\varphi}^N = 0 \tag{3.2}$$

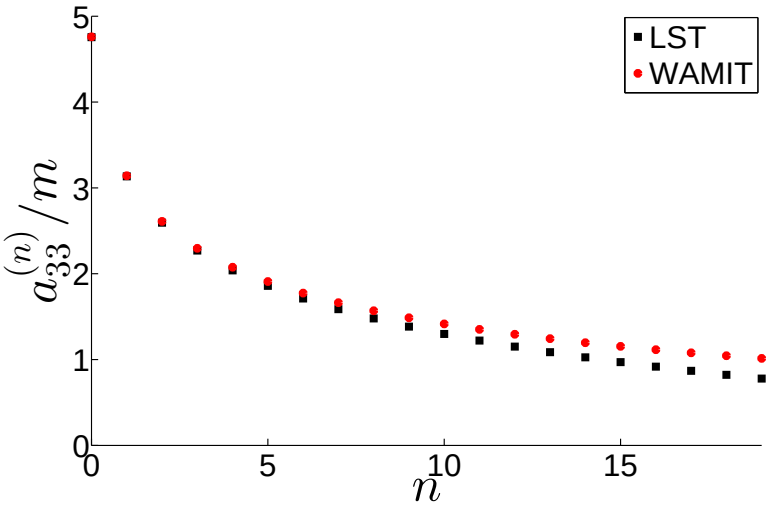

Figure 3.10: Prediction of vertical added mass coefficients $a_{33}^{(n)}$ of a torus with $a/c = 0.0253$ at frequency $\omega = 0$ as a function of mode number n by means of the low-frequency slender-body theory (LST) and WAMIT. m is displaced cross-sectional mass.

We have also compared WAMIT with Newman (1977*b*) who derived an asymptotic theory for a floating rigid torus by means of matched asymptotic expansions with different assumptions than ours. He assumes the wavelength is the order of the cross-sectional radius and small relative to the torus radius. Linear theory with the same free-surface condition as ours is assumed. The far-field solution of the velocity potential inside the torus is expressed as $A_n J_n(\nu\rho)\exp(\nu z)\cos(n\beta)$. Here $n = 0$ and 1 correspond to forced heave and pitch, respectively. The inner expansion at the cross-section is expressed by the following asymptotic expression valid for large $\nu\rho$.

$$A_n\sqrt{\frac{2}{\pi\nu\rho}}\cos\left(\nu\rho - 0.5n\pi - 0.25\pi\right)\exp(\nu z)\cos(n\beta) \tag{3.3}$$

The inner domain solution contains strip theory results with the consequence that heave and pitch added mass are singular when $\nu a \to 0$. The comparisons of heave and pitch sectional added mass and damping with WAMIT for our analyzed torus are presented in Figures 3.11 and 3.12.

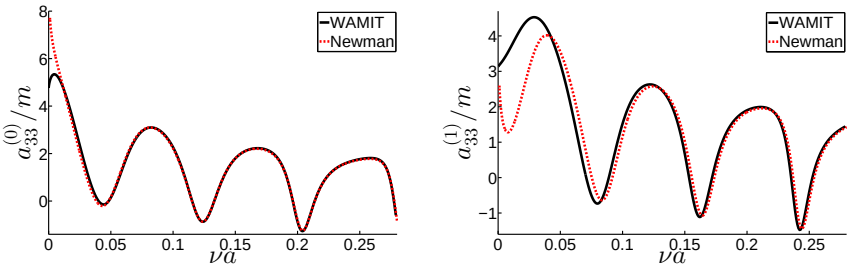

Figure 3.11: Comparison of sectional added mass coefficients $a_{33}^{(n)}$ of a torus for heave and pitch with $a/c = 0.0253$ by means of WAMIT and Newman (1977*b*)'s theory versus nondimensional wave number νa. m is displaced cross-sectional mass.

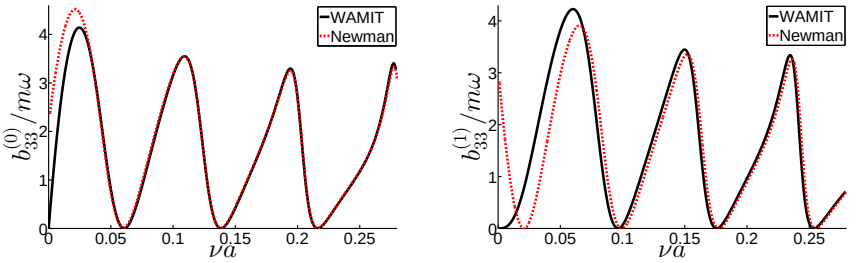

Figure 3.12: Comparison of sectional damping coefficients $b_{33}^{(n)}$ of a torus for heave and pitch with $a/c = 0.0253$ by means of WAMIT and Newman (1977*b*)'s theory versus nondimensional wave number νa. m is displaced cross-sectional mass.

The agreement is good except for small values of νa. When considering the heave and pitch response, Froude-Kriloff forces and hydrostatic terms are dominant. So the disagreement in added mass and damping for small values of νa may be secondary for heave and pitch response. Newman (1977*b*)'s theory can easily be generalized to flexible modes. However, the asymptotic expansion given by Eq. (3.3) for $n \geq 2$ becomes then poor for our considered range of νa with unsatisfactory predictions of added mass and damping as a consequence.

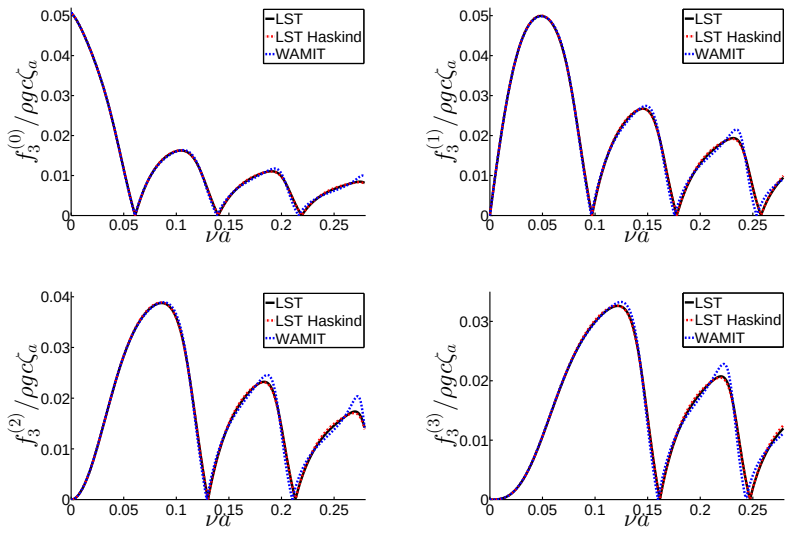

Figure 3.13: Comparison of sectional vertical wave excitation force amplitude $f_3^{(n)}$ of a torus for the modes number $n = 0, 1, 2, 3$ with $a/c = 0.0253$ by means of the low-frequency slender-body theory (LST) with and without Haskind relationship and WAMIT versus nondimensional wave number νa.

3.2 Verification of generalized vertical excitation forces and response amplitude operators

The sectional vertical wave excitation force amplitudes are made non-dimensional as $f_3^{(n)}/\rho g c \zeta_a$. Calculated values of the sectional vertical wave-excitation force amplitudes $f_3^{(n)}, n = 0, 1, ..., 11$ by means of the low-frequency slender-body theory with and without Haskind relationship and WAMIT versus nondimensional wave number νa are presented in Figures 3.13 to 3.15. The diffraction part of the force by means of the low-frequency slender-body theory has been calculated by means of Eq. (2.85) with $z_m = -4a/3\pi$. The agreement between the low-frequency slender-body theory with and without Haskind relationship and WAMIT is similar as for the added mass and damping coefficients. The excitation force amplitudes are according to the low-frequency slender-body theory zero for certain frequencies corresponding to zeroes of the Bessel function $J_n(\nu a)$.

We should note that the phases of excitation force are different due to different definitions of incident wave between the low-frequency slender-body theory and WAMIT. The incident wave potential and incident wave elevation have been defined as Eqs. (2.72) and (2.73) respectively in our study while they are defined as follows in WAMIT

$$\varphi_0 = \frac{ig\zeta_a}{\omega} \exp(\nu z + i\omega t - i\nu x) \tag{3.4}$$

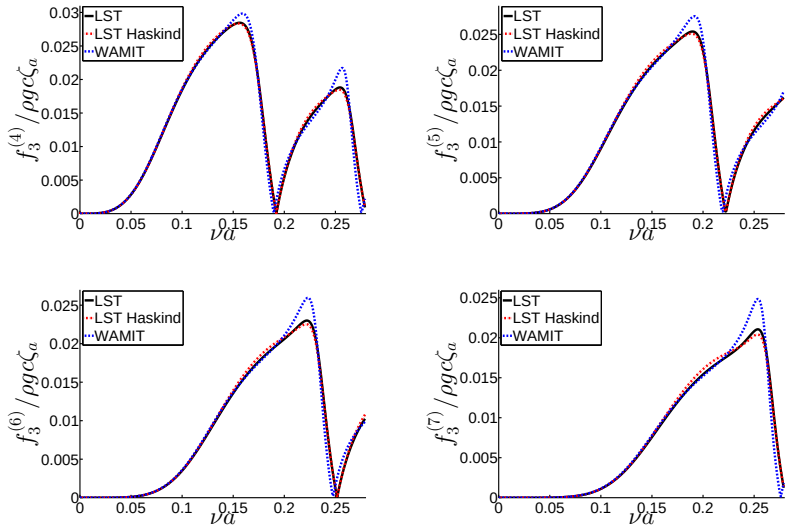

Figure 3.14: Comparison of sectional vertical wave excitation force amplitude $f_3^{(n)}$ of a torus for the modes number $n = 4, 5, 6, 7$ with $a/c = 0.0253$ by means of the low-frequency slender-body theory (LST) with and without Haskind relationship and WAMIT versus nondimensional wave number νa.

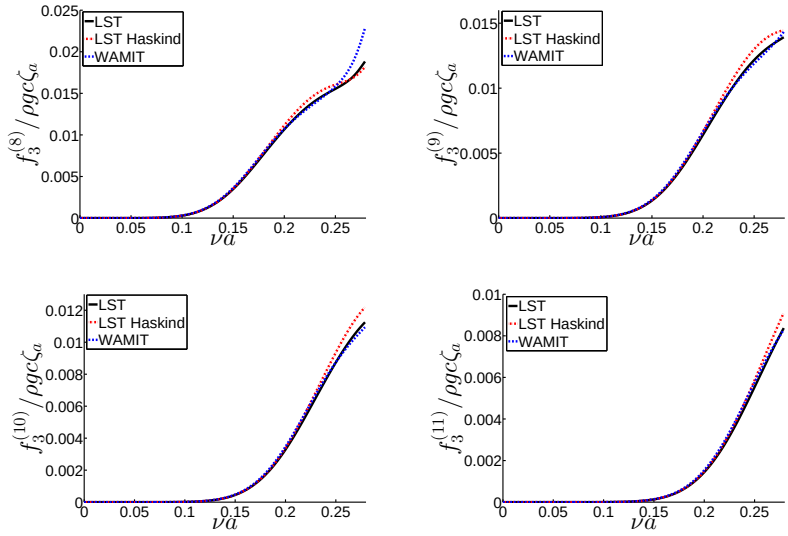

Figure 3.15: Comparison of sectional vertical wave excitation force amplitude $f_3^{(n)}$ of a torus for the modes number $n = 8, 9, 10, 11$ with $a/c = 0.0253$ by means of the low-frequency slender-body theory (LST) with and without Haskind relationship and WAMIT versus nondimensional wave number νa.

$$\zeta = \zeta_a \exp(i\omega t - i\nu x) \tag{3.5}$$

The linear excitation force is obtained by integrating the dynamic pressure due to incident wave potential φ_0 and diffraction potential φ_D over the mean wetted cross-sectional area of the torus as follows

$$f_3^{\text{wave excit}} = -\rho \int_{S_C} \frac{\partial(\varphi_0 + \varphi_D)}{\partial t} n_3 \, \mathrm{d}s \tag{3.6}$$

This leads to that the amplitude of the excitation forces which are complex values agree well between the low-frequency slender-body theory and WAMIT, but the phases of excitation force are different, more specifically, the real and imaginary parts of excitation force are different. This must be accounted for when calculate the transfer functions of absolute vertical motion.

The calculated damping coefficients by the low-frequency slender-body theory and WAMIT have been also verified by generalizing the relationship between global damping and the wave excitation force (moment) amplitude derived by Newman (1962) to include elastic modes. This means we can write

$$F_3^{(n)} = \zeta_a \sqrt{2AB_{33}^{(n)} \frac{\rho g^3}{\omega^3}}, \quad n = 0, 1... \tag{3.7}$$

where $A = 1$ for $n = 0$ and $A = 2$ for the other modes, $B_{33}^{(n)}$ is the 3D damping coefficient and $F_{33}^{(n)}$ is the vertical excitation force (moment) amplitude. Further, $F_3^{(n)} = f_3^{(n)} c \int_0^{2\pi} \cos^2(n\beta) d\beta$ and $B_3^{(n)} = b_3^{(n)} c \int_0^{2\pi} \cos^2(n\beta) d\beta$. The generalized Newman's formula does not tell us what the phase of the wave excitation forces are relative to the incident waves. It has been controlled in Figure 3.16 that both the low-frequency slender-body theory and WAMIT predictions satisfy the generalized Newman's relationship.

Figures 3.17 to 3.19 show predicted values of the *RAO*'s of the twelve lowest modes by means of the low-frequency slender-body theory with and without Haskind relationship and WAMIT versus nondimensional wave number νa. The *RAO*'s are defined as $RAO_3^{(n)} = |a_{n,a}/\zeta_a|$, where $|a_{n,a}|$ is the motion amplitude of mode n and can be obtained as follows.

$$\begin{aligned}
w(\beta, t) &= \sum_{n=0}^{\infty} a_{n,a} \cos(n\beta) \exp(-i\omega t) \\
\frac{a_{0,a}}{\zeta_a} &= \frac{\left[\left(1 - \frac{\pi\nu a}{4}\right)\rho g b_w - \left(\omega^2 a_{33}^{(0)} + i\omega b_{33}^{(0)}\right)\exp(\nu z_m)\right] i J_0(\nu c) + T_A}{-\omega^2\left(m + a_{33}^{(0)}\right) - i\omega b_{33}^{(0)} + \rho g b_w} \\
\frac{a_{n,a}}{\zeta_a} &= \frac{\left[\left(1 - \frac{\pi\nu a}{4}\right)\rho g b_w - \left(\omega^2 a_{33}^{(n)} + i\omega b_{33}^{(n)}\right)\exp(\nu z_m)\right] 2i^{n+1} J_n(\nu c) + T_B}{-\omega^2\left(m + a_{33}^{(n)}\right) - i\omega b_{33}^{(n)} + \rho g b_w + \frac{EI}{c^4}(n^4 - n^2) + T_C}
\end{aligned} \tag{3.8}$$

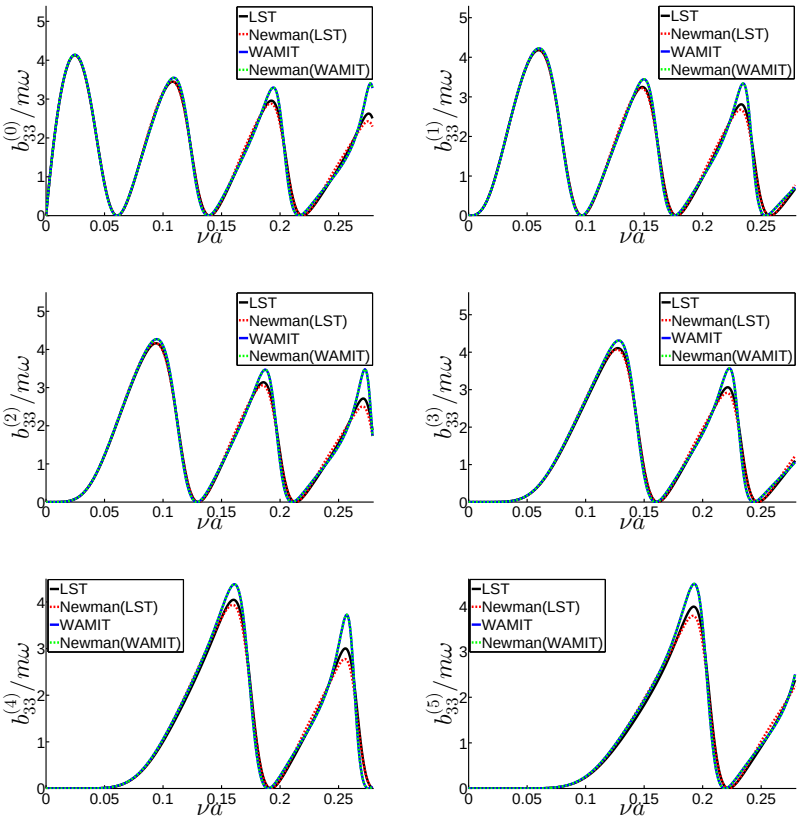

Figure 3.16: Comparison of sectional damping coefficients $b_{33}^{(n)}$ of a torus for the modes number $n = 0, 1, 2, 3, 4, 5$ with $a/c = 0.0253$ by means of the low-frequency slender-body theory (LST), WAMIT and Newman relationship versus nondimensional wave number νa. m is displaced cross-sectional mass.

The expressions of T_A, T_B and T_C are as follows.

$$
\begin{aligned}
T_A &= \frac{1}{2\pi}\int_0^{2\pi}\sum_{i=1}^{8} T_{p,3}\delta\left(\beta-\beta_i\right)\,\mathrm{d}\beta \\
T_B &= \frac{1}{\pi}\int_0^{2\pi}\sum_{i=1}^{8} T_{p,3}\delta\left(\beta-\beta_i\right)\cos\left(m\beta\right)\,\mathrm{d}\beta \\
T_C &= \frac{1}{\pi c^2}\sum_{n=1}^{\infty}\sum_{i=1}^{8} n^2 T_{as}^{(i)}\int_{\beta_i}^{\beta_{i+1}}\cos\left(n\beta\right)\cos\left(m\beta\right)\,\mathrm{d}\beta
\end{aligned}
\tag{3.9}
$$

$a_{n,a}$ are complex values taking the phase angle between the incident wave and the response of each mode into account. The lowest mode is rigid body heave and

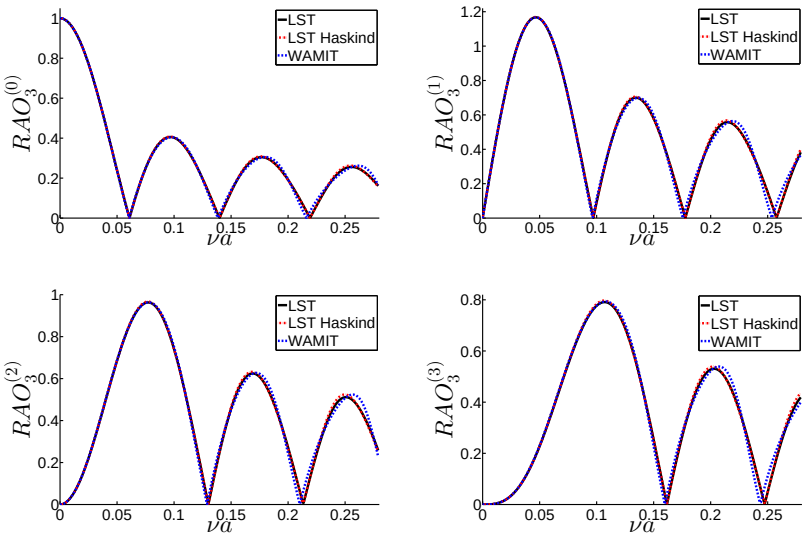

Figure 3.17: Comparison of RAO's $|a_{n,a}/\zeta_a|$ of a torus for the modes number $n = 0, 1, 2, 3$ with $a/c = 0.0253$ by means of the low-frequency slender-body theory (LST) with and without Haskind relationship and WAMIT versus nondimensional wave number νa.

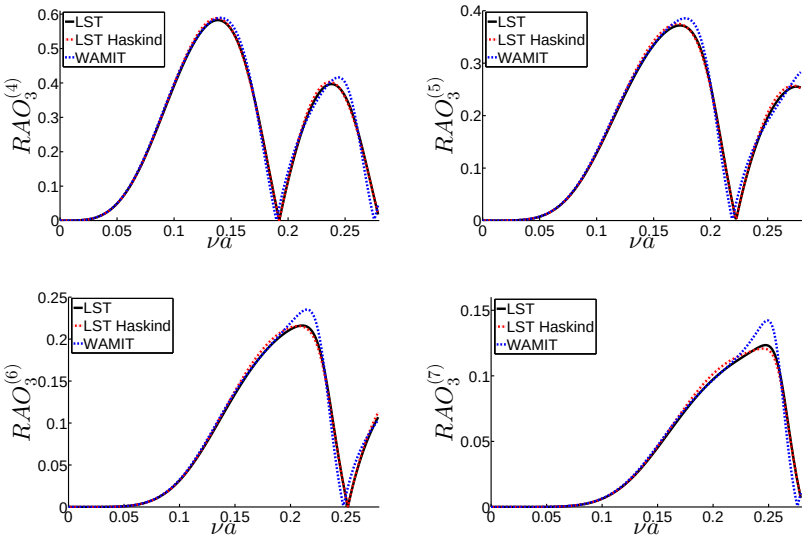

Figure 3.18: Comparison of RAO's $|a_{n,a}/\zeta_a|$ of a torus for the modes number $n = 4, 5, 6, 7$ with $a/c = 0.0253$ by means of the low-frequency slender-body theory (LST) with and without Haskind relationship and WAMIT versus nondimensional wave number νa.

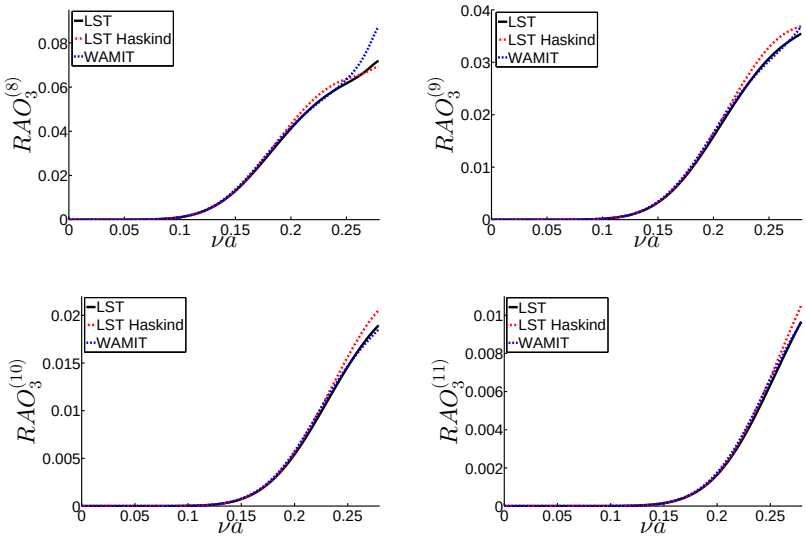

Figure 3.19: Comparison of RAO's $|a_{n,a}/\zeta_a|$ of a torus for the modes number $n = 8, 9, 10, 11$ with $a/c = 0.0253$ by means of the low-frequency slender-body theory (LST) with and without Haskind relationship and WAMIT versus nondimensional wave number νa.

the second mode is similar as rigid body pitch but coupled with elastic modes. From Figures 3.17 and 3.19 it can be seen as expected that the heave motion follows the waves for long waves and pitch and the elastic modes go to zero when $\omega \to 0$. The RAO predictions of higher modes depend on the non-dimensional parameter $EI/\rho g a c^4$. The considered bending stiffness and mass density of water are $EI = 0.464 Nm^2$ and $\rho = 1000 kg/m^3$, respectively. The value of bending stiffness has been chosen according to an elastic semi-submerged torus used in model tests which is detailed described in Chapter 4. The agreement between the low-frequency slender-body theory with and without Haskind relationship and WAMIT is very satisfactory. There is also as expected an increasing difference with increasing of νa similar for the added mass and damping coefficients and the vertical excitation forces.

The cancellation effect is pronounced at certain frequencies according to the low-frequency slender-body theory which correspond to zeros of excitation force amplitudes that is zeroes of the Bessel function $J_n(\nu a)$. Although cancellations appear for the different modes, the cancellation frequencies for the different modes are different. Therefore, the total vertical response of the torus is not equal to zero. The predicted values of the RAO's start to decrease from $n = 2$ with the increasing of mode number n and the values are close to zero for the modes number $n = 8, 9, 10, 11$ for $\nu a < 0.15$. This means that when the wave-induced vertical motions are considered for $\nu a < 0.15$, the eight lowest modes are dominant and the

twelve lowest modes are dominant for $\nu a > 0.15$.

3.3 Verification of wave-induced vertical motions

Eq. (3.8) gives the absolute motion for each position β and time t on the torus and is assumed to be on the form $w(\beta,t) = w_a(\beta,\omega)\exp(-i\omega t)$. The transfer functions of absolute vertical motion by means of the low-frequency slender-body theory without using Haskind relation are the absolute values of the amplitude of absolute vertical motion $w_a(\beta,\omega)$ divided by the amplitude of incident wave as follows.

$$\left|\frac{w_a(\beta,\omega)}{\zeta_a}\right| = \left|\sum_{n=0}^{\infty}\frac{a_{n,a}(\omega)}{\zeta_a}\cos(n\beta)\right| \tag{3.10}$$

The transfer functions of absolute vertical motion by means of the low-frequency slender-body theory using Haskind relation can be obtained in a similar way by replacing the linear diffraction force in Eq. (3.8) by Eq. (2.91). Since the absolute vertical motion at a given position β on the torus is the sum of each mode amplitude multiplied with $\cos(n\beta)$ and $a_{n,a}$ are complex values taking the phase angle between the incident wave and the response of each mode into account. Thus, the absolute vertical motion $w(\beta,t)$ will also account for the phase angle between the incident wave and the total response.

For a fish farm it matters for possible fish escapeis very important to know the relative vertical motion between the torus and the water surface in waves, even though there is net cover the free-surface area of the fish farm. If parts of the torus becomes completely submerged, the net might not give a complete protection against fish escape. The transfer functions of relative vertical motion $r(\beta,t)$ can be estimated by subtracting the incident wave elevation $\zeta(\beta,t) = i\zeta_a\exp(i\nu c\cos\beta - i\omega t)$ from the total vertical displacement as follows.

$$\begin{aligned} r(\beta,t) &= w(\beta,t) - \zeta(\beta,t) \\ &= \left[\sum_{n=0}^{\infty} a_{n,a}\cos(n\beta) - i\zeta_a\exp(i\nu c\cos\beta)\right]\exp(-i\omega t) \end{aligned} \tag{3.11}$$

The latter expression should ideally have accounted for the effect of the torus on the free-surface elevation. Eq. (3.11) gives the relative motion for each position β and time t on the torus and is assumed to be on the form $r(\beta,t) = r_a(\beta,\omega)\exp(-i\omega t)$. The transfer functions of relative vertical motion are then the absolute value of the amplitude of relative vertical motion $r_a(\beta,\omega)$ divided by the amplitude of incident wave as follows.

$$\left|\frac{r_a(\beta,\omega)}{\zeta_a}\right| = \left|\sum_{n=0}^{\infty}\frac{a_{n,a}(\omega)}{\zeta_a}\cos(n\beta) - i\exp(i\nu c\cos\beta)\right| \tag{3.12}$$

Figures 3.20 and 3.21 show the transfer functions of absolute vertical motion and relative vertical motion at five positions of a torus, receptively, based on adding the effect of twenty modes by means of the low-frequency slender-body theory with

and without Haskind relationship and WAMIT versus nondimensional wave number νa. However, it is only about twelve modes that matter based on the discussion of *RAO*'s.

Figure 3.20 shows good agreement of the transfer functions of absolute vertical motion between the low-frequency slender-body theory with and without Haskind relationship and WAMIT at $\beta = 0, \beta = \pi/4$ and $\beta = \pi/2$ for the calculated range of νa and at $\beta = 3\pi/4$ and $\beta = \pi$ for $\nu a \lessapprox 0.15$. Figure 3.21 shows good agreement of the transfer functions of relative vertical motion between the low-frequency slender-body theory with and without Haskind relationship and WAMIT at $\beta = \pi/4$ and $\beta = \pi/2$ for the calculated range of νa and at $\beta = 0, \beta = 3\pi/4$ and $\beta = \pi$ for $\nu a \lessapprox 0.15$. Figure 3.21 implies that the torus follows closely the incident waves for small νa especially for $\nu a \lessapprox 0.05$, since the pitch motion follows the incident wave slope and the elastic modes make the torus follow the incident wave profile. We note differences for both the transfer functions of absolute vertical motion and relative vertical motion at the higher considered frequencies at some positions of the torus. The differences were unexpected based on the good agreement demonstrated for added mass and damping coefficients, excitation forces and *RAO*'s of individual modes. One reason is that the absolute vertical motion is based on adding all the individual modes multiplied with $\cos(n\beta)$ which includes the information of any position on the torus. The factor $\cos(n\beta)$ may amplify the effect of phase differences when the absolute and relative vertical motion are considered at different positions on the torus. However, it is the results for $\nu a \lessapprox 0.15$ that are of most practical relevance.

3.4 Summary

The low-frequency slender-body theory for wave-induced response of an elastic semi-submerged torus has been verified by the linear potential flow frequency-domain panel code WAMIT with higher-order Boundary Element Method. Satisfactory agreements between WAMIT and the low-frequency slender-body theory have been obtained except for absolute and relative motions for large $\nu a > 0.15$. There is as expected an increasing difference with increasing νa and a small increasing difference occur with increasing mode number. The presented results illustrate the strong limitations of strip theory and 3D effects cause pronounced frequency-dependent hydrodynamic interaction on the scale of the torus diameter. Wave amplitudes caused by heave oscillations have been studied for frequencies corresponding to zero and maximum damping. The damping coefficients obtained by low-frequency slender-body theory and WAMIT have been also verified by generalizing the relationship between global damping and the wave excitation force (moment). The torus nearly follows the waves in long wave lengths.

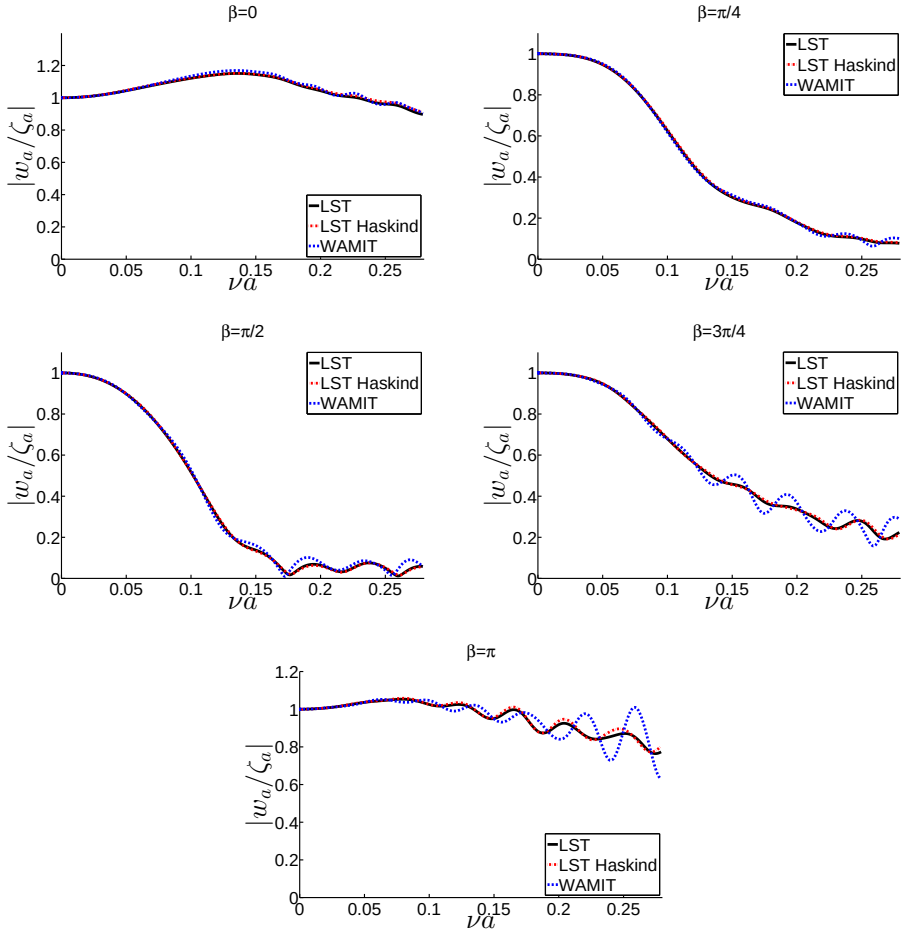

Figure 3.20: Transfer functions of absolute vertical motion $|w_a/\zeta_a|$ at five positions of a torus with $a/c = 0.0253$ by means of the low-frequency slender-body theory (LST) with and without Haskind relationship and WAMIT versus nondimensional wave number νa. The twenty lowest modes are used. Here $\beta = 0$, $\beta = \pi/2$ and $\beta = \pi$ correspond to the aft, side and front of the torus.

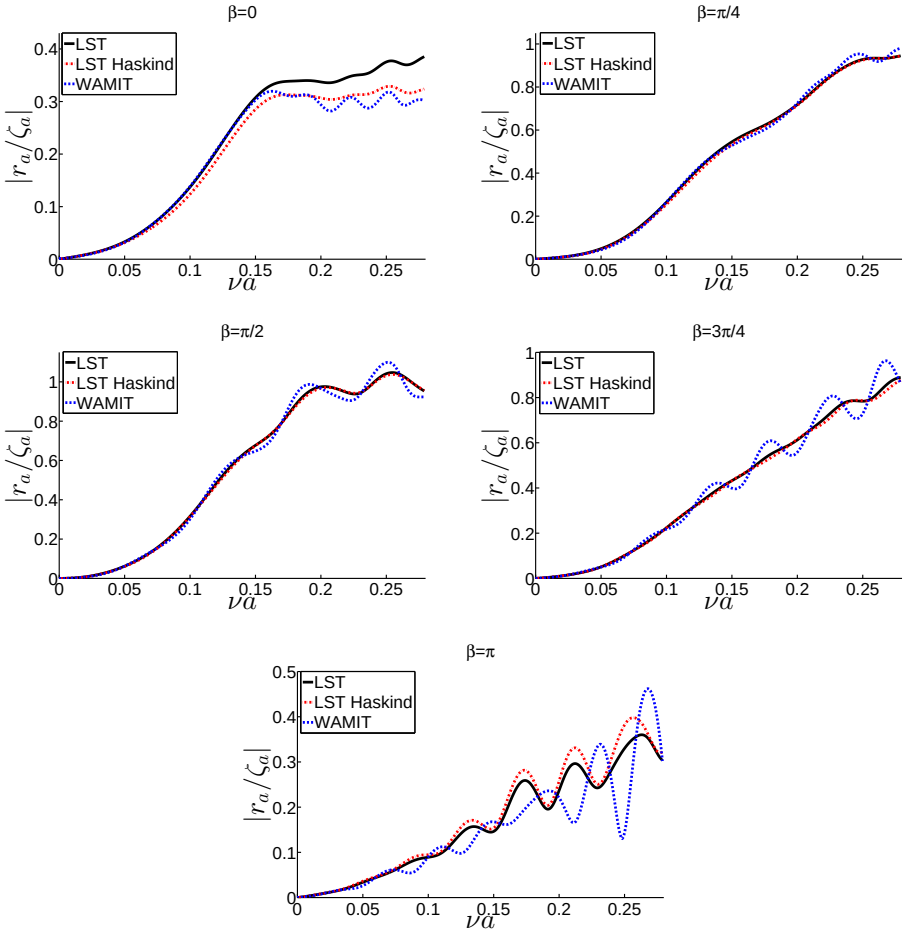

Figure 3.21: Transfer functions of relative vertical motion $|r_a/\zeta_a|$ at five positions of a torus with $a/c = 0.0253$ by means of the low-frequency slender-body theory (LST) with and without Haskind relationship and WAMIT versus nondimensional wave number νa. The twenty lowest modes are used. Here $\beta = 0$, $\beta = \pi/2$ and $\beta = \pi$ correspond to the aft, side and front of the torus.

Chapter 4

Model tests of a floating torus

In order to validate the low-frequency slender-body theory, two sets of model tests have been performed. The Marine Cybernetics Laboratory at Norwegian University of Science and Technology, in Trondheim, Norway was used during January 2013. In both experiments the models tested were circular plastic collar used as a floater of an aquaculture plant subjected to regular deep-water waves. In the first test a nearly semi-submerged elastic circular torus was used, while in the second test we considered a nearly semi-submerged rigid circular torus.

In the model tests, the wave-induced vertical motions of a moored torus in regular deep-water waves were studied. Focus was on the vertical wave-induced accelerations at different positions on the tori and nonlinear effects like wave overtopping on the models. Results from these experiments have been published in Li et al. (2014) and Li et al. (2016).

4.1 Model tests

Two sets of model tests of wave-induced vertical motions of moored torus subjected to regular deep-water waves were conducted at the Marine Cybernetics Laboratory. The wave tank is $40.00m$ long, $6.45m$ wide, and $1.50m$ deep. It is equipped with a towing carriage, a flap-piston wave maker and a damping beach covered by a rough, porous mat to increase its energy dissipation ability. The damping beach showed, in general, to be effective for damping out waves and making the water surface calm after each test run, reducing the waiting time between the runs. The wave maker is digitally controlled by software, which applies linear wave maker theory to estimate the necessary stroke of the piston for generating waves with a given height and period. An active wave absorption control system (AWACS 2) is included in the wave maker software. The wave maker has a DHI wave synthesizer which can produce regular and irregular waves. The capacity of the wave maker generating regular waves is wave height $< 0.25m$ and wave period between $0.3s$

and 3.0s.

4.1.1 The models

Since gravity waves are involved in the experiments, Froude scaling must be applied. Reynolds number scaling associated with viscous effects can, therefore, not be satisfied. When flow separation does not happen, viscous effects are associated with the boundary layer flow and negligible relative to potential-flow effects. Moreover, since the Keulegan-Carpenter number is always small in our studies, the wave force amplitude will be dominated by potential-flow effects. However, we cannot outrule that viscous damping matters in case of flow separation. The latter may occur in steep waves with overtopping, as demonstrated in 2D numerical studies of a semi-submerged circular cylinder in waves by Kristiansen and Faltinsen (2008*b*).

Table 4.1: Main dimensions in the experiments. Model scale 1 : 25 and full scale. Full scale dimensions are based on a typical circular collar of a floating fish farm. E: Elastic; R: Rigid.

Description	Parameter	Model scale	Full scale
Torus diameter	$D = 2c$	1.5m	37.5m
Cross-sectional diameter of torus	$2a_E$	38mm	0.95m
	$2a_R$	36mm	0.90m
Torus mass per unit length	m_E	0.602kg/m	376.0kg/m
	m_R	0.607kg/m	379.6kg/m
Torus bending stiffness	EI_E	0.464Nm^2	4.53×10^{6}Nm^2
	EI_R	23.74Nm^2	2.32×10^{8}Nm^2
Spring stiffness	k_s	17N/m	10.63kN/m

A model test scale of 1 : 25 was in mind for the two models in the experiments. Corresponding full scale values are given in Table 4.1 for reference. The parameters were chosen from typical values for existing circular collars of a floating fish farm. The elastic torus model was made from a corrugated tube used by Kristiansen and Faltinsen (2015) during the fall of 2011, which is the standard type used to cover electric cables in houses. The plastic flexible tube and waterproof adhesive electrical tape were covered to make the torus semi-submerged in calm conditions and smooth respectively as shown in Figure 4.1 and upper right in Figure 4.2. In order to get a cross-sectional diameter similar to the elastic torus model, *i.e.* 38mm, a 32mm nearly rigid standard water pipe for houses was covered by a transparent plastic flexible tube of thickness 1.5mm and a waterproof adhesive electrical tape as shown in the lower left of Figure 4.2. The draft of the rigid torus model is 0.0214m.

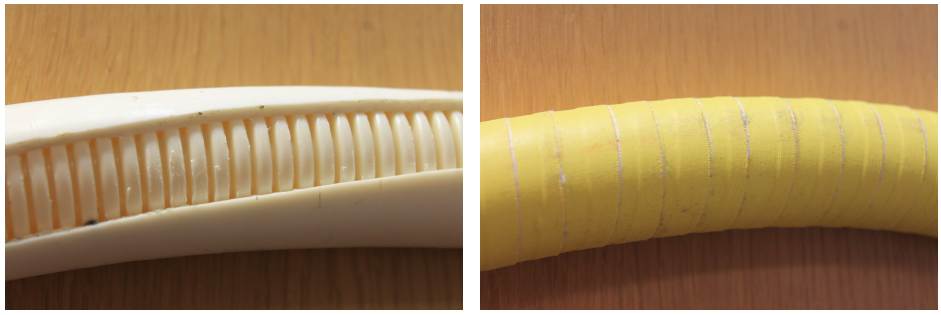

Figure 4.1: Part view of the elastic torus model (Left: corrugated tube covered with plastic flexible tube; right: tube covered with waterproof adhesive electrical tape).

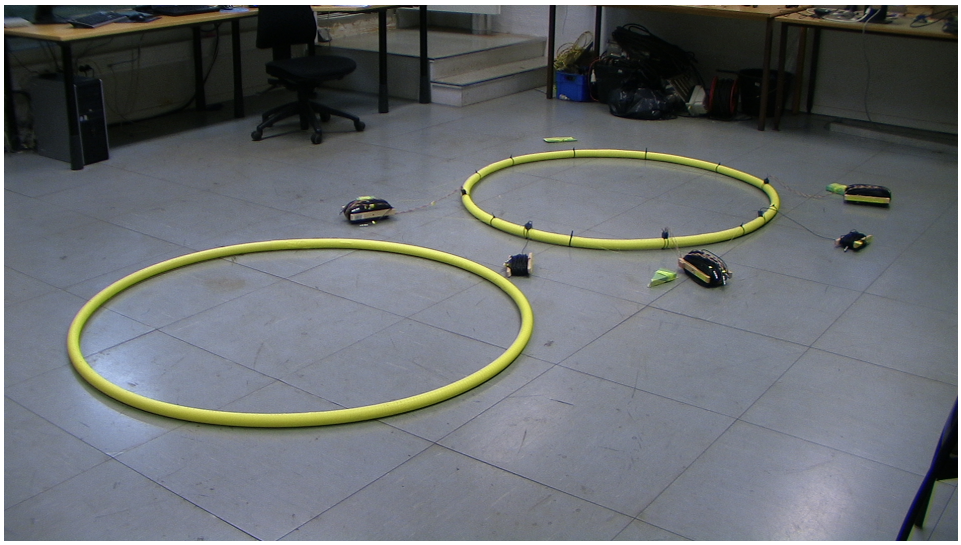

Figure 4.2: View of the elastic and rigid torus models. Elastic torus model arranged with five accelerometers with an equal interval of $\pi/4$.

Special attention was paid to the structural bending stiffness. A typical high-density polyethylene (HDPE) type plastic has a Young's modulus of elasticity $E \approx 1000MPa$. The combined bending stiffness of the HDPE plastic tube, flexible tube and the adhesive electrical tape was found by static tests in the elastic regime. This means that EI was estimated by using the static deflection equation of a cantilever curved beam of length L and with a fixed end support at one end and an increasing load F, whose range was comparable with the one recorded during the tests in waves, applied at the other end of the beam. EI follows then from measuring the deflection W at the free beam end. For a cantilever curved beam,

the deflection is as follows (Love, 1906).

$$W(s) = \frac{FR^2}{EI}\left[L - s - \cos\left(\frac{s}{R}\right)L + \sin\left(\frac{s}{R}\right)R\right] \tag{4.1}$$

Here R is radius of curvature and s is the arc length on the beam, respectively. We should note that

$$\lim_{R\to\infty} W(s) = \frac{Fs^2}{6EI}(3L - s) \tag{4.2}$$

which agrees with result for a straight beam. For our tested elastic torus model segment, $L = 0.5m$ and $R \approx 2.6m$, the vertical deflections at the free beam end for the curved beam and the straight beam are $0.0415F/EI$ and $0.0417F/EI$, respectively. For our tested nearly rigid torus model segment, $L = 0.47m$ and the radius of curvature is much larger than elastic torus model segment's which leads to the vertical deflections at the free beam end for the curved beam and the straight beam are closer. The static tests confirmed the linear behavior of the material and the obtained bending stiffness for the elastic torus model is $EI = 0.464Nm^2$ and for the nearly rigid torus model is $EI = 23.74Nm^2$. The bending stiffness of the nearly rigid model is fifty-one times the bending stiffness of the elastic model and two hundred times the bending stiffness used in the experiments by Kristiansen and Faltinsen (2015). This model scale gave a realistic bending stiffness for the elastic model according to Froude scaling. Alternatively, bending stiffness can be obtained analytically according to Young's modulus and the second moment of area. The second moment of area of the nearly rigid standard water pipe in bending is $I = \pi\left(D_2^4 - D_1^4\right)/64$, where the inner and outer diameter are $D_1 = 26mm$ and $D_2 = 32mm$, respectively. This means a bending stiffness $EI = 23.23Nm^2$ of the nearly rigid torus model. The reason to the difference of bending stiffness between the static tests and analytical calculation is due to the influence of covered flexible tube and the adhesive electrical tape. The yield stress $(23°\mathrm{C}, 50mm/min)$ of the nearly rigid pipe is $22MPa$. The largest moment in the torus due to the dominant elastic mode is about $10.3Nm$. So, the largest stress in the cross-section is $6.2MPa$, which is much smaller than the yield stress.

4.1.2 Instrumentation

The vertical accelerations were measured by accelerometers at five points with an equal interval of $\pi/4$ as shown in Figure 4.2, starting from the front of the torus. The used accelerometers were Model $3032 - 050$ by Measurement Specialists, with a sensitivity of $1.318mV/g$. Four resistance wave probes were used to measure the wave elevation. The wave probes were composed of two parallel steel rods, each with $3mm$ diameter, $7mm$ apart. The mooring line forces were measured in each of the four moorings by four Hottinger Baldwin $(18kg)$ force transducers that were fixed to the rig. These force transducers with accuracy class C3 (OIML, 2000) are proved to be very accurate and stable by Kristiansen (2010). Finally two cameras were used to record the global behavior of the torus and the accuracy of overtopping and out-of-water phenomena. One camera is underwater with a frame rate of $25fps$ and a resolution of 768×576 pixels. The second, in air and almost perpendicular to the

free-surface plane has a frame rate of $25 fps$ and a resolution of 1920×1080 pixels. The measured signals from all sensors went through a Hottinger Baldwin amplifier of type MGCplus. No filtering of the signals was performed before logging and the acquisition data were stored with a sampling frequency of $100 Hz$. The Hottinger Baldwin software Catman was used for logging of the measured data. All sensors were calibrated before measurements.

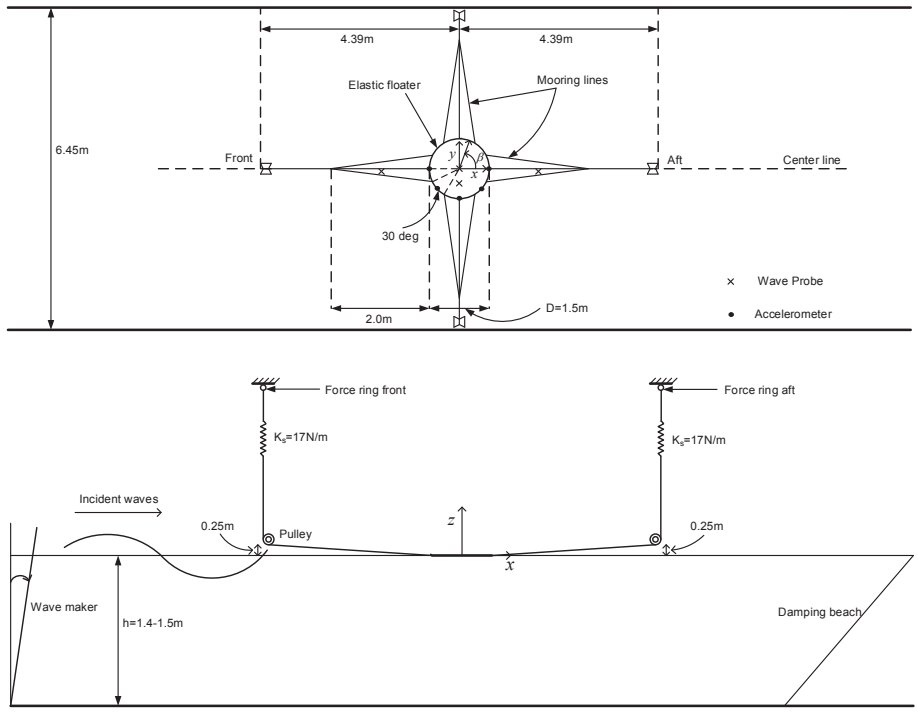

Figure 4.3: Experimental set-up of the elastic torus model. Upper: top view; lower: side view. The damping beach is out of scale. Definition of Earth-fixed coordinate system $Oxyz$ and angle β.

4.1.3 Experimental set-up

The experimental set-up of the elastic torus model and the rigid torus model are illustrated in Figures 4.3 and 4.4, respectively. The Earth-fixed Cartesian coordinate system $Oxyz$ is also defined in Figure 4.3 with the mean free-surface at $z = 0$. The z-axis coincides with the torus axis at rest and is vertical with positive direction upwards. A body-fixed Cartesian coordinate system $Ox_B y_B z_B$ with origin in the center of gravity (COG) of the torus is also introduced. When the torus is at rest, the x_B, y_B and z_B-axes are parallel with the x, y and z-axes, respectively.

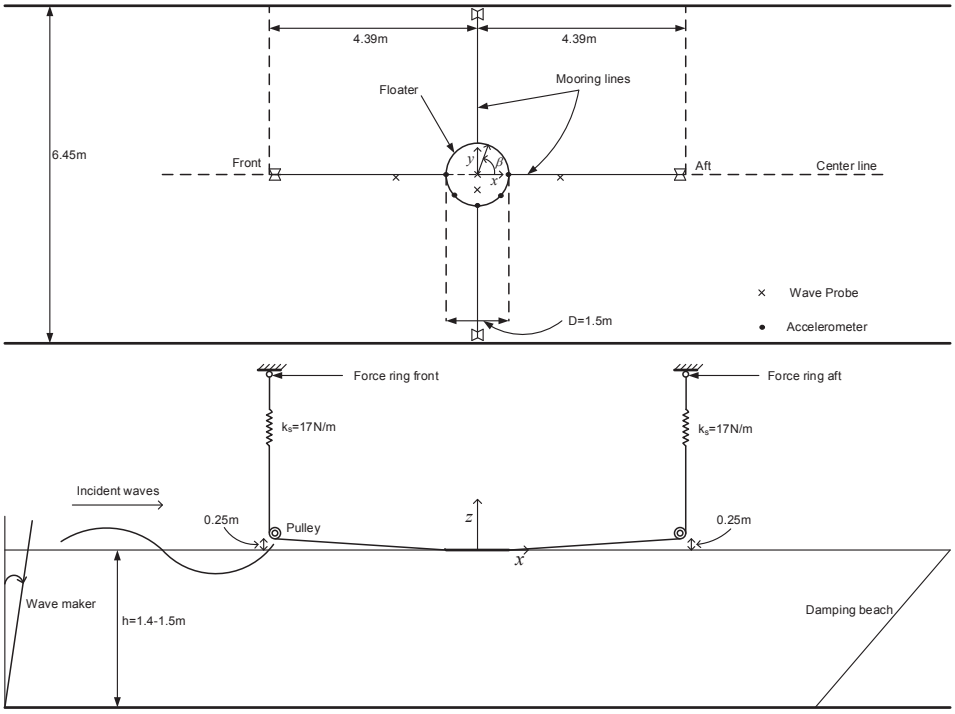

Figure 4.4: Experimental set-up of the rigid torus model. Upper: top view; lower: side view. The damping beach is out of scale. Definition of Earth-fixed coordinate system $Oxyz$ and angle β.

Further, the COG at rest is right above or below the origin of the $Oxyz$ system. The experimental set-up of these two model tests are the same except the way of connecting the mooring lines to the torus. The elastic torus model was attached to the stationary carriage in the middle of the tank by means of four identical nearly horizontal mooring lines, at front, aft, left and right. They were connected to the torus through 12 attachment points with an equal interval of $30deg$. The rigid torus model was also attached to the stationary carriage in the middle of the tank by means of four identical nearly horizontal mooring lines, at front, aft, left and right and they were connected to the torus through 4 attachment points with an equal interval of $90deg$. Springs with stiffness $k_s = 17N/m$ were used to connect the torus to the carriage. This corresponds to almost half of the full scale spring stiffness ($27kN/m$) by Froude scaling. The pre-tension was $T_p = 5N$. The high pre-tension was needed to avoid slack due to large horizontal motion when testing large wave steepness and long wave periods and also to keep the elastic torus model almost circular. The frictional coefficient in each individual pulley was low enough and it did not matter for the motion of the model, *i.e.* such that any hysteresis effect in the mooring system could be considered negligible. A snapshot of the partly experimental set-up of the elastic torus model is shown in Figure 4.5 which

includes mooring lines, five accelerometers and two wave probes.

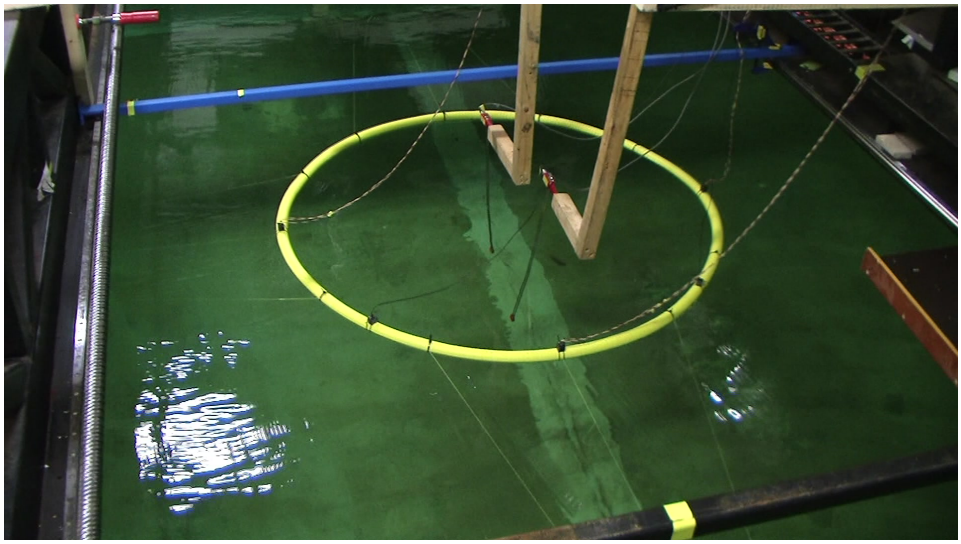

Figure 4.5: Snapshot of the elastic torus model arranged with five accelerometers with an equal interval of $\pi/4$ was attached to the stationary carriage in the middle of the tank. The photo is taken towards the positive y direction defined in Figure 4.3.

4.1.4 Test conditions

We wanted the waves in the model tests to be representative for a typical design wave condition for the floating fish farms. Incident waves with prescribed wave steepnesses $H/\lambda = 1/120$, $1/60$, $1/30$ and $1/15$ propagating along the x-axis were tested. The wave period $T = 2\pi/\omega$ vary within $[0.6, 1.6]\,s$ with a step of $0.05s$. Here ω is the circular frequency. Twenty one wave periods and four wave steepnesses yielded eighty one different wave conditions, which are presented in Table 4.2. All test cases are repeated two to four times in order to assess the experimental errors. Each test-series was performed with constant wave steepness and gradually increasing the wave period. The waiting time was chosen as at least 3 minutes between each test to damp out waves. The time it took for the waves to decay was longer for larger wave steepness and longer period waves due to that these waves were strongly reflected by the beach. In general, nearly steady-state conditions are reached after 10 wave periods.

No experimental vertical free-decay tests were done to identify wet natural periods and damping for the elastic and rigid tori. Such tests are difficult to perform because the strong frequency dependency of added mass as shown in Figure 3.1 causes several natural frequencies for the dominant modes, *i.e.* heave, pitch and the lowest vertical elastic mode. The theoretical ten lowest undamped natural frequency for uncoupled heave, pitch and the lowest vertical elastic mode of the nearly rigid torus are presented in Table 4.3. They are calculated by setting the

Table 4.2: Test wave conditions.

T [s]	λ [m]	$H/\lambda = 1/120$ H [m]	$H/\lambda = 1/60$ H [m]	$H/\lambda = 1/30$ H [m]	$H/\lambda = 1/15$ H [m]
0.60	0.562	0.0047	0.0094	0.0187	0.0375
0.65	0.660	0.0055	0.0110	0.0220	0.0440
0.70	0.765	0.0064	0.0128	0.0255	0.0510
0.75	0.878	0.0073	0.0146	0.0293	0.0585
0.80	0.999	0.0083	0.0167	0.0333	0.0666
0.85	1.128	0.0094	0.0188	0.0376	0.0752
0.90	1.265	0.0105	0.0211	0.0422	0.0843
0.95	1.409	0.0117	0.0235	0.0470	0.0939
1.00	1.561	0.0130	0.0260	0.0520	0.1041
1.05	1.721	0.0143	0.0287	0.0574	0.1148
1.10	1.889	0.0157	0.0315	0.0630	0.1259
1.15	2.065	0.0172	0.0344	0.0688	0.1377
1.20	2.248	0.0187	0.0375	0.0750	0.1499
1.25	2.440	0.0203	0.0407	0.0813	0.1626
1.30	2.639	0.0220	0.0440	0.0880	0.1759
1.35	2.845	0.0237	0.0474	0.0949	0.1897
1.40	3.060	0.0255	0.0510	0.1020	0.2040
1.45	3.282	0.0274	0.0547	0.1094	0.2188
1.50	3.513	0.0293	0.0585	0.1171	0.2342
1.55	3.751	0.0312	0.0625	0.1250	0.2501
1.60	3.997	0.0333	0.0666	0.1332	0.2665

damping equal to zero and finding numerically the zeros of the function $F(\omega)$ defined as:

$$F(\omega) = -\omega^2 \left(m + a_{33}^{(n)}\right) + \rho g b_w + \frac{EI}{c^4}\left(n^4 - n^2\right), \quad n = 0, 1, 2 \tag{4.3}$$

The natural frequencies are higher than the experimental frequency range of the linear incident regular waves. The lowest theoretical undamped natural frequency in uncoupled surge due to the mooring system is $2.17 rad/s$, which is clearly smaller than the experimental frequency range.

Large vertical and lateral deformations and waves overtopping of the torus were observed in several tests of both the elastic and nearly rigid torus models. The linear, second, third and fourth order harmonics of the measured signals were found from two sets of model tests. Hydroelastic effects of the nearly rigid model were believed to be present.

Table 4.3: The ten lowest numerically predicted undamped natural frequencies in rad/s for the dominant vertical modes of nearly rigid torus.

Heave	22.63	23.49	24.35	25.17	25.97
	26.37	26.89	27.65	28.39	29.11
Pitch	23.07	23.93	24.75	25.57	26.34
	26.51	27.27	28.01	28.75	29.45
The lowest purely vertical elastic mode	33.08	33.70	34.30	34.89	35.47
	36.05	36.61	37.17	37.73	38.27

4.2 Check of the wave generation

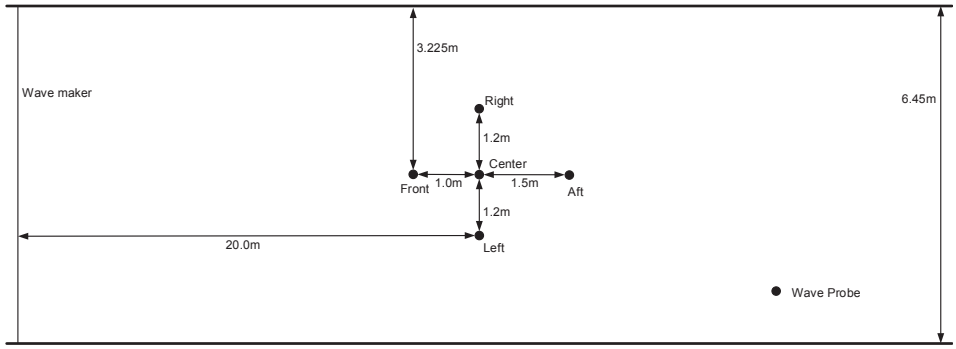

Figure 4.6: Top view of experimental set-up for wave measurements without the torus present.

Analysis of the results from the wave probes after performing the model tests, showed a discrepancy between the theoretical and achieved wave height given by the wave maker. This introduced a practical problem when attempting to analyse the model test results. To estimate the error in the generation of the incident regular wave system with respect to the nominal values, tests without the torus in the tank were carried out for all the tested wave periods and wave steepnesses. Five resistance wave probes with rod diameter $3mm$ were positioned as illustrated in Figure 4.6. Three wave probes were placed at the same longitudinal position but at different positions in the transverse direction in order to check for two-dimensionality of the waves. The waiting time between each test was $4-5$ minutes. Each test was repeated $2-3$ times showing good repeatability.

A zoomed view of the ratio between the measured first harmonic component and the nominal wave amplitude is shown in Figure 4.7 for the different prescribed wave steepness as function of the non-dimensional wave number νa where $\nu = \omega^2/g$

with g meaning acceleration of gravity. The mean values and the corresponding standard deviations, estimated through the time histories of the five wave probes, are reported. One reason to the disagreement between measured and nominal wave amplitude is the flow due to leakage around the sides and bottom of the paddle and the wave generation capability of the wave maker is in general less than that predicted by two-dimensional potential theory, and decreases in practice with decreasing water depth. Other possible reasons are wave reflections from the beach, meniscus effect on the wave probe wire, calibration linearity error and nonlinear effects in the wave propagation.

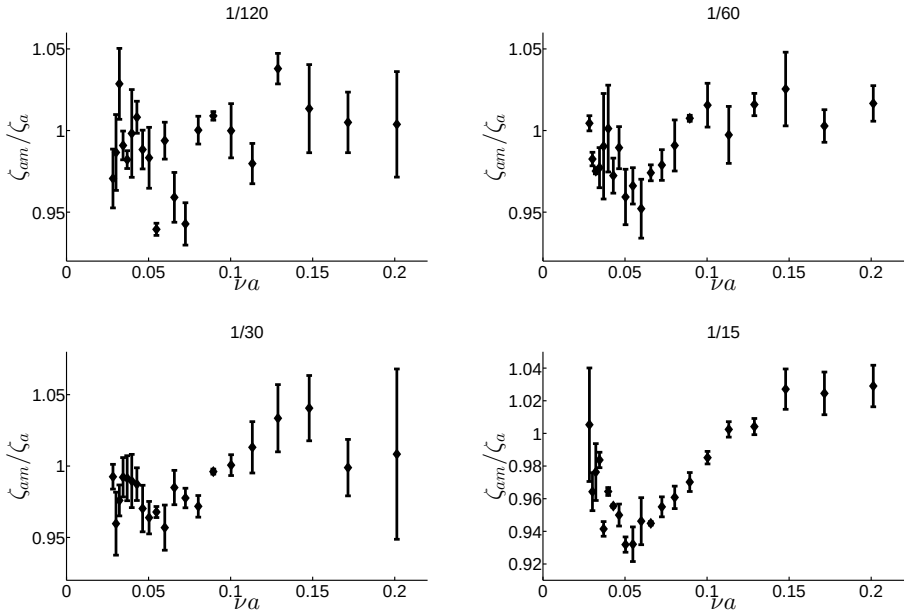

Figure 4.7: Zoomed view of ratio between measured and prescribed wave amplitude versus non-dimensional wave number νa without the torus present. ζ_{am} is the mean wave amplitude of the five measurement positions in Figure 4.6. ζ_a is the prescribed wave amplitude. The height of the experimental error bars is two times the estimated standard deviation. The numbers 1/120, 1/60, 1/30 and 1/15 on the top of each graph is the prescribed wave steepness.

4.3 Torus vertical acceleration measurements

Accelerations were measured along the body-fixed z_B-axis, which coincides with the vertical z-axis when the torus is at rest. Five positions along the torus corresponding to the angles $\beta = 0,\ \pi/4,\ \pi/2,\ 3\pi/4,\ \pi$ as defined in Figure 4.3 were used. They are referred to as aft, aft left, left, front left and front positions, respectively. All test cases were repeated two to four times in order to check their

repeatability. The time histories of all the sensor readings that acquired from each repeated cases may best describe repeatability, and a maximum repeatability error of about 1.0% was assessed. At least 3 minutes of waiting time between two consecutive tests was chosen to get almost calm water conditions. The time recording started at least 20 seconds earlier than the wave maker to ensure the acquisition of the longitudinal seiching mode effect, as well as of the residual waves generated in the previous test. Seiching refers to the first sloshing mode for the longitudinal direction in a wave tank. The seiching period of the Marine Cybernetics lab is $T_{seich} = 2L_{tank}/\sqrt{gh} \approx 20.9s$ (Faltinsen and Timokha, 2009). Here L_{tank} is the length of the wave tank and h is the depth of the wave tank. In particular, when a small difference in the period between the previous and the actual incident waves exists, weak beating effect arises in the actual time history of the torus motions. Possible drift in the accelerometers was detected before the wave maker started and used to correct the signal in the subsequent run. Time series of experimental vertical acceleration at the front of the elastic torus model with wave steepness $H/\lambda = 1/30$ and wave period $T = 0.6s$ is shown in Figure 4.8.

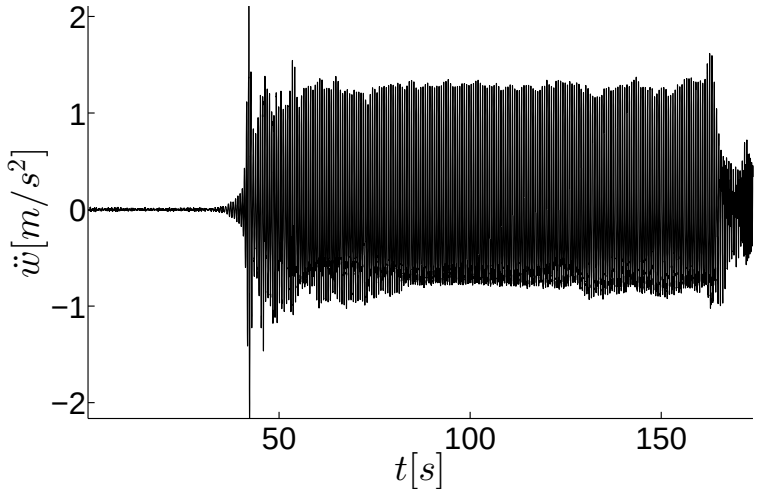

Figure 4.8: Time series of experimental vertical acceleration at the front of the elastic torus model with wave steepness $H/\lambda = 1/30$ and wave period $T = 0.6s$.

Possible reflected waves from the tank walls will contaminate the test results. The distance of the model to a tank wall is approximately $2.475m$. The group velocity of the generated surface waves can be calculated based on the oscillation period and wave tank depth. The time before the reflected waves from tank wall reach the plate can be estimated. However, it is more practical to examine the vertical acceleration records of the torus model, as well as to check the time histories from the wave elevation probes. Reflection from the beach is another error source in the model tests. Incident waves generated by flap-piston wave maker do not fully dissipate at the damping beach and reflect back to the torus models. When the

possible reflected wave reaches the torus models is then dependent on the group velocity of the incident waves.

Careful choice of the time series used for calculations of mean value and standard deviation of measured vertical accelerations is important. The starting time of time history used for the calculation should be away from the initial stage when the torus model starts to oscillate, in order to minimize the transient effect. Transient effects will exponentially decay with time. In general, nearly steady-state oscillations are reached after 10 wave periods. The steady-state time window were band-pass filtered in order to remove noise out of the prescribed frequency range. The lower and upper cut-off frequencies are $0.95/T$ and $1.05/T$, $1.95/T$ and $2.05/T$, $2.95/T$ and $3.05/T$, $3.95/T$ and $4.05/T$ in order to get first, second, third and fourth-order harmonics of acceleration, respectively. The sampling frequency was $100Hz$. The steady-state time window contained about $70 - 130$ wave periods. Figure 4.9 shows time series of the first harmonics of experimental vertical acceleration at the front of the elastic torus model with wave steepness $H/\lambda = 1/30$ and wave period $T = 0.6s$.

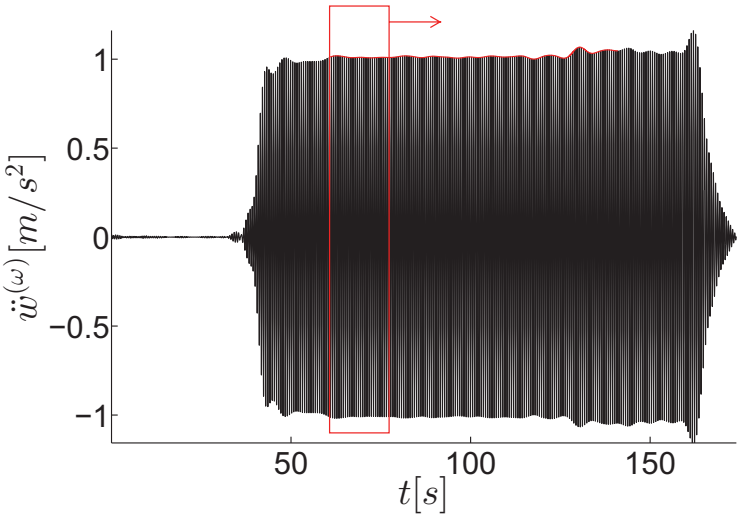

Figure 4.9: Time series of the first harmonics of experimental vertical acceleration at the front of the elastic torus model with wave steepness $H/\lambda = 1/30$ and wave period $T = 0.6s$.

A sliding Discrete Fourier Transform (DFT) technique is used to determine the time variation of each harmonic contribution. A time window corresponding to 20 wave periods is analyzed through DFT as shown in the rectangular of Figure 4.9; then the time window is slid one wave period along the direction of arrow in Figure 4.9 and the DFT analysis is repeated for the new time interval. The procedure

is repeated until the end of the steady-state region, enabling the evaluation of the mean value and standard deviation of each harmonic component. A second method was used to calculate mean values and standard deviation. It is based on the envelope curve of the absolute values of the acceleration extrema (maxima and minima) in the same steady-state time window as illustrated in Figure 4.9. The corresponding mean and standard deviation values are used as the measurements of the mean value and error estimation. Mean values obtained by the two methods are very close, however differences on the standard deviations are relative large since the second method only consider the peak in each period in the selected time window of time series.

Large relative vertical motions with waves overtopping the torus locally and local out-of-water effect of the torus were observed in the model scale experiments of both elastic and nearly rigid torus models (see Figure 4.10). Similar phenomena are demonstrated in Figure 4.11 for the torus of a fish cage without netting in a storm. Overtopping occurs for all wave periods with wave steepness 1/15 and for wave periods larger than $T = 1.05s$ with wave steepness 1/30 in two sets of model tests (see Figure 4.10). There is no overtopping occurring for wave steepness 1/60 and 1/120 in the two sets of model tests. To properly examine the nonlinear features of the phenomena, first, second, third and fourth-order harmonics of the measured acceleration signals were estimated. Harmonics higher than fourth-order were small as shown in Figure 4.12.

4.4 Longitudinal and transverse motion measurements

The longitudinal motions of the nearly rigid torus model were determined by using the mooring load registrations at the front and aft positions of torus together with the known stiffness ($k_s = 17N/m$) of the springs. The transverse motions were similarly estimated by using the mooring load registrations at the left and right torus positions. The time series were analyzed as described above for the vertical accelerations by considering only the first harmonic part.

4.5 Summary

An elastic and an nearly rigid torus model tests have been performed in order to validate the low-frequency slender-body theory. Wave generation tests without the torus present have been carried out for all test wave periods and wave steepnesses. All the tests are repeated and show good repeatability. Overtopping and out of water of parts of the torus models occur for some of the test conditions. Higher order harmonics of the measured acceleration are important.

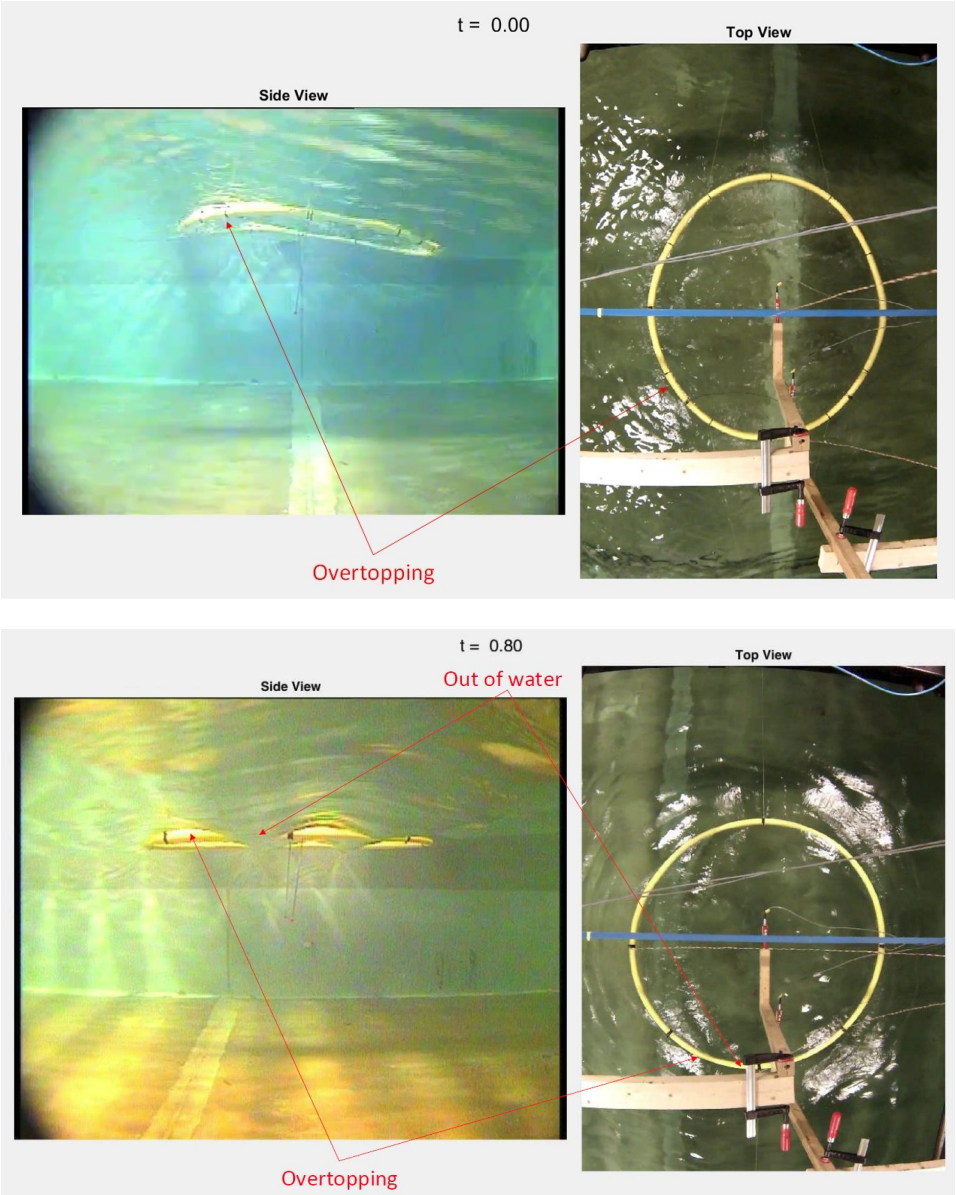

Figure 4.10: Illustrations of overtopping and out of water of parts of the tori in two sets of model tests. Upper: elastic torus model; lower: nearly rigid torus model. Left: side view from underwater camera; right: top view from the camera in air.

Figure 4.11: Illustrations of overtopping and out of water on the torus of a fish cage without net in a storm. (Photo: Marius Dahle Olsen)

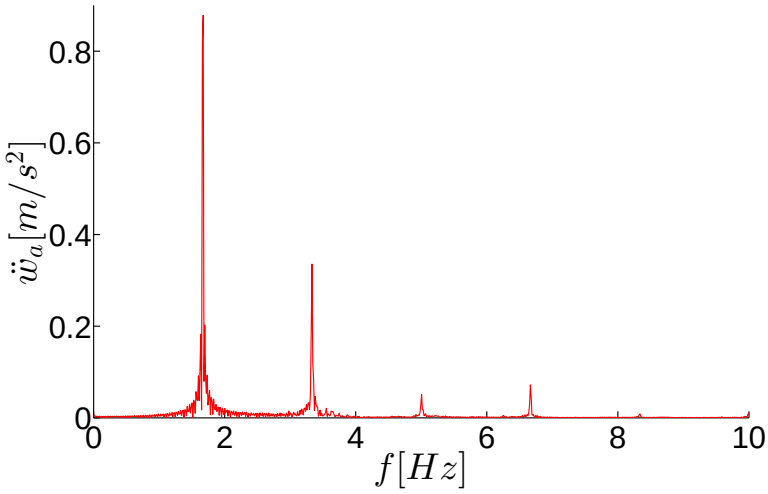

Figure 4.12: Fourier experimental vertical acceleration amplitude spectra at the front of the elastic torus model with wave steepness $H/\lambda = 1/30$ and wave period $T = 0.6s$ as a function of frequency in Hz.

Chapter 5

A study of a floating nearly rigid torus in regular waves

In this chapter we investigate theoretically and experimentally the longitudinal motions and vertical accelerations of a floating nearly rigid torus in regular waves. Wave motions inside the torus are also investigated. Comparisons of vertical accelerations are made with linear and partly with second-order potential-flow theory for the smallest examined experimental wave steepness 1/120. Experimental third and fourth harmonic accelerations of the torus have also been examined. This work has resulted in one publication (Li et al., 2016).

5.1 Theoretical methods

Ideally, we need a fully nonlinear 3D CFD method that accounts for hydroelasticity to compare with the experiments. We say 3D because the linear hydroelastic calculations of vertical accelerations of a torus in regular waves described and verified in Chapters 2 and 3 showed significant 3D hydrodynamic effects. We say fully nonlinear because the experiments show that even fourth order harmonics of the measured torus vertical accelerations mattered in steeper waves and that perturbation methods are only practical for linear (first-order) and second-order problems, which determine only the first and second-harmonics of the torus acceleration in regular waves. Furthermore, Navier-Stokes equation is needed because flow separation may matter for steeper waves. Kristiansen and Faltinsen (2009) demonstrated the latter fact by 2D fully nonlinear CFD simulations of a semi-submerged circular section in regular waves of relevance for fish farms. Laminar flow was assumed, which is appropriate in model test conditions at least for the boundary layer flow. The numerical method combined the Finite Difference Method and Chorin's projection method with the Constrained Interpolation Profile (CIP) method in the advection step. Furthermore, color functions were applied to capture the free-surface. The numerical calculations agreed well with the presented experimental results. However, the fully nonlinear 3D CFD method for our case will need very

long CPU time with state-of-the-art computational resources. The more efficient potential flow theory and codes have been used in the following study.

The two used numerical methods are based on potential flow theory for incompressible liquid and a perturbation scheme with the wave steepness as a small parameter, which is most relevant for the smallest experimental wave steepness. Surface tension is not included. Surface tension may affect the contact line between water and the torus. However, the difference appears as a thin layer of water rising up, but it does not affect the loading. In order for surface tension to matter, the wave length should be of the order of $1cm$ and smaller. These dimensions are clearly out of the range for incident waves and important nonlinear waves generated by the torus.

One solver is HydroStar, which is a low-order Boundary Element Method solving the linear and second-order frequency-domain potential-flow problem in bichromatic incident waves in a consistent way. Therefore, our needed first and second-order response in monochromatic waves can easily be obtained. Deep-water conditions were assumed. The effect of mooring lines was included in the linear problem, but proved to be small. The commercial version of HydroStar accounts for tank wall interference in the linear problem but does not account for hydroelasticity, which matters in the experiments. The numerical results without tank wall interference were verified by convergence studies, which for the second-order problem involved decreasing panel sizes on the mean free-surface as well as on the mean wetted body surface. For the linear problem without tank wall interference, we ensured that, the wave excitation force and moment by Haskind relationship and direct pressure integration agreed as shown in Figures 3.13 to 3.15. Furthermore, it was controlled that the Newman (1962) relationship between excitation force/moment amplitudes and corresponding wave radiation damping for an axisymmetric vertical body was satisfied as shown in Figure 3.16.

The second used solver is WAMIT which uses a higher-order Boundary Element Method (see Chapter 3). WAMIT provides linear generalized forces due to elastic vibration modes. It was combined with the curved beam equation Eq. (2.10). Because of the model set up (see Figure 4.4), there is no influence of the axial tension term T_{as}. The hydroelastic model neglects mooring forces and coupling with longitudinal motions. Separate numerical studies with a rigid model showed small effects of mooring loads and coupling between surge and pitch. We do not know the structural damping, which is of concern for the resonance oscillations of elastic modes in case of small hydrodynamic damping. However, the numerical studies by Li et al. (2014) for a similar problem as ours indicate that structural damping within realistic limits have a small effect.

Due to the different theoretical features of the solvers, four different numerical models are used in the following studies and are listed in Table 5.1.

5.2 Experimental and numerical results

The numerical (model A) and experimental longitudinal motions and vertical accelerations were compared for the smallest tested wave steepness 1/120 when we

can expect that a perturbation method is most appropriate.

Table 5.1: Numerical models used in this chapter to consider a rigid or an elastic torus, tank wall interference, linear and second order hydrodynamic effects.

	Rigid	Elastic	Tank wall	Linear	Second order
HydroStar (model A)	YES	NO	NO	YES	NO
HydroStar (model B)	YES	NO	YES	YES	NO
HydroStar (model C)	YES	NO	NO	NO	YES
WAMIT (model D)	NO	YES	NO	YES	NO

5.2.1 Linear frequency-domain horizontal torus motion

Estimates of the longitudinal and transverse motions have been obtained by considering the measured mooring line tensions together with the spring stiffness for the mooring lines. It means that we for the longitudinal motion subtracted the aft tension time series from the front tension time series then divided by two. The tension time series for the transverse motion applies the same method but using right and left tension time series. Due to small angles between the mooring lines and calm water surface, this would give a good estimate of the longitudinal and transverse motions. Applying the sliding DFT technique described in Section 4.3 for the mooring line forces as for the accelerations and wave elevations, an estimation of the longitudinal and transverse motions of the nearly rigid torus model is found as $\eta_{1,2} = F_{1,2}/k_{1,2}$, where η_1 and η_2 are longitudinal (surge) and transverse (sway) motions, respectively, F_1 and F_2 are the mooring line tension time series for longitudinal and transverse motions and k_1 and k_2 are the equivalent spring stiffness which is found by the sum of the spring stiffness of the mooring line considered in longitudinal and transverse directions respectively.

Figure 5.1 presents comparisons between experimental measurements and linear numerical (model A) predictions of longitudinal motion response-amplitude-operators (RAO). The fact that experimental RAO's obtained by measuring the mooring lines forces in front and aft differ means that hydroelasticity matters, but without being so clear as we will see for the vertical accelerations in the next section. Hydroelasticity effects were also observed in the forces of the two transverse mooring lines along with small transverse rigid-body motions. An error source is that the presented torus is slightly deformed (see Figure 5.2). A satisfactory agreement between theory and experiments is shown in Figure 5.1. However, the theoretical cancellation effect at certain frequencies is not so pronounced in the experiments as in the numerical calculations. Figure 5.3 shows the experimental values for transverse motions. The frequency of the peak at $\nu a = 0.1132$ is close to the natural frequency of a transverse sloshing mode of the tank with a node at the

center plane of the tank. Since roll and transverse motions are coupled, the results in Figure 5.3 imply non-zero roll.

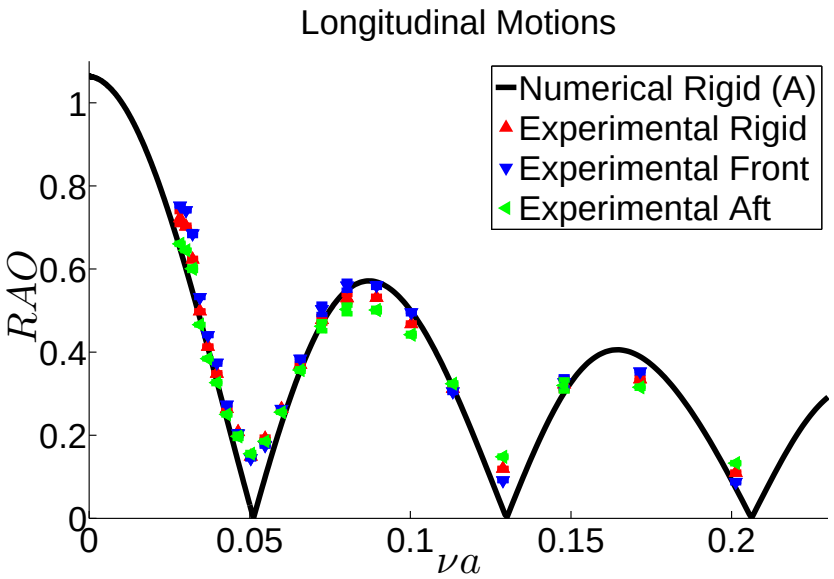

Figure 5.1: Theoretical and experimental linear frequency-domain results of longitudinal motions versus non-dimensional wave number νa. RAO = longitudinal motion amplitude divided by prescribed incident wave amplitude ζ_a. The height of the experimental error bars is two times the estimated standard deviation. The wave steepness $H/\lambda = 1/120$.

5.2.2 Linear frequency-domain vertical torus accelerations

Figure 5.4 shows the numerical predictions of the non-dimensional linear frequency-domain vertical acceleration amplitude along five positions of the torus. Linear numerical results from HydroStar (with and without tank wall interference, *i.e.* model B and A, respectively, see Table 5.1) and WAMIT (with hydroelastic model, *i.e.* model D in Table 5.1) are reported as a function of the non-dimensional wave number νa, and compared with the corresponding experimental data.

The experimental results are given with an error bar whose height is two times the standard deviation, which implies that the oscillations are not steady state. The reason why the experimental results are not steady state can be wave reflections from the wave beach and the wave maker, build-up of transverse sloshing due to tank wall interference as well as beating effects induced by residual waves from the previous run with different period. The elastic modes $\cos 2\beta$, $\cos 3\beta$ and $\cos 4\beta$ influence the numerical hydroelastic results with the $\cos 2\beta$-mode giving the dominant contribution. The latter mode does not contribute at the front left and aft left positions with the consequence that the rigid and

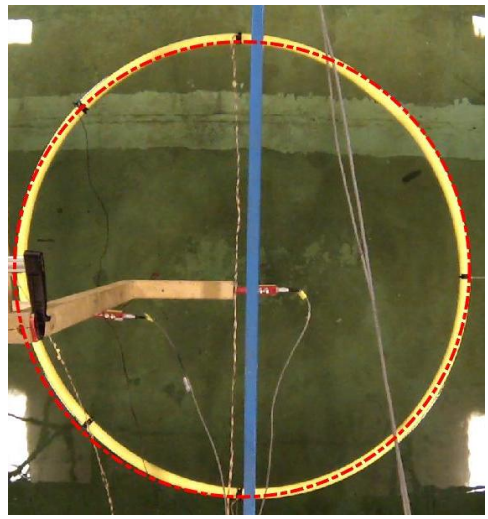

Figure 5.2: Torus deformation in calm conditions. Red line: prescribed torus; yellow colour: actual torus.

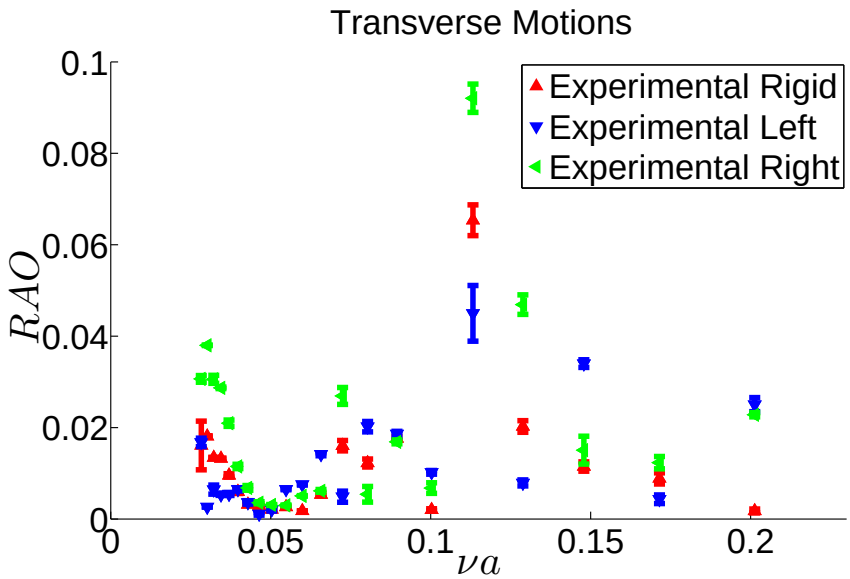

Figure 5.3: Experimental linear frequency-domain results of transverse motions versus non-dimensional wave number νa. RAO = transverse motion amplitude divided by prescribed incident wave amplitude ζ_a. The height of the experimental error bars is two times the estimated standard deviation. The wave steepness $H/\lambda = 1/120$. Right is defined along positive y-axis in Figure 4.4.

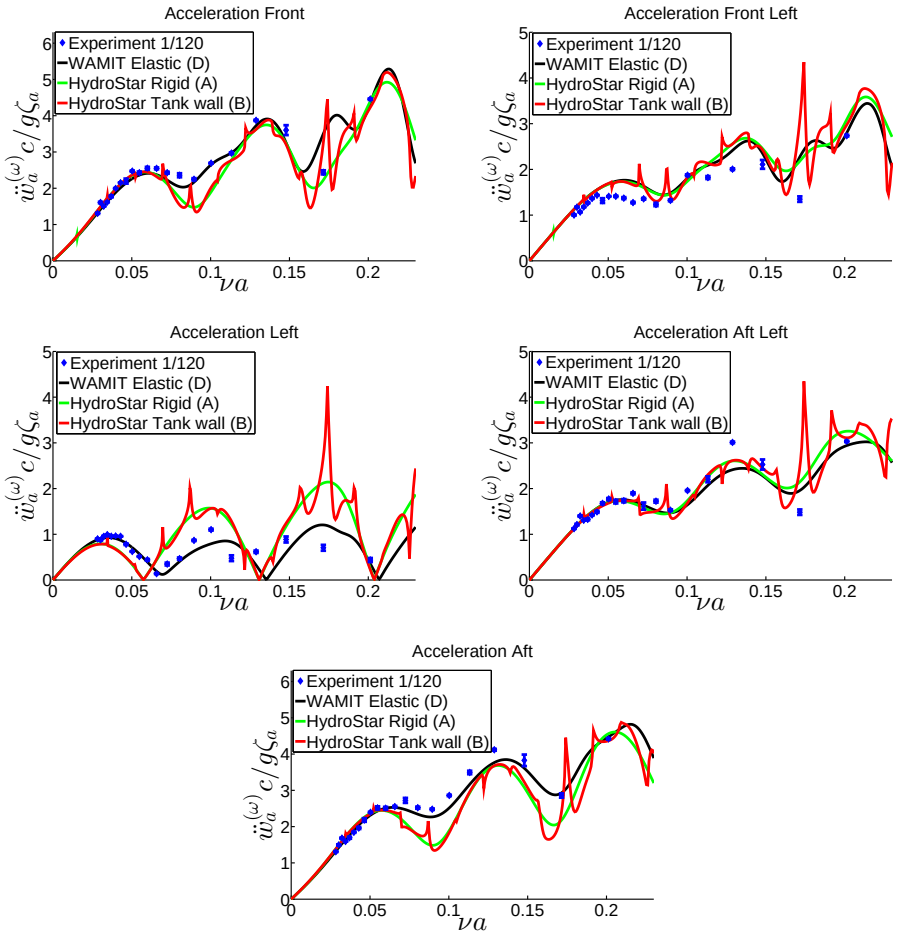

Figure 5.4: Comparison of linear frequency-domain results of vertical acceleration amplitude $\ddot{w}_a^{(\omega)}$ along the torus by means of HydroStar and WAMIT with experiments versus non-dimensional wave number νa. WAMIT results are combined with hydroelastic curved-beam theory. The height of the experimental error bars is two times the estimated standard deviation. The wave steepness $H/\lambda = 1/120$.

elastic results are closest there. Bending stiffness matters and causes the theoretical results coming closer to the experiments except at the front left position. The peaks in the numerical results with tank wall interference (model B) occurs at $\nu a = 0.0349, 0.0526, 0.0701, 0.0877, 0.1052, 0.1227, 0.1403, 0.1578, 0.1753, 0.1929$, which correspond to the natural frequencies ω_i associated with 2D transverse sloshing modes that are symmetric with respect to the longitudinal center-plane of

the tank. The expression for ω_i is

$$\omega_i = \sqrt{g\frac{2\pi i}{b_{tank}}\tanh\left(\frac{2\pi i}{b_{tank}}h\right)} \quad i = 1, 2, ... \tag{5.1}$$

Here g is the acceleration of gravity, h is the depth of the wave tank and b_{tank} is the width of the wave tank. The fact that the response is not infinite at the resonance frequencies as a 2D linear frequency domain theory predicts is a consequence of 3D flow. However, the calculations with tank wall interference do not improve the agreement between theory and experiments. For instance, the experimental results at $\nu a = 0.1715$, which is close to the 2D natural sloshing frequency $\omega_{10} = 9.7740 rad/s$ corresponding to $\nu a = 0.1753$, do not seem to be influenced by the clear theoretical resonance demonstrated for the rigid torus. However, the experimental time-domain results show a beating effect associated with the difference frequency between the forcing frequency $\omega = 9.6662 rad/s$ corresponding to $\nu a = 0.1715$ and the sloshing frequency $\omega_{10} = 9.7740 rad/s$ corresponding to $\nu a = 0.1753$, which indicates that a build-up of resonance occurs.

Amplitudes $\ddot{a}_{na}$ and phase angles α_n of the different acceleration modes defined by $\ddot{a}_n = \ddot{a}_{na}\cos(\omega t + \alpha_n)$ with the incident wave elevation given by $\zeta = \zeta_a \sin(\omega t - \nu x)$ were experimentally and theoretically (model D) identified. Experimentally we determined amplitudes and phases for $n = 0, 1, 2, 3, 4$ by satisfying:

$$\ddot{w} = \ddot{a}_0(t) + \ddot{a}_1(t)\cos\beta + \ddot{a}_2(t)\cos 2\beta + \ddot{a}_3(t)\cos 3\beta + \ddot{a}_4(t)\cos 4\beta \tag{5.2}$$

at the five measurement points. The procedure was to consider the time instant when the experimental vertical acceleration at the front point had a maximum value close to the experimental mean amplitude. In more detail, it means that we first expressed the experimental values of the different acceleration modes as $\ddot{a}_{na}\cos(\omega t' + \gamma_n)$ with $t' = 0$ corresponding to when the front vertical acceleration had the considered maximum. By selecting also the time instant $\omega t' = \pi/2$ we have sufficient equations to determine the amplitudes $\ddot{a}_{na}$ and the phase angles γ_n. Sensitivity to selecting different time instants was small. Since we did not measure the incident waves, we used the theoretical values of the vertical acceleration at the front point as a reference to determine the experimental phases relative to the theoretical incident wave elevation. It means that we write $t = t' - \delta$ in the theoretical vertical acceleration at the front point with five modes, *i.e.*

$$\begin{aligned}
\ddot{w}|_{\beta=0} &= \left(\sum_{n=0}^{4}\ddot{a}_{na}\cos\alpha_n\right)\cos(\omega t' - \omega\delta) - \left(\sum_{n=0}^{4}\ddot{a}_{na}\sin\alpha_n\right)\sin(\omega t' - \omega\delta) \\
&= \left[\left(\sum_{n=0}^{4}\ddot{a}_{na}\cos\alpha_n\right)\cos\omega\delta + \left(\sum_{n=0}^{4}\ddot{a}_{na}\sin\alpha_n\right)\sin\omega\delta\right]\cos\omega t' \\
&+ \left[\left(\sum_{n=0}^{4}\ddot{a}_{na}\cos\alpha_n\right)\sin\omega\delta - \left(\sum_{n=0}^{4}\ddot{a}_{na}\sin\alpha_n\right)\cos\omega\delta\right]\sin\omega t'
\end{aligned} \tag{5.3}$$

By requiring the theoretical vertical acceleration at the front point to behave as $A\cos\omega t'$, $A > 0$ we get the following requirements:

$$\begin{aligned}\left(\sum_{n=0}^{4}\ddot{a}_{na}\cos\alpha_n\right)\sin\omega\delta \;-\; \left(\sum_{n=0}^{4}\ddot{a}_{na}\sin\alpha_n\right)\cos\omega\delta \;&=\; 0\\ \left(\sum_{n=0}^{4}\ddot{a}_{na}\cos\alpha_n\right)\cos\omega\delta \;+\; \left(\sum_{n=0}^{4}\ddot{a}_{na}\sin\alpha_n\right)\sin\omega\delta \;&>\; 0\end{aligned} \tag{5.4}$$

This determines δ. By substituting $t' = t + \delta$ into $\ddot{a}_{na}\cos(\omega t' + \gamma_n)$ we determine experimental phase angles α_n. The comparison between theory (model D) and experiments are presented in Figures 5.5 and 5.6 for $n = 0, 1, 2$, *i.e.* for heave, pitch and the lowest elastic mode. The amplitudes for $n = 3, 4$ are small relative to the values for $n = 0, 1, 2$ and are therefore not shown. The fact that the heave motion should follow the incident wave elevation at $x = 0$ and pitch with a positive value in an $Oxyz$ coordinate system as defined in Faltinsen (1990) should be 180° out of phase with the incident wave slope at $x = 0$ when $\nu a \to 0$ is confirmed. General good agreement is obtained, in particular for pitch acceleration amplitudes. Differences between theoretical (model D) and experimental accelerations of heave and lowest elastic mode amplitude are noted for $\nu a = 0.1715$ and are the reasons for the differences noted at this frequency in Figure 5.4. The difference is largest for heave accelerations.

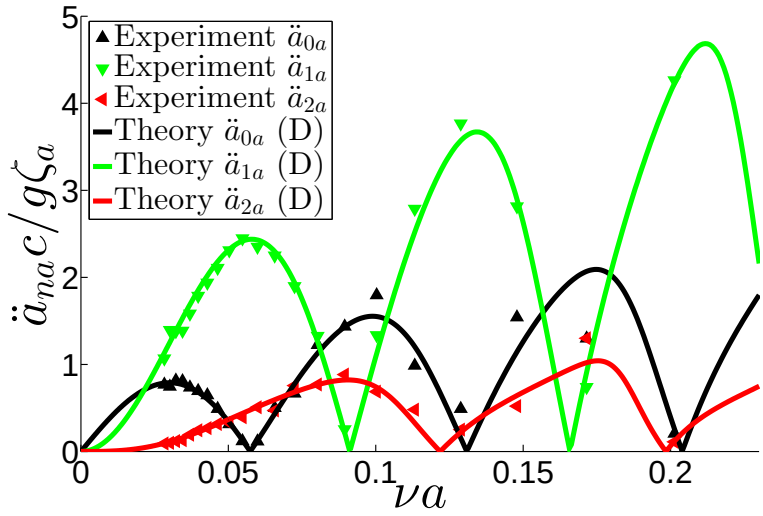

Figure 5.5: Comparison of experimental and theoretical linear frequency-domain results of vertical acceleration amplitudes $\ddot{a}_{na}$ of heave ($n = 0$), pitch ($n = 1$) and lowest elastic mode ($n = 2$) versus non-dimensional wave number νa. The wave steepness $H/\lambda = 1/120$.

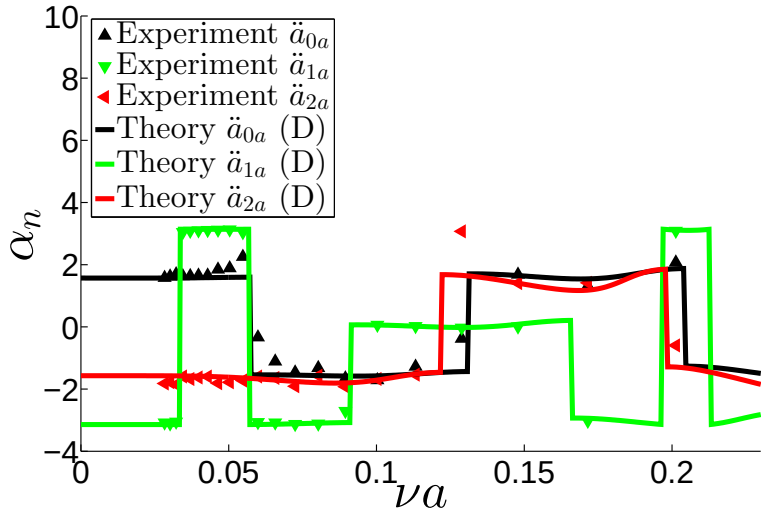

Figure 5.6: Comparison of experimental and theoretical linear frequency-domain results of vertical acceleration phase angles α_n of heave ($n = 0$), pitch ($n = 1$) and lowest elastic mode ($n = 2$) versus non-dimensional wave number νa. The wave steepness $H/\lambda = 1/120$.

We investigated in more detail possible tank wall interference effects by analyzing the wave amplitude due to torus motions at the tank walls along a wave-propagation direction perpendicular to the tank walls by using theory without tank wall effects. The analysis is done by relating the far-field wave amplitudes due to forced oscillations of the different modes to the generalized damping coefficients for the different modes by using conservation of kinetic and potential energy in the water.

The far-field expression of the velocity potential for a given mode can be obtained by a line distribution of sources along the centerline of the torus as shown in Chapter 2. A frequency-domain analysis in infinite water depth and infinite horizontal water extent was considered. The sources satisfy the classical linearized free-surface condition and radiation condition. The far-field waves are expressed in terms of Hankel functions. The analysis in Chapter 2 shows that the source density associated with mode n varies as $\cos n\beta$. It follows by combining the latter fact with properties of Bessel functions that the far-field velocity potential associated with mode n can be approximated as:

$$\varphi_n = \frac{g}{\omega}\frac{A_n \cos n\theta}{\sqrt{\nu r}} exp\,(\nu z)\cos\left(\omega t - \nu r + \delta_n\right) \tag{5.5}$$

Here (r, θ, z) are polar coordinates with the angle θ having the same definition as the angle β in Figure 4.4. Energy considerations based on a general formula within potential flow of an incompressible liquid (see, for instance, Newman (1977*b*)) imply

that:

$$\frac{dE}{dt} = \int_{\bar{S}_B} (p - p_a)\, U_n ds - \rho \int_{S_\infty} \frac{\partial \varphi_n}{\partial t} \frac{\partial \varphi_n}{\partial n} ds \tag{5.6}$$

Here $\bar{S}_B$ is the mean wetted body surface and S_∞ is a vertical circular cylindrical control surface at large $r = R$ extending from $z = 0$ to $z = -\infty$. E is the sum of the kinetic and potential energy in the water domain Ω between $\bar{S}_B$ and S_∞. The positive direction of the normal coordinate n is into the water domain Ω. p is the pressure with subscript a indicating atmospheric pressure. U_n means the normal velocity of $\bar{S}_B$. We integrate Eq. (5.6) over the oscillation period T with the consequence that the term on the left hand side does not contribute due to periodicity of E. The first term on the right hand side leads to

$$\omega^2 \frac{T}{2} B_{33}^{(n)} a_{na}^2, \quad B_{33}^{(n)} = \int_0^{2\pi} b_{33}^{(n)} \cos^2 n\beta c d\beta \tag{5.7}$$

The second term on the right hand side is

$$- \frac{\rho g^2 A_n^2}{\omega 2\nu} \frac{T}{2} I_n \tag{5.8}$$

where $I_0 = 2\pi, I_n = \pi$ when $n = 1, 2, ...$ This means

$$\left(\frac{A_n}{a_{na}}\right)^2 = \frac{2B_{33}^{(n)} \nu^3}{\rho \omega I_n} \tag{5.9}$$

We consider now the wave propagation direction perpendicular to the tank wall, *i.e.* $\theta = \pm\pi/2$. Eq. (5.5) shows no contribution from pitch at $\theta = \pm\pi/2$. The effect of heave and the lowest elastic mode will be considered. The corresponding wave amplitudes at the tank walls normalized by the incident wave amplitude can be expressed as:

$$\frac{A_n}{\zeta_a \sqrt{\nu b_{tank}/2}} = 2\nu \frac{a_{na}}{\zeta_a} \sqrt{\frac{B_{33}^{(n)}}{\rho \omega I_n b_{tank}}} \tag{5.10}$$

The results are shown in Figure 5.7 and should be interpreted as an excitation of tank wall interference. The amplitudes are small relative to the incident wave amplitude and show a strong frequency dependency with zeroes and peaks. For instance, there is a peak at $\nu a = 0.1792$, which is close to the 2D sloshing frequency corresponding to $\nu a = 0.1753$.

Even though the agreement between linear theory (model A, B and D) and experiments presented in Figures 5.4 to 5.6 is generally satisfactory we investigated error sources. It has already been mentioned that coupling between longitudinal and vertical motions is present and is neglected in the hydroelastic analysis. Another error source is that the measured incident wave amplitude differed from the intended wave amplitude as illustrated in Figure 4.7. Since small-amplitude sway occurred in the experiments, small-amplitude roll must be present due to coupling and cause a vertical motion.

Viscous effects matter when significant viscous flow separation occurs. A measure of flow separation for ambient oscillatory planar 2D flow with flow velocity

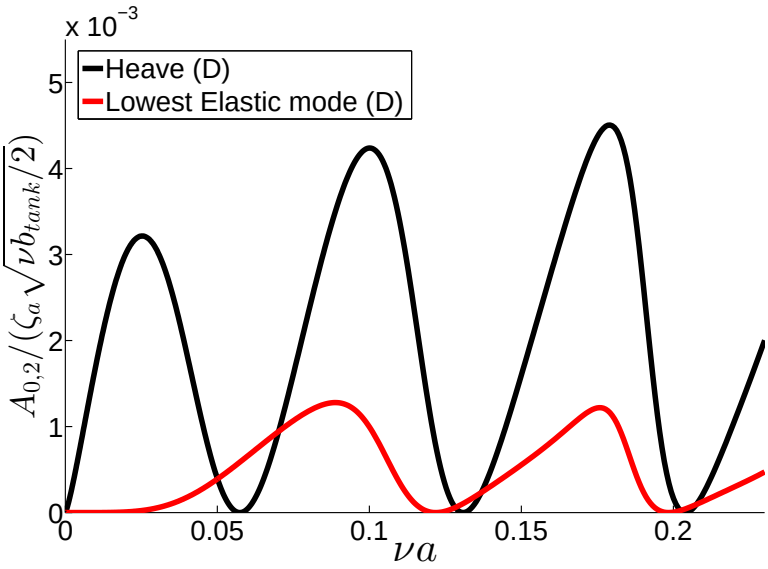

Figure 5.7: Wave amplitude at the tank walls along a wave-propagation direction perpendicular to the tank due to torus motions in heave and lowest elastic mode (model D) normalized by incident wave amplitude walls versus non-dimensional wave number νa. Note that the effect of the tank wall is not included in model D.

amplitude U_a and period T past a stationary circular cylinder of diameter $2a$ in infinite fluid is the Keulegan-Carpenter number $KC = U_a T/(2a)$. When $KC < 2-3$, flow separation does not occur (Faltinsen, 1990). We can generalize these findings to our case with a rigid torus and define the vertical and radial Keulegan-Carpenter numbers $KC_{vert.} = \pi\eta_{rel.ver.}/a$ and $KC_{rad.} = u_{rel.rad.}T/(2a)$. Here $\eta_{rel.vert.}$ is the amplitude of the relative vertical motion between the torus and the incident waves. $u_{rel.rad.}$ means the amplitude of the relative velocity component in the radial direction between the torus and the incident waves. Since the torus follows the waves when $\nu a \to 0$, $\eta_{rel.vert.}/\zeta_a$ and $u_{rel.rad.}T/\zeta_a$ go to zero when $\nu a \to 0$. Calculated values of $KC_{vert.}$ and $KC_{rad.}$ by HydroStar (model A) are presented in Figure 5.8 versus the non-dimensional wave number for five positions along the torus. Because the wave height for a given wave steepness goes to infinity when $\nu a \to 0$, $KC_{rad.}$ does not tend to zero when $\nu a \to 0$. The results indicate that flow separation is insignificant for our considered small wave steepness and that we have an attached boundary layer flow.

The attached viscous boundary-layer flow along the torus has been analyzed by assuming laminar boundary-layer flow and ambient longitudinal flow velocity $U_a \cos\omega t$ together with a rigid free-surface condition. The latter fact avoids the necessity to consider all the details of the frequency-dependent pressure distribution. The torus is assumed semi-submerged. We apply the cross-flow principle together with strip theory and well-established 2D results based on Stokes second problem

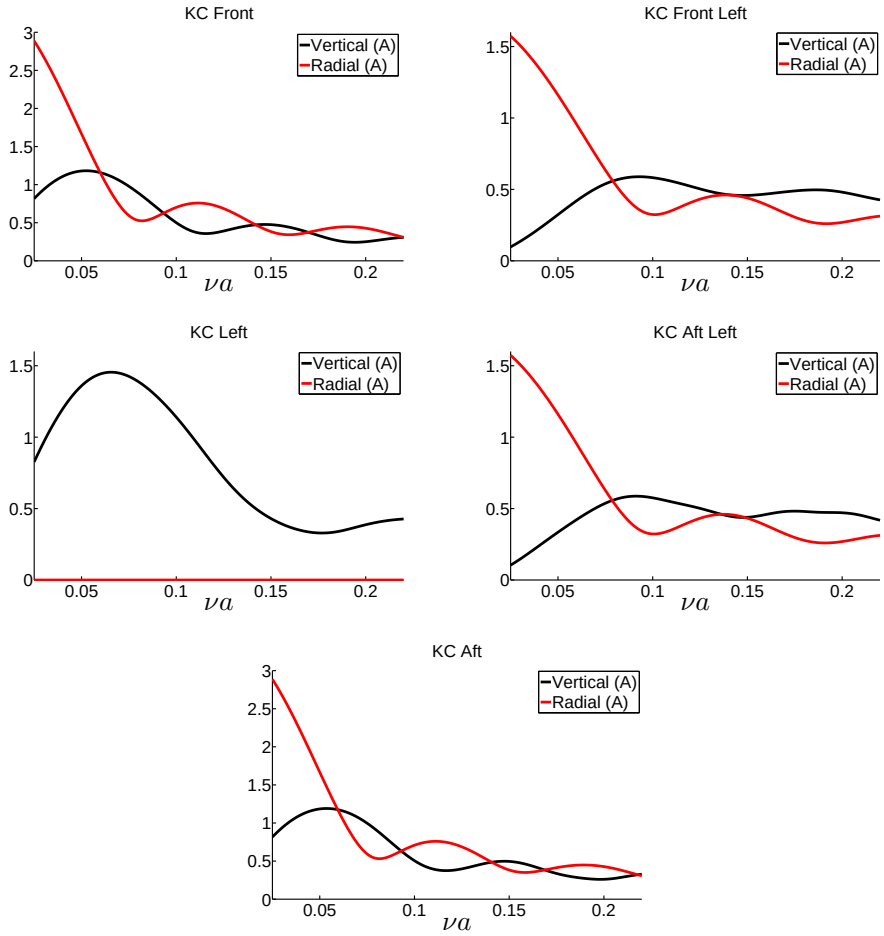

Figure 5.8: Calculated vertical and radial Keulegan-Carpenter numbers versus non-dimensional wave number νa for five positions along the torus. The wave steepness $H/\lambda = 1/120$.

(Faltinsen, 1990), which gives:

$$F_1^{visc} = U_a \sqrt{\frac{\omega\mu}{\rho}} \cos(\omega t + \pi/4)\, 2ac\pi^2 \tag{5.11}$$

as the longitudinal viscous force on the semi-submerged torus. Here μ is the dynamic viscosity coefficient. We consider the viscous force in phase with the acceleration and compare it with the measure $\rho\pi^2 a^2 2c\omega U_a \sin\omega t$ of the sum of the mass and added mass acceleration force on the torus. Here we have not accounted for the fact that the added mass in surge is frequency dependent. The ratio of the viscous force

amplitude and the measure of the mass and added mass force can be expressed as:

$$\frac{F_v}{F_{mass}} = \sqrt{\frac{\mu}{2\omega\rho a^2}} \tag{5.12}$$

The results are presented in Figure 5.9 as a function of νa in our considered frequency range. Since the maximum value of $\frac{F_v}{F_{mass}}$ is about 0.02, we confirm that viscous effects are not dominant.

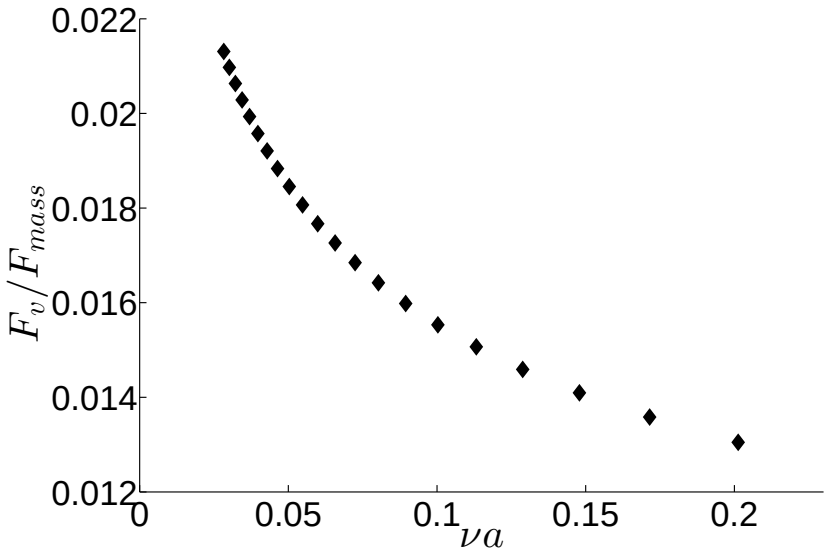

Figure 5.9: The ratio F_v/F_{mass} of the amplitudes of viscous force in phase with surge acceleration and a measure of the mass and added mass force in surge on the torus as a function of non-dimensional wave number νa.

Nonlinear effects may cause oscillations with frequency ω. For instance, if we apply a third-order theory with steady-state oscillations in regular waves, there are oscillations with frequencies ω and 3ω. The corresponding amplitudes are expected to be of the same order of magnitude. Our arguments for saying this is that a third-order analysis, for instance involves terms $\cos^3\omega t = \frac{1}{4}\cos 3\omega t + \frac{3}{4}\cos\omega t$. Therefore, we present in Figure 5.10 the experimental ratio $\ddot{w}_a^{(3\omega)}/\ddot{w}_a^{(\omega)}$ versus non-dimensional wave number νa for the five considered positions along the torus. Here $\ddot{w}_a^{(3\omega)}$ and $\ddot{w}_a^{(\omega)}$ are the vertical acceleration amplitudes of the oscillations with frequencies 3ω and ω, respectively. The mean values obtained from the DFT analysis are the basis for the estimates, *i.e.* we do not involve an error band associated with the standard deviation. The results indicate that third order effects cannot be neglected in estimating the experimental accelerations oscillating with frequency ω for $\nu a \lessapprox 0.1$. One contributing factor to the larger relative influence for small νa is

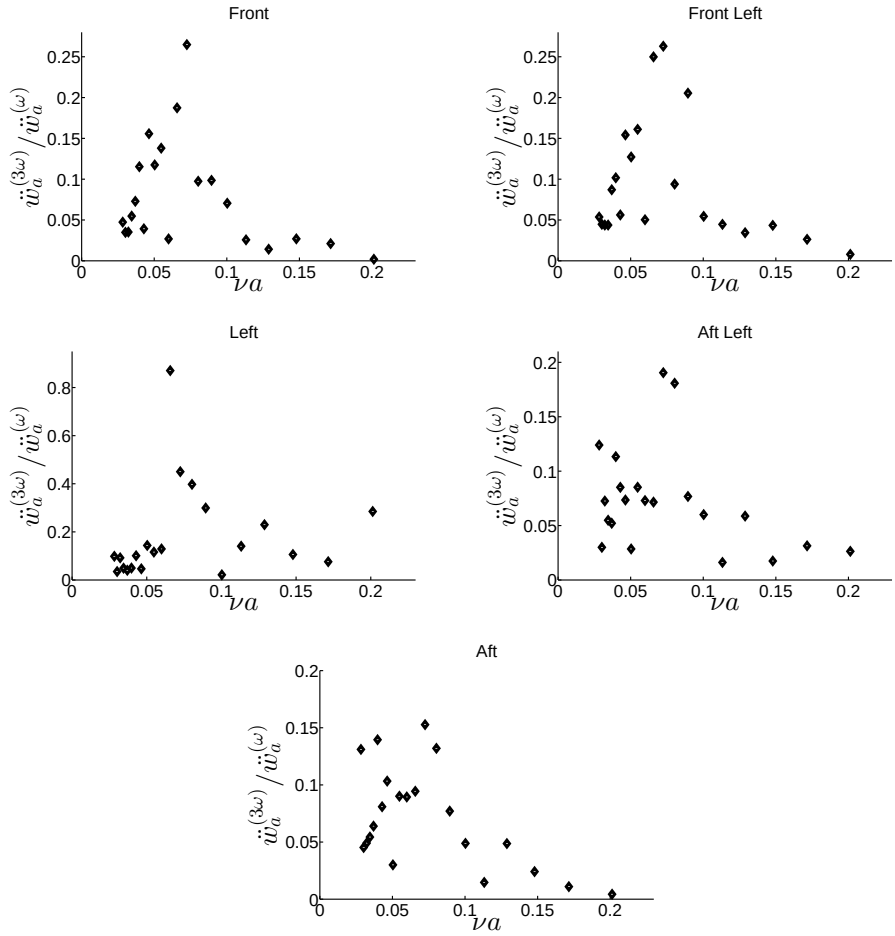

Figure 5.10: Experimental ratio $\ddot{w}_a^{(3\omega)}/\ddot{w}_a^{(\omega)}$ versus non-dimensional wave number νa for five positions along the torus. Here $\ddot{w}_a^{(3\omega)}$ and $\ddot{w}_a^{(\omega)}$ are the vertical acceleration amplitudes of the oscillations with frequencies 3ω and ω, respectively. The wave steepness $H/\lambda = 1/120$.

that the incident wave amplitude-to-cross-sectional radius ratio $\zeta_a/a = (\pi/120)/\nu a$ increases with decreasing νa.

5.2.3 Sum-frequency vertical torus accelerations

Since the measurements are relative to a body-fixed coordinate system $Ox_By_Bz_B$, which coincides with the $Oxyz$-system at rest and the calculations by HydroStar (model C) are in an inertial coordinate system, we have to add the sum-frequency part of $\ddot{\eta}_1\eta_5 + \frac{1}{2}g\eta_5^2$ to the sum-frequency calculations of vertical accelerations. Here

$\ddot{\eta}_1$ and η_5 are the surge acceleration and pitch angle, respectively. The influence of the correction term was negligible.

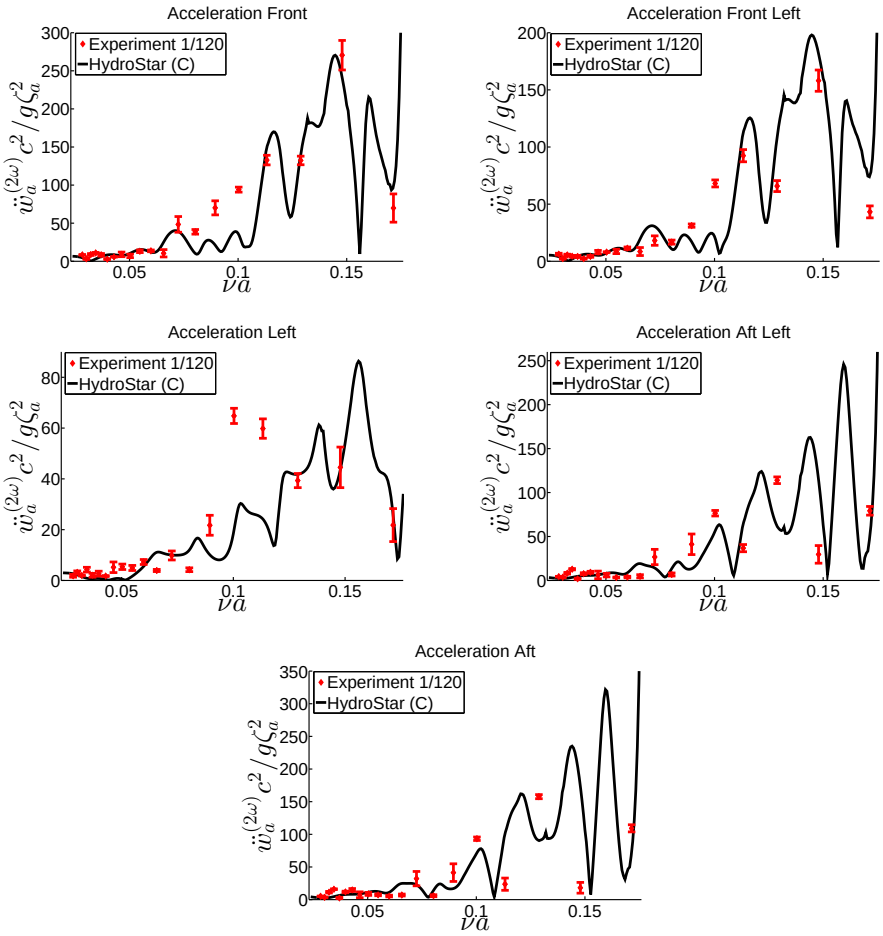

Figure 5.11: Second-order sum-frequency non-dimensional vertical acceleration amplitude $\ddot{w}_a^{(2\omega)} c^2 / \left(g\zeta_a^2\right)$ along the z_B-axis for five positions of the torus by HydroStar (model C) together with experimental results versus non-dimensional wave number νa in the range of $[0.023, 0.176]$. The height of the experimental error bars is two times the estimated standard deviation. The wave steepness $H/\lambda = 1/120$.

Figures 5.11 and 5.12 show numerically predicted second-order sum-frequency non-dimensional acceleration amplitude $\ddot{w}_a^{(2\omega)} c^2 / \left(g\zeta_a^2\right)$ along the z_B-axis for five positions of the torus by HydroStar (model C) together with experimental results versus non-dimensional wave number νa. The large differences in vertical scale of the two figures should be noted. The agreement is not perfect but we should have in mind the error sources discussed in the section on linear frequency-domain results,

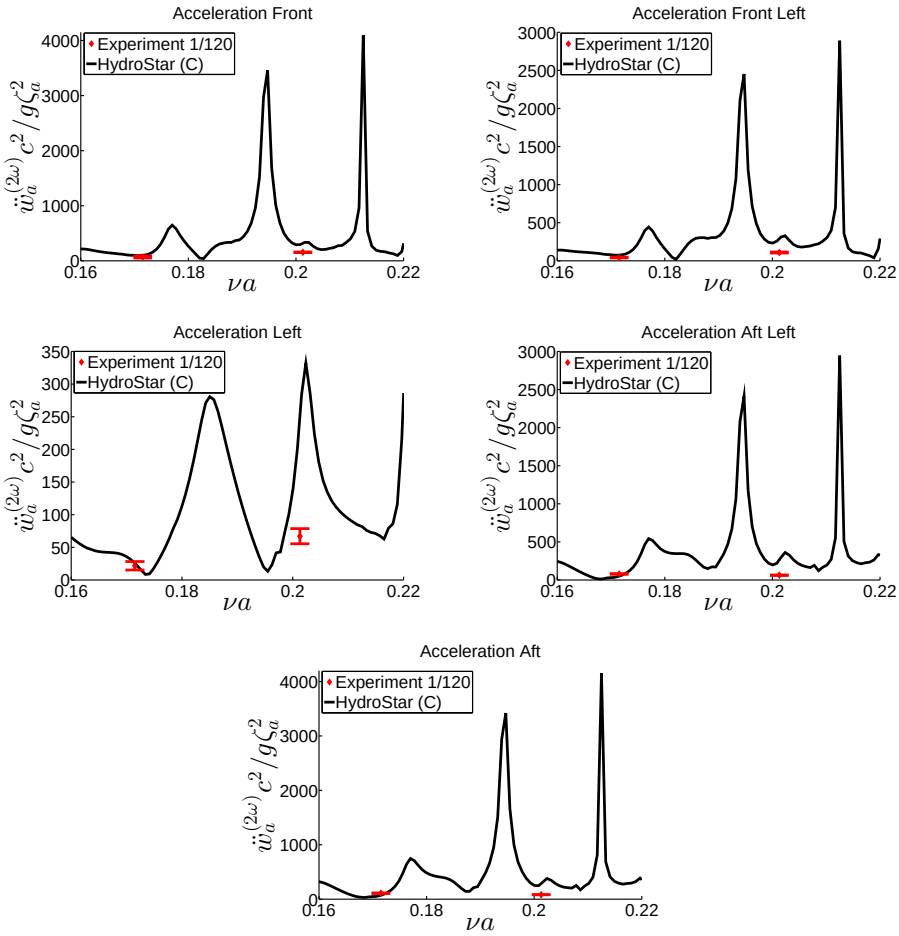

Figure 5.12: Second-order sum-frequency non-dimensional vertical acceleration amplitude $\ddot{w}_a^{(2\omega)} c^2 / \left(g\zeta_a^2\right)$ along the z_B-axis for five positions of the torus by HydroStar (model C) together with experimental results versus non-dimensional wave number νa in the range of $[0.16, 0.22]$. The height of the experimental error bars is two times the estimated standard deviation. The wave steepness $H/\lambda = 1/120$.

which implicitly have consequences for the second-order solution. Additional tank wall interference effects occur for the second-order problem since the second-order potential involves contributions from the non-homogenous free-surface conditions over an infinite domain of the mean free-surface, which is in conflict with the tank walls. We documented for the linear problem the fact that there was in the experiments non-negligible oscillations with frequency 3ω meant that there were contributing oscillations with ω from a third-order theory. In theory, we may say that there are contributions with frequencies 2ω and 4ω from a fourth-order

theory. However, since the measured 4ω-component was small, we anticipate that the corresponding 2ω-component can be neglected. The numerical results show clear peaks at the higher frequencies, but there are no experimental values at those peak frequencies.

We can partly explain the numerical results by setting up the frequency-domain equations of motions for the second-order response. The solutions contain the factors:

$$\begin{aligned} R_3 &= \frac{1}{\sqrt{\left[-4\omega^2\left(M + A_{33}\right) + C_{33}\right]^2 + \left[2\omega B_{33}\right]^2}} \\ R_{51} &= \frac{1}{\sqrt{Re^2 + Im^2}} \\ Re &= -4\omega^2\left(M + A_{11}\right)\left[-4\omega^2\left(I_{55} + A_{55}\right) + C_{55}\right] - 4\omega^2 B_{11}B_{55} \\ &\quad - 16\omega^4\left(Mz_G + A_{15}\right)\left(Mz_G + A_{51}\right) + 4\omega^2 B_{15}B_{51} \\ Im &= -2\omega B_{11}\left[-4\omega^2\left(I_{55} + A_{55}\right) + C_{55}\right] + 8\omega^3 B_{55}\left(M + A_{11}\right) \\ &\quad -8\omega^3 B_{15}\left(Mz_G + A_{51}\right) - 8\omega^3 B_{51}\left(Mz_G + A_{15}\right) \end{aligned} \tag{5.13}$$

involving torus parameters as a function of νa and defined relative to the coordinate system $Oxyz$ (see Figure 4.4). Here A_{33} and B_{33} are added mass and wave-radiation damping coefficients in heave as a function of 2ω, respectively. A_{ij} and B_{ij}, $i = 1$, 5; $j = 1$, 5 are added mass and wave-radiation damping coefficients in surge, pitch and coupling between surge and pitch as a function of 2ω. M is the mass and I_{55} is the mass moment of inertia in pitch, C_{33} and C_{55} are the hydrostatic restoring terms in heave and pitch, respectively. z_G is the z-coordinate of the center of gravity. Heave and coupling motions between surge and pitch can be considered as single and two-degree oscillating system, respectively. The second-order sum-frequency heave and pitch amplitudes are proportional to R_3 and R_{51}, respectively.

The results are presented in Figure 5.13. The strongly oscillating behavior as a function of νa is a consequence of the strong frequency dependency of the added mass and damping coefficients as shown in Figures 3.1 and 3.4. The consequence is many frequencies corresponding to peaks in the response curves, which differ for heave and pitch. This behavior is also reflected in the calculations presented in Figure 5.13. However, more frequencies ought to be experimentally studied to reveal the strong oscillatory behavior as a function of non-dimensional wave number νa. The peaks in the response curves are associated with peaks in the excitation loads. There are no resonance effects caused by 2ω being equal to an undamped natural frequency as listed in Table 4.3.

5.2.4 Wave elevation inside torus

The wave elevation inside the torus was investigated experimentally and theoretically. The linear potential flow theory predicts, for instance, zero heave and pitch wave radiation damping at certain frequencies, which differ for heave and pitch. The latter fact suggests that wave resonances inside are possible. Figure 5.14 shows

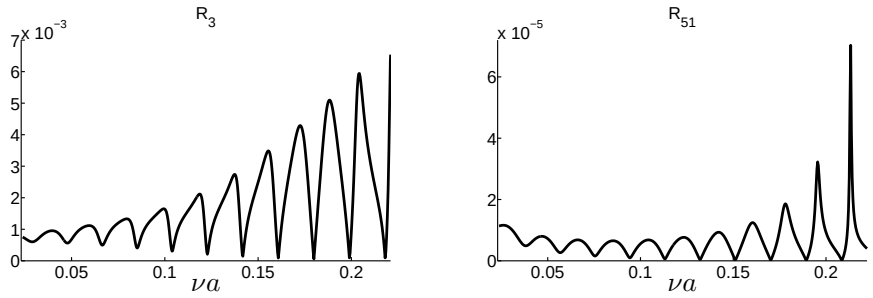

Figure 5.13: The multiplying factors R_3 for heave and R_{51} for pitch defined in Eq. (5.13) versus non-dimensional wave number νa. R_3 and R_{51} are calculated by HydroStar and are proportional to the second-order sum-frequency heave and pitch amplitudes, respectively.

the results. Linear potential flow theory for the rigid torus without tank wall interference (model A) has been applied. The left graph is for the center of the inside of the torus. There is no evidence of resonance neither in experiments nor theory. However, since linear resonant waves would have a node at that point, we have numerically also studied the wave elevation at the front and aft of the inside of the torus versus non-dimensional wave number (see Figure 5.14). Still we do not see any clear evidence of resonance.

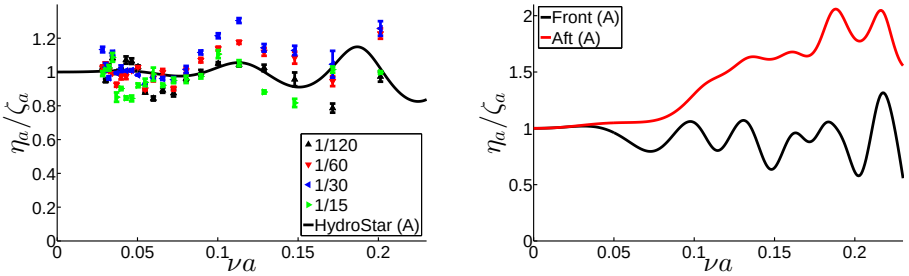

Figure 5.14: Left drawing: Measured and numerically predicted wave amplitude η_a in the center of the inside of the torus. Right drawing: Numerically predicted wave amplitude in the front and aft of the inside of the torus. Linear potential flow theory for the rigid torus without tank wall interference (model A) is used. The height of the experimental error bars is two times the estimated standard deviation. Experiments are for wave steepnesses 1/120, 1/60, 1/30 and 1/15.

5.3 Experimental higher-harmonic torus accelerations in waves of different steepness

Steady-state amplitudes of experimental non-dimensional harmonic acceleration $\ddot{w}_a^{(\omega)}$, second-harmonic acceleration $\ddot{w}_a^{(2\omega)}$, third-harmonic acceleration $\ddot{w}_a^{(3\omega)}$ and fourth-harmonic acceleration $\ddot{w}_a^{(4\omega)}$ along body-fixed z_B-axis versus non-dimensional wave number νa for wave steepnesses 1/120, 1/60, 1/30 and 1/15 for five measured

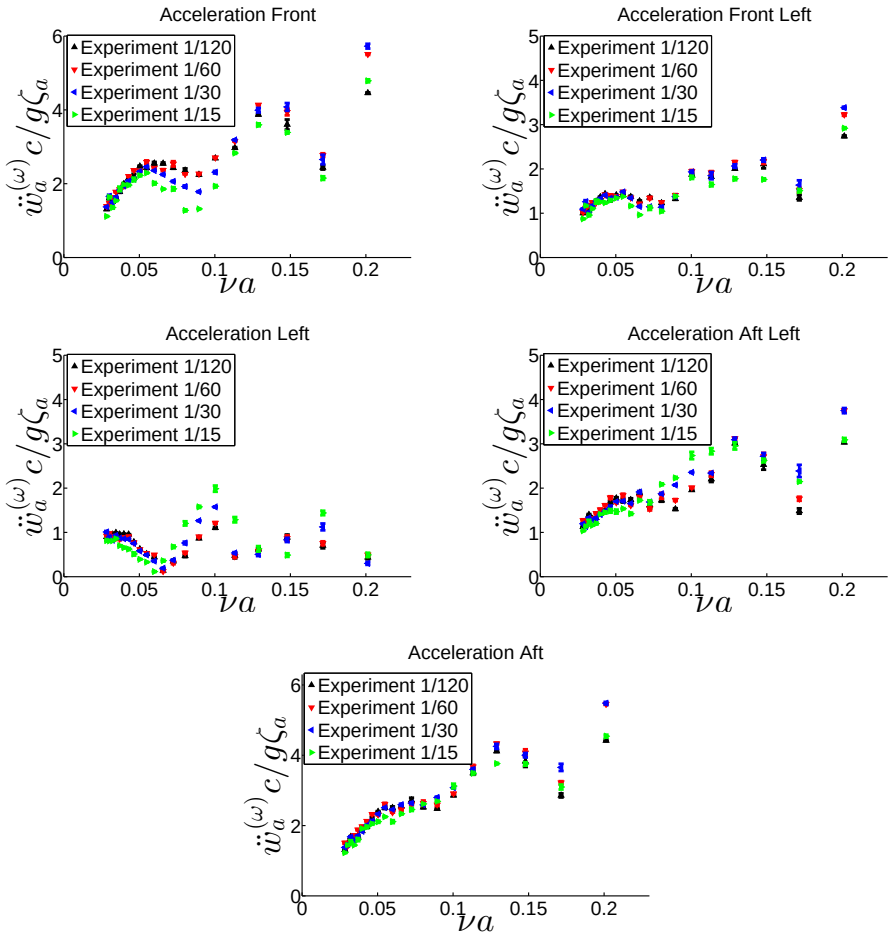

Figure 5.15: Steady-state amplitudes of experimental non-dimensional first-harmonic acceleration $\ddot{w}_a^{(\omega)}$ along body-fixed z_B-axis versus non-dimensional wave number νa for wave steepnesses 1/120, 1/60, 1/30 and 1/15 for five measured positions of the torus in incident regular waves with frequency ω and amplitude ζ_a. The height of the experimental error bars is two times the estimated standard deviation.

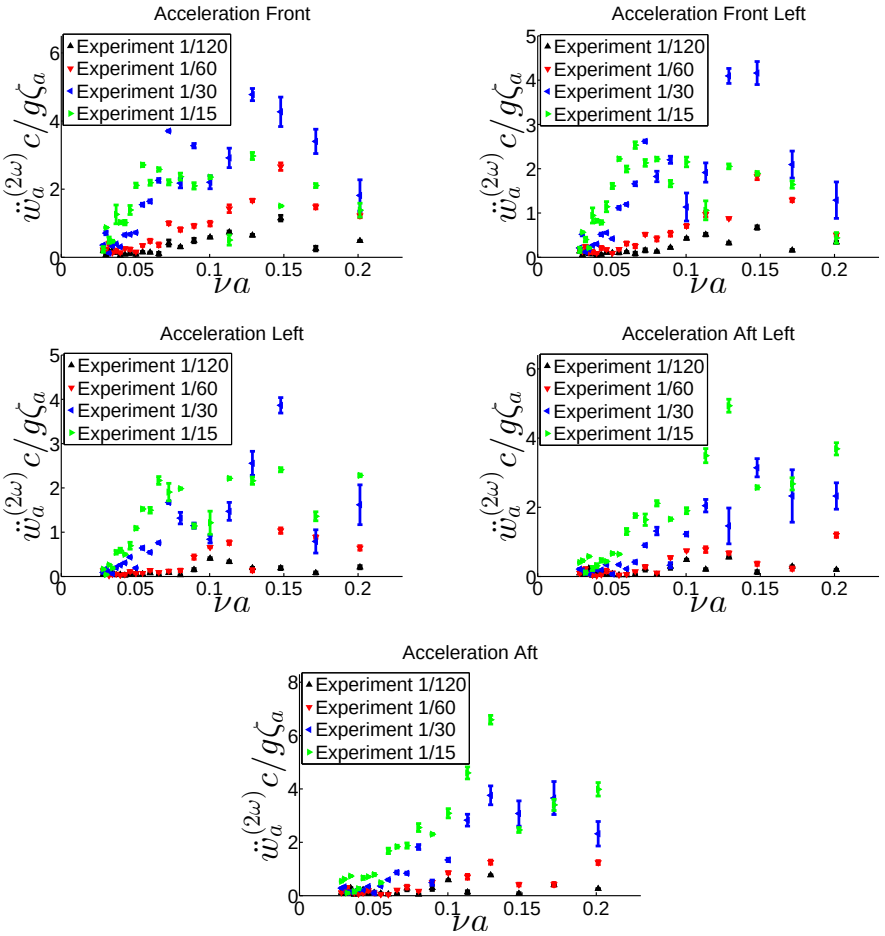

Figure 5.16: Steady-state amplitudes of experimental non-dimensional second-harmonic acceleration $\ddot{w}_a^{(2\omega)}$ along body-fixed z_B-axis versus non-dimensional wave number νa for wave steepnesses 1/120, 1/60, 1/30 and 1/15 for five measured positions of the torus in incident regular waves with frequency ω and amplitude ζ_a. The height of the experimental error bars is two times the estimated standard deviation.

positions of the torus in incident regular waves with frequency ω and amplitude ζ_a have been presented in Figures 5.15 to 5.18. We decided to make the harmonic terms non-dimensional in the same manner in order to compare the magnitudes of the different harmonic terms. The results show significant contributions from all the presented harmonic terms, in particular for larger wave steepnesses. The contributions from higher than fourth-order terms were not significant and are not presented as presented in Figure 4.12.

Since $\ddot{w}_a^{(\omega)}$, $\ddot{w}_a^{(2\omega)}$, $\ddot{w}_a^{(3\omega)}$ and $\ddot{w}_a^{(4\omega)}$ are according to a perturbation method

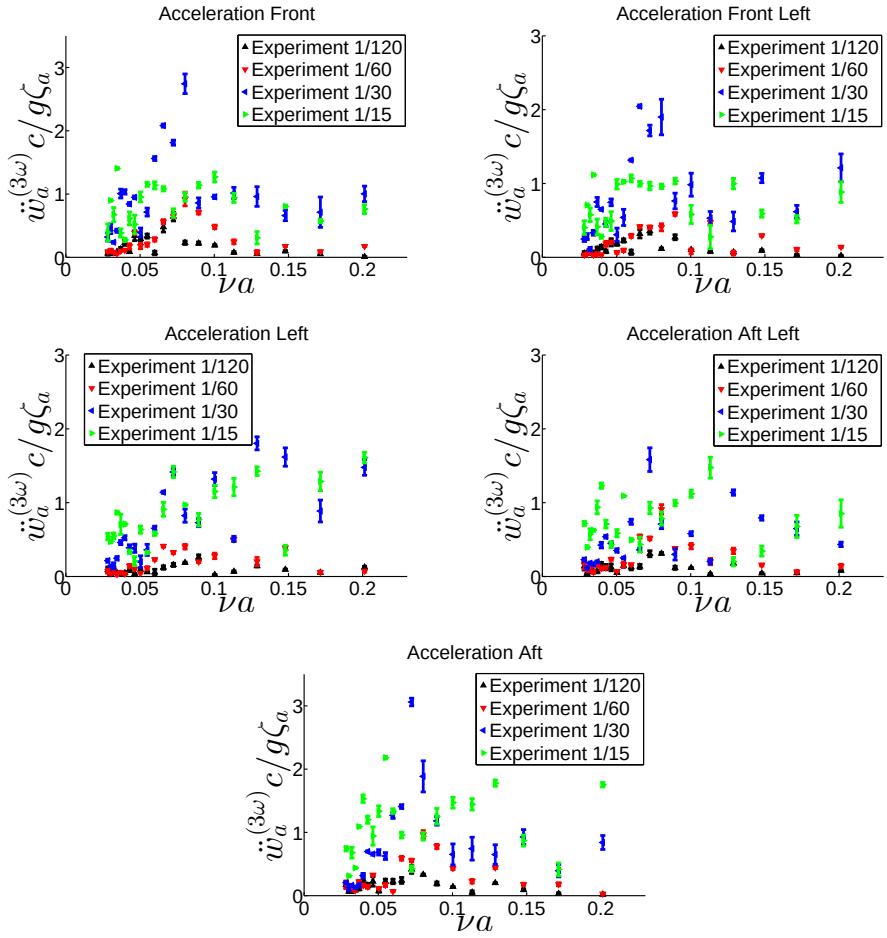

Figure 5.17: Steady-state amplitudes of experimental non-dimensional third-harmonic acceleration $\ddot{w}_a^{(3\omega)}$ along body-fixed z_B-axis versus non-dimensional wave number νa for wave steepnesses 1/120, 1/60, 1/30 and 1/15 for five measured positions of the torus in incident regular waves with frequency ω and amplitude ζ_a. The height of the experimental error bars is two times the estimated standard deviation.

mainly proportional to respectively ζ_a, ζ_a^2, ζ_a^3 and ζ_a^4, $\ddot{w}_a^{(2\omega)}/\zeta_a^2$, $\ddot{w}_a^{(3\omega)}/\zeta_a^3$, $\ddot{w}_a^{(4\omega)}/\zeta_a^4$ along body-fixed z_B-axis versus wave number νa for different wave steepness for five measured positions of the torus have been presented in Figures 5.19 to 5.21. We should note that $\ddot{w}_a^{(4\omega)}/\zeta_a^4$ is very large for high frequencies is because ζ_a is very small. We start by examining $\ddot{w}_a^{(\omega)}/\zeta_a$ in Figure 5.15, which shows that $\ddot{w}_a^{(\omega)}$ is mainly proportional to ζ_a for the different wave steepness $1/120, 1/60, 1/30$ and $1/15$. However, there ought to be a dependence on ζ_a^3 as earlier argued, for

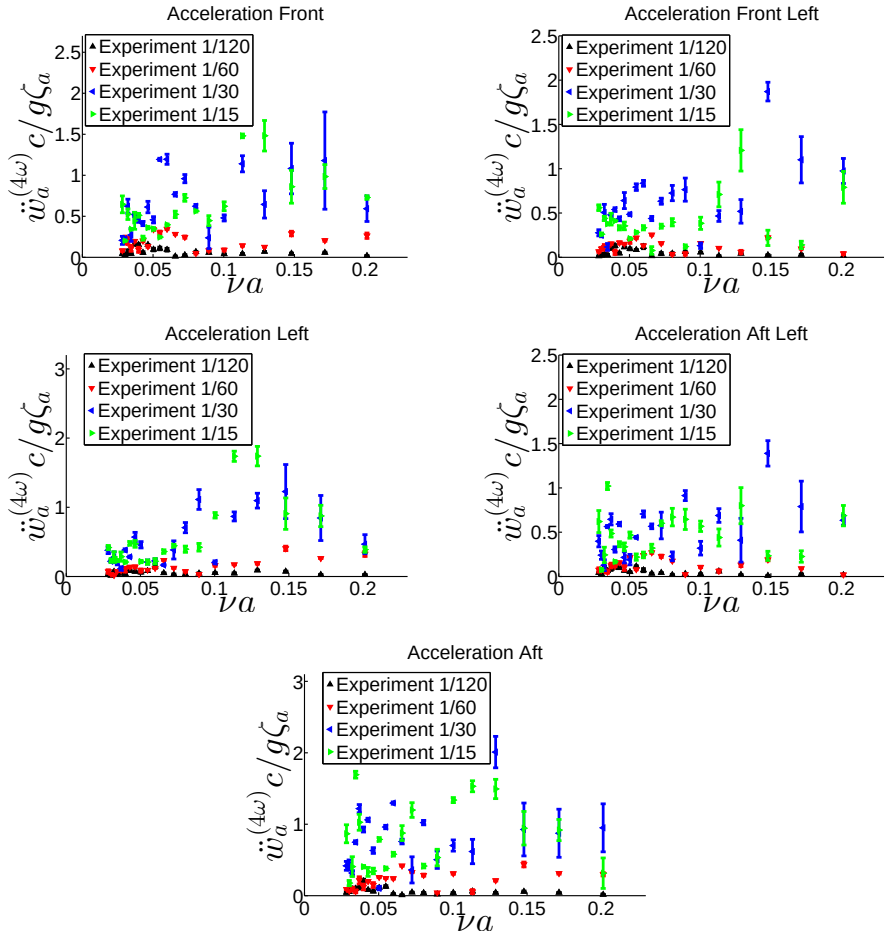

Figure 5.18: Steady-state amplitudes of experimental non-dimensional fourth-harmonic acceleration $\ddot{w}_a^{(4\omega)}$ along body-fixed z_B-axis versus non-dimensional wave number νa for wave steepnesses 1/120, 1/60, 1/30 and 1/15 for five measured positions of the torus in incident regular waves with frequency ω and amplitude ζ_a. The height of the experimental error bars is two times the estimated standard deviation.

instance the term $\cos^3 \omega t = \frac{1}{4}\cos 3\omega t + \frac{3}{4}\cos \omega t$. When it comes to $\ddot{w}_a^{(2\omega)}/\zeta_a^2$ and we disregard the results for the highest wave steepness 1/15, $\ddot{w}_a^{(2\omega)}$ is mainly proportional to ζ_a^2 for the wave steepness $1/120, 1/60$ and 1/30 at the front, front left and aft of the torus (see Figure 5.19). However, there ought to be also a dependence on ζ_a^4 as earlier argued. When it comes to $\ddot{w}_a^{(3\omega)}$ and $\ddot{w}_a^{(4\omega)}$, we cannot say that they are mainly proportional to ζ_a^3 and ζ_a^4, respectively (see Figures 5.20

and 5.21). It means that we cannot explain the behavior of $\ddot{w}_a^{(3\omega)}$ and $\ddot{w}_a^{(4\omega)}$ by a perturbation method with the wave steepness as a small parameter.

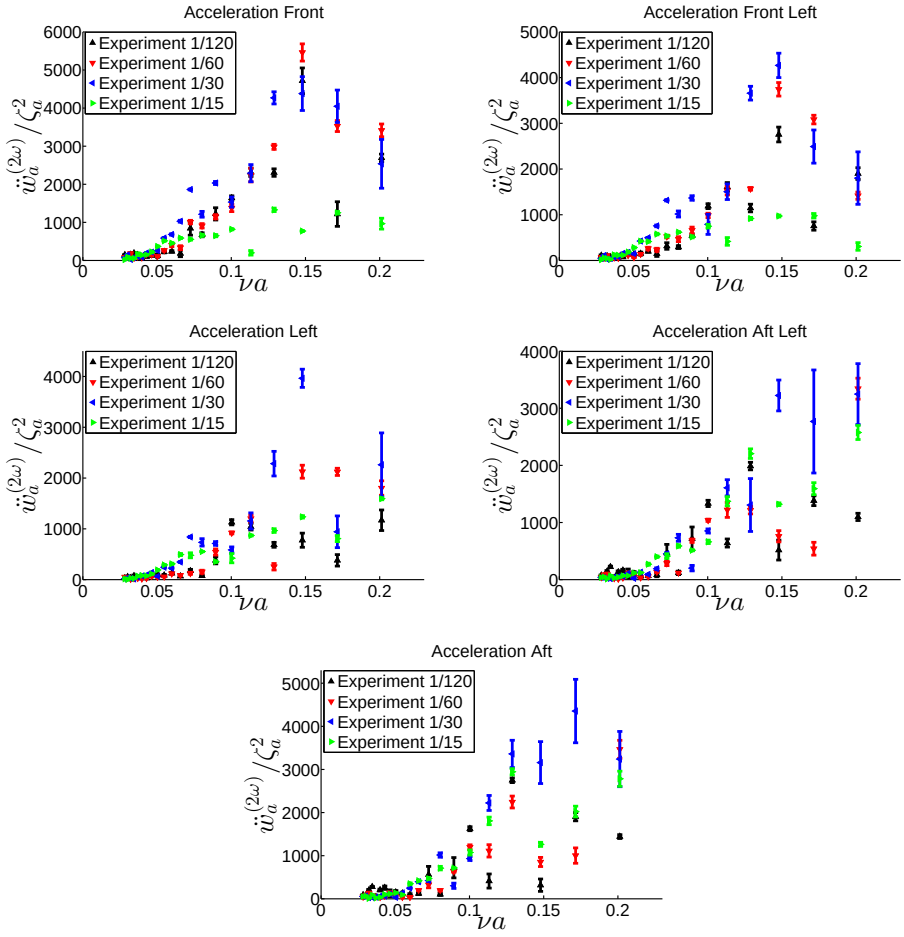

Figure 5.19: Steady-state amplitudes of experimental non-dimensional second-harmonic acceleration $\ddot{w}_a^{(2\omega)}/\zeta_a^2$ along body-fixed z_B-axis versus non-dimensional wave number νa for wave steepnesses 1/120, 1/60, 1/30 and 1/15 for five measured positions of the torus in incident regular waves with frequency ω and amplitude ζ_a. The height of the experimental error bars is two times the estimated standard deviation.

The torus shape above the mean free-surface becomes a factor. Actually, ζ_a/a ought to be considered as a small parameter. However, wave overtopping was observed during the experiments as shown in Figure 4.10. An estimate of occurrence of wave overtopping can be made by means of the vertical Keulegan-Carpenter number $KC_{vert.} = \pi\eta_{rel.vert.}/a$ presented in Figure 5.8 for different frequencies

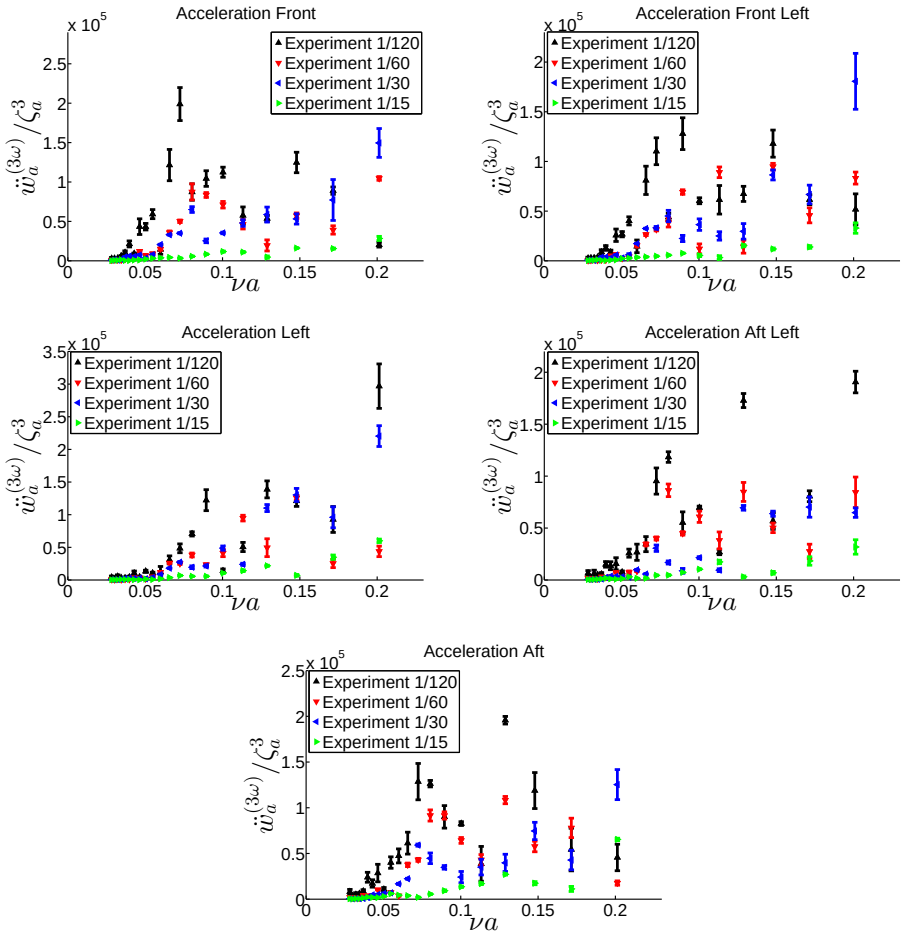

Figure 5.20: Steady-state amplitudes of experimental non-dimensional third-harmonic acceleration $\ddot{w}_a^{(3\omega)}/\zeta_a^3$ along body-fixed z_B-axis versus non-dimensional wave number νa for wave steepnesses 1/120, 1/60, 1/30 and 1/15 for five measured positions of the torus in incident regular waves with frequency ω and amplitude ζ_a. The height of the experimental error bars is two times the estimated standard deviation.

and torus positions and wave steepness $H/\lambda = 1/120$. We consider as an example $\pi\eta_{rel.vert.}/a = 1.5$ from Figure 5.8, which means that wave overtopping occurs for $H/\lambda > 1.4/120$. However, the latter estimate does not account for nonlinearities and local free-surface effects at the torus. An attempt was made to follow a common engineering approach in seakeeping analysis of ships by calculating correctly non-linear Froude-Kriloff forces and unsteady hydrostatic forces in nonlinear incident waves together with linear hydrodynamic forces. However, we could not explain

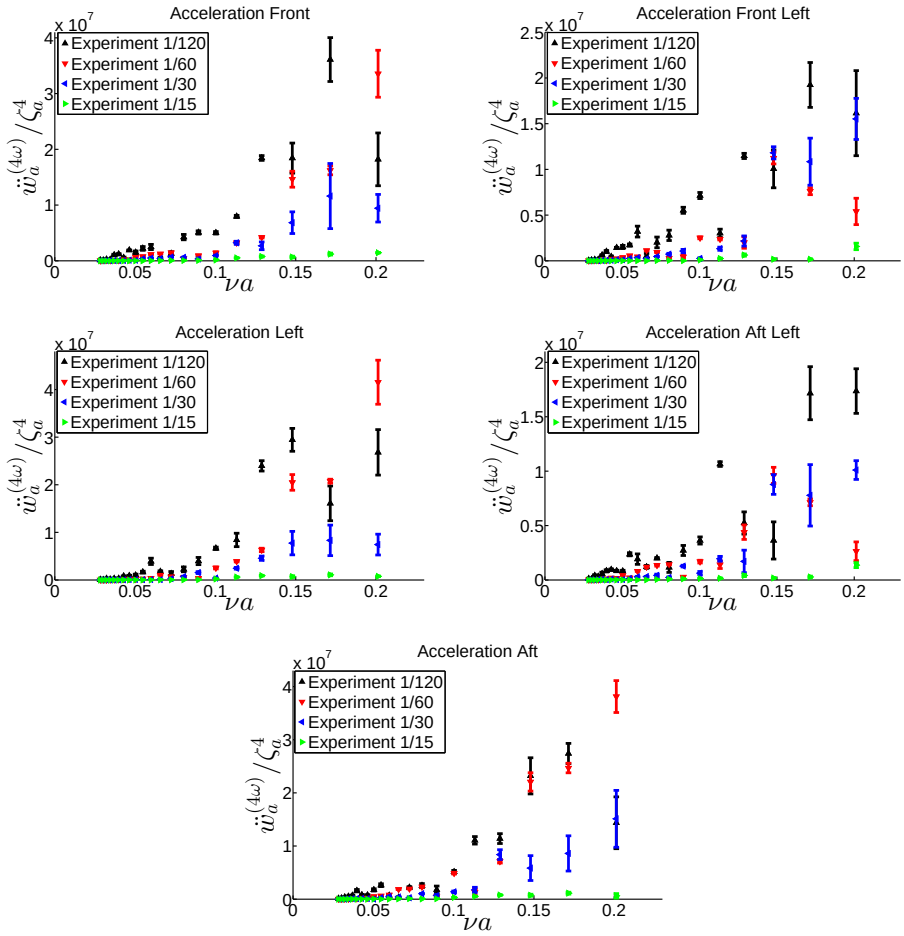

Figure 5.21: Steady-state amplitudes of experimental non-dimensional fourth-harmonic acceleration $\ddot{w}_a^{(4\omega)}/\zeta_a^4$ along body-fixed z_B-axis versus non-dimensional wave number νa for wave steepnesses 1/120, 1/60, 1/30 and 1/15 for five measured positions of the torus in incident regular waves with frequency ω and amplitude ζ_a. The height of the experimental error bars is two times the estimated standard deviation.

the experimental results by following such an approach. The fact that part of the torus may go out of the water in cases with overtopping is also illustrated in Figure 4.10 together with a photo from a torus of a full scale fish farm without net in a storm illustrating that the same phenomena occur in real life (see Figure 4.11).

5.4 Summary

Longitudinal motions deduced from the measured mooring line forces and vertical accelerations of a nearly rigid torus model in regular waves have been studied based on model tests from 2013. The experimental results are compared with numerical results computed by HydroStar. Reasonable agreements are obtained for longitudinal motions and first-harmonic component of vertical accelerations but not perfect agreement of second-harmonic component. Hydroelasticity is one reason of the differences in the first and second harmonics response. Further, it was found that higher order wave-body interaction effects cannot be neglected. Numerical errors due to viscous effects are found to be secondary. The experimental and numerical results show that resonant wave motion does not occur inside the torus. The experimental results for different wave steepness in steady-state conditions show that first, second, third and fourth harmonics vertical acceleration of the torus matter. A perturbation method is only practical for first-order and second-order problems and cannot explain the third and fourth harmonics response with the wave steepness as a small parameter. A fully nonlinear 3D CFD method that accounts for hydroelasticity to compare with the experiments may be needed and requires future studies.

Chapter 6

A study of a floating elastic torus in regular waves

In this chapter results from numerical simulations and experiments of an elastic circular collar of a floating fish farm in regular waves are presented. The focus is on the vertical accelerations along the torus as a function of wave frequency and steepness. For the examined problem, hydroelasticity matters due to the relatively small flexural rigidity of the torus and resonances are possible due to high-order wave load excitation.

Our study on wave-induced vertical accelerations of the elastic torus-shaped floater of a fish farm has resulted in one publication (Li et al., 2014).

6.1 Theoretical methods

In order to perform numerical simulations of the floating elastic torus subject to regular waves as in the experiments from 2013, two solution strategies based on potential-flow theory are used to predict the wave-torus interaction problem. We applied in Chapter 5 the second-order numerical results for a rigid body based on consistent potential-flow theory. We have not available such a method for an elastic body. One applied method is the low-frequency slender-body theory (see Chapter 2), which considers only the linear frequency-domain effects. A difference from the present linear frequency-domain theoretical calculation is that Li et al. (2014) did not include the curvature effect on the bending stiffness. However, the latter effect is small for the studied elastic torus. The other method generalizes the weak-scatter method (Greco and Lugni, 2012) with original theory due to Pawlowski (1991). The computer program was developed by Marilena Greco. The weak-scatterer hypothesis assumes that the amplitudes of the incident waves and body motions are large relative to wave amplitudes due to scattering and radiation effects. The equations of motions are formulated in a body-fixed reference frame $Ox_By_Bz_B$ and nonlinear Froude-Kriloff and hydrostatic restoring loads are included. The nonlinearities are kept up to the second order. Elastic

torus motions are accounted for in the low-frequency slender-body theory as well as weak-scatter method. As in the model tests and the linear frequency-domain method, the weak-scatter method assumes no current either.

The incident regular waves propagate along the x-axis and are described by a second-order Stokes theory in deep water. For sinusoidal unidirectional progressive deep water waves, the wave elevation is expressed as (Faltinsen, 1990):

$$\zeta = \zeta_a \sin(\omega t - \nu x) - 0.5\zeta_a^2 \nu \cos[2(\omega t - \nu x)] \tag{6.1}$$

where ζ_a is the first-order wave amplitude. When the torus is at rest in calm water, the torus is semi-submerged. The equations of rigid-body motions of the torus follow from Newton's second law (Faltinsen, 2005), which is heave, pitch and surge motions in our studies. The external loads in the equations of rigid-body motions are due to the mooring, nonlinear Froude-Kriloff and hydrostatic loads as well as hydrodynamic loads associated with flow caused by the torus velocity and scattering of the incident waves. The hydrodynamic loads are consistent within linear theory but include nonlinear effects due to satisfaction of the body-boundary conditions.

The flexible vertical (w) torus motion is described by Eq. (2.10) but do not include the bending stiffness term $\frac{EI}{c^2}\frac{\partial^2 w}{\partial s^2}$, which is a consequence of curvature. The flexible lateral (radial, v_r) torus motion is described by the following modified beam equations with tension and curvature effects:

$$\begin{aligned} &m\frac{\partial^2 v_r}{\partial t^2} + EI\frac{\partial^4 v_r}{\partial s^4} + \frac{EI}{c^2}\frac{\partial^2 v_r}{\partial s^2} - \frac{\partial}{\partial s}\left(T_{as}\frac{\partial v_r}{\partial s}\right) \\ &= f_r^{\text{FK}+\text{hydrostatic}} + f_r^{\text{hydrodynamic}} + f_r^{\text{str.}+\text{mooring}} \end{aligned} \tag{6.2}$$

Here $f_r^{\text{FK}+\text{hydrostatic}}$ is the radial nonlinear Froude-Kriloff and hydrostatic forces per unit length and $f_r^{\text{hydrodynamic}}$ is the radial hydrodynamic force per unit length due to the torus velocity and scattering of the incident waves. Further, $f_r^{\text{str.}+\text{mooring}}$ describes the effect of structural damping and mooring. The flexible vertical motion is expressed as Eq. (2.11) and starts with $n = 2$. The flexible radial motion is expressed as:

$$v_r = \sum_{n=2}^{\infty} b_n(t)\cos(n\beta) \tag{6.3}$$

here b_2 represents the first lateral elastic mode. The weak-scatter method follows a similar procedure as linear frequency-domain method in re-expressing the vertical and radial modified beam equations for the flexible modes by multiplying the equations with $\cos(m\beta)$ and integrating from 0 to 2π. This leads to an equation system for the unknowns a_n and b_n.

The nonlinear Froude-Kriloff and hydrostatic loads involve pressure integration on the instantaneous wetted surface. The latter is found by approximating the free-surface elevation at the torus as the incident wave elevation as shown in Figure 6.1. The effect of rigid-body and elastic torus motions is considered. Both overtopping and dry cross-sections may occur due to large relative vertical torus

motion. The difference between the water pressure and the atmospheric pressure on the instantaneous position of the torus is $-\rho g z + p_1$ with

$$p_1 = \begin{cases} -\rho \dfrac{\partial \varphi_0}{\partial t} - \dfrac{\rho}{2} \left| \nabla \varphi_0 \right|^2, & z \leq 0 \\ -\rho \dfrac{\partial \varphi_0}{\partial t}, & z > 0 \end{cases} \tag{6.4}$$

Here φ_0 is the incident wave potential.

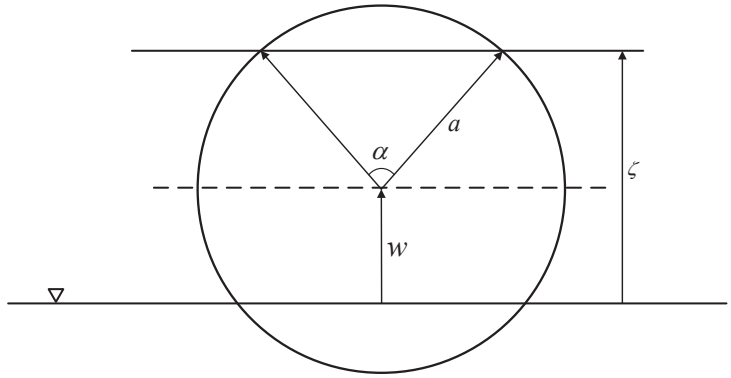

Figure 6.1: Definitions related to calculations of submerged cross-sectional area of a circular section. ζ is wave elevation, w is vertical displacement, a is the radius of circular section and α is the sector angle of dry surface.

The rest of the hydrodynamic loads are partly linearized in the time domain and represented in terms of convolution integrals (Cummins, 1962). A correction of the linear scattering and radiation loads is obtained by satisfying averagely in time the impermeability condition along the instantaneous wetted torus surface defined by the incident waves and the torus motions. The frequency-domain added mass and damping coefficients needed in calculating the retardation functions follow by satisfying the body-boundary conditions on the mean oscillatory position and properly integrating linear hydrodynamic pressure. The linear potential-flow frequency-domain panel code WAMIT was used for both flexible and rigid-body modes.

The effect of mooring on $f_3^{\text{str.}+\text{mooring}}$ is small and neglected. Since the structural damping associated with the different flexible modes is unknown, the following strategy was tried out. A damping of the form $[q_1 + \triangle q \cdot (j-1)]\, B_{cr,j}$, is assumed for each vertical and radial flexible mode j, with $B_{cr,j}$ the corresponding critical damping, $q_1 = 0.05$ and $\triangle q = 0.01$. With this formula a structural damping equal to the 5% of the critical damping is used for the first flexible vertical/radial mode and increased with a step of 1% with the number of mode. This arbitrary choice is qualitatively reasonable since it is expected a greater effect of the structural damping in limiting the higher modes. The comparison with a similar formula using

$q_1 = 0.01$ gave very close results for the longer incident-wave cases while indicated higher-mode amplitudes much larger than observed in the physical case. Since the experiments are performed with horizontal mooring lines, a restoring is caused for the surge, sway and radial elastic modes. Using free-decay tests in surge with only the two mooring lines in x-direction, the restoring and damping for surge and sway (due to the symmetry of the body and of the mooring lines set-up) were obtained (see Figure 4.3). In this way viscous-damping corrections were included in the simulations.

Both linear frequency-domain method and weak-scatter method include the tension effect. T_{as} is assumed constant and equal to $T_{as}^{(i)}$ between each mooring line as illustrated in Figure 4.3. The values of $T_{as}^{(i)}$ used in the presented case studies are $\left[T_{as}^{(1,3,5,7)}, T_{as}^{(2,4,6,8)}\right] = [0.4108, 0.7071] \times T_p$, where T_p is the pre-tension of the mooring lines.

The weak-scatter equations are solved numerically in time using a fourth-order Runge-Kutta scheme. Convergence of the weak-scatter results has been checked in terms of spatial body discretization, time step and number of modes. The discretization of the geometry must ensure that the variation of forces between the discrete points on the torus give good approximation of the actual forces since the wave elevation and torus motion are spatial dependent. The time steps in the analysis need to be sufficiently small in order to get convergence and reliable results. However, many discrete points on the torus and very small time increments will result in a long computational time. It was found that 24 panels along the cross-sectional diameter and 988 panels along the global diameter of the torus were suitable to have nearly converged results. $\Delta t = 0.0025T$, with T the incident wave period, was confirmed to be a suitable time step. Ten vertical and ten radial flexible modes have been considered. Additional modes would have demanded increased accuracy in the spatial discretization. The resulting weak-scatter solver is quite efficient if compared with more general fully-nonlinear potential-flow methods since it requires in the time integration only the discretization of the instantaneous wetted body surface, the estimation of nonlinear Froude-Kriloff and hydostatic loads and the satisfaction of the nonlinear body-boundary condition in the hydrodynamic problem.

An investigation of retardation functions show that if rigid motions dominate the torus response, steady-state conditions would be reached quickly in time. Things are different for the first vertical and radial elastic modes. In this case the memory effects are of similar importance along the time axis, suggesting that steady-state conditions require longer time to be reached when these modes are important for the torus response. This behaviour of the retardation functions is very special and probably connected with the ring shape of the elastic body and the very complicated frequency dependency for added-mass and damping coefficients with several peaks and troughs, and occurrence of negative added mass and almost zero damping.

The weak-scatter method was applied to the cases with smallest, intermediate and largest incident-wave periods, *i.e.* $T = 0.6s$, $1.05s$ and $1.6s$. For longer incident waves rigid motions tend to dominate the torus response, so we can expect that

steady-state conditions are reached sooner than for shorter waves. The numerics indicates that they are reached after $20T$ for the longest wave while the experiments show important variation between the measurements done after $20T$ and those made after $50T$. For $T = 1.05s$, steady-state conditions are nearly reached numerically and experimentally after $50T$, while both of them indicate a difficulty in reaching steady-state conditions for the shortest wave even after $100T$. This is consistent with the fact that in this case rigid motions are comparable with the elastic motions and can interact with them, so memory effects need longer times to die out. Each case is simulated $80T$ in our studies.

6.2 First-harmonic torus accelerations in waves of different steepness

We will separately compare the frequency-domain experimental results with the linear and weak-scatter theoretical methods. It is referred to Chapters 4 and 5 for an extensive discussion of experimental error sources. Figure 6.2 compares amplitudes of experimental and linear theoretical predictions of the first harmonics of vertical accelerations along the torus as a function of nondimensional wave number νa and wave steepness. Twenty modes are used. Increasing number of modes has a negligible effect. Experimental error bars defined as two times the standard deviation are presented in the figure. The experimental mean value and total standard deviation are defined as μ and $\sigma = \sqrt{\sigma_{ea}^2 + \sigma_{re}^2}$, respectively, where σ_{ea} is the standard deviation of each case due to the time-dependent amplitude variation and σ_{re} is the standard deviation due to repeating the tests three or four times for each wave condition. Relative error σ/μ caused by repetition was less than 0.01. Thus, the obtained time series showed good repeatability and we use $\sigma \approx \sigma_{ea}$ for all the presented results.

The time series of the experimental accelerations obtained by filtering out higher harmonics than ω was previously shown in Figure 4.9 when $H/\lambda = 1/30$ and $\nu a = 0.2125$. It has been described in Section 4.3 that there are two strategies to calculate the mean values μ and standard deviations σ_{re}. The more accurate sliding DFT technique is used here. The maximum relative error is respectively 3.2%, 5.76%, 10.65%, 9.28% and 2.32% from front to aft at five positions on the torus by examining all the test cases. However, there is in general a small relative error, which means the standard deviation σ_{ea} of each case is very small for first harmonics of vertical accelerations. This can be understood as the time-dependent amplitude variation is very small. The reason why the experimental results are not steady state have been explained in Section 5.2.

The low-frequency slender-body theory agrees, in general, satisfactorily with experiments at the front, front left and aft positions. An error source is that the accelerometer is body-fixed and can only measure the acceleration in normal direction while the theories predict vertical accelerations. However, theoretical estimates of the latter effect showed a negligible error. There are clear differences for the other positions when $\nu a \gtrapprox 0.0848$. We note, for instance, a large relative error on the left part of the torus at $\nu a = 0.181$. Wave lengths of practical interest are

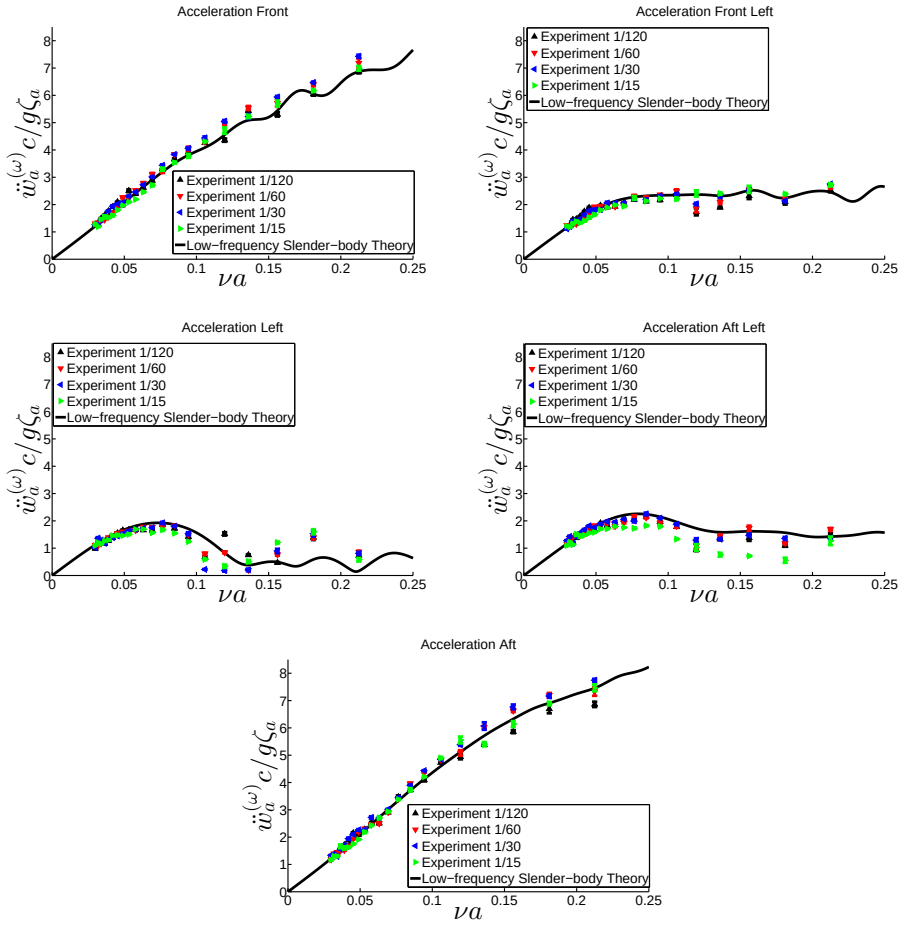

Figure 6.2: Steady-state amplitudes of experimental and numerical non-dimensional first-harmonic acceleration $\ddot{w}_a^{(\omega)}$ along body-fixed z_B-axis versus non-dimensional wave number νa for wave steepnesses 1/120, 1/60, 1/30 and 1/15 for five measured positions of the torus in incident regular waves with frequency ω and amplitude ζ_a. The height of the experimental error bars is two times the estimated standard deviation.

of the order of the torus diameter but long relative to the cross-sectional diameter. The wave length is $1.128m$ corresponding to $T = 0.85s$ and $\nu a = 0.1059$. This means that low-frequency slender-body theory can not give a very good prediction for $\nu a > 0.1$.

The weak scatter results of the amplitude of the first harmonics of vertical accelerations at the front, left and aft of the torus presented in Li et al. (2014) are compared in Table 6.1 with experiments and the low-frequency slender-body theory for $\nu a = 0.0299$, 0.0694, 0.2125 and different wave steepnesses. Ten vertical

and ten radial flexible modes have been considered by weak-scatter method here. The linear results shown in Table 6.1 for $\nu a = 0.0694$ at the front position and $\nu a = 0.2125$ at the front and left positions of torus are smaller compared with the same νa and positions results presented in Li et al. (2014). The other linear results shown in Table 6.1 are larger than Li et al. (2014)'s results. The reason to this difference is that the bending stiffness term $\frac{EI}{c^2}\frac{\partial^2 w}{\partial s^2}$ as a consequence of curvature effect of the torus is included in Eq. (2.10). However, the differences are small. It should be noted that the experimental mean values μ and standard deviations σ between Table 6.1 and Li et al. (2014) are different as well. The reason to this difference is that the experimental results presented in Li et al. (2014) were obtained by the envelope curve method described in Section 4.3 while the more accurate sliding DFT technique is applied in our present study. However, the differences are negligible.

The weak-scatter method agrees well with the experiments under the same wave conditions except for the results at the left position when $\nu a = 0.2125$. However, the acceleration level is small relative to the values at the front and aft position of torus. In general, the weak-scatter method tends to underestimate the experimental first-harmonic accelerations under the same wave conditions. The underestimation does not seem to be connected with the use of a too large structural damping for the elastic modes. The weak-scatter results with two different structural damping strategies are identical for the two lower frequencies cases, as expected since the torus responses in these two cases are dominated by the rigid motions. Moreover the reduction of the damping does not improve the agreement with the experiments for the highest frequency case.

Table 6.1: Experimental, weak-scatter and linear theory values of $\ddot{w}_a^{(\omega)} c/g\zeta_a$ for three non-dimensional wave numbers νa and wave steepnesses $H/\lambda = 1/120$, $1/60$, $1/30$ and $1/15$. $\ddot{w}_a^{(\omega)}$ is the amplitude of the first harmonics of vertical accelerations, c is the radius of the torus, g is the acceleration of gravity and ζ_a is the amplitude of incident wave. Furthermore, μ and σ are the experimental mean value and standard deviation, respectively.

νa	H/λ	Front				Left				Aft			
		Exp. μ	Exp. σ	Weak Scatter	Linear	Exp. μ	Exp. σ	Weak Scatter	Linear	Exp. μ	Exp. σ	Weak Scatter	Linear
0.0299	1/120	1.256	0.009	1.238	1.214	0.987	0.026	1.100	1.124	1.245	0.011	1.232	1.216
	1/60	1.304	0.021	1.224		1.116	0.001	1.089		1.181	0.013	1.218	
	1/30	1.262	0.009	1.194		1.018	0.003	1.062		1.337	0.009	1.186	
	1/15	1.287	0.016	1.148		1.094	0.008	0.903		1.170	0.023	1.094	
0.0694	1/120	2.880	0.040	2.846	2.904	1.649	0.030	1.735	1.920	2.908	0.015	2.905	3.006
	1/60	3.109	0.050	2.838		1.771	0.032	1.722		2.916	0.027	2.902	
	1/30	3.014	0.013	2.781		1.750	0.021	1.683		3.020	0.016	2.851	
	1/15	2.710	0.043	2.588		1.563	0.006	1.114		2.934	0.026	2.833	
0.2125	1/120	6.860	0.056	6.716	6.878	0.732	0.057	0.323	0.184	6.860	0.096	7.328	7.471
	1/60	7.187	0.163	6.713		0.853	0.058	0.327		7.332	0.156	7.325	
	1/30	7.432	0.056	6.686		0.812	0.049	0.338		7.745	0.052	7.293	
	1/15	6.990	0.087	6.663		0.578	0.061	0.502		7.466	0.125	7.281	

6.3 Experimental higher-harmonic torus accelerations in waves of different steepness

The steady-state amplitude of the second harmonics of vertical accelerations from experiments and by the weak-scatter method are compared in Table 6.2 for the same positions and the same νa as in Table 6.1. Similar like Table 6.1, sliding DFT technique is applied in our present study, which leads to the experimental mean values μ and standard deviations σ have small difference with the results presented in Li et al. (2014). The maximum relative experimental error is respectively 20.4%, 35.41%, 40.36%, 39.87% and 31.4% from front to aft at five positions on the torus by examining all the test cases. As discussed already, relative error caused by repetition was negligible. Thus, the main contribution comes from the time variation of measured amplitude of vertical acceleration. The experimental error is the same order of magnitude as for the amplitude of the second harmonics of the accelerations for some cases.

The weak-scatter method has a reasonable agreement with experiments for wave steepness 1/120 and in some cases for wave steepnesses 1/60 and 1/30. Similar as the analysis of the first harmonics of vertical accelerations, the acceleration level at the left position is small relative to values at the front and aft positions. The differences are larger for the highest wave steepness 1/15, $\nu a = 0.0299$ at the front position for wave steepness 1/30 and $\nu a = 0.0694$ and 0.2125 at the aft position for wave steepnesses 1/60 and 1/30. A reason in the latter case can be flow separation. Kristiansen and Faltinsen (2009) demonstrated by the CIP method that flow separation occurs during overtopping of waves on a semi-submerged circular cross-section. The method of nonlinear Froude-Kriloff and restoring forces does not consider the effect of flow separation.

When linear effects dominate, the two considered potential-flow methods are rational. However, the calculated effect of axial tension on flexible modes are approximated by using constant tension between each mooring-line attachment points. When nonlinear Froude-Kriloff and hydrostatic loads dominate, the weak-scatter method is partially reasonable. An error source is that the local free-surface elevation influenced by the flow caused by torus velocities and scattering has not been used in finding the wetted surface. The semi-submerged torus surface is not vertical in the free-surface zone, therefore, it is impossible with the considered method to find the local free-surface elevation. Since higher-order harmonics of wave loads can cause resonant excitation of flexible modes, structural damping may matter at this stage. We do not know what the structural damping was for the different modes of the tested model and, therefore, what the error due to structural damping was in the weak-scatter method.

Table 6.2: Experimental and weak-scatter values of $\ddot{w}_a^{(2\omega)} c/g\zeta_a$ for three non-dimensional wave numbers νa and wave steepnesses $H/\lambda = 1/120$, $1/60$, $1/30$ and $1/15$. $\ddot{w}_a^{(2\omega)}$ is the amplitude of the second harmonics of vertical accelerations, c is the radius of the torus, g is the acceleration of gravity and ζ_a is the amplitude of incident wave. Furthermore, μ and σ are the experimental mean value and standard deviation, respectively.

νa	H/λ	Front			Left			Aft		
		Exp. μ	Exp. σ	Weak Scatter	Exp. μ	Exp. σ	Weak Scatter	Exp. μ	Exp. σ	Weak Scatter
0.0299	1/120	0.091	0.013	0.070	0.078	0.016	0.013	0.144	0.020	0.065
	1/60	0.184	0.014	0.130	0.078	0.026	0.044	0.186	0.023	0.124
	1/30	0.773	0.004	0.220	0.092	0.006	0.093	0.443	0.015	0.237
	1/15	0.825	0.016	0.296	0.263	0.011	0.217	0.716	0.048	0.324
0.0694	1/120	0.137	0.017	0.175	0.028	0.005	0.051	0.121	0.038	0.186
	1/60	0.223	0.032	0.333	0.027	0.009	0.102	0.094	0.007	0.352
	1/30	0.420	0.021	0.501	0.072	0.017	0.198	0.140	0.007	0.511
	1/15	0.805	0.088	1.396	0.974	0.041	0.553	0.691	0.045	1.207
0.2125	1/120	0.565	0.048	0.474	0.166	0.067	0.300	0.509	0.058	0.497
	1/60	1.303	0.253	1.016	0.977	0.093	0.683	2.082	0.082	1.045
	1/30	2.622	0.203	2.305	1.278	0.219	1.731	5.888	0.472	2.267
	1/15	4.234	0.400	1.933	2.233	0.350	4.044	5.418	0.370	1.397

As have been analyzed for experimental higher-harmonic accelerations of the nearly rigid torus model in Section 5.3, two non-dimensional strategies are applied in analyzing the experimental higher-harmonic accelerations of the elastic torus model. One method is to make the harmonic terms non-dimensional in the same manner as shown in Figure 6.2 in order to compare the magnitudes of the different harmonic terms. Another method is based on a perturbation method. Therefore, $\ddot{w}_a^{(\omega)}$, $\ddot{w}_a^{(2\omega)}$, $\ddot{w}_a^{(3\omega)}$ and $\ddot{w}_a^{(4\omega)}$ should be mainly proportional to ζ_a, ζ_a^2, ζ_a^3 and ζ_a^4, respectively.

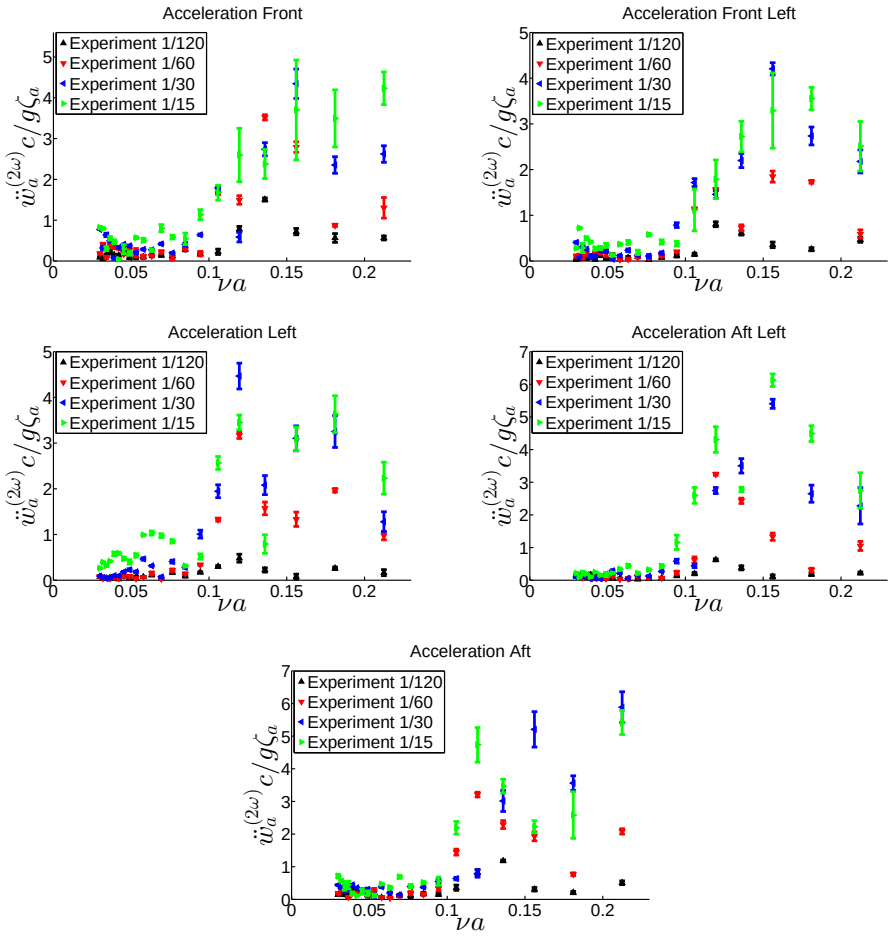

Figure 6.3: Steady-state amplitudes of experimental non-dimensional second-harmonic acceleration $\ddot{w}_a^{(2\omega)}$ along body-fixed z_B-axis versus non-dimensional wave number νa for wave steepnesses 1/120, 1/60, 1/30 and 1/15 for five measured positions of the torus in incident regular waves with frequency ω and amplitude ζ_a. The height of the experimental error bars is two times the estimated standard deviation.

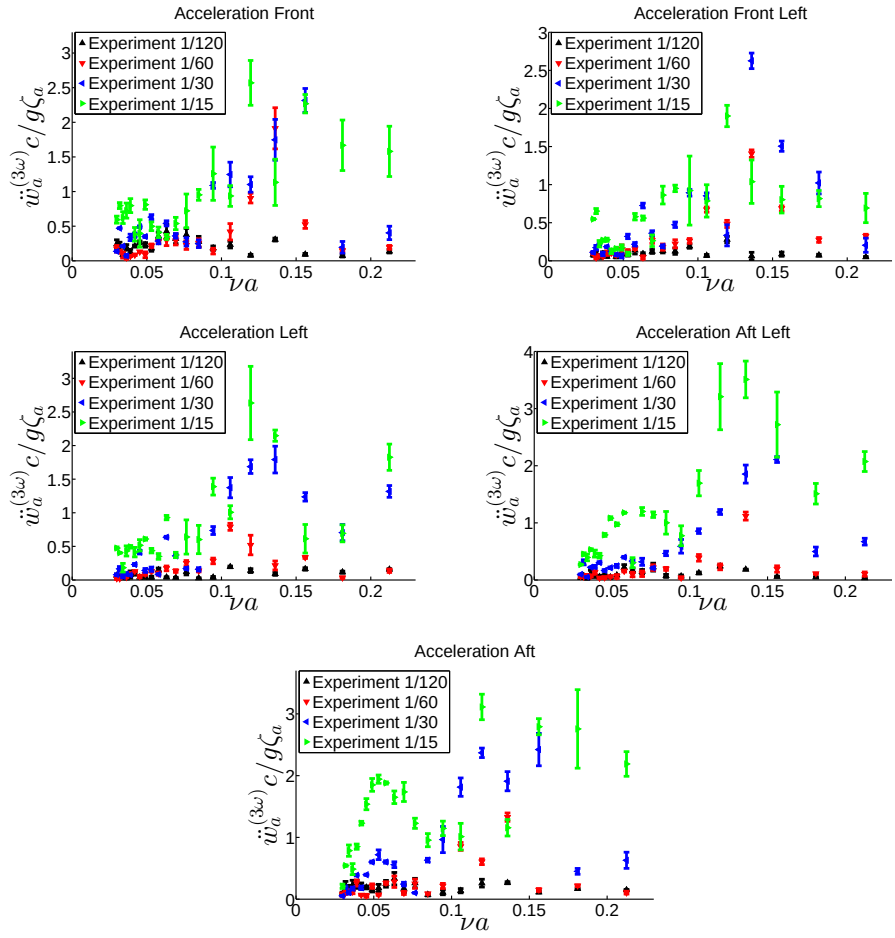

Figure 6.4: Steady-state amplitudes of experimental non-dimensional third-harmonic acceleration $\ddot{w}_a^{(3\omega)}$ along body-fixed z_B-axis versus non-dimensional wave number νa for wave steepnesses 1/120, 1/60, 1/30 and 1/15 for five measured positions of the torus in incident regular waves with frequency ω and amplitude ζ_a. The height of the experimental error bars is two times the estimated standard deviation.

Steady-state amplitudes of experimental non-dimensional second-harmonic acceleration $\ddot{w}_a^{(2\omega)}$, third-harmonic acceleration $\ddot{w}_a^{(3\omega)}$ and fourth-harmonic acceleration $\ddot{w}_a^{(4\omega)}$ along body-fixed z_B-axis versus non-dimensional wave number νa for wave steepnesses 1/120, 1/60, 1/30 and 1/15 for five measured positions of the torus in incident regular waves with frequency ω and amplitude ζ_a have been presented in Figures 6.3 to 6.5. It can be found that all the presented harmonic terms have significant contributions compared with the first harmonic part presented in Figure 6.2, in particular for larger wave steepness for instance 1/30 and

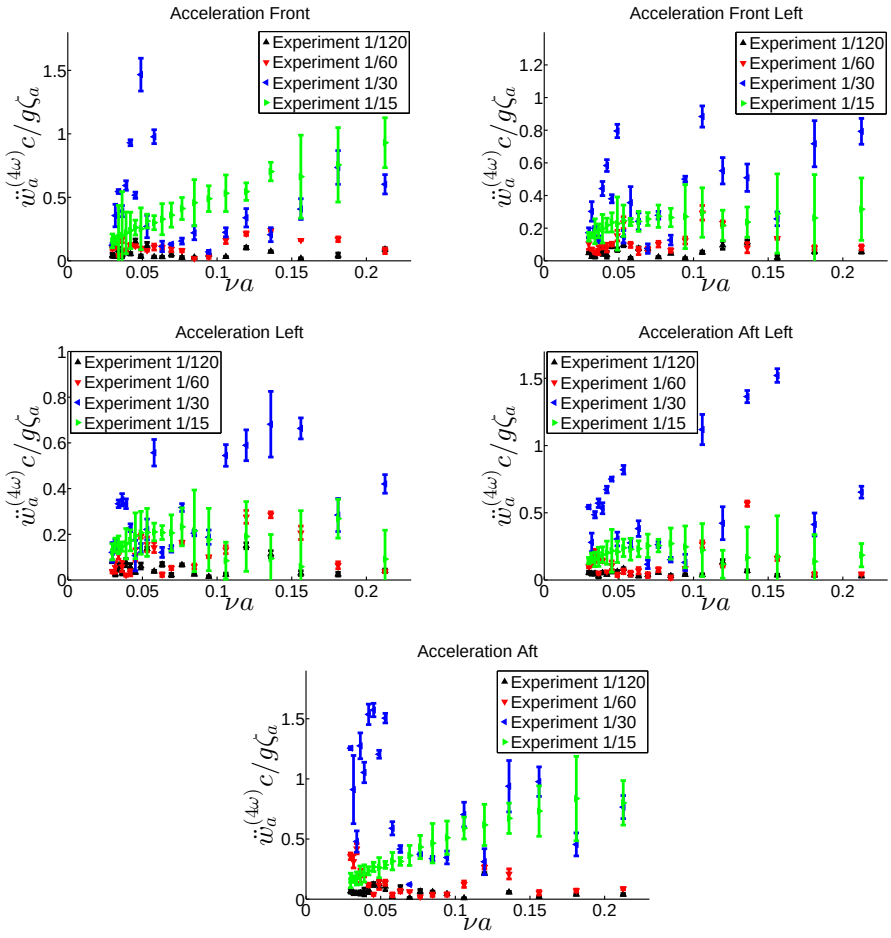

Figure 6.5: Steady-state amplitudes of experimental non-dimensional fourth-harmonic acceleration $\ddot{w}_a^{(4\omega)}$ along body-fixed z_B-axis versus non-dimensional wave number νa for wave steepnesses 1/120, 1/60, 1/30 and 1/15 for five measured positions of the torus in incident regular waves with frequency ω and amplitude ζ_a. The height of the experimental error bars is two times the estimated standard deviation.

1/15. The magnitude of higher than fourth-harmonic acceleration were small as presented in Figure 4.12 and are not presented. Predicted values of the amplitude of the third and fourth harmonics of accelerations by the weak-scatter method for different wave steepnesses were very low relative to the experimental results shown in Figures 6.4 and 6.5.

We have presented $\ddot{w}_a^{(2\omega)}/\zeta_a^2$, $\ddot{w}_a^{(3\omega)}/\zeta_a^3$, $\ddot{w}_a^{(4\omega)}/\zeta_a^4$ along body-fixed z_B-axis versus wave number νa for different wave steepness for five measured positions of the

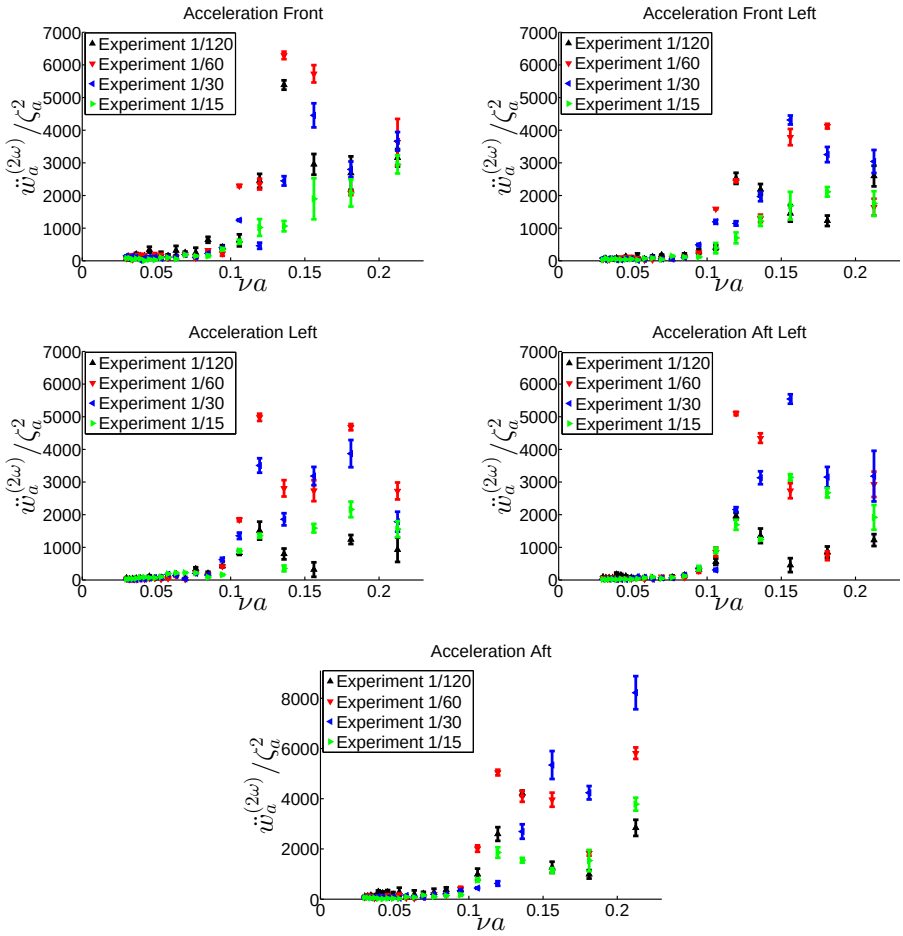

Figure 6.6: Steady-state amplitudes of experimental non-dimensional second-harmonic acceleration $\ddot{w}_a^{(2\omega)}/\zeta_a^2$ along body-fixed z_B-axis versus non-dimensional wave number νa for wave steepnesses 1/120, 1/60, 1/30 and 1/15 for five measured positions of the torus in incident regular waves with frequency ω and amplitude ζ_a. The height of the experimental error bars is two times the estimated standard deviation.

torus in Figures 6.6 to 6.8. Same conclusion as for the first-harmonic acceleration of nearly rigid torus model can be obtained by examining $\ddot{w}_a^{(\omega)}/\zeta_a$ in Figure 6.2, which shows that $\ddot{w}_a^{(\omega)}$ is mainly proportional to ζ_a for the different wave steepness 1/120, 1/60, 1/30 and 1/15. However, $\ddot{w}_a^{(2\omega)}$ is mainly proportional to ζ_a^2 for the different wave steepness at the front, front left and left of the torus by examining $\ddot{w}_a^{(2\omega)}/\zeta_a^2$ (see Figure 6.6). When it comes to $\ddot{w}_a^{(3\omega)}$ and $\ddot{w}_a^{(4\omega)}$, we cannot say that they are mainly proportional to ζ_a^3 and ζ_a^4, respectively (see Figures 6.7 and 6.8).

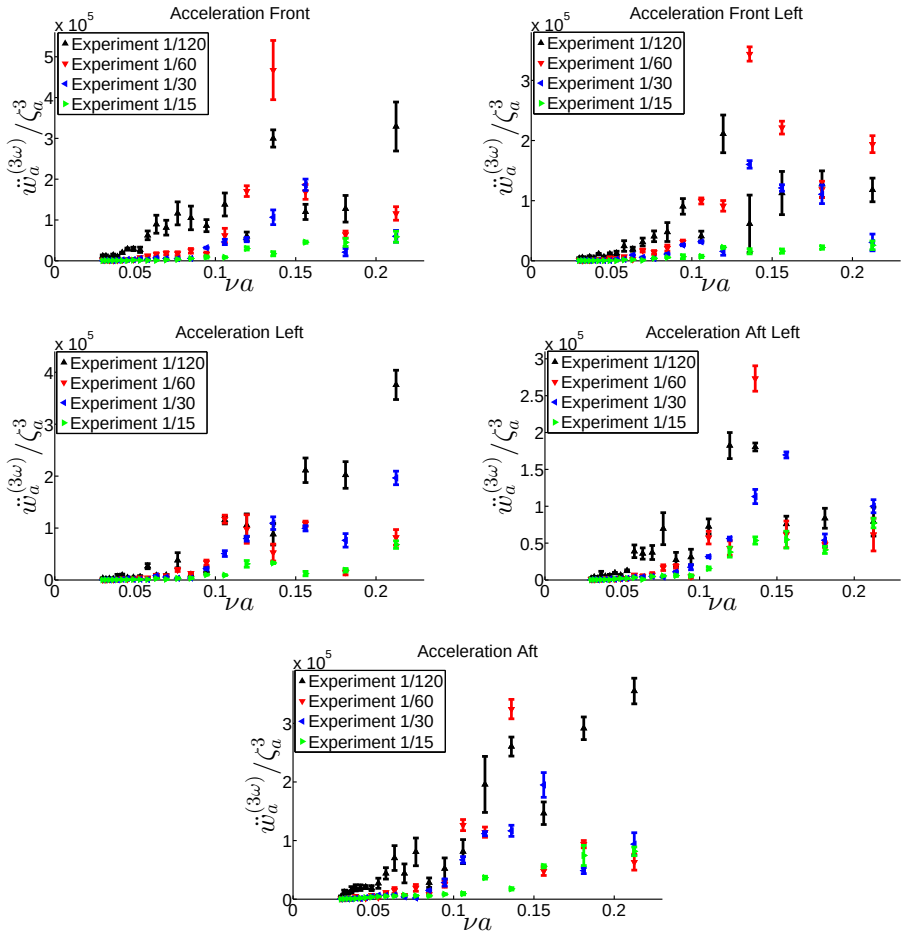

Figure 6.7: Steady-state amplitudes of experimental non-dimensional third-harmonic acceleration $\ddot{w}_a^{(3\omega)}/\zeta_a^3$ along body-fixed z_B-axis versus non-dimensional wave number νa for wave steepnesses 1/120, 1/60, 1/30 and 1/15 for five measured positions of the torus in incident regular waves with frequency ω and amplitude ζ_a. The height of the experimental error bars is two times the estimated standard deviation.

It means that we cannot explain the behavior of $\ddot{w}_a^{(3\omega)}$ and $\ddot{w}_a^{(4\omega)}$ by a perturbation method with the wave steepness as a small parameter as for the nearly rigid torus model.

As discussed in Section 5.3, one reason is that the torus shape above the mean free-surface matters since ζ_a/a ought to be considered as a small parameter. However, wave overtopping occurred during the experiments as shown in Figure 4.10. Another reason may be that the elastic torus has an infinite number of natural

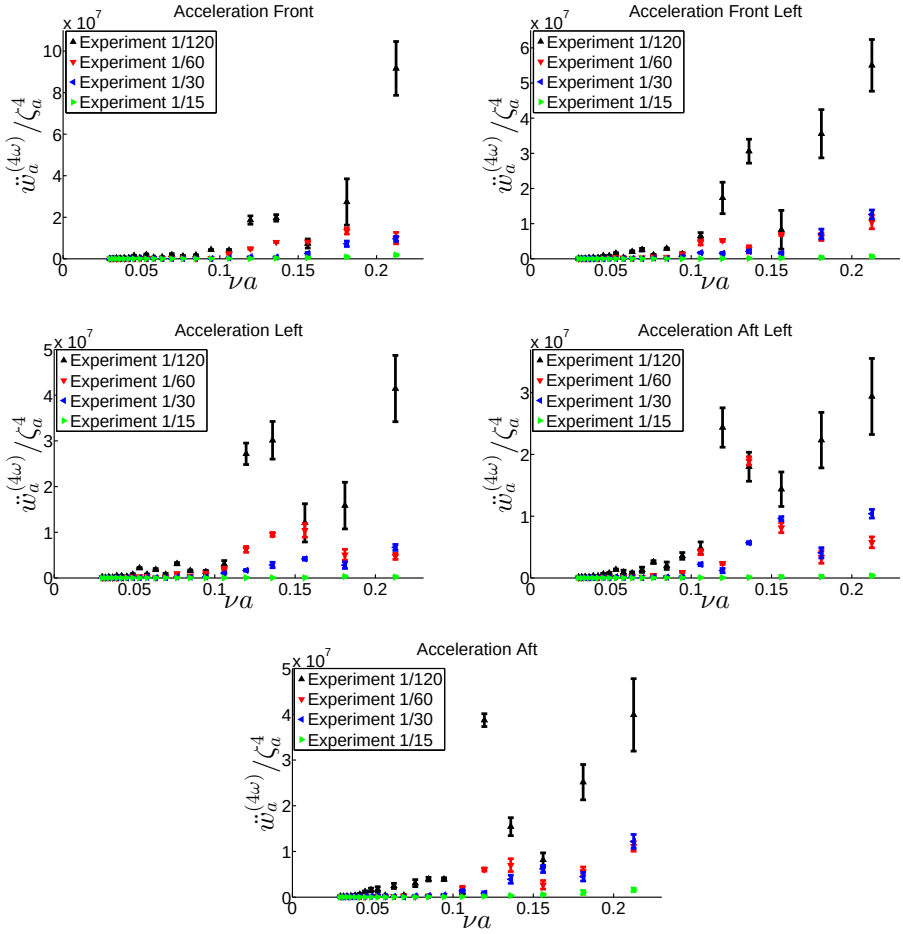

Figure 6.8: Steady-state amplitudes of experimental non-dimensional fourth-harmonic acceleration $\ddot{w}_a^{(4\omega)}/\zeta_a^4$ along body-fixed z_B-axis versus non-dimensional wave number νa for wave steepnesses 1/120, 1/60, 1/30 and 1/15 for five measured positions of the torus in incident regular waves with frequency ω and amplitude ζ_a. The height of the experimental error bars is two times the estimated standard deviation.

frequencies, and resonant oscillations can be excited when higher-order harmonics of the wave loads $n\omega$ is close to the natural frequency of a mode. Table 6.3 lists predicted undamped natural frequencies for different vertical modes. It increases from left to right in each row and up to the largest value of 4ω in the model tests. There are 100 natural frequencies from the first one $22.61 rad/s$ to $45.15 rad/s$. The very strong frequency dependency of generalized added mass for vertical modes causes a small interval between successive natural frequencies. This increases the possi-

Table 6.3: Predicted undamped natural frequencies in rad/s for vertical modes.

22.61	23.11	23.49	23.99	24.33	25.15	25.67	25.83	26.11	26.73
26.97	27.49	28.21	28.61	28.93	29.37	29.63	30.11	30.31	30.83
30.99	31.32	31.75	32.17	32.29	32.61	32.81	33.01	33.11	33.45
33.54	33.73	34.07	34.33	34.67	34.76	34.93	35.16	35.27	35.35
35.53	35.85	35.95	36.11	36.41	36.53	36.67	36.88	36.97	37.09
37.23	37.42	37.53	37.65	37.79	38.03	38.21	38.33	38.51	38.61
38.75	38.87	39.04	39.15	39.28	39.39	39.57	39.67	39.80	39.92
40.08	40.18	40.32	40.43	40.59	40.64	40.94	41.10	41.20	41.34
41.44	41.59	41.70	41.83	42.08	42.21	42.32	42.57	42.66	42.81
43.05	43.29	43.53	43.75	43.99	44.23	44.45	44.69	44.91	45.15

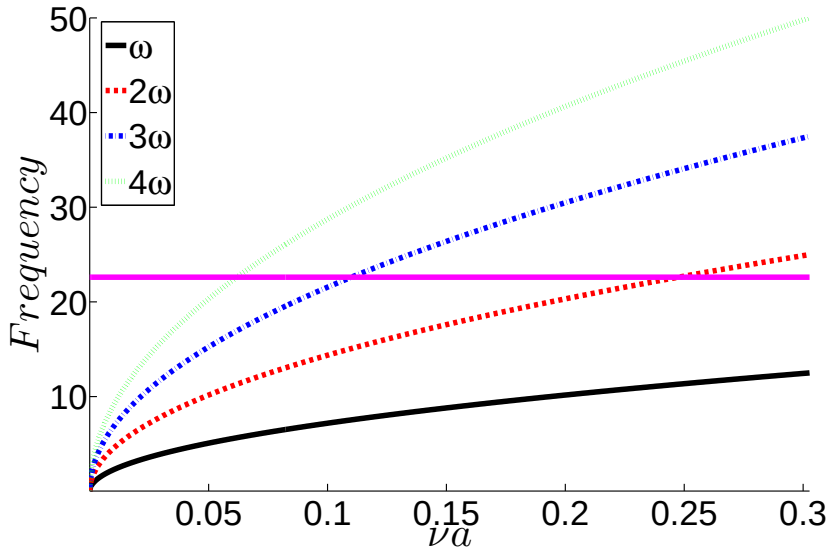

Figure 6.9: Frequencies ω, 2ω, 3ω and 4ω in rad/s as a function of $\nu a = \omega^2 a/g$. The lower bond for the natural frequencies of vertical modes is indicated with the horizontal pink line.

bility of encounter the wave frequencies testing in experiment. Figure 6.9 presents frequencies ω, 2ω, 3ω and 4ω in rad/s as a function of $\nu a = \omega^2 a/g$. The pink solid straight line is the first natural frequency $22.61 rad/s$. When ω, 2ω, 3ω and/or 4ω

is above the pink line for a given νa, it indicates that resonant oscillations may occur depending on the magnitude of the generalized excitation force and damping. If we relate this fact to the experimental results in Figures 6.3 to 6.5, we note that not all large higher harmonic accelerations can be explained to be a consequence of resonance.

6.4 Summary

The study on an elastic circular collar of a floating fish farm subjected to regular waves has been presented. A linear frequency-domain method and a weak-scatter method have been applied to compare with the results of model tests performed in 2013. Satisfactory agreement was achieved for the first harmonic component of measured vertical accelerations at the five measured positions on the torus for both methods. Discrete Fourier Transform of the measured vertical accelerations show that higher-order harmonic components are important. The second harmonic acceleration component is predicted well by the weak-scatter method for wave steepness 1/120 and in some cases for wave steepnesses 1/60 and 1/30. The differences are larger for the highest wave steepness 1/15. It is speculated if higher-order wave loads may cause resonant vertical accelerations of the torus. The analysis showed that flexible motions, 3D flow and frequency dependency are important. Wave overtopping may occur in steeper waves.

Chapter 7

Summary and further work

7.1 Summary of the present work

Wave-induced response of a circular collar of a floating fish farm have been investigated in regular deep-water waves based on a low-frequency slender-body theory, model tests and numerical simulations.

Wave lengths of practical interest are of the order of the torus diameter. Hydroelasticity plays a major role for the considered torus-shaped floater. The elasticity effect of the torus is described by a curved beam equation with tension effects. A low-frequency linear slender-body theory has been derived by matched asymptotic expansions with a near-field and far-field solution. In the near field we see the cross-sectional shape of the torus, while the flow in the far field appears as a line distribution of 3D sources along the center line of the torus. The problem is solved in the frequency domain with radiating waves. By low frequency is meant that the corresponding wavelength is long relative to the cross-sectional radius a of the torus. The derived theory can be used to calculate the generalized vertical added mass and damping loads on an elastic semi-submerged circular collar used as a floater of an aquaculture plant. Two types of expressions of the generalized vertical diffraction loads are also presented either based on solving the diffraction problem with a cross-sectional averaged vertical incident wave velocity along the torus or by using a generalized Haskind relation. The linear potential flow frequency-domain panel code WAMIT with a higher-order Boundary Element Method has been used to verify the theory. Satisfactory agreements between WAMIT and the low-frequency slender-body theory have been obtained. There is as expected an increasing difference with increasing non-dimensional wave number νa and a small increasing difference occur with increasing mode number which probably is due to the fact that 2D Helmholtz equation should be used instead of the 2D Laplace equation in the near-field problem. The results demonstrate pronounced frequency-dependent 3D hydrodynamic interaction on the scale of the torus diameter, which limits the application of strip theory.

Two sets of model tests have been performed in 2013 in order to validate the low-frequency slender-body theory. In these two sets of model tests, the elastic torus

model was tightly moored by springs and mooring lines through 12 attachment points while the nearly rigid torus model was connected with mooring lines through 4 attachment points. The bending stiffness of the elastic model was obtained by Froude scaling of an elastic full-scale floater. Both of these two models were subjected to regular waves. 4 wave steepnesses and 21 wave periods were examined. The focus was on steady-state periodic response. Vertical accelerations along the torus, mooring line forces and the free-surface elevation at four positions in the wave tank were measured. The longitudinal and transverse floater motions were estimated by means of the mooring loads together with the known stiffness of the springs. Overtopping and out of water of parts of the torus models were observed for some of the test conditions. In order to find the error between the theoretical and achieved wave height given by the wave maker, incident regular wave tests without the torus in the tank have been carried out. Satisfactory agreements were achieved between the measured first harmonic component and the nominal wave amplitude. Since the strong frequency dependency of added mass may cause several undamped natural frequencies for the dominant modes, free-decay tests have not been done to identify wet natural periods and damping. The theoretical ten lowest undamped natural frequency for uncoupled heave, pitch and the lowest vertical elastic mode of the nearly rigid torus are higher than the experimental frequency range of the linear incident regular waves.

Two separate studies based on the two sets of model tests have been performed. In the first study, the nearly rigid torus model has been considered. Linear experimental longitudinal motions have been compared with computed results by the potential-flow frequency-domain panel code HydroStar and reasonable agreement were shown. The calculation with HydroStar assume a rigid body. Hydroelasticity effects were experimentally observed in the longitudinal and transverse motions. Linear experimental vertical accelerations for wave steepness $H/\lambda = 1/120$ where H is the wave height and λ is the wave length have been also compared with numerical results from HydroStar with and without tank wall interference and WAMIT with hydroelastic effect. However, the calculations with tank wall interference do not improve the agreement between numerical and experimental results. Investigations showed that the lowest elastic mode matters. The study of Keulegan-Carpenter number and viscous force indicate that flow separation and viscous effects are insignificant for our considered small wave steepness $H/\lambda = 1/120$. We found that third-order effects cannot be neglected in estimating the experimental first-order component by analyzing the experimental ratio between third-harmonic acceleration and first-harmonic acceleration and by using that third-order terms by a perturbation theory will contain both first-harmonic and third-harmonic therms. Numerically predicted second-order sum-frequency accelerations by HydroStar do not agree well with the experimental results, which may be caused by hydroelasticity and higher order wave-body interaction effects. The experimental and numerical results show that resonant wave motion does not occur inside the torus. Higher harmonic components of the experimental vertical acceleration for wave steepness 1/120, 1/60, 1/30 and 1/15 in steady-state conditions are also investigated and found to matter. Third and fourth harmonics response cannot be explained by a perturbation method with the wave steepness as a small parameter since the torus

shape above the mean free-surface is likely to matter and the ratio between the incident wave amplitude and the cross-sectional torus radius ought to be considered as a small parameter.

The elastic torus model has been studied in the second study. The focus was on the vertical accelerations along the torus as a function of wave frequency and wave steepness. The linear low-frequency slender-body theory and the potential-flow weak-scatter method with partly nonlinear effects were compared with the measured vertical accelerations. Satisfactory agreements of the first harmonic component of vertical acceleration are shown. The weak-scatter results of three typical non-dimensional wave number νa demonstrate a reasonable agreement with experimental second harmonic acceleration component for wave steepness 1/120 and in some cases for wave steepnesses 1/60 and 1/30 but become invalid for 1/15. Predictions of third and fourth harmonic acceleration components are less satisfactory which means the weak-scatter method can only partly explain the nonlinearities present in the measured vertical accelerations.

7.2 Recommendations for further work

The present studies can be pursued further in many different perspectives and several are presented here.

Further developments of the low-frequency slender-body theory can consider radial modes by following the similar procedure for vertical modes for the added mass, damping and wave excitation loads where 3D and frequency effects matter but are less pronounced than for the vertical modes. The latter has been demonstrated by using WAMIT. In the present study one torus has been considered, but two concentric pipe circles that are linked together are often used in a fish farm. The low-frequency slender-body theory can be further developed to consider two tori. In order to improve the numerical model, the structural damping in the HDPE plastic needs further investigation and should be included. Further challenges are irregular waves as well as the fact that the torus can get an oval form in current.

Future studies of using a fully nonlinear 3D CFD method that accounts for hydroelasticity should be attempted. We say fully nonlinear because the present studies show that even fourth-order harmonics of the measured torus accelerations mattered in steeper waves and that perturbation methods are only practical for linear and second-order problems, which accounts only for first and second order harmonics of the torus acceleration in regular waves. Difficulties with a perturbation method may also arise because of singularities at the contact line between the mean free-surface and the torus (Faltinsen and Timokha, 2010). Furthermore, Navier-Stokes equation is needed because flow separation is likely to matter for steeper waves.

A further step is to investigate a more complete fish farm set-up,including net cage with bottom weight ring, chains, ropes and a realistic mooring system in waves and current where all components behave under mutual influence. Therefore, the total system needs to be considered simultaneously. In reality there are several closely spaced aquaculture net cages. The hydrodynamic interaction between

different net cages is a matter of further investigations.

Bibliography

Abramowitz, M. and Stegun, I. A. (1964), *Handbook of Mathematical Functions: with Formulas, Graphs, and Mathematical Tables*, Dover Publications, INC., New York, USA.

Bardestani, M. and Faltinsen, O. M. (2013), A two-dimensional approximation of a floating fish farm in waves and current with the effect of snap loads, *in* 'Proceedings of the ASME 2013 32nd International Conference on Ocean, Offshore and Arctic Engineering', Vol. 9, Nantes, France. OMAE2013-10487.

Beveridge, M. (2008), *Cage Aquaculture*, John Wiley & Sons, Oxford, England.

Bishop, R. E. D. and Price, W. G. (1979), *Hydroelasticity of Ships*, Cambridge University Press, Cambridge, England.

Cummins, W. E. (1962), "The impulse response function and ship motions", *Symposium on Ship Theory, Schiffstechnik*, Vol. 9, pp. 101–109.

Dean, R. G. and Dalrymple, R. A. (1991), *Water Wave Mechanics for Engineers and Scientists*, World Scientific Publishing Co. Pte. Ltd.

Dong, G. H., Hao, S. H., Zhao, Y. P., Zong, Z. and Gui, F. K. (2010), "Elastic responses of a flotation ring in water waves", *Journal of Fluids and Structures*, Vol. 26, pp. 176–192.

Faltinsen, O. M. (1990), *Sea Loads on Ships and Offshore Structures*, Cambridge University Press, Cambridge, England.

Faltinsen, O. M. (2005), *Hydrodynamics of High-Speed Marine Vehicles*, Cambridge University Press, Cambridge, England.

Faltinsen, O. M. (2011), Hydrodynamic aspects of a floating fish farm with circular collar, *in* 'Proceedings of the 26th International Workshop on Water Waves and Floating Bodies', Athens, Greece.

Faltinsen, O. M. and Timokha, A. N. (2009), *Sloshing*, Cambridge University Press, Cambridge, England.

Faltinsen, O. M. and Timokha, A. N. (2010), "A multimodal method for liquid sloshing in a two-dimensional circular tank", *Journal of Fluid Mechanics*, Vol. 665, pp. 457–479.

FAO (2005), National aquaculture sector overview: Norway, Technical report, Food and Agriculture Organization of the United Nations, Rome, Italy.

FAO (2010), Aquaculture development, Technical report, Food and Agriculture Organization of the United Nations, Rome, Italy.

FAO (2014), The state of world fisheries and aquaculture 2014, Technical report, Food and Agriculture Organization of the United Nations, Rome, Italy.

FAO (2015), Aquaculture operations in floating hdpe cages: A field handbook, Technical report, Food and Agriculture Organization of the United Nations, Rome, Italy.

Gradshteyn, I. S. and Ryzhik, I. M. (1994), *Table of Integrals, Series, and Products*, Academic Press, Inc., San Diego, CA, USA.

Greco, M. and Lugni, C. (2012), "3D seakeeping analysis with water on deck and slamming. part 1: numerical solver", *Journal of Fluids and Structures*, Vol. 33, pp. 127–147.

Haskind, M. D. (1948), "The pressure of waves on a barrier", *Inzhen. Sb*, Vol. 4, pp. 147–160.

Havelock, T. H. (1942), "The damping of the heaving and pitching motion of a ship", *The London, Edinburgh, and Dublin Philosophical Magazine and Journal of Science*, Vol. 33, pp. 666–673.

Havelock, T. H. (1955), Waves due to a floating sphere making periodic heaving oscillations, *in* 'Proceedings of the Royal Society of London A: Mathematical, Physical and Engineering Sciences', Vol. 231, pp. 1–7.

Heller, S. R. and Abramson, H. N. (1959), "Hydroelasticity: a new naval science", *Journal of the American Society for Naval Engineers*, Vol. 71, pp. 205–209.

Huang, C. C., Tang, H. J. and Liu, J. Y. (2006), "Dynamical analysis of net cage structures for marine aquaculture: Numerical simulation and model testing", *Aquacultural Engineering*, Vol. 35, pp. 258–270.

ITTC (1990), Report of the panel on validation procedures, *in* 'Proceedings of the 19th ITTC', Madrid, Spain, pp. 577–604.

Jensen, Ø., Dempster, T., Thorstad, E. B., Uglem, I. and Fredheim, A. (2010), "Escapes of fishes from norwegian sea-cage aquaculture: causes, consequences and prevention", *Aquaculture Environment Interactions*, Vol. 1, pp. 71–83.

Klebert, P., Patursson, Ø., Endresen, P. C., Rundtop, P., Birkevold, J. and Rasmussen, H. W. (2015), "Three-dimensional deformation of a large circular flexible sea cage in high currents: Field experiment and modeling", *Ocean Engineering*, Vol. 104, pp. 511–520.

Kristiansen, D. (2010), Wave induced effects on floaters of aquaculture plants, Phd thesis, Department of Marine Technology, Norwegian University of Science and Technology, Trondheim, Norway.

Kristiansen, D. and Faltinsen, O. M. (2008*a*), A study of wave loads on fixed horizontal cylinders in the free surface, *in* 'Proceedings of the 8th International Conference on Hydrodynamics'.

Kristiansen, D. and Faltinsen, O. M. (2008*b*), Wave loads on floaters of aquaculture plants, *in* 'Proceedings of the ASME 27th International Conference on Offshore Mechanics and Arctic Engineering', Vol. 6, Estoril, Portugal, pp. 69–78. OMAE2008-57084.

Kristiansen, D. and Faltinsen, O. M. (2009), "Non-linear wave-induced motions of cylindrical-shaped floaters of fish farms", *Proceedings of the Institution of Mechanical Engineers, Part M: Journal of Engineering for the Maritime Environment*, Vol. 223, pp. 361–375.

Kristiansen, T. and Faltinsen, O. M. (2012), Mooring loads of a circular net cage with an elastic floater in waves and current, *in* 'Proceedings of the Sixth International Conference on Hydroelasticity in Marine Technology', Tokyo, Japan.

Kristiansen, T. and Faltinsen, O. M. (2015), "Experimental and numerical study of an aquaculture net cage with floater in waves and current", *Journal of Fluids and Structures*, Vol. 54, pp. 1–26.

Li, L., Fu, S. X., Xu, Y. W., Wang, J. G. and Yang, J. M. (2013), "Dynamic responses of floating fish cage in waves and current", *Ocean Engineering*, Vol. 72, pp. 297–303.

Li, P. and Faltinsen, O. M. (2012), Wave induced response of an elastic circular collar of a floating fish farm, *in* 'Proceedings of 10th International Conference on Hydrodynamics', Vol. 2, St. Petersburg, Russia, pp. 58–64.

Li, P., Faltinsen, O. M. and Greco, M. (2014), Wave-induced accelerations of a fish-farm elastic floater: experimental and numerical studies, *in* 'Proceedings of the ASME 2014 33rd International Conference on Ocean, Offshore and Arctic Engineering', Vol. 7, San Francisco, California, USA. OMAE2014-23302.

Li, P., Faltinsen, O. M. and Lugni, C. (2016), "Nonlinear vertical accelerations of a floating torus in regular waves", *Journal of Fluids and Structures*, Vol. 66, pp. 589–608.

Li, Y. C., Gui, F. K. and Teng, B. (2007), "Hydrodynamic behavior of a straight floating pipe under wave conditions", *Ocean engineering*, Vol. 34, pp. 552–559.

Love, A. E. H. (1906), *A treatise on the mathematical theory of elasticity*, Cambridge University Press, Cambridge, England.

Loverich, G. F. and Gace, L. (1997), "The effect of currents and waves on several classes of offshore sea cages", *Charting the Future of Ocean Farming*, pp. 131–144.

Newman, J. N. (1962), "The exciting forces on fixed bodies in waves", *Journal of Ship Research*, Vol. 6, pp. 10–17.

Newman, J. N. (1977*a*), *Marine Hydrodynamics*, MIT press, Cambridge, Massachusetts, USA.

Newman, J. N. (1977*b*), "The motion of a floating slender torus", *Journal of Fluid Mechanics*, Vol. 83, pp. 721–735.

Newman, J. N. (1978), "The theory of ship motions", *Advances in Applied Mechanics*, Vol. 18, pp. 221–283.

Newman, J. N. and Lee, C. H. (1992), Sensitivity of wave loads to the discretisation of bodies, *in* 'BOSS'92, London, England'.

Newman, J. N. and Tuck, E. O. (1964), Current progress in the slender body theory for ship motions, *in* 'Proceedings of the 5th ONR Symp. Naval Hydrodynamics', pp. 129–162.

OIML (2000), Metrological regulation for load cells (OIML R60), Regulation report, International Organization of Legal Metrology.

Olivares, A. E. V. and Brynjolfsson, S. (2003), Design of a cage culture system for farming in mexico, Final report, The United Nations University Fisheries Training Programme, Reykjavik, Iceland.

Ormberg, H. (1991), Non-linear response analysis of floating fish farm systems, Phd thesis, Department of Marine Technology, Norwegian University of Science and Technology, Trondheim, Norway.

Pawlowski, J. S. (1991), A theoretical and numerical model of ship motions in heavy seas, *in* 'SNAME Transactions', Vol. 99, pp. 315–319.

Shen, Y. G., Greco, M. and Faltinsen, O. M. (2016), Numerical study of a coupled well boat-fish farm system in waves and current during loading operations, *in* 'Proceedings of 12th International Conference on Hydrodynamics', Egmond aan Zee, The Netherlands.

Tang, H. J., Huang, C. C. and Chen, W. M. (2011), "Dynamics of dual pontoon floating structure for cage aquaculture in a two-dimensional numerical wave tank", *Journal of Fluids and Structures*, Vol. 27, pp. 918–936.

Ursell, F. (1949), "On the heaving motion of a circular cylinder on the surface of a fluid", *The Quarterly Journal of Mechanics and Applied Mathematics*, Vol. 2, pp. 218–231.

WBG (2014), Fish to 2030 : prospects for fisheries and aquaculture, Technical report, The World Bank Group, Washington DC, U.S.

Zhao, Y. P., Li, Y. C., Dong, G. H., Teng, B. and Gui, F. K. (2009), "Numerical simulation of hydrodynamic behaviors of gravity cage in current and waves", *International Journal of Offshore and Polar Engineering*, Vol. 19.

Appendices

Appendix A

Bending stiffness terms in curved beam equation

Tore H. Søreide (personal communication, 2015) has made the following analysis. We are not aware of similar published results. We consider a beam that is curved in a plane with a curvature radius c and deforms w perpendicularly to the plane in the z-direction. We introduce a coordinate system with curvilinear coordinate s along the beam and a radial coordinate r with origin in the curvature center of the beam when there is no beam deformation. A cut of small length ds of the beam is considered (see Figure A.1). There is in the figure introduced the internal forces and moments acting on the beam part. Those are bending moment M_r about the r-axis, torsional moment M_t about the s-axis and vertical shear force V along the z-axis.

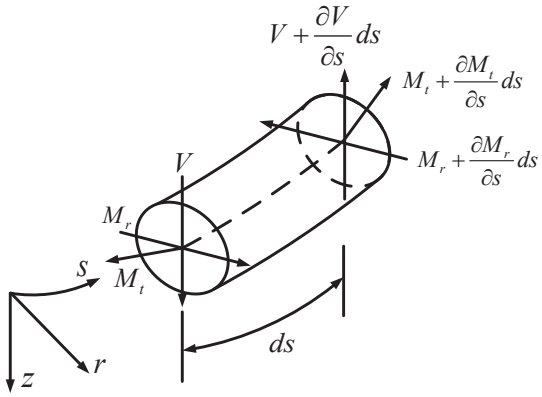

Figure A.1: A small section of length ds of a curved beam with definition of coordinate system, bending moment M_r about the r-axis, torsional moment M_t about the s-axis and vertical shear force V along the z-axis.

We start with steady moment about the r-axis at s and must realize that the moment axis at s and $s + ds$ changes direction relative to a Cartesian coordinate system. It means that we must be aware of contribution from M_t. We can write as a first approximation:

$$V ds = \frac{\partial M_r}{\partial s} ds + M_t \frac{ds}{c} \tag{A.1}$$

where the small angle ds/c is defined in Figure A.2. It follows that:

$$V = \frac{\partial M_r}{\partial s} + \frac{M_t}{c} \tag{A.2}$$

We now consider the moment about the s-axis at s and note a contribution from M_r due to changes in moment direction relative to a Cartesian coordinate system. We can write:

$$\frac{\partial M_t}{\partial s} ds = M_r \frac{ds}{c} \tag{A.3}$$

It means by using the previous expressions that the internal vertical force $\partial V/\partial s \cdot ds$ on the considered beam section can be expressed by:

$$\frac{\partial V}{\partial s} = \frac{\partial^2 M_r}{\partial s^2} + \frac{M_r}{c^2} \tag{A.4}$$

Using the fact that $M_r = EI \dfrac{\partial^2 w}{\partial s^2}$ gives the bending stiffness terms in Eq. (2.10).

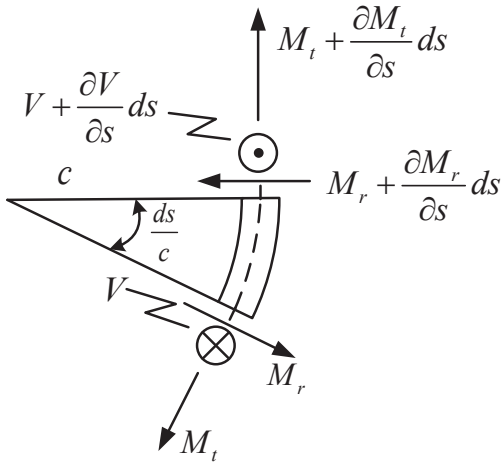

Figure A.2: Contributions of terms in the equilibrium analysis of a curved beam.

Appendix B

Axial tension in the torus

The following simplified calculations is based on Kristiansen and Faltinsen (2015). The torus is divided in eight segments as illustrated in Figure B.1. We assume that the axial tension T_{as} is piecewise constant in each segment, denoted N_1 to N_5. Due to symmetry about the x-axis, N_6 to N_8 are not explicitly needed.

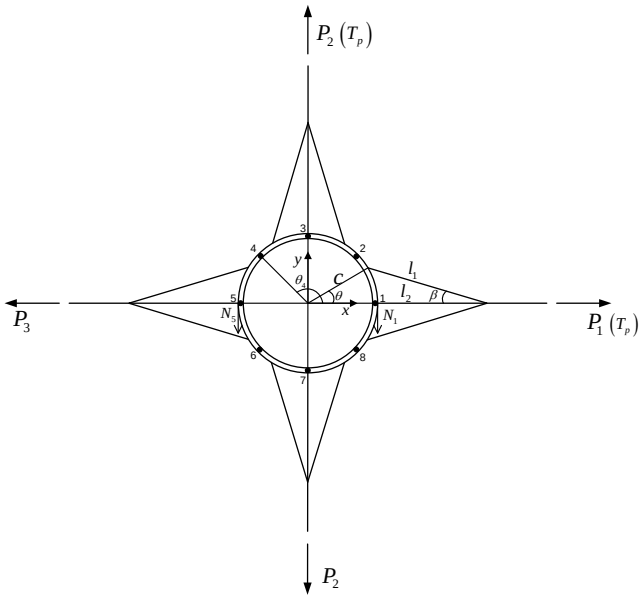

Figure B.1: Illustration of simplified calculation method for obtaining approximate values of the axial tension T_{as}. Note that P_2 is the y-component only of the line tension.

We define the following geometrical relations:

$$l_1 \sin\beta \;=\; c \sin\theta \tag{B.1}$$

$$l_2 \;+\; c \;=\; l_1 \cos\beta \;+\; c \cos\theta \tag{B.2}$$

Global equilibrium of forces in the x-direction yields

$$P_1 \;=\; P_3 \;=\; T_p \tag{B.3}$$

Here T_p is the pre-tension of the mooring lines. Global equilibrium of moments around the origin yields

$$N_1 c \;-\; N_5 c \;=\; 0 \tag{B.4}$$

Global equilibrium of forces in the y-direction yields

$$N_1 \;+\; N_5 \;=\; P_2 \;-\; \frac{P_1 + P_3}{2} \tan\beta \tag{B.5}$$

Combining the above equations, defining $P_2 = T_p$ and re-arranging terms gives the axial tensions as

$$N_1 \;=\; N_3 \;=\; N_5 \;=\; \frac{T_p}{2}\,(1 - \tan\beta) \tag{B.6}$$

$$N_2 \;=\; N_1 \cos\theta_2 \;+\; \frac{P_1}{2\cos\beta} \sin\left(\theta_2 + \beta\right) \;=\; \frac{T_p}{2}\left(\sin\theta_2 \;+\; \cos\theta_2\right) \tag{B.7}$$

$$N_4 \;=\; N_5 \cos\left(\pi - \theta_4\right) \;+\; \frac{P_3}{2\cos\beta} \sin\left(\theta_4 - \beta\right) \;=\; \frac{T_p}{2}\left(\sin\theta_4 \;-\; \cos\theta_4\right) \tag{B.8}$$

Appendix C

Verification of generalized added mass and damping coefficients, vertical excitation forces and response amplitude operators

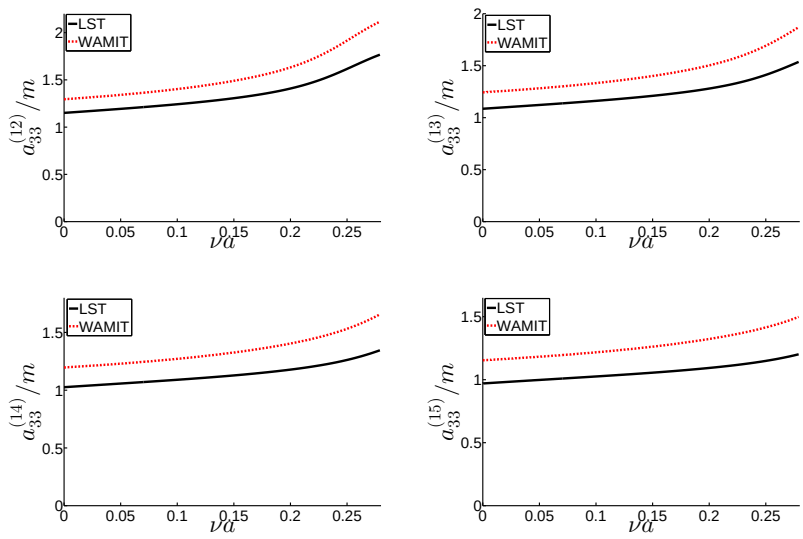

Figure C.1: Comparison of sectional vertical added mass coefficients $a_{33}^{(n)}$ of a torus for the modes number $n = 12, 13, 14, 15$ with $a/c = 0.0253$ by means of the low-frequency slender-body theory (LST) and WAMIT versus nondimensional wave number νa. m is displaced cross-sectional mass.

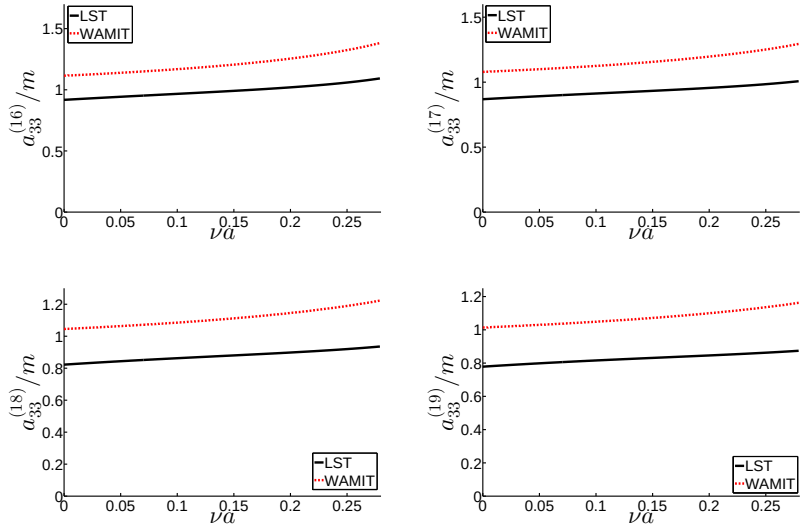

Figure C.2: Comparison of sectional vertical added mass coefficients $a_{33}^{(n)}$ of a torus for the modes number $n = 16, 17, 18, 19$ with $a/c = 0.0253$ by means of the low-frequency slender-body theory (LST) and WAMIT versus nondimensional wave number νa. m is displaced cross-sectional mass.

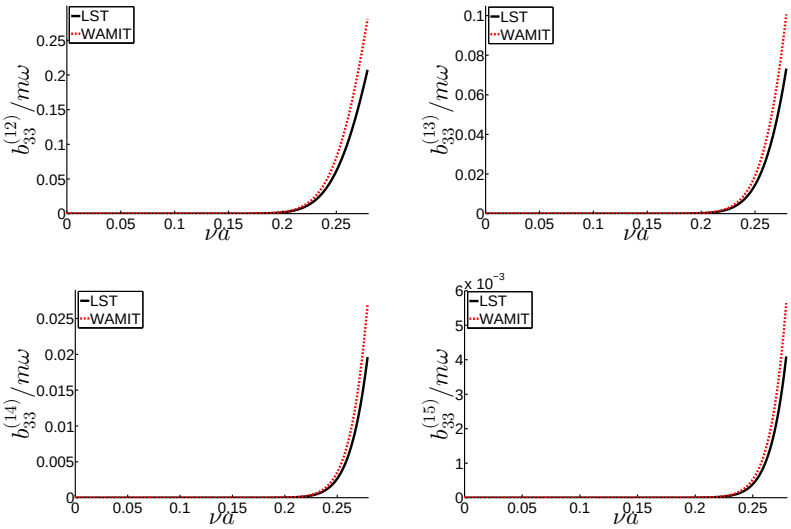

Figure C.3: Comparison of sectional vertical damping coefficients $b_{33}^{(n)}$ of a torus for the modes number $n = 12, 13, 14, 15$ with $a/c = 0.0253$ by means of the low-frequency slender-body theory (LST) and WAMIT versus nondimensional wave number νa. m is displaced cross-sectional mass.

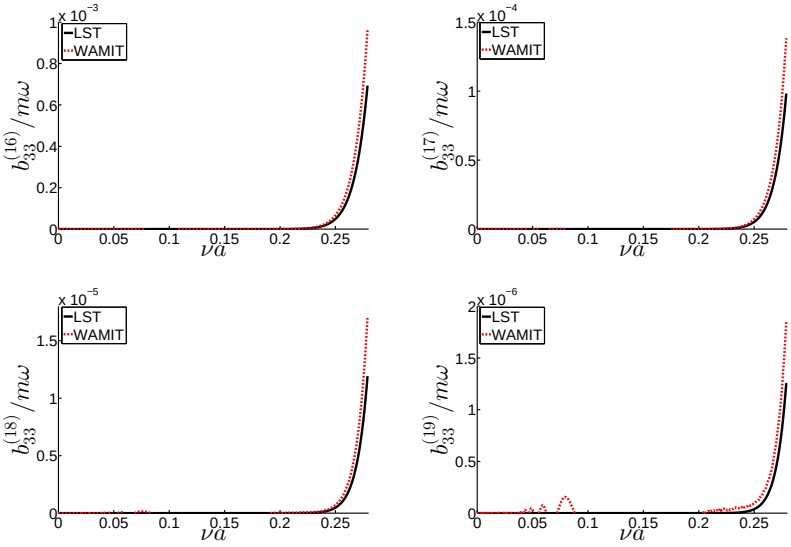

Figure C.4: Comparison of sectional vertical damping coefficients $b_{33}^{(n)}$ of a torus for the modes number $n = 16, 17, 18, 19$ with $a/c = 0.0253$ by means of the low-frequency slender-body theory (LST) and WAMIT versus nondimensional wave number νa. m is displaced cross-sectional mass.

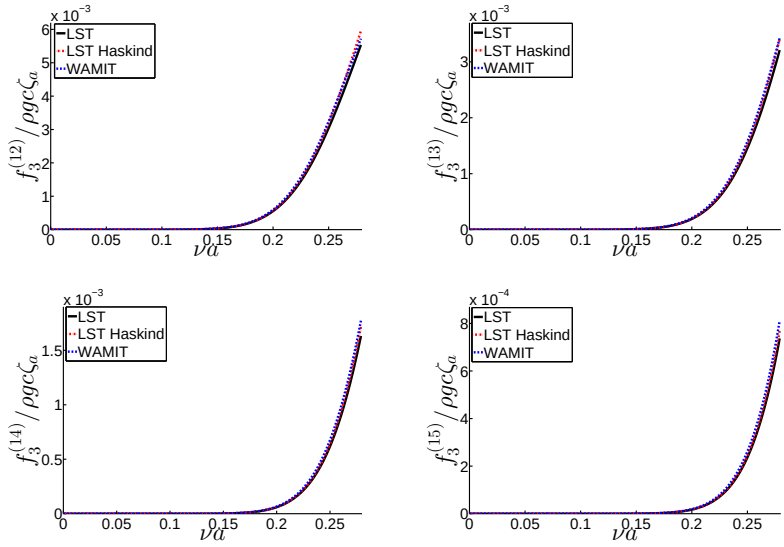

Figure C.5: Comparison of sectional vertical wave excitation force amplitude $f_3^{(n)}$ of a torus for the modes number $n = 12, 13, 14, 15$ with $a/c = 0.0253$ by means of the low-frequency slender-body theory (LST) with and without Haskind relationship and WAMIT versus nondimensional wave number νa.

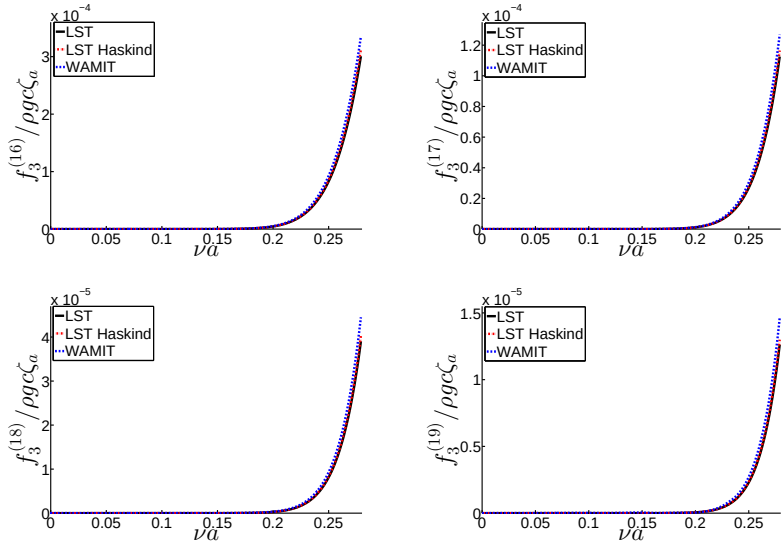

Figure C.6: Comparison of sectional vertical wave excitation force amplitude $f_3^{(n)}$ of a torus for the modes number $n = 16, 17, 18, 19$ with $a/c = 0.0253$ by means of the low-frequency slender-body theory (LST) with and without Haskind relationship and WAMIT versus nondimensional wave number νa.

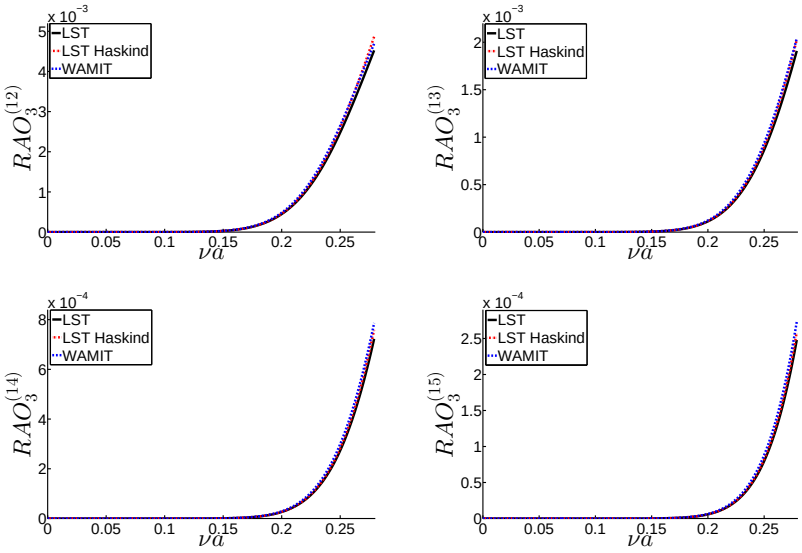

Figure C.7: Comparison of RAO's $|a_{n,a}/\zeta_a|$ of a torus for the modes number $n = 12, 13, 14, 15$ with $a/c = 0.0253$ by means of the low-frequency slender-body theory (LST) with and without Haskind relationship and WAMIT versus nondimensional wave number νa.

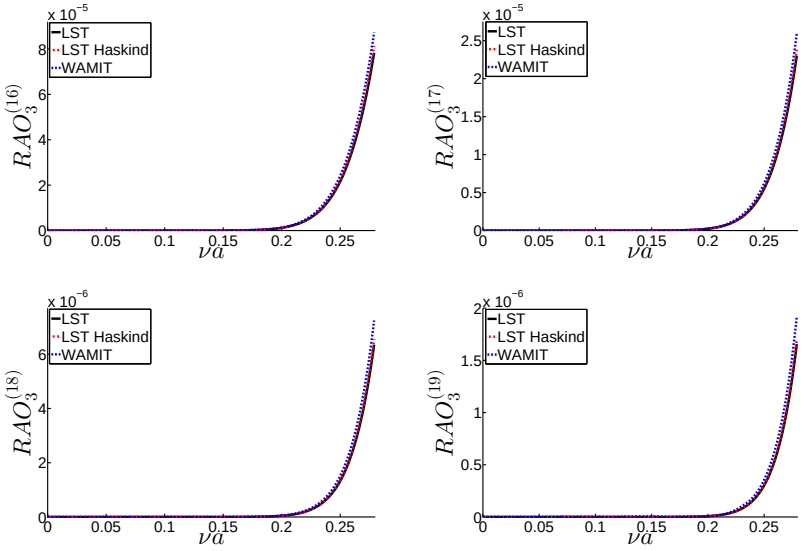

Figure C.8: Comparison of RAO's $|a_{n,a}/\zeta_a|$ of a torus for the modes number $n = 16, 17, 18, 19$ with $a/c = 0.0253$ by means of the low-frequency slender-body theory (LST) with and without Haskind relationship and WAMIT versus nondimensional wave number νa.

Previous PhD theses published at the Departement of Marine Technology
(earlier: Faculty of Marine Technology)
NORWEGIAN UNIVERSITY OF SCIENCE AND TECHNOLOGY

Report No.	Author	Title
	Kavlie, Dag	Optimization of Plane Elastic Grillages, 1967
	Hansen, Hans R.	Man-Machine Communication and Data-Storage Methods in Ship Structural Design, 1971
	Gisvold, Kaare M.	A Method for non-linear mixed -integer programming and its Application to Design Problems, 1971
	Lund, Sverre	Tanker Frame Optimalization by means of SUMT-Transformation and Behaviour Models, 1971
	Vinje, Tor	On Vibration of Spherical Shells Interacting with Fluid, 1972
	Lorentz, Jan D.	Tank Arrangement for Crude Oil Carriers in Accordance with the new Anti-Pollution Regulations, 1975
	Carlsen, Carl A.	Computer-Aided Design of Tanker Structures, 1975
	Larsen, Carl M.	Static and Dynamic Analysis of Offshore Pipelines during Installation, 1976
UR-79-01	Brigt Hatlestad, MK	The finite element method used in a fatigue evaluation of fixed offshore platforms. (Dr.Ing. Thesis)
UR-79-02	Erik Pettersen, MK	Analysis and design of cellular structures. (Dr.Ing. Thesis)
UR-79-03	Sverre Valsgård, MK	Finite difference and finite element methods applied to nonlinear analysis of plated structures. (Dr.Ing. Thesis)
UR-79-04	Nils T. Nordsve, MK	Finite element collapse analysis of structural members considering imperfections and stresses due to fabrication. (Dr.Ing. Thesis)
UR-79-05	Ivar J. Fylling, MK	Analysis of towline forces in ocean towing systems. (Dr.Ing. Thesis)
UR-80-06	Nils Sandsmark, MM	Analysis of Stationary and Transient Heat Conduction by the Use of the Finite Element Method. (Dr.Ing. Thesis)
UR-80-09	Sverre Haver, MK	Analysis of uncertainties related to the stochastic modeling of ocean waves. (Dr.Ing. Thesis)
UR-81-15	Odland, Jonas	On the Strength of welded Ring stiffened cylindrical Shells primarily subjected to axial Compression
UR-82-17	Engesvik, Knut	Analysis of Uncertainties in the fatigue Capacity of

		Welded Joints
UR-82-18	Rye, Henrik	Ocean wave groups
UR-83-30	Eide, Oddvar Inge	On Cumulative Fatigue Damage in Steel Welded Joints
UR-83-33	Mo, Olav	Stochastic Time Domain Analysis of Slender Offshore Structures
UR-83-34	Amdahl, Jørgen	Energy absorption in Ship-platform impacts
UR-84-37	Mørch, Morten	Motions and mooring forces of semi submersibles as determined by full-scale measurements and theoretical analysis
UR-84-38	Soares, C. Guedes	Probabilistic models for load effects in ship structures
UR-84-39	Aarsnes, Jan V.	Current forces on ships
UR-84-40	Czujko, Jerzy	Collapse Analysis of Plates subjected to Biaxial Compression and Lateral Load
UR-85-46	Alf G. Engseth, MK	Finite element collapse analysis of tubular steel offshore structures. (Dr.Ing. Thesis)
UR-86-47	Dengody Sheshappa, MP	A Computer Design Model for Optimizing Fishing Vessel Designs Based on Techno-Economic Analysis. (Dr.Ing. Thesis)
UR-86-48	Vidar Aanesland, MH	A Theoretical and Numerical Study of Ship Wave Resistance. (Dr.Ing. Thesis)
UR-86-49	Heinz-Joachim Wessel, MK	Fracture Mechanics Analysis of Crack Growth in Plate Girders. (Dr.Ing. Thesis)
UR-86-50	Jon Taby, MK	Ultimate and Post-ultimate Strength of Dented Tubular Members. (Dr.Ing. Thesis)
UR-86-51	Walter Lian, MH	A Numerical Study of Two-Dimensional Separated Flow Past Bluff Bodies at Moderate KC-Numbers. (Dr.Ing. Thesis)
UR-86-52	Bjørn Sortland, MH	Force Measurements in Oscillating Flow on Ship Sections and Circular Cylinders in a U-Tube Water Tank. (Dr.Ing. Thesis)
UR-86-53	Kurt Strand, MM	A System Dynamic Approach to One-dimensional Fluid Flow. (Dr.Ing. Thesis)
UR-86-54	Arne Edvin Løken, MH	Three Dimensional Second Order Hydrodynamic Effects on Ocean Structures in Waves. (Dr.Ing. Thesis)
UR-86-55	Sigurd Falch, MH	A Numerical Study of Slamming of Two-Dimensional Bodies. (Dr.Ing. Thesis)
UR-87-56	Arne Braathen, MH	Application of a Vortex Tracking Method to the Prediction of Roll Damping of a Two-Dimension Floating Body. (Dr.Ing. Thesis)

UR-87-57	Bernt Leira, MK	Gaussian Vector Processes for Reliability Analysis involving Wave-Induced Load Effects. (Dr.Ing. Thesis)
UR-87-58	Magnus Småvik, MM	Thermal Load and Process Characteristics in a Two-Stroke Diesel Engine with Thermal Barriers (in Norwegian). (Dr.Ing. Thesis)
MTA-88-59	Bernt Arild Bremdal, MP	An Investigation of Marine Installation Processes – A Knowledge - Based Planning Approach. (Dr.Ing. Thesis)
MTA-88-60	Xu Jun, MK	Non-linear Dynamic Analysis of Space-framed Offshore Structures. (Dr.Ing. Thesis)
MTA-89-61	Gang Miao, MH	Hydrodynamic Forces and Dynamic Responses of Circular Cylinders in Wave Zones. (Dr.Ing. Thesis)
MTA-89-62	Martin Greenhow, MH	Linear and Non-Linear Studies of Waves and Floating Bodies. Part I and Part II. (Dr.Techn. Thesis)
MTA-89-63	Chang Li, MH	Force Coefficients of Spheres and Cubes in Oscillatory Flow with and without Current. (Dr.Ing. Thesis
MTA-89-64	Hu Ying, MP	A Study of Marketing and Design in Development of Marine Transport Systems. (Dr.Ing. Thesis)
MTA-89-65	Arild Jæger, MH	Seakeeping, Dynamic Stability and Performance of a Wedge Shaped Planing Hull. (Dr.Ing. Thesis)
MTA-89-66	Chan Siu Hung, MM	The dynamic characteristics of tilting-pad bearings
MTA-89-67	Kim Wikstrøm, MP	Analysis av projekteringen for ett offshore projekt. (Licenciat-avhandling)
MTA-89-68	Jiao Guoyang, MK	Reliability Analysis of Crack Growth under Random Loading, considering Model Updating. (Dr.Ing. Thesis)
MTA-89-69	Arnt Olufsen, MK	Uncertainty and Reliability Analysis of Fixed Offshore Structures. (Dr.Ing. Thesis)
MTA-89-70	Wu Yu-Lin, MR	System Reliability Analyses of Offshore Structures using improved Truss and Beam Models. (Dr.Ing. Thesis)
MTA-90-71	Jan Roger Hoff, MH	Three-dimensional Green function of a vessel with forward speed in waves. (Dr.Ing. Thesis)
MTA-90-72	Rong Zhao, MH	Slow-Drift Motions of a Moored Two-Dimensional Body in Irregular Waves. (Dr.Ing. Thesis)
MTA-90-73	Atle Minsaas, MP	Economical Risk Analysis. (Dr.Ing. Thesis)
MTA-90-74	Knut-Aril Farnes, MK	Long-term Statistics of Response in Non-linear Marine Structures. (Dr.Ing. Thesis)
MTA-90-75	Torbjørn Sotberg, MK	Application of Reliability Methods for Safety Assessment of Submarine Pipelines. (Dr.Ing.

		Thesis)
MTA-90-76	Zeuthen, Steffen, MP	SEAMAID. A computational model of the design process in a constraint-based logic programming environment. An example from the offshore domain. (Dr.Ing. Thesis)
MTA-91-77	Haagensen, Sven, MM	Fuel Dependant Cyclic Variability in a Spark Ignition Engine - An Optical Approach. (Dr.Ing. Thesis)
MTA-91-78	Løland, Geir, MH	Current forces on and flow through fish farms. (Dr.Ing. Thesis)
MTA-91-79	Hoen, Christopher, MK	System Identification of Structures Excited by Stochastic Load Processes. (Dr.Ing. Thesis)
MTA-91-80	Haugen, Stein, MK	Probabilistic Evaluation of Frequency of Collision between Ships and Offshore Platforms. (Dr.Ing. Thesis)
MTA-91-81	Sødahl, Nils, MK	Methods for Design and Analysis of Flexible Risers. (Dr.Ing. Thesis)
MTA-91-82	Ormberg, Harald, MK	Non-linear Response Analysis of Floating Fish Farm Systems. (Dr.Ing. Thesis)
MTA-91-83	Marley, Mark J., MK	Time Variant Reliability under Fatigue Degradation. (Dr.Ing. Thesis)
MTA-91-84	Krokstad, Jørgen R., MH	Second-order Loads in Multidirectional Seas. (Dr.Ing. Thesis)
MTA-91-85	Molteberg, Gunnar A., MM	The Application of System Identification Techniques to Performance Monitoring of Four Stroke Turbocharged Diesel Engines. (Dr.Ing. Thesis)
MTA-92-86	Mørch, Hans Jørgen Bjelke, MH	Aspects of Hydrofoil Design: with Emphasis on Hydrofoil Interaction in Calm Water. (Dr.Ing. Thesis)
MTA-92-87	Chan Siu Hung, MM	Nonlinear Analysis of Rotordynamic Instabilities in Highspeed Turbomachinery. (Dr.Ing. Thesis)
MTA-92-88	Bessason, Bjarni, MK	Assessment of Earthquake Loading and Response of Seismically Isolated Bridges. (Dr.Ing. Thesis)
MTA-92-89	Langli, Geir, MP	Improving Operational Safety through exploitation of Design Knowledge - an investigation of offshore platform safety. (Dr.Ing. Thesis)
MTA-92-90	Sævik, Svein, MK	On Stresses and Fatigue in Flexible Pipes. (Dr.Ing. Thesis)
MTA-92-91	Ask, Tor Ø., MM	Ignition and Flame Growth in Lean Gas-Air Mixtures. An Experimental Study with a Schlieren System. (Dr.Ing. Thesis)
MTA-86-92	Hessen, Gunnar, MK	Fracture Mechanics Analysis of Stiffened Tubular Members. (Dr.Ing. Thesis)

MTA-93-93	Steinebach, Christian, MM	Knowledge Based Systems for Diagnosis of Rotating Machinery. (Dr.Ing. Thesis)
MTA-93-94	Dalane, Jan Inge, MK	System Reliability in Design and Maintenance of Fixed Offshore Structures. (Dr.Ing. Thesis)
MTA-93-95	Steen, Sverre, MH	Cobblestone Effect on SES. (Dr.Ing. Thesis)
MTA-93-96	Karunakaran, Daniel, MK	Nonlinear Dynamic Response and Reliability Analysis of Drag-dominated Offshore Platforms. (Dr.Ing. Thesis)
MTA-93-97	Hagen, Arnulf, MP	The Framework of a Design Process Language. (Dr.Ing. Thesis)
MTA-93-98	Nordrik, Rune, MM	Investigation of Spark Ignition and Autoignition in Methane and Air Using Computational Fluid Dynamics and Chemical Reaction Kinetics. A Numerical Study of Ignition Processes in Internal Combustion Engines. (Dr.Ing. Thesis)
MTA-94-99	Passano, Elizabeth, MK	Efficient Analysis of Nonlinear Slender Marine Structures. (Dr.Ing. Thesis)
MTA-94-100	Kvålsvold, Jan, MH	Hydroelastic Modelling of Wetdeck Slamming on Multihull Vessels. (Dr.Ing. Thesis)
MTA-94-102	Bech, Sidsel M., MK	Experimental and Numerical Determination of Stiffness and Strength of GRP/PVC Sandwich Structures. (Dr.Ing. Thesis)
MTA-95-103	Paulsen, Hallvard, MM	A Study of Transient Jet and Spray using a Schlieren Method and Digital Image Processing. (Dr.Ing. Thesis)
MTA-95-104	Hovde, Geir Olav, MK	Fatigue and Overload Reliability of Offshore Structural Systems, Considering the Effect of Inspection and Repair. (Dr.Ing. Thesis)
MTA-95-105	Wang, Xiaozhi, MK	Reliability Analysis of Production Ships with Emphasis on Load Combination and Ultimate Strength. (Dr.Ing. Thesis)
MTA-95-106	Ulstein, Tore, MH	Nonlinear Effects of a Flexible Stern Seal Bag on Cobblestone Oscillations of an SES. (Dr.Ing. Thesis)
MTA-95-107	Solaas, Frøydis, MH	Analytical and Numerical Studies of Sloshing in Tanks. (Dr.Ing. Thesis)
MTA-95-108	Hellan, Øyvind, MK	Nonlinear Pushover and Cyclic Analyses in Ultimate Limit State Design and Reassessment of Tubular Steel Offshore Structures. (Dr.Ing. Thesis)
MTA-95-109	Hermundstad, Ole A., MK	Theoretical and Experimental Hydroelastic Analysis of High Speed Vessels. (Dr.Ing. Thesis)
MTA-96-110	Bratland, Anne K., MH	Wave-Current Interaction Effects on Large-Volume Bodies in Water of Finite Depth. (Dr.Ing. Thesis)
MTA-96-111	Herfjord, Kjell, MH	A Study of Two-dimensional Separated Flow by a Combination of the Finite Element Method and

		Navier-Stokes Equations. (Dr.Ing. Thesis)
MTA-96-112	Æsøy, Vilmar, MM	Hot Surface Assisted Compression Ignition in a Direct Injection Natural Gas Engine. (Dr.Ing. Thesis)
MTA-96-113	Eknes, Monika L., MK	Escalation Scenarios Initiated by Gas Explosions on Offshore Installations. (Dr.Ing. Thesis)
MTA-96-114	Erikstad, Stein O., MP	A Decision Support Model for Preliminary Ship Design. (Dr.Ing. Thesis)
MTA-96-115	Pedersen, Egil, MH	A Nautical Study of Towed Marine Seismic Streamer Cable Configurations. (Dr.Ing. Thesis)
MTA-97-116	Moksnes, Paul O., MM	Modelling Two-Phase Thermo-Fluid Systems Using Bond Graphs. (Dr.Ing. Thesis)
MTA-97-117	Halse, Karl H., MK	On Vortex Shedding and Prediction of Vortex-Induced Vibrations of Circular Cylinders. (Dr.Ing. Thesis)
MTA-97-118	Igland, Ragnar T., MK	Reliability Analysis of Pipelines during Laying, considering Ultimate Strength under Combined Loads. (Dr.Ing. Thesis)
MTA-97-119	Pedersen, Hans-P., MP	Levendefiskteknologi for fiskefartøy. (Dr.Ing. Thesis)
MTA-98-120	Vikestad, Kyrre, MK	Multi-Frequency Response of a Cylinder Subjected to Vortex Shedding and Support Motions. (Dr.Ing. Thesis)
MTA-98-121	Azadi, Mohammad R. E., MK	Analysis of Static and Dynamic Pile-Soil-Jacket Behaviour. (Dr.Ing. Thesis)
MTA-98-122	Ulltang, Terje, MP	A Communication Model for Product Information. (Dr.Ing. Thesis)
MTA-98-123	Torbergsen, Erik, MM	Impeller/Diffuser Interaction Forces in Centrifugal Pumps. (Dr.Ing. Thesis)
MTA-98-124	Hansen, Edmond, MH	A Discrete Element Model to Study Marginal Ice Zone Dynamics and the Behaviour of Vessels Moored in Broken Ice. (Dr.Ing. Thesis)
MTA-98-125	Videiro, Paulo M., MK	Reliability Based Design of Marine Structures. (Dr.Ing. Thesis)
MTA-99-126	Mainçon, Philippe, MK	Fatigue Reliability of Long Welds Application to Titanium Risers. (Dr.Ing. Thesis)
MTA-99-127	Haugen, Elin M., MH	Hydroelastic Analysis of Slamming on Stiffened Plates with Application to Catamaran Wetdecks. (Dr.Ing. Thesis)
MTA-99-128	Langhelle, Nina K., MK	Experimental Validation and Calibration of Nonlinear Finite Element Models for Use in Design of Aluminium Structures Exposed to Fire. (Dr.Ing. Thesis)
MTA-99-	Berstad, Are J., MK	Calculation of Fatigue Damage in Ship Structures.

129		(Dr.Ing. Thesis)
MTA-99-130	Andersen, Trond M., MM	Short Term Maintenance Planning. (Dr.Ing. Thesis)
MTA-99-131	Tveiten, Bård Wathne, MK	Fatigue Assessment of Welded Aluminium Ship Details. (Dr.Ing. Thesis)
MTA-99-132	Søreide, Fredrik, MP	Applications of underwater technology in deep water archaeology. Principles and practice. (Dr.Ing. Thesis)
MTA-99-133	Tønnessen, Rune, MH	A Finite Element Method Applied to Unsteady Viscous Flow Around 2D Blunt Bodies With Sharp Corners. (Dr.Ing. Thesis)
MTA-99-134	Elvekrok, Dag R., MP	Engineering Integration in Field Development Projects in the Norwegian Oil and Gas Industry. The Supplier Management of Norne. (Dr.Ing. Thesis)
MTA-99-135	Fagerholt, Kjetil, MP	Optimeringsbaserte Metoder for Ruteplanlegging innen skipsfart. (Dr.Ing. Thesis)
MTA-99-136	Bysveen, Marie, MM	Visualization in Two Directions on a Dynamic Combustion Rig for Studies of Fuel Quality. (Dr.Ing. Thesis)
MTA-2000-137	Storteig, Eskild, MM	Dynamic characteristics and leakage performance of liquid annular seals in centrifugal pumps. (Dr.Ing. Thesis)
MTA-2000-138	Sagli, Gro, MK	Model uncertainty and simplified estimates of long term extremes of hull girder loads in ships. (Dr.Ing. Thesis)
MTA-2000-139	Tronstad, Harald, MK	Nonlinear analysis and design of cable net structures like fishing gear based on the finite element method. (Dr.Ing. Thesis)
MTA-2000-140	Kroneberg, André, MP	Innovation in shipping by using scenarios. (Dr.Ing. Thesis)
MTA-2000-141	Haslum, Herbjørn Alf, MH	Simplified methods applied to nonlinear motion of spar platforms. (Dr.Ing. Thesis)
MTA-2001-142	Samdal, Ole Johan, MM	Modelling of Degradation Mechanisms and Stressor Interaction on Static Mechanical Equipment Residual Lifetime. (Dr.Ing. Thesis)
MTA-2001-143	Baarholm, Rolf Jarle, MH	Theoretical and experimental studies of wave impact underneath decks of offshore platforms. (Dr.Ing. Thesis)
MTA-2001-144	Wang, Lihua, MK	Probabilistic Analysis of Nonlinear Wave-induced Loads on Ships. (Dr.Ing. Thesis)
MTA-2001-145	Kristensen, Odd H. Holt, MK	Ultimate Capacity of Aluminium Plates under Multiple Loads, Considering HAZ Properties. (Dr.Ing. Thesis)
MTA-2001-146	Greco, Marilena, MH	A Two-Dimensional Study of Green-Water

		Loading. (Dr.Ing. Thesis)
MTA-2001-147	Heggelund, Svein E., MK	Calculation of Global Design Loads and Load Effects in Large High Speed Catamarans. (Dr.Ing. Thesis)
MTA-2001-148	Babalola, Olusegun T., MK	Fatigue Strength of Titanium Risers – Defect Sensitivity. (Dr.Ing. Thesis)
MTA-2001-149	Mohammed, Abuu K., MK	Nonlinear Shell Finite Elements for Ultimate Strength and Collapse Analysis of Ship Structures. (Dr.Ing. Thesis)
MTA-2002-150	Holmedal, Lars E., MH	Wave-current interactions in the vicinity of the sea bed. (Dr.Ing. Thesis)
MTA-2002-151	Rognebakke, Olav F., MH	Sloshing in rectangular tanks and interaction with ship motions. (Dr.Ing. Thesis)
MTA-2002-152	Lader, Pål Furset, MH	Geometry and Kinematics of Breaking Waves. (Dr.Ing. Thesis)
MTA-2002-153	Yang, Qinzheng, MH	Wash and wave resistance of ships in finite water depth. (Dr.Ing. Thesis)
MTA-2002-154	Melhus, Øyvin, MM	Utilization of VOC in Diesel Engines. Ignition and combustion of VOC released by crude oil tankers. (Dr.Ing. Thesis)
MTA-2002-155	Ronæss, Marit, MH	Wave Induced Motions of Two Ships Advancing on Parallel Course. (Dr.Ing. Thesis)
MTA-2002-156	Økland, Ole D., MK	Numerical and experimental investigation of whipping in twin hull vessels exposed to severe wet deck slamming. (Dr.Ing. Thesis)
MTA-2002-157	Ge, Chunhua, MK	Global Hydroelastic Response of Catamarans due to Wet Deck Slamming. (Dr.Ing. Thesis)
MTA-2002-158	Byklum, Eirik, MK	Nonlinear Shell Finite Elements for Ultimate Strength and Collapse Analysis of Ship Structures. (Dr.Ing. Thesis)
IMT-2003-1	Chen, Haibo, MK	Probabilistic Evaluation of FPSO-Tanker Collision in Tandem Offloading Operation. (Dr.Ing. Thesis)
IMT-2003-2	Skaugset, Kjetil Bjørn, MK	On the Suppression of Vortex Induced Vibrations of Circular Cylinders by Radial Water Jets. (Dr.Ing. Thesis)
IMT-2003-3	Chezhian, Muthu	Three-Dimensional Analysis of Slamming. (Dr.Ing. Thesis)
IMT-2003-4	Buhaug, Øyvind	Deposit Formation on Cylinder Liner Surfaces in Medium Speed Engines. (Dr.Ing. Thesis)
IMT-2003-5	Tregde, Vidar	Aspects of Ship Design: Optimization of Aft Hull with Inverse Geometry Design. (Dr.Ing. Thesis)
IMT-	Wist, Hanne Therese	Statistical Properties of Successive Ocean Wave

2003-6		Parameters. (Dr.Ing. Thesis)
IMT-2004-7	Ransau, Samuel	Numerical Methods for Flows with Evolving Interfaces. (Dr.Ing. Thesis)
IMT-2004-8	Soma, Torkel	Blue-Chip or Sub-Standard. A data interrogation approach of identity safety characteristics of shipping organization. (Dr.Ing. Thesis)
IMT-2004-9	Ersdal, Svein	An experimental study of hydrodynamic forces on cylinders and cables in near axial flow. (Dr.Ing. Thesis)
IMT-2005-10	Brodtkorb, Per Andreas	The Probability of Occurrence of Dangerous Wave Situations at Sea. (Dr.Ing. Thesis)
IMT-2005-11	Yttervik, Rune	Ocean current variability in relation to offshore engineering. (Dr.Ing. Thesis)
IMT-2005-12	Fredheim, Arne	Current Forces on Net-Structures. (Dr.Ing. Thesis)
IMT-2005-13	Heggernes, Kjetil	Flow around marine structures. (Dr.Ing. Thesis
IMT-2005-14	Fouques, Sebastien	Lagrangian Modelling of Ocean Surface Waves and Synthetic Aperture Radar Wave Measurements. (Dr.Ing. Thesis)
IMT-2006-15	Holm, Håvard	Numerical calculation of viscous free surface flow around marine structures. (Dr.Ing. Thesis)
IMT-2006-16	Bjørheim, Lars G.	Failure Assessment of Long Through Thickness Fatigue Cracks in Ship Hulls. (Dr.Ing. Thesis)
IMT-2006-17	Hansson, Lisbeth	Safety Management for Prevention of Occupational Accidents. (Dr.Ing. Thesis)
IMT-2006-18	Zhu, Xinying	Application of the CIP Method to Strongly Nonlinear Wave-Body Interaction Problems. (Dr.Ing. Thesis)
IMT-2006-19	Reite, Karl Johan	Modelling and Control of Trawl Systems. (Dr.Ing. Thesis)
IMT-2006-20	Smogeli, Øyvind Notland	Control of Marine Propellers. From Normal to Extreme Conditions. (Dr.Ing. Thesis)
IMT-2007-21	Storhaug, Gaute	Experimental Investigation of Wave Induced Vibrations and Their Effect on the Fatigue Loading of Ships. (Dr.Ing. Thesis)
IMT-2007-22	Sun, Hui	A Boundary Element Method Applied to Strongly Nonlinear Wave-Body Interaction Problems. (PhD Thesis, CeSOS)
IMT-2007-23	Rustad, Anne Marthine	Modelling and Control of Top Tensioned Risers. (PhD Thesis, CeSOS)
IMT-2007-24	Johansen, Vegar	Modelling flexible slender system for real-time simulations and control applications
IMT-2007-25	Wroldsen, Anders Sunde	Modelling and control of tensegrity structures.

		(PhD Thesis, CeSOS)
IMT-2007-26	Aronsen, Kristoffer Høye	An experimental investigation of in-line and combined inline and cross flow vortex induced vibrations. (Dr. avhandling, IMT)
IMT-2007-27	Gao, Zhen	Stochastic Response Analysis of Mooring Systems with Emphasis on Frequency-domain Analysis of Fatigue due to Wide-band Response Processes (PhD Thesis, CeSOS)
IMT-2007-28	Thorstensen, Tom Anders	Lifetime Profit Modelling of Ageing Systems Utilizing Information about Technical Condition. (Dr.ing. thesis, IMT)
IMT-2008-29	Refsnes, Jon Erling Gorset	Nonlinear Model-Based Control of Slender Body AUVs (PhD Thesis, IMT)
IMT-2008-30	Berntsen, Per Ivar B.	Structural Reliability Based Position Mooring. (PhD-Thesis, IMT)
IMT-2008-31	Ye, Naiquan	Fatigue Assessment of Aluminium Welded Box-stiffener Joints in Ships (Dr.ing. thesis, IMT)
IMT-2008-32	Radan, Damir	Integrated Control of Marine Electrical Power Systems. (PhD-Thesis, IMT)
IMT-2008-33	Thomassen, Paul	Methods for Dynamic Response Analysis and Fatigue Life Estimation of Floating Fish Cages. (Dr.ing. thesis, IMT)
IMT-2008-34	Pákozdi, Csaba	A Smoothed Particle Hydrodynamics Study of Two-dimensional Nonlinear Sloshing in Rectangular Tanks. (Dr.ing.thesis, IMT/ CeSOS)
IMT-2007-35	Grytøyr, Guttorm	A Higher-Order Boundary Element Method and Applications to Marine Hydrodynamics. (Dr.ing.thesis, IMT)
IMT-2008-36	Drummen, Ingo	Experimental and Numerical Investigation of Nonlinear Wave-Induced Load Effects in Containerships considering Hydroelasticity. (PhD thesis, CeSOS)
IMT-2008-37	Skejic, Renato	Maneuvering and Seakeeping of a Singel Ship and of Two Ships in Interaction. (PhD-Thesis, CeSOS)
IMT-2008-38	Harlem, Alf	An Age-Based Replacement Model for Repairable Systems with Attention to High-Speed Marine Diesel Engines. (PhD-Thesis, IMT)
IMT-2008-39	Alsos, Hagbart S.	Ship Grounding. Analysis of Ductile Fracture, Bottom Damage and Hull Girder Response. (PhD-thesis, IMT)
IMT-2008-40	Graczyk, Mateusz	Experimental Investigation of Sloshing Loading and Load Effects in Membrane LNG Tanks Subjected to Random Excitation. (PhD-thesis, CeSOS)
IMT-2008-41	Taghipour, Reza	Efficient Prediction of Dynamic Response for Flexible amd Multi-body Marine Structures. (PhD-

		thesis, CeSOS)
IMT-2008-42	Ruth, Eivind	Propulsion control and thrust allocation on marine vessels. (PhD thesis, CeSOS)
IMT-2008-43	Nystad, Bent Helge	Technical Condition Indexes and Remaining Useful Life of Aggregated Systems. PhD thesis, IMT
IMT-2008-44	Soni, Prashant Kumar	Hydrodynamic Coefficients for Vortex Induced Vibrations of Flexible Beams, PhD thesis, CeSOS
IMT-2009-45	Amlashi, Hadi K.K.	Ultimate Strength and Reliability-based Design of Ship Hulls with Emphasis on Combined Global and Local Loads. PhD Thesis, IMT
IMT-2009-46	Pedersen, Tom Arne	Bond Graph Modelling of Marine Power Systems. PhD Thesis, IMT
IMT-2009-47	Kristiansen, Trygve	Two-Dimensional Numerical and Experimental Studies of Piston-Mode Resonance. PhD-Thesis, CeSOS
IMT-2009-48	Ong, Muk Chen	Applications of a Standard High Reynolds Number Model and a Stochastic Scour Prediction Model for Marine Structures. PhD-thesis, IMT
IMT-2009-49	Hong, Lin	Simplified Analysis and Design of Ships subjected to Collision and Grounding. PhD-thesis, IMT
IMT-2009-50	Koushan, Kamran	Vortex Induced Vibrations of Free Span Pipelines, PhD thesis, IMT
IMT-2009-51	Korsvik, Jarl Eirik	Heuristic Methods for Ship Routing and Scheduling. PhD-thesis, IMT
IMT-2009-52	Lee, Jihoon	Experimental Investigation and Numerical in Analyzing the Ocean Current Displacement of Longlines. Ph.d.-Thesis, IMT.
IMT-2009-53	Vestbøstad, Tone Gran	A Numerical Study of Wave-in-Deck Impact usin a Two-Dimensional Constrained Interpolation Profile Method, Ph.d.thesis, CeSOS.
IMT-2009-54	Bruun, Kristine	Bond Graph Modelling of Fuel Cells for Marine Power Plants. Ph.d.-thesis, IMT
IMT 2009-55	Holstad, Anders	Numerical Investigation of Turbulence in a Sekwed Three-Dimensional Channel Flow, Ph.d.-thesis, IMT.
IMT 2009-56	Ayala-Uraga, Efren	Reliability-Based Assessment of Deteriorating Ship-shaped Offshore Structures, Ph.d.-thesis, IMT
IMT 2009-57	Kong, Xiangjun	A Numerical Study of a Damaged Ship in Beam Sea Waves. Ph.d.-thesis, IMT/CeSOS.
IMT 2010-58	Kristiansen, David	Wave Induced Effects on Floaters of Aquaculture Plants, Ph.d.-thesis, CeSOS.

IMT 2010-59	Ludvigsen, Martin	An ROV-Toolbox for Optical and Acoustic Scientific Seabed Investigation. Ph.d.-thesis IMT.
IMT 2010-60	Hals, Jørgen	Modelling and Phase Control of Wave-Energy Converters. Ph.d.thesis, CeSOS.
IMT 2010- 61	Shu, Zhi	Uncertainty Assessment of Wave Loads and Ultimate Strength of Tankers and Bulk Carriers in a Reliability Framework. Ph.d. Thesis, IMT/ CeSOS
IMT 2010-62	Shao, Yanlin	Numerical Potential-Flow Studies on Weakly-Nonlinear Wave-Body Interactions with/without Small Forward Speed, Ph.d.thesis,CeSOS.
IMT 2010-63	Califano, Andrea	Dynamic Loads on Marine Propellers due to Intermittent Ventilation. Ph.d.thesis, IMT.
IMT 2010-64	El Khoury, George	Numerical Simulations of Massively Separated Turbulent Flows, Ph.d.-thesis, IMT
IMT 2010-65	Seim, Knut Sponheim	Mixing Process in Dense Overflows with Emphasis on the Faroe Bank Channel Overflow. Ph.d.thesis, IMT
IMT 2010-66	Jia, Huirong	Structural Analysis of Intect and Damaged Ships in a Collission Risk Analysis Perspective. Ph.d.thesis CeSoS.
IMT 2010-67	Jiao, Linlin	Wave-Induced Effects on a Pontoon-type Very Large Floating Structures (VLFS). Ph.D.-thesis, CeSOS.
IMT 2010-68	Abrahamsen, Bjørn Christian	Sloshing Induced Tank Roof with Entrapped Air Pocket. Ph.d.thesis, CeSOS.
IMT 2011-69	Karimirad, Madjid	Stochastic Dynamic Response Analysis of Spar-Type Wind Turbines with Catenary or Taut Mooring Systems. Ph.d.-thesis, CeSOS.
IMT - 2011-70	Erlend Meland	Condition Monitoring of Safety Critical Valves. Ph.d.-thesis, IMT.
IMT – 2011-71	Yang, Limin	Stochastic Dynamic System Analysis of Wave Energy Converter with Hydraulic Power Take-Off, with Particular Reference to Wear Damage Analysis, Ph.d. Thesis, CeSOS.
IMT – 2011-72	Visscher, Jan	Application of Particla Image Velocimetry on Turbulent Marine Flows, Ph.d.Thesis, IMT.
IMT – 2011-73	Su, Biao	Numerical Predictions of Global and Local Ice Loads on Ships. Ph.d.Thesis, CeSOS.
IMT – 2011-74	Liu, Zhenhui	Analytical and Numerical Analysis of Iceberg Collision with Ship Structures. Ph.d.Thesis, IMT.
IMT – 2011-75	Aarsæther, Karl Gunnar	Modeling and Analysis of Ship Traffic by Observation and Numerical Simulation. Ph.d.Thesis, IMT.

Imt – 2011-76	Wu, Jie	Hydrodynamic Force Identification from Stochastic Vortex Induced Vibration Experiments with Slender Beams. Ph.d.Thesis, IMT.
Imt – 2011-77	Amini, Hamid	Azimuth Propulsors in Off-design Conditions. Ph.d.Thesis, IMT.
IMT – 2011-78	Nguyen, Tan-Hoi	Toward a System of Real-Time Prediction and Monitoring of Bottom Damage Conditions During Ship Grounding. Ph.d.thesis, IMT.
IMT- 2011-79	Tavakoli, Mohammad T.	Assessment of Oil Spill in Ship Collision and Grounding, Ph.d.thesis, IMT.
IMT- 2011-80	Guo, Bingjie	Numerical and Experimental Investigation of Added Resistance in Waves. Ph.d.Thesis, IMT.
IMT- 2011-81	Chen, Qiaofeng	Ultimate Strength of Aluminium Panels, considering HAZ Effects, IMT
IMT- 2012-82	Kota, Ravikiran S.	Wave Loads on Decks of Offshore Structures in Random Seas, CeSOS.
IMT- 2012-83	Sten, Ronny	Dynamic Simulation of Deep Water Drilling Risers with Heave Compensating System, IMT.
IMT- 2012-84	Berle, Øyvind	Risk and resilience in global maritime supply chains, IMT.
IMT- 2012-85	Fang, Shaoji	Fault Tolerant Position Mooring Control Based on Structural Reliability, CeSOS.
IMT- 2012-86	You, Jikun	Numerical studies on wave forces and moored ship motions in intermediate and shallow water, CeSOS.
IMT- 2012-87	Xiang ,Xu	Maneuvering of two interacting ships in waves, CeSOS
IMT- 2012-88	Dong, Wenbin	Time-domain fatigue response and reliability analysis of offshore wind turbines with emphasis on welded tubular joints and gear components, CeSOS
IMT- 2012-89	Zhu, Suji	Investigation of Wave-Induced Nonlinear Load Effects in Open Ships considering Hull Girder Vibrations in Bending and Torsion, CeSOS
IMT- 2012-90	Zhou, Li	Numerical and Experimental Investigation of Station-keeping in Level Ice, CeSOS
IMT- 2012-91	Ushakov, Sergey	Particulate matter emission characteristics from diesel enignes operating on conventional and alternative marine fuels, IMT
IMT- 2013-1	Yin, Decao	Experimental and Numerical Analysis of Combined In-line and Cross-flow Vortex Induced Vibrations, CeSOS

IMT-2013-2	Kurniawan, Adi	Modelling and geometry optimisation of wave energy converters, CeSOS
IMT-2013-3	Al Ryati, Nabil	Technical condition indexes doe auxiliary marine diesel engines, IMT
IMT-2013-4	Firoozkoohi, Reza	Experimental, numerical and analytical investigation of the effect of screens on sloshing, CeSOS
IMT-2013-5	Ommani, Babak	Potential-Flow Predictions of a Semi-Displacement Vessel Including Applications to Calm Water Broaching, CeSOS
IMT-2013-6	Xing, Yihan	Modelling and analysis of the gearbox in a floating spar-type wind turbine, CeSOS
IMT-7-2013	Balland, Océane	Optimization models for reducing air emissions from ships, IMT
IMT-8-2013	Yang, Dan	Transitional wake flow behind an inclined flat plate-----Computation and analysis, IMT
IMT-9-2013	Abdillah, Suyuthi	Prediction of Extreme Loads and Fatigue Damage for a Ship Hull due to Ice Action, IMT
IMT-10-2013	Ramìrez, Pedro Agustìn Pèrez	Ageing management and life extension of technical systems- Concepts and methods applied to oil and gas facilities, IMT
IMT-11-2013	Chuang, Zhenju	Experimental and Numerical Investigation of Speed Loss due to Seakeeping and Maneuvering. IMT
IMT-12-2013	Etemaddar, Mahmoud	Load and Response Analysis of Wind Turbines under Atmospheric Icing and Controller System Faults with Emphasis on Spar Type Floating Wind Turbines, IMT
IMT-13-2013	Lindstad, Haakon	Strategies and measures for reducing maritime CO2 emissons, IMT
IMT-14-2013	Haris, Sabril	Damage interaction analysis of ship collisions, IMT
IMT-15-2013	Shainee, Mohamed	Conceptual Design, Numerical and Experimental Investigation of a SPM Cage Concept for Offshore Mariculture, IMT
IMT-16-2013	Gansel, Lars	Flow past porous cylinders and effects of biofouling and fish behavior on the flow in and around Atlantic salmon net cages, IMT
IMT-17-2013	Gaspar, Henrique	Handling Aspects of Complexity in Conceptual Ship Design, IMT
IMT-18-2013	Thys, Maxime	Theoretical and Experimental Investigation of a Free Running Fishing Vessel at Small Frequency of Encounter, CeSOS
IMT-19-2013	Aglen, Ida	VIV in Free Spanning Pipelines, CeSOS

IMT-1-2014	Song, An	Theoretical and experimental studies of wave diffraction and radiation loads on a horizontally submerged perforated plate, CeSOS
IMT-2-2014	Rogne, Øyvind Ygre	Numerical and Experimental Investigation of a Hinged 5-body Wave Energy Converter, CeSOS
IMT-3-2014	Dai, Lijuan	Safe and efficient operation and maintenance of offshore wind farms ,IMT
IMT-4-2014	Bachynski, Erin Elizabeth	Design and Dynamic Analysis of Tension Leg Platform Wind Turbines, CeSOS
IMT-5-2014	Wang, Jingbo	Water Entry of Freefall Wedged – Wedge motions and Cavity Dynamics, CeSOS
IMT-6-2014	Kim, Ekaterina	Experimental and numerical studies related to the coupled behavior of ice mass and steel structures during accidental collisions, IMT
IMT-7-2014	Tan, Xiang	Numerical investigation of ship's continuous- mode icebreaking in leverl ice, CeSOS
IMT-8-2014	Muliawan, Made Jaya	Design and Analysis of Combined Floating Wave and Wind Power Facilities, with Emphasis on Extreme Load Effects of the Mooring System, CeSOS
IMT-9-2014	Jiang, Zhiyu	Long-term response analysis of wind turbines with an emphasis on fault and shutdown conditions, IMT
IMT-10-2014	Dukan, Fredrik	ROV Motion Control Systems, IMT
IMT-11-2014	Grimsmo, Nils I.	Dynamic simulations of hydraulic cylinder for heave compensation of deep water drilling risers, IMT
IMT-12-2014	Kvittem, Marit I.	Modelling and response analysis for fatigue design of a semisubmersible wind turbine, CeSOS
IMT-13-2014	Akhtar, Juned	The Effects of Human Fatigue on Risk at Sea, IMT
IMT-14-2014	Syahroni, Nur	Fatigue Assessment of Welded Joints Taking into Account Effects of Residual Stress, IMT
IMT-1-2015	Bøckmann, Eirik	Wave Propulsion of ships, IMT
IMT-2-2015	Wang, Kai	Modelling and dynamic analysis of a semi-submersible floating vertical axis wind turbine, CeSOS
IMT-3-2015	Fredriksen, Arnt Gunvald	A numerical and experimental study of a two-dimensional body with moonpool in waves and current, CeSOS
IMT-4-2015	Jose Patricio Gallardo Canabes	Numerical studies of viscous flow around bluff bodies, IMT

IMT-5-2015	Vegard Longva	Formulation and application of finite element techniques for slender marine structures subjected to contact interactions, IMT
IMT-6-2015	Jacobus De Vaal	Aerodynamic modelling of floating wind turbines, CeSOS
IMT-7-2015	Fachri Nasution	Fatigue Performance of Copper Power Conductors, IMT
IMT-8-2015	Oleh I Karpa	Development of bivariate extreme value distributions for applications in marine technology,CeSOS
IMT-9-2015	Daniel de Almeida Fernandes	An output feedback motion control system for ROVs, AMOS
IMT-10-2015	Bo Zhao	Particle Filter for Fault Diagnosis: Application to Dynamic Positioning Vessel and Underwater Robotics, CeSOS
IMT-11-2015	Wenting Zhu	Impact of emission allocation in maritime transportation, IMT
IMT-12-2015	Amir Rasekhi Nejad	Dynamic Analysis and Design of Gearboxes in Offshore Wind Turbines in a Structural Reliability Perspective, CeSOS
IMT-13-2015	Arturo Jesùs Ortega Malca	Dynamic Response of Flexibles Risers due to Unsteady Slug Flow, CeSOS
IMT-14-2015	Dagfinn Husjord	Guidance and decision-support system for safe navigation of ships operating in close proximity, IMT
IMT-15-2015	Anirban Bhattacharyya	Ducted Propellers: Behaviour in Waves and Scale Effects, IMT
IMT-16-2015	Qin Zhang	Image Processing for Ice Parameter Identification in Ice Management, IMT
IMT-1-2016	Vincentius Rumawas	Human Factors in Ship Design and Operation: An Experiential Learning, IMT
IMT-2-2016	Martin Storheim	Structural response in ship-platform and ship-ice collisions, IMT
IMT-3-2016	Mia Abrahamsen Prsic	Numerical Simulations of the Flow around single and Tandem Circular Cylinders Close to a Plane Wall, IMT
IMT-4-2016	Tufan Arslan	Large-eddy simulations of cross-flow around ship sections, IMT

IMT-5-2016	Pierre Yves-Henry	Parametrisation of aquatic vegetation in hydraulic and coastal research,IMT
IMT-6-2016	Lin Li	Dynamic Analysis of the Instalation of Monopiles for Offshore Wind Turbines, CeSOS
IMT-7-2016	Øivind Kåre Kjerstad	Dynamic Positioning of Marine Vessels in Ice, IMT
IMT-8-2016	Xiaopeng Wu	Numerical Analysis of Anchor Handling and Fish Trawling Operations in a Safety Perspective, CeSOS
IMT-9-2016	Zhengshun Cheng	Integrated Dynamic Analysis of Floating Vertical Axis Wind Turbines, CeSOS
IMT-10-2016	Ling Wan	Experimental and Numerical Study of a Combined Offshore Wind and Wave Energy Converter Concept
IMT-11-2016	Wei Chai	Stochastic dynamic analysis and reliability evaluation of the roll motion for ships in random seas, CeSOS
IMT-12-2016	Øyvind Selnes Patricksson	Decision support for conceptual ship design with focus on a changing life cycle and future uncertainty, IMT
IMT-13-2016	Mats Jørgen Thorsen	Time domain analysis of vortex-induced vibrations, IMT
IMT-14-2016	Edgar McGuinness	Safety in the Norwegian Fishing Fleet – Analysis and measures for improvement, IMT
IMT-15-2016	Sepideh Jafarzadeh	Energy effiency and emission abatement in the fishing fleet, IMT
IMT-16-2016	Wilson Ivan Guachamin Acero	Assessment of marine operations for offshore wind turbine installation with emphasis on response-based operational limits, IMT
IMT-17-2016	Mauro Candeloro	Tools and Methods for Autonomous Operations on Seabed and Water Coumn using Underwater Vehicles, IMT
IMT-18-2016	Valentin Chabaud	Real-Time Hybrid Model Testing of Floating Wind Tubines, IMT
IMT-1-2017	Mohammad Saud Afzal	Three-dimensional streaming in a sea bed boundary layer, IMT
IMT-2-2017	Peng Li	A Theoretical and Experimental Study of Wave-induced Hydroelastic Response of a Circular Floating Collar, IMT